Petrogenese der Alkalimagmatite der südlichen Zentraleuropäischen Vulkanprovinz

Dissertation

der Mathematisch-Naturwissenschaftlichen Fakultät
der Eberhard Karls Universität Tübingen
zur Erlangung des Grades eines
Doktors der Naturwissenschaften
(Dr. rer. nat.)

vorgelegt von
Thomas Binder, M.Sc.
aus Salzgitter

Tübingen
2024

Gedruckt mit Genehmigung der Mathematisch-Naturwissenschaftlichen Fakultät der Eberhard Karls Universität Tübingen.

Tag der mündlichen Qualifikation:	24.01.2025
Dekan:	Prof. Dr. Thilo Stehle
1. Berichterstatter:	Prof. Dr. Ronny Schönberg
2. Berichterstatter:	PD Dr. Michael A. W. Marks

Inhalt

Danksagung vii

Zusammenfassung viii

Abstract x

Liste der Publikationen der Dissertation xii

Arbeit 1 xii

Arbeit 2 xiii

Arbeit 3 xiii

1. Einleitung 1

1.1. Die südliche Zentraleuropäische Vulkanprovinz (ZEVP) als Untersuchungsgebiet 1

1.1.1. Strukturgeologische Aspekte 2

1.1.2. Modelle für die geodynamische Entwicklung des Untersuchungsgebiets 2

1.2. Petrogenese alkalischer SiO_2-untersättigter Intraplattenvulkanite 5

2. Material, Methoden und Zielsetzung 8

2.1. U-Pb-Geochronologie und Petrografie 8

2.2. Geochemische Zusammensetzung des Gesamtgesteins und der Minerale der primitiven Melilithite, Nephelinite und Basanite 9

2.3. Geochemische Zusammensetzung des Gesamtgesteins und der Minerale der Nosean-Phonolithe und (Nephelin-)Syenit-Einschlüsse des Hegaus 10

3. Ergebnisse und Diskussion 11

3.1. Verlauf und Dauer des Vulkanismus in der südlichen ZEVP 11

3.1.1. Rückschlüsse auf die chronologische und petrografische Entwicklung der gesamten ZEVP 13

3.2. Petrogenese der Melilithite, Foidite und Basanite 15

3.2.1. Kristallisationsbedingungen 16

3.2.2. Kristallfracht als Schlüssel zum Verständnis von Schmelzentwicklung, Magmeninteraktion und Aufstiegsprozessen 17

3.2.3. Frühmagmatische Kristallisation: Die unterschiedliche Rolle von CO_2 und Karbonaten in der Magmaquelle 19
3.2.4. Spätmagmatische Entwicklung, die Bedeutung von Volatilen und Entgasung 21
3.2.5. Der geringe Einfluss von fraktionierter Kristallisation, Magmamischung und Nebengesteinsinteraktion in den primitiven Gesteinen 23
3.2.6. Petrogenese der entwickelten Haüyn/Nosean-reichen Gesteine 24
3.2.7. Magmaquelle(n) und Aufschmelzgrade 25
3.2.8. Magmagenese im Rahmen der regionalen geodynamischen Entwicklung 27
3.3. Entstehung der Nosean-Phonolithe im Hegau als Folge von Differentiationsprozessen 31
3.3.1. Ijolithische Schlieren als Folge von In-situ-Differentiation: ein Bindeglied zwischen melilithitischen bis nephelinitischen und phonolithischen Magmen? .. 32
3.3.2. Fraktionierte Kristallisation melilithitischer bis nephelinitischer Schmelzen ermöglicht die Entwicklung zu Nosean-Phonolithen 33
3.3.3. Die Bunsen-Daly-Lücke und Konsequenzen für die vulkanische Entwicklung 35
4. Fazit 38
Literaturverzeichnis 40
Akzeptierte Publikationen und eingereichte Manuskripte……Anhänge I, II & III

Danksagung

Mein besonderer Dank gilt Prof. Dr. Gregor Markl für die Vergabe und vertrauensvolle Betreuung des Promotionsthemas, die finanzielle Unterstützung während der Promotionszeit und darüber hinaus sowie für die zahlreichen konstruktiven Diskussionen, Kommentare und Vorschläge zur konzeptionellen und inhaltlichen Gestaltung der Manuskripte. Mein größter Respekt gilt dem überaus zügigen, konstruktiven und effektiven Umgang mit Revisionen von Manuskripten und dazugehörigen Antwortschreiben sowie dem nachhaltigen und zielorientierten Lösen unvorhergesehener oder bürokratischer Probleme.
Ebenso großer Dank gebührt PD Dr. Michael Marks für die kontinuierliche, umfangreiche und produktive Betreuung während der gesamten Projektzeit und die zahlreichen Gespräche mit Vorschlägen, Anregungen und Ideen zu Publikationen, Konferenzbeiträgen, Präsentationen und Analysenverfahren. Die kritischen, detailreichen und umfassenden Beiträge und Anmerkungen zu meinen Manuskriptentwürfen und unsere anregenden Fachdiskussionen sind besonders hervorzuheben. Des Weiteren danke ich PD Dr. Michael Marks und PD Dr. Benjamin Walter für die Arbeit und Zeit, die sie für den Forschungsantrag (Deutsche Forschungsgemeinschaft, Förder-Nr. MA 2563/19 und WA 3116/6) aufgewendet haben, über welchen mir eine dreijährige Finanzierung und die Forschung im Rahmen dieser Promotion ermöglicht wurde. Außerdem danke ich Prof. Dr. Ronny Schönberg und PD Dr. Michael Marks für die Begutachtung dieser Arbeit.
Ich danke PD Dr. Thomas Wenzel für die effektive, kompetente und leidenschaftliche Einweisung in die Bedienung der Elektronenstrahlmikrosonde sowie für die vielen Vorschläge und Anregungen zur bestmöglichen Optimierung der Analytik. Ebenfalls dankbar bin ich für die motivierenden und konstruktiven Kommentare zu Manuskripten und unsere vielen Gespräche während der Mittags- und Kaffeepause.
Darüber hinaus bedanke ich mich bei Dr. Axel Gerdes, Dr. Jens Grimmer, Dr. Aratz Beranoaguirre, Brian-Eric Friedrichsen und allen bereits genannten Mitautoren der Publikationen für die erfolgreiche Zusammenarbeit und ihre unverzichtbaren Beiträge. Zudem gilt mein Dank Beate Fritz für die unbürokratische und schnelle Bearbeitung von Verwaltungsangelegenheiten. Für die Bereitstellung, Aufbereitung, Präparation und Analyse von Probenmaterial sowie verschiedenste Vorarbeiten und Voruntersuchungen zu meinem Projekt bedanke ich mich bei PD Dr. Benjamin Walter, Dr. Udo Neumann, Simone Schafflick, PD Dr. Elisabeth Eiche, Claudia Mößner, Janine Wagner, Philip Werner, Alexander Rettenberger, Tim Langner, Tim Treiber, Gabriele Stoschek, Per Jeisecke, Laura Paskert, Noam Poremba, David Günzler, Cyrille Delangle, Luc Jaillard, Klaus Brauch, Prof. Dr. Horst Marschall, Prof. Dr. Peter Prinz-Grimm, Dr. Dieter Nesbor, L. Behr und Prof. Dr. Kirsten Grimm.
Besonderer Dank gilt meinen Freunden, Kollegen und noch nicht genannten aktuellen oder ehemaligen Mitgliedern der Arbeitsgruppe Nicolas Meyer, Dr. Manuel Scharrer, Dr. Simon Braunger, Benjamin Möller, Fabian Schmitt, Andreja Ladišić, Dominic Raisch, Lukas Mössinger, Dr. Sebastian Staude, Dr. Tatjana Epp, Dr. Hans Eggenkamp, Dr. Dominik Gudelius, Dr. Johannes Giebel, Curtis Rooks und Rebekka Reich für die vielen Fachdiskussionen und Gespräche abseits der Geologie, die großartige Arbeitsatmosphäre und den unvergleichlichen Teamgeist.
Nicht zuletzt danke ich meiner Familie, insbesondere meinen Eltern Anke und Ralf Binder, für die immerwährende Unterstützung, ohne die diese Promotion nicht möglich gewesen wäre.

Zusammenfassung

Der südliche Teil der oberkretazischen bis holozänen Zentraleuropäischen Vulkanprovinz (ZEVP) in SW-Deutschland und Ostfrankreich umfasst überwiegend primitive, seltener entwickelte alkalische, SiO_2-untersättigte Gesteine, deren Entstehung bislang nur unzureichend verstanden wird, da zuverlässige Altersdaten sowie umfangreiche und flächendeckende geo- und mineralchemische Untersuchungen fehlten. In dieser Arbeit wird ein petrogenetisches, geochronologisch unterstütztes Modell präsentiert, das zur Entschlüsselung der Ursachen des Vulkanismus beiträgt und auf neuen Daten aus zehn Vulkangebieten basiert. Damit konnten erstmals zwei kompositionell, räumlich und zeitlich unterscheidbare Gesteinsserien mit jeweils einem primitiven und einem entwickelten Magmatyp in der südlichen ZEVP nachgewiesen werden:

1) Eine ältere oberkretazische bis eozäne Gruppe (~73–47 Ma) umfasst überwiegend (A) primitive Olivin-Nephelinite, basanitische Nephelinite und Nephelinbasanite sowie (B) wenig verbreitete, stärker entwickelte (phonolithische) Haüynite/Noseanite und Haüyn-Nephelinite (~68–62 Ma), die durch Differentiation und begrenzte krustale Kontamination aus Typ A hervorgingen.
2) Eine jüngere oligozäne bis miozäne Gruppe (~27–9 Ma) ist durch (C) Olivin-Melilithite und Melilith-führende Olivin-Nephelinite dominiert, die im Hegau gemeinsam mit (D) stark entwickelten Nosean-Phonolithen (~14–11 Ma) auftreten, womit diese Region als einzige mit ausgeprägt bimodalem Vulkanismus im Untersuchungsgebiet eine Besonderheit darstellt.

Die unterschiedlichen geo- und mineralchemischen Zusammensetzungen, Paragenesen, Kristallisationstrends und Xenokristalle der beiden primitiven Gesteinsserien weisen auf verschiedene Magmaquellen, ein variables Ausmaß von Anreicherung, Rückhaltevermögen und Abgabe von volatilen Elementen sowie begrenzte Nebengesteinsinteraktion hin. Gelegentlich auftretende partiell resorbierte, Forsterit-verarmte Olivin-Kerne in den jüngeren Gesteinen und Grünkernpyroxene in den älteren deuten außerdem in beiden Fällen frühe, quantitativ limitierte Magmamischungsprozesse an.

Die nephelinitischen bis basanitischen Magmen (A) entstanden durch partielles Aufschmelzen (<6 %) Amphibol-führenden Granat/Spinell-Lherzoliths an der Basis der Lithosphäre, welche zuvor überwiegend durch wasserhaltige Schmelzen oder wässrige Fluide metasomatisch verändert wurde. Im Gegensatz dazu stammen die Melilith-führenden Gesteine (C) vermutlich aus der oberen Asthenosphäre, gekennzeichnet durch geringere Aufschmelzgrade (<3,5 %) eines Amphibol- ± Phlogopit-füh-

renden Granat-Wehrlits. Diese Lithologie war einer Metasomatose ausgesetzt, die im Zusammenhang mit variszischen Subduktionsprozessen steht und deren Schmelzen/Fluide durch hohe CaO-MgO- und CO_2-(CO_2+H_2O)-Verhältnisse charakterisiert sind. Ihre Infiltration und Speicherung erfolgten im Zuge des kontinuierlichen partiellen Recyclings ozeanischer Kruste, was die Abgabe von Ca, CO_2, H_2O sowie weiteren volatilen und inkompatiblen Elementen an die untere Lithosphäre umfasste, welche spätestens mit Beginn des jüngeren Magmatismus durch Aufwölbung der Asthenosphäre partiell von dieser inkorporiert wurde.

Thermodynamische Modellierung sowie mineralogische und geochemische Entwicklungstrends in den bimodal zusammengesetzten und jüngsten Vulkaniten der südlichen ZEVP im Hegau zeigen, dass sich die primitiven Schmelzen (C) unter oberkrustalen Drücken durch fraktionierte Kristallisation zu Nosean-Phonolithen (D) entwickeln können, ohne dass es zwingend signifikanter Assimilation kontinentaler Kruste bedarf. Die ausgeprägte Differenzierung primitiver Schmelzen in einem Fall und der schnelle Aufstieg im anderen lassen sich durch lokale rheologische und strukturelle Inhomogenitäten im Grundgebirge sowie zeitliche Veränderungen des Spannungsfelds während der Entwicklung des Hegau-Grabens erklären.

Beide vulkanischen Episoden in der südlichen ZEVP decken sich zeitlich mit topografischer Hebung, Erosion, Rifting und der Reaktivierung tiefgreifender Störungszonen und stehen sehr wahrscheinlich im Zusammenhang mit Phasen starker mechanischer Verschränkung des Alpenbogens mit seinem Vorland. Die ältere Periode überschnitt sich mit einer Ära anhaltender, nach Norden gerichteter kompressiver Intraplattenspannungen infolge der Kollision der Adriatischen mit der Eurasischen Platte, was zu großräumiger Deformation, isostatischem Ausgleich, Erosion und daraus resultierender Ausdünnung der Lithosphäre in der künftigen ZEVP führte. Die jüngere Periode geht mit der Hauptphase der Entwicklung des Europäischen Känozoischen Rift-Systems einher. Der Beginn der vulkanischen Tätigkeit wurde von einer Änderung der Deformation im Oberrheingraben von WNW-Extension zu ONO-Extension und -Transtension als Folge eines komplexen Zusammenspiels von Ausweichbewegungen in Reaktion auf die Krusteneinengung in den Alpen und im Französischen und Schweizer Jura flankiert. Die Magmazusammensetzungen, nur schwach magmatisch geprägte Grabenstrukturen, vulkanische Aktivität außerhalb von Gräben und die beträchtliche topografische Hebung deuten an, dass als Reaktion auf das Rifting auch Konvektion und Aufwölbung der Asthenosphäre zum Magmatismus beigetragen haben.

Abstract

The southern part of the Upper Cretaceous to Holocene Central European Volcanic Province (CEVP) in SW Germany and eastern France comprises predominantly primitive, less frequently evolved, alkaline, SiO_2-undersaturated rocks, whose genesis has so far been poorly understood due to a lack of both reliable age data and comprehensive area-wide geochemical and mineral-chemical studies. This work presents a petrogenetic model supported by geochronology that contributes to deciphering the causes of volcanism and is based on new data from ten volcanic regions. For the first time, two compositionally, spatially, and temporally distinct rock series, each with a primitive and an evolved magma type, have been identified in the southern CEVP:

1) An older Upper Cretaceous to Eocene group (~73–47 Ma) comprises predominantly (A) primitive olivine nephelinites, basanitic nephelinites and nepheline basanites, and (B) less widespread, more evolved (phonolitic) haüynites/noseanites and haüyne nephelinites (~68–62 Ma), which evolved from type A by differentiation and limited crustal contamination.
2) A younger Oligocene to Miocene group (~27–9 Ma) is dominated by (C) olivine melilitites and melilite-bearing olivine nephelinites, which occur in the Hegau region together with (D) strongly evolved nosean phonolites (~14–11 Ma), rendering this region the only one with bimodal volcanism in the study area.

Distinct geochemical and mineral-chemical compositions, parageneses, crystallization trends, and xenocrysts of the two primitive rock series indicate different magma sources, a variable degree of enrichment, retention and release of volatiles, and limited wall-rock interaction. Partly resorbed forsterite-depleted olivine cores in the younger rocks and green-core pyroxenes in the older ones further indicate quantitatively limited, early magma mixing processes in both cases.

The nephelinitic to basanitic magmas (A) were formed by partial melting (<6 %) of amphibole-bearing garnet/spinel lherzolite at the base of the lithosphere, which was previously metasomatically overprinted mainly by hydrous melts or aqueous fluids. In contrast, the melilite-bearing magmas (C) probably originate from the upper asthenosphere, characterized by lower degrees of melting (<3.5 %) of an amphibole-± phlogopite-bearing garnet wehrlite. This lithology was affected by metasomatism related to Variscan subduction processes with melts/fluids characterized by high CaO/MgO and $CO_2/(CO_2+H_2O)$ ratios. Infiltration and storage of the metasomatic

agents occurred as a result of continuous recycling of parts of the oceanic crust, including the release of Ca, CO_2, H_2O, further volatiles, and incompatible elements into the lower lithosphere, which was partially incorporated by the asthenosphere no later than the onset of younger magmatism due to asthenospheric upwelling.

Thermodynamic modelling as well as mineralogical and geochemical trajectories in the youngest volcanic rocks of the southern CEVP in the bimodal Hegau region show that the primitive melts (C) can evolve towards nosean phonolites (D) by fractional crystallization under upper crustal pressures without necessarily requiring significant assimilation of continental crust. The pronounced differentiation of primitive melts in one case and the rapid ascent in the other can be explained by local rheological and structural inhomogeneities in the basement as well as temporal changes in the stress field during the emergence of the Hegau Graben.

Both volcanic episodes in the southern CEVP coincide with topographic uplift, erosion, rifting, and the reactivation of deep-seated fault zones and are most likely related to phases of strong mechanical coupling of the Alpine orogen with its foreland. The first period overlapped with an era of persistent N-directed intraplate compressional stresses due to the collision of the Adriatic and Eurasian plates, which caused large-scale deformation, isostatic compensation, erosion, and consequent lithosphere thinning in the future CEVP. The second period coincides with the main evolution stage of the European Cenozoic Rift System. The onset of volcanic activity was accompanied by a change in deformation in the Upper Rhine Graben from (W)NW extension to (E)NE extension and transtension by a complex interplay of evasive movements in response to shortening in the Alps and the Jura Mountains. The magma compositions, barely magmatic graben structures, volcanic activity outside rifts, and remarkable exhumation indicate that in response to rifting, asthenospheric flow and upwelling also contributed to magmatism.

Liste der Publikationen der Dissertation

Die vorgelegte Dissertation befasst sich mit den folgenden aufgelisteten Publikationen. Die beigefügten Tabellen dokumentieren die Beiträge der Autoren an der jeweiligen Arbeit.

Arbeit 1

Binder T, Marks MAW, Gerdes A, Walter BF, Grimmer J, Beranoaguirre A, Wenzel T, Markl G (2023) Two distinct age groups of melilitites, foidites, and basanites from the southern Central European Volcanic Province reflect lithospheric heterogeneity. Int. J. Earth Sci. 112:881–905. https://doi.org/10.1007/s00531-022-02278-y.

Status: akzeptiert und veröffentlicht

Autor	*Wissenschaftliche Konzeption [%]*	*Datengenerierung [%]*	*Analyse und Interpretation [%]*	*Verfassen des Texts [%]*
Binder, Thomas	**50**	**55**	**65**	**55**
Marks, Michael A. W.	20	0	15	15
Gerdes, Axel	0	20	0	0
Walter, Benjamin F.	10	0	0	0
Grimmer, Jens	0	0	15	15
Beranoaguirre, Aratz	0	25	0	5
Wenzel, Thomas	5	0	0	5
Markl, Gregor	15	0	5	5

Arbeit 2

Binder T, Marks MAW, Walter BF, Wenzel T, Markl G (2024b) Two Distinct Metasomatized Mantle Sources Produced Two Groups of Alkaline SiO_2-Undersaturated Rocks in the Southern Central European Volcanic Province. J. Petrol. 65(7):1–29. https://doi.org/10.1093/petrology/egae070.

Status: akzeptiert und veröffentlicht

Autor	*Wissenschaftliche Konzeption [%]*	*Datengenerierung [%]*	*Analyse und Interpretation [%]*	*Verfassen des Texts [%]*
Binder, Thomas	**60**	**90**	**75**	**70**
Marks, Michael A. W.	20	0	10	20
Walter, Benjamin F.	5	0	0	5
Wenzel, Thomas	5	10	10	0
Markl, Gregor	10	0	5	5

Arbeit 3

Binder T, Marks MAW, Friedrichsen B-E, Walter BF, Wenzel T, Markl G (2024a) Bimodal volcanism in the Hegau region (SW Germany): Differentiation of primitive melilititic to nephelinitic rocks produces evolved nosean phonolites. Lithos 472–473:107565. https://doi.org/10.1016/j.lithos.2024.107565.

Status: akzeptiert und veröffentlicht

Autor	*Wissenschaftliche Konzeption [%]*	*Datengenerierung [%]*	*Analyse und Interpretation [%]*	*Verfassen des Texts [%]*
Binder, Thomas	**60**	**80**	**75**	**75**
Marks, Michael A. W.	20	0	20	10
Friedrichsen, Brian-Eric	0	20	0	0
Walter, Benjamin F.	5	0	0	5
Wenzel, Thomas	5	0	0	5
Markl, Gregor	10	0	5	5

1. Einleitung

1.1. Die südliche Zentraleuropäische Vulkanprovinz (ZEVP) als Untersuchungsgebiet

Die oberkretazische bis holozäne Zentraleuropäische Vulkanprovinz (ZEVP) ist Teil der Zirkummediterranen Anorogenen Känozoischen Magmatischen Provinz (Lustrino & Wilson 2007) und umfasst mehrere Vulkanregionen in Ostfrankreich, West-, Mittel- und Süddeutschland, Tschechien und Westpolen (z. B. Lustrino & Wilson 2007, Schmitt et al. 2007, Sirocko et al. 2013). Alle Vorkommen sind infolge von Intraplattenvulkanismus entstanden, dessen Ursachen bis heute nicht vollständig geklärt sind. Sie zeichnen sich durch eine große geomorphologische und petrografische Variabilität aus. So finden sich sowohl polygenetische als auch monogenetische Vulkanregionen, die ausgedehnte Lava- oder Tuffdecken aber auch Ansammlungen oder Einzelvorkommen von Tuffschloten, Staukuppen und subvulkanischen Gängen bilden können. Der nördliche Teil der ZEVP ist größtenteils durch basanitische bis basaltische Gesteine und ihre Differentiate charakterisiert, wobei untergeordnet auch Foidite und Melilithite anzutreffen sind (Abratis et al. 2009, Bogaard & Wörner 2003, Braunger et al. 2018, Büchner et al. 2015, Dunworth & Wilson 1998, Jung & Hoernes 2000, Jung et al. 2005, 2006, 2011, Kolb et al. 2012, Kramm & Wedepohl 1990, Schubert et al. 2015, Skála et al. 2015, Ulrych et al. 2016, Wörner et al. 1986).

Demgegenüber zeichnet sich das Untersuchungsgebiet dieser Arbeit, der südliche Teil der ZEVP (südlich einer Linie Eifel–Vogelsberg–Rhön–Heldburg), vorwiegend durch primitive, stark SiO_2-untersättigte alkalische Vulkanite aus, darunter überwiegend Olivin-reiche Melilithite, Nephelinite und Basanite. Seltener finden sich entwickelte (phonolitische) Haüynite/Noseanite, Haüyn-Nephelinite, Phonolithe, Karbonatite und Trachyte. Im Vergleich zum nördlichen Teil der ZEVP dominieren monogenetische isolierte Vorkommen und Vulkangebiete mit einer Vielzahl räumlich separierter Vulkangebäude in verschiedenen Regionen. Dazu gehören der Taunus, die Untermainebene, der Odenwald und der Kraichgau, der Bonndorfer Graben und die Freiburger Bucht, die Vogesen und der Pfälzerwald, Lothringen, der südliche Oberrheingraben, das Uracher Vulkangebiet und der Hegau. In den vier letztgenannten Regionen herrschen sehr stark SiO_2-untersättigte, primitive Olivin-Melilithite, Melilith-führende Olivin-Nephelinite und entwickelte Nosean-Phonolithe (nur Hegau) vor, während die übrigen Gebiete vorwiegend Melilith-freie Olivin-Nephelinite, basanitische Nephelinite und Nephelinbasanite umfassen. Haüynite/Noseanite und Haüyn-Nephelinite sind auf Odenwald und

Kraichgau und Trachyte auf die Untermainebene beschränkt. Der Vulkankomplex des Kaiserstuhls bildet eine markante Ausnahme, da hier verschiedene alkalische Gesteine (Haüyn-Melilithite, Olivin-Nephelinite, Basanite, Tephrite, Phonotephrite, Tephriphonolithe, Phonolithe, Haüynite, Noseanite) und Karbonatite (Sövite, Alvikite, Beforsite, Karbonatit-Lapillituffe) auftreten (Braunger et al. 2018).

1.1.1. Strukturgeologische Aspekte

Viele Vulkanregionen der südlichen ZEVP sind an prominente tektonische Strukturen gebunden (z. B. Eynatten et al. 2020, Grimmer et al. 2017, Ring & Bolhar 2020). Der Kaiserstuhl und weitere isolierte Diatreme und subvulkanische Gänge liegen im südlichen Teil des Oberrheingrabens zwischen den Variszischen Grundgebirgssockeln des Schwarzwalds und der Vogesen. Innerhalb dieser Massive selbst treten weitere Vorkommen alkalischer Vulkanite auf, die sich vor allem auf die Flanken des Oberrheingrabens (z. B. Freiburger Bucht) und auf den WNW-OSO-streichenden Bonndorfer Graben konzentrieren. Dieser verläuft quer durch den Schwarzwald und geht im Osten in den NW-SO-streichenden Hegau-Graben über. Die wenige Kilometer breite und seismisch aktive Albstadt-Scherzone verläuft parallel zum Oberrheingraben und verbindet den Hegau mit den westlichen Ausläufern des Uracher Vulkangebiets (Mader et al. 2021). Die Region ist durch mehrere kleinräumige Störungszonen charakterisiert, darunter Filder-Graben, Bebenhausen-Störung, Hohenzollern-Graben, Lauchert-Graben und Schwäbisches Lineament. Weiter nördlich an der Ostflanke des Oberrheingrabens liegen die vulkanischen Gesteine der Untermainebene (Sprendlinger Horst) und an der Westflanke das Vorkommen Forst (Pfälzerwald). Die Basanit- und Nephelinit-Vorkommen im Taunus verlaufen parallel zur Südlichen Hunsrück-Taunus-Grenzstörung, während die Vulkanite des Odenwalds, des Kraichgaus und Lothringens an keine markanten Deformationsstrukturen gebunden sind.

1.1.2. Modelle für die geodynamische Entwicklung des Untersuchungsgebiets

Die magmatische Entwicklung in der südlichen ZEVP ist eng mit der geodynamischen Entwicklung der Region verknüpft, welche stark von der Alpidischen Orogenese beeinflusst wurde. In der Oberkreide vor ~95–70 Ma führte Kompressionstektonik zu Krustenverdickung, die auf großflächige Inversionstektonik in Mitteleuropa zurückgeht und durch die Konvergenz zwischen Iberischem Mikrokontinent und Eurasien verursacht wurde (Dielforder et al. 2019, Eynatten et al. 2020, Voigt et al. 2021). Im Paläozän

resultierte aus der Schließung der Neotethys infolge der Kollision der Adriatischen mit der Eurasischen Platte schließlich der Aufbau anhaltender kompressiver Intraplattenspannungen (Dèzes et al. 2004). Ein Krustenblock der Eurasischen Platte, das Briançonnais-Terran, setzte seiner weiteren Subduktion starken Widerstand entgegen, sodass die Spannungen teilweise weit nach Norden bis in die Gebiete der künftigen ZEVP verlagert wurden und dort großräumige Deformation, Hebung und Erosion der Lithosphäre verursachten (Ziegler & Dèzes 2005). Möglicherweise wurden diese Prozesse durch die spätkretazische bis früheozäne Aufwölbung der Asthenosphäre sowie thermische Erosion und Ausdünnung der Lithosphäre überlagert, begünstigt und verstärkt (~75–55 Ma; Dèzes et al. 2004, Ziegler & Dèzes 2005).

Seit dem frühen Eozän nahmen die Konvergenzraten zwischen Afrika und Europa wieder zu, was zur Reaktivierung der Subduktion europäischer Lithosphäre unter die Gebirgswurzel des Alpengürtels führte (~52–35 Ma; Rosenbaum et al. 2002, Ziegler et al. 2002, Ziegler & Dèzes 2005). Die kompressiven Intraplattenspannungen wurden dadurch abgebaut und das Alpine Orogen entkoppelte sich mechanisch weitgehend von der nördlich vorgelagerten Lithosphärenplatte, bis die Subduktion des Walliser Ozeans im Obereozän abgeschlossen war. Zur selben Zeit kam es zum *slab roll-back* und einem starken Schub des Orogens in Richtung Norden, verbunden mit einer massiven Aufweitung und Subsidenz des Molassebeckens (Dèzes et al. 2004, Ring & Bolhar 2020). Anschließend baute sich erneut Subduktionswiderstand auf, der sich zunehmend verstärkte und die nordwärts gerichteten Intraplattenspannungen sowie Krustenverkürzung im Alpenvorland reaktivierte. Diese Phase war durch sinistrale Transversalverschiebungen und schiefe Extension in der heutigen ZEVP gekennzeichnet. Sie führte zur Reaktivierung variszischer bis permischer Großstörungen und leitete die Entstehung des Europäischen Kontinentalen Rift-Systems (EKRiS; Dèzes et al. 2004) ein, wozu auch die Frühphase der Bildung des Oberrheingrabens gehört (*kollisionsbedingte Vorlandspaltung*; Ring & Gerdes 2016, Ziegler & Dèzes 2005).

Im frühen Oligozän vor ~32 Ma kam es zum Abriss der subduzierten Platte im Zentral- und Ostalpin, was vorübergehend zu isostatisch bedingter Hebung und Erosion führte (Blanckenburg & Davies 1995). Indessen dauerte die NW-gerichtete Konvergenz von Adriatischer und Eurasischer Platte an, wodurch weiterhin Druckspannungen auf das nördliche Alpenvorland ausgeübt wurden (Dèzes et al. 2004, Ziegler & Dèzes 2005). Gemeinsam mit den nordwärts gerichteten Spannungen der immer noch aktiven Kollisionszone im Pyrenäengürtel wurden durch *konstruktive Interferenz* die O-W-Exten-

sion in der Hauptphase der Entwicklung des EKRiS sowie die Subsidenz im Oberrheingraben während des Oligozäns kontrolliert (Schumacher 2002). Dabei könnten die zunehmende Krümmung des Westalpenbogens und die damit verbundene moderate tangentiale Streckung in den inneren Zentralalpen für die O-W-Ausdehnung im Alpenvorland ursächlich sein (Ring & Gerdes 2016).

Im Oberoligozän bis Untermiozän vor ~25–18 Ma veränderte sich die Deformation im Oberrheingraben von (W)NW-Dehnung zu NW-gerichteter Einengung bei (E)NE-Extension und -Transtension, was erneut Transversalverschiebungen und regionale Hebung zur Folge hatte (Grimmer et al. 2017, Ring & Gerdes 2016, Schumacher 2002). Diese Phase überschnitt sich mit dem fortschreitenden Übergreifen des Alpenorogens auf bisher undeformierte europäische Kruste im frühen Miozän (Dèzes et al. 2004, Rosenbaum et al. 2002). Die zunehmende kollisionsbedingte Kopplung zwischen Gebirgskern und Vorland war entscheidend für die weitere EKRiS-Entwicklung und spiegelt sich im komplexen Zusammenspiel von NW-gerichteter Stauchung in Alpen und Jura mit Grabenbildung in der nahen Umgebung wider (Ring & Gerdes 2016). Vor rund 18–16 Ma begannen schließlich die Verkippung der Süddeutschen Blockscholle in Richtung Süden sowie Hebung, Erosion und bruchhafte Deformation im Untersuchungsgebiet (Hoffmann 2017, Ring & Bolhar 2020, Ziegler & Dèzes 2005). Diese Prozesse dauerten bis ins Neogen an und wurden durch Verlagerung der Alpen weiter Richtung Norden und Nordwesten bei hohen Sedimentationsraten im Molassebecken verursacht und von großmaßstäblicher Faltung und Verschuppung außerhalb der Alpen liegender Gebirgszüge wie beispielsweise dem Vogesisch-Schwäbischen Bogen begleitet (Dèzes et al. 2004, Ring & Bolhar 2020).

1.2. Petrogenese alkalischer SiO_2-untersättigter Intraplattenvulkanite

Wenngleich die vulkanische Aktivität in der ZEVP mit Änderungen im Spannungsfeld des Alpenvorlandes und der Reaktivierung von Großstörungen in der Lithosphäre einhergeht (Goes et al. 1999, Merle 2011), sind die Zusammenhänge zwischen Hebung, Grabenbildung und Vulkanismus bis heute nicht vollständig verstanden (z. B. Goes et al. 1999, Lustrino & Wilson 2007). Allgemein kann zwischen zwei sich mitunter widersprechenden Theorien unterschieden werden: Einige Konzepte setzen konvektionsbedingte Auftriebsprozesse im asthenosphärischen Mantel voraus, die durch thermische Instabilitäten verursacht wurden (aktive Grabenbildung); andere führen die Schmelzbildung allein auf Lithosphärendeformation und -ausdünnung infolge plattentektonischer Prozesse wie Gebirgsbildungen und die Reaktionen darauf zurück (passive Grabenbildung; Fichtner & Villaseñor 2015, Lustrino & Carminati 2007, Lustrino & Wilson 2007, Pfänder et al. 2018, Przybyla et al. 2018). Erstgenannte Modelle erfordern ein großräumiges Manteldiapir-System, dessen Ursprung bis zur Kern-Mantel-Grenze hinabreichen könnte (Albers & Christensen 1996, Goes et al. 1999, Ritter et al. 2001), oder mehrere kleine fingerartige Diapire, die in die Asthenosphäre oder die Übergangszone zurückzuverfolgen sind (Granet et al. 1995, Haase et al. 2004, Hegner et al. 1995, Mertz et al. 2015, Ritter et al. 2001, Wedepohl & Baumann 1999).

Kritiker der Manteldiapir-Theorie lehnen maßgeblich thermisch gesteuerte Anomalien des Erdmantels als Ursache für Intraplattenvulkanismus ab und setzen stattdessen eine partielle und inhomogene metasomatische Überprägung des oberen Mantels unter der ZEVP voraus, womit Schmelzbildung ermöglicht oder mindestens vereinfacht würde (Blusztajn & Hegner 2002, Jung et al. 2005, Lustrino & Carminati 2007, Pfänder et al. 2018, Ulrych et al. 2008). Als Urheber gelten dabei wässrige oder überkritische Fluide und/oder Schmelzen, die aus dem partiellen Recycling alter, subduzierter Lithosphäre hervorgingen und zur Bildung wasserhaltiger, teilweise Karbonat-führender sowie mit weiteren volatilen und inkompatiblen Elementen angereicherten Bereichen im oberen Erdmantel führten (z. B. Green 2015, Lustrino & Wilson 2007, Pfänder et al. 2012, 2018; Wedepohl & Baumann 1999, Wilson et al. 1995, Yaxley et al. 2022). Schmelzbildung und -mobilisierung in Folge von Dekompression wären demnach überwiegend die Ergebnisse passiver Aufwölbung der Asthenosphäre durch das Zusammenspiel von Hebung, Erosion und Ausdünnung der Lithosphäre aufgrund von Tektonik.

Vorherige Arbeiten legten nahe, dass Melilith-führende Gesteine des Uracher Vulkangebiets und des Hegaus aus extrem niedrigen Aufschmelzgraden des angereicherten subkontinentalen Mantels hervorgegangen seien (Dunworth & Wilson 1998). Demzufolge infiltrierten aus dem Dolomit-Granat-Peridotit-Stabilitätsfeld stammende asthenosphärische Schmelzen den darüberliegenden lithosphärischen Mantel, wodurch dieser metasomatisch überprägt und ebenfalls partiell aufgeschmolzen wurde. Andere Konzepte gehen hingegen entweder von einem direkten Aufstieg bis an die Oberfläche ohne Beteiligung der Lithosphäre an der Magmagenese aus (Hegner et al. 1995, Jung et al. 2006, Schubert et al. 2015) oder verorten die Schmelzbildung an der Basis der Lithosphäre (Blusztajn & Hegner 2002, Pfänder et al. 2018). Trotz aller Unklarheiten bezüglich des Zeitpunkts, der Herkunft und des Ablaufs der Anreicherung bzw. Metasomatose in der ZEVP besteht inzwischen weitgehend Einigkeit über die Mitwirkung subduzierter und partiell recycelter, variszischer ozeanischer und/oder kontinentaler Lithosphäre an der Modifizierung des subkontinentalen Mantels und daraus hervorgehender Partialschmelzen (z. B. Blusztajn & Hegner 2002, Hegner & Vennemann 1997, Lustrino & Wilson 2007, Pfänder et al. 2018, Puziewicz et al. 2020, Ulrych et al. 2011, Witt-Eickschen & Kramm 1998).

Für Melilith-freie nephelinitische bis basanitische Gesteine werden insgesamt etwas höhere Aufschmelzgrade und geringere Tiefen bei der Schmelzbildung angenommen (im Spinell-Peridotit-Stabilitätsfeld oder der Granat-Spinell-Übergangszone; Mertz et al. 2015, Pfänder et al. 2018, Schubert et al. 2015, Ulrych et al. 2013). Meist wird ein lithosphärischer Ursprung vermutet, der sich entweder durch ein niedrigeres CO_2-(CO_2+H_2O)-Verhältnis bei der metasomatischen Überprägung (Melluso et al. 2011, Mertes & Schmincke 1985, Seifert & Thomas 1995, Ulianov et al. 2007, Veksler & Lentz 2006) oder eine generell schwächere Metasomatose gegenüber Lithologien, aus denen Melilith-führende Gesteine hervorgehen, auszeichnet (Pfänder et al. 2018, Ulrych et al. 2013). Andere Autoren schließen auch für Melilith-freie Gesteine die Beteiligung zweier Magmaquellen nicht aus und favorisieren intensive Asthenosphäre-Lithosphäre-Wechselwirkungen, d. h. thermale Erosion der Basis der erheblich metasomatisch veränderten Lithosphäre durch die Asthenosphäre (Jung et al. 2011, Mertz et al. 2015, Schubert et al. 2015). Die etwas weniger primitive Natur einiger Nephelinite und Basanite wird in diesen Fällen zumeist durch Fraktionierung von Olivin, Klinopyroxen und Chromspinell an der Mohorovičić-Diskontinuität oder in der Unterkruste sowie durch Kontamination und/oder Magmamischung erklärt.

Die Entstehung der entwickelten Phonolithe im Hegau wurde auf fraktionierte Kristallisation eines bislang nicht weiter charakterisierten primitiven melilithitischen bis foiditischen Stammmagmas zurückgeführt (Mahfoud & Beck 1989). Ob bei der Entwicklung krustale Assimilation einen nennenswerten oder gar bedeutenden Einfluss hatte, ist ungeklärt. Bei denjenigen Trachyten in der ZEVP, für welche ein SiO_2-untersättigtes Stammmagma angenommen wird, gilt dies hingegen als wahrscheinlich, um unter anderem deren SiO_2-Sättigung zu erklären (Jung et al. 2013, Schmitt 2006).
Unter Berücksichtigung der variablen Zusammensetzung, der unterschiedlichen Alter und der schwankenden Volumina geförderter Magmen in der ZEVP ist davon auszugehen, dass ein generalisierendes Modell allein nicht ausreicht, um die Petrogenese aller Vorkommen zu erklären, zumal es mitunter an räumlicher Überlappung von Vulkanismus und Grabenbildung mangelt (Dunworth & Wilson 1998, Eynatten et al. 2020, Goes et al. 1999, Lustrino & Wilson 2007, Mertz et al. 2015, Pfänder et al. 2018). Vielmehr müssen die chemische Heterogenität des unteren lithosphärischen Mantels, Entstehungstiefe und Ursprung der Magmen sowie die variierende Lage der Grenze zwischen Lithosphäre und Asthenosphäre in ein zusammenhängendes geodynamisches Szenario integriert werden (Lustrino & Carminati 2007, Lustrino & Wilson 2007, Puziewicz et al. 2020). Insgesamt zeigt die Vielzahl der entwickelten Modelle für die Magmagenese in der ZEVP die Komplexität der zugrundeliegenden Prozesse und trotz aller Fortschritte ein unzureichendes Gesamtverständnis des Intraplattenvulkanismus im Zusammenhang mit der geodynamischen Entwicklung Mitteleuropas. Berücksichtigt man die weit auseinandergehenden Definitionen von Manteldiapirismus bzw. Mantel-Plumes, so können viele moderne Modelle als hybride Konzepte aufgefasst werden (Lustrino & Wilson 2007). Diese führen den Vulkanismus in der ZEVP weder ausschließlich auf thermale oder kompositionelle Anomalien der Asthenosphäre und Störungen im Zusammenhang mit der Mantelkonvektion zurück noch allein auf Metasomatose gefolgt von Ausdünnung und Hebung der Lithosphäre durch Plattenbewegung.

2. Material, Methoden und Zielsetzung

2.1. U-Pb-Geochronologie und Petrografie

Wurden im nördlichen Teil der ZEVP inzwischen zahlreiche Proben vulkanischer Gesteine aus einer Vielzahl von Vulkanregionen unter anderem mit dem $^{40}Ar/^{39}Ar$-Verfahren datiert (z. B. Abratis et al. 2007, Büchner et al. 2015, Linthout et al. 2009, Mayer et al. 2014, Mertz et al. 2000, 2007, 2015, Pfänder et al. 2018, Schubert et al. 2015, Shaw 2004, Singer et al. 2008, van den Bogaard 1995), so mangelt es an modernen geochronologischen Arbeiten aus der südlichen ZEVP (Fekiacova et al. 2007, Keller et al. 2002, Schmitt et al. 2007), wodurch präzise Altersdaten für die meisten dortigen Vorkommen nahezu fehlen. Existierende Altersangaben basieren auf K-Ar-Gesamtgesteinsaltern (Baranyi et al. 1976, Horn et al. 1972, Lippolt et al. 1963, 1975, 1976, Lippolt 1983), bei denen sich inzwischen gezeigt hat, dass sie mindestens unpräzise und in einigen Fällen fehlerhaft sind (z. B. Baranyi et al. 1976, Keller et al. 2002, Lippolt et al. 1963). Daher wurde in einem ersten Schritt zunächst eine Auswahl (56 Dünnschliffe von 45 Lokalitäten, fünf Schwermineralkonzentrate von fünf Lokalitäten) vulkanischer Gesteine und plutonischer Einschlüsse darin aus insgesamt zehn Regionen der südlichen ZEVP mittels Massenspektrometrie mit induktiv gekoppeltem Plasma und Laserablation (LA-ICP-MS) basierend auf U-Pb-Geochronologie datiert. Insgesamt wurden dazu etwa 3000 Punktanalysen in situ an den Mineralen Perowskit, Apatit, Titanit, Zirkon und Pyrochlor durchgeführt.

Um mögliche zeitliche, räumliche und kompositionelle Verteilungsmuster zwischen und/oder innerhalb der Vulkanregionen entdecken und statistisch gesichert belegen zu können, wurden außerdem insgesamt 232 Proben von etwa 130 Vorkommen sowie darin enthaltene plutonische Einschlüsse detailliert petrografisch untersucht, anhand ihres modalen Mineralbestands und Gefüges charakterisiert und nach Le Maitre et al. (2002) klassifiziert. Kombiniert ermöglicht dies ein besseres Verständnis und eine präzise Auflösung der Chronologie des Magmatismus in der südlichen ZEVP sowie Rückschlüsse auf die für die vulkanische Aktivität ursächlichen Triebkräfte, die eng mit der geodynamischen Entwicklung Mitteleuropas und Aufschmelzprozessen im oberen Erdmantel verknüpft sind.

2.2. Geochemische Zusammensetzung des Gesamtgesteins und der Minerale der primitiven Melilithite, Nephelinite und Basanite

Im nächsten Schritt wurden Gesamtgesteinsanalysen mittels Röntgenfluoreszenzanalyse (RFA) und Massenspektrometrie mit induktiv gekoppeltem Plasma (ICP-MS; Haupt- und Spurenelemente an 34 Proben von 27 Lokalitäten) für primitive Gesteine aus jenen Vulkanregionen durchgeführt, für die geochemische Daten aus der Literatur fehlen oder unzureichend sind. Hauptbestandteil dieser Arbeit war jedoch die systematische Bestimmung der chemischen Zusammensetzung der unterschiedlichen Mineralphasen (Olivin, Pyroxen, Oxyspinell, Ilmenit, Melilith, Sodalith-Gruppe, Glimmer, Perowskit, Apatit, Amphibol) mittels Elektronenstrahlmikroanalytik (ESMA) an insgesamt 83 Dünnschliffen aus 60 repräsentativen Vorkommen primitiver alkalischer SiO_2-untersättigter Gesteine aller Vulkanregionen der südlichen ZEVP mit Ausnahme des Kaiserstuhls (dazu siehe Braunger et al. 2018). Mithilfe der Mineral- und Gesamtgesteinszusammensetzungen erfolgten außerdem thermodynamische Berechnungen (Software QUILF; Andersen et al. 1993) und geothermobarometrische Abschätzungen (Neave & Putirka 2017, Putirka 2008). Unter Einbeziehung der vorherigen petrografischen und geochronologischen Ergebnisse ergibt sich damit schließlich ein umfassendes petrogenetisches Modell. Dazu gehören die Rekonstruktion von Aufschmelz- und Kristallisationsbedingungen sowie der Rolle von volatilen Elementen und Entgasung, die Eingrenzung der Lithologie der Magmaquelle(n) und die Identifikation von möglichen Kontaminations-, Assimilations- und fraktionierten Kristallisationsprozessen sowie Magmamischung. Dadurch werden weitere Rückschlüsse im Hinblick auf die vulkanische Geschichte der ZEVP im Kontext der Alpidischen Orogenese, der Entwicklung des Europäischen Kontinentalen Rift-Systems, der Süddeutschen Blockscholle und ihrer Vorläuferstrukturen ermöglicht. Der Vergleich verschiedener Vulkanregionen unterschiedlichen Alters innerhalb derselben Provinz gewährt dabei neue Einblicke in die räumliche und zeitliche Entwicklung der Magmagenese und die Heterogenität des subkontinentalen Mantels unter der ZEVP.

2.3. Geochemische Zusammensetzung des Gesamtgesteins und der Minerale der Nosean-Phonolithe und (Nephelin-)Syenit-Einschlüsse des Hegaus

Gemeinsam mit dem Phonolith vom Katzenbuckel (Odenwald) und denen des Kaiserstuhls stellen entwickelte Nosean-Phonolithe und grobkristalline (Nephelin-)Syenit-Einschlüsse des bimodalen Hegau-Vulkanismus eine Besonderheit in der südlichen ZEVP dar. Mithilfe von Petrografie, Gesamtgesteinsanalysen (zwölf Proben aller sechs Lokalitäten) und ESMA (14 Proben aller sechs Phonolith-Lokalitäten; Analysen an Klinopyroxen, Alkalifeldspat, der Sodalith-Gruppe, Titanit, Apatit) wird ihr möglicher genetischer Zusammenhang zu den primitiven melilithitischen bis nephelinitischen Hegau-Vulkaniten und darin enthaltenen ijolithischen Schlieren untersucht. Neben dem Vergleich von Haupt- und Spurenelement-Verteilungen und -Mustern sowie der Mineralchemie liefert die fraktionierte Kristallisationsmodellierung mit der Software-Plattform MELTS (Ghiorso et al. 2002, Ghiorso & Gualda 2015, Ghiorso & Sack 1995) einen weiteren Beitrag dazu. Basierend auf den Ergebnissen und unter Berücksichtigung der regionalen geodynamischen Entwicklung können Mechanismen des Magmaaufstiegs, der Differentiation und Platznahme rekonstruiert werden, wobei die vulkanische Geschichte der Region dabei lehrbuchhaft Ursachen und Prozesse bimodalen alkalischen Vulkanismus demonstriert und einen Erklärungsansatz für die die kompositionelle Lücke zwischen primitiven und entwickelten Gesteinen (*Bunsen-Daly-Lücke*) liefert.

3. Ergebnisse und Diskussion

In diesem Kapitel werden die wichtigsten Ergebnisse der drei Arbeiten des Promotionsprojekts in der Reihenfolge ihrer obigen Auflistung in zusammengefasster Form vorgestellt und dabei im Rahmen der geochronologischen, petrogenetischen und geodynamischen Entwicklung der südlichen ZEVP diskutiert.

3.1. Verlauf und Dauer des Vulkanismus in der südlichen ZEVP

Die Ergebnisse aus früherer K-Ar-Geochronologie in der südlichen ZEVP ließen auf räumlich variierende, aber kontinuierliche vulkanische Aktivität zwischen der Oberkreide und dem Pliozän schließen, da die individuellen Alter der Lokalitäten mit ihrer Fehlerspannweite den gesamten Zeitraum abdeckten (Baranyi et al. 1976, Horn et al. 1972, Kraml et al. 1995, 1999, Lippolt et al. 1963, 1975, 1976, Lippolt 1983). Die neuen U-Pb-Datierungen (Binder et al. 2023) offenbaren jedoch erstmals zwei deutlich voneinander getrennte Phasen vulkanischer Aktivität, die zudem räumliche und kompositionelle Verteilungsmuster aufweisen.

Weitgehend Melilith-freie Olivin-Nephelinite, basanitische Nephelinite und Nephelinbasanite sind auf einen Zeitraum zwischen später Oberkreide und frühem Eozän beschränkt und treten im Taunus (~68–55 Ma), im Bonndorfer Graben und in der Freiburger Bucht (~67–58 Ma), in den Vogesen (~61 Ma; Keller et al. 2002), im Pfälzerwald (~51–50 Ma) sowie in der Untermainebene auf (~56–47 Ma; Fekiacova et al. 2007, Lenz et al. 2015, Lutz et al. 2013). In diese Altersgruppe fallen auch die (phonolithischen) Haüynite/Noseanite und Haüyn-Nephelinite des Odenwalds und des Kraichgaus (~70–62 Ma) und die Trachyte der Untermainebene (~73–65 Ma), sodass sich insgesamt eine Altersspanne von ~26 Mio. Jahren zwischen 73 und 47 Ma ergibt. Im Gegensatz dazu beschränkt sich die Entstehung von Melilith-führenden Olivin-Nepheliniten und Olivin-Melilithiten auf einen Zeitraum zwischen spätem Oligozän und spätem Miozän in Lothringen (~27–26 Ma), im südlichen Oberrheingraben (~26–25 Ma und ~17–16 Ma), im Uracher Vulkangebiet (~19–12 Ma) und im Hegau (~12–9 Ma). Zu dieser Zeit eruptierten auch der polygenetische Vulkankomplex des Kaiserstuhls (~19–15 Ma; Binder et al. 2023, Ghobadi et al. 2022, Kraml et al. 1995, 1999) sowie die Nosean-Phonolithe (~14–11 Ma) und Augit-Hornblende-Phlogopit-Tuffe (~15–12 Ma) des Hegaus. Dementsprechend repräsentieren diese Alter nach einer Ruhephase von ~20 Mio. Jahren eine zweite Periode vulkanischer Aktivität mit einer Dauer von ~18 Mio. Jahren vor ~27–9 Ma.

Für die Entstehung des Uracher Vulkangebiets kann der wiederholt und zuletzt von Ring & Bolhar (2020) postulierte kausale Zusammenhang mit dem Ries-Impakt durch Druckentlastung des Erdmantels eindeutig widerlegt werden. Mehrere Eruptionen im Uracher Vulkangebiet fanden eindeutig vor dem Ries-Impakt statt, der sich erst vor 14,6 ± 0,2 Ma ereignete (Buchner et al. 2010). Dies zeigen auch biostratigrafische Befunde an Randecker-Maar-Sedimenten, die ebenfalls älter sind und zwischen 17,0 und 14,8 Ma datieren (Rasser et al. 2013). Außerdem konnte eine lange Dauer vulkanischer Aktivität (~7 Mio a) im Uracher Vulkangebiet nachgewiesen werden, während zwischenzeitlich maximal 2 Ma angenommen wurden (Kröchert et al. 2009, Ring & Bolhar 2020). Etwa zeitgleich mit den letzten Eruptionen in der Region verlagerte sich der Vulkanismus vom nördlichen ans südliche Ende der Albstadt-Scherzone in den Hegau, wo zunächst die entwickelten Nosean-Phonolithe (~14–11 Ma) und mafischen Lapilli-Tuffe (~15–12 Ma) sowie wenig später die primitiven melilithitischen bis nephelinitischen Vulkanite (~12–9 Ma) gefördert wurden. Diese stellen das letzte magmatische Signal in der südlichen ZEVP dar und belegen gemeinsam mit U-Pb-Altern von entwickelten Nephelin-Syenit-Einschlüssen (~15–11 Ma) in den Tuffen, in den melilithitischen bis nephelinitischen Gesteinen und in den Phonolithen, dass sich auch die magmatische Aktivität im Hegau über ~6 Mio. Jahre erstreckte.

Die überlappenden Alter für primitive und entwickelte Extrusivgesteine, Tuffe und die in all diesen Lithologien enthaltenen plutonischen Einschlüsse verweisen auf eine enge Verwandtschaft zwischen diesen Gesteinstypen und auf anhaltende, ausgedehnte und komplexe oberkrustale Stagnations- und Differentiationsprozesse. Die räumliche Separation der Melilith-führenden Olivin-Nephelinite und Olivin-Melilithite von den Nosean-Phonoliten könnte darauf hindeuten, dass geringfügige strukturelle oder lithologische Unterschiede im Aufbau der oberen Lithosphäre in einigen Fällen zu direkter Eruption und in anderen Fällen zu anhaltenden Fraktionierungs- und möglicherweise Assimilationsprozessen in Magmakammern geführt haben könnten. Ebenfalls datierte grobkörnige Schlieren ijolithischer Zusammensetzung in den primitiven Vulkaniten vom Hohenstoffeln werden als In-situ-Differentiate interpretiert, da ihr Alter mit dem des nephelinitischen Wirtsgesteins übereinstimmt.

3.1.1. Rückschlüsse auf die chronologische und petrografische Entwicklung der gesamten ZEVP

Neben den in der Literatur beschriebenen petrografischen und geomorphologischen Unterschieden zwischen den vulkanischen Gesteinen der nördlichen und der südlichen ZEVP ergeben sich aus den neuen geochronologischen Ergebnissen dieser Studie zusätzliche Differenzen aber auch Überschneidungen. Anders als bei den ermittelten Altersdaten für den südlichen Teil der Provinz deuten die Altersdaten aus der Literatur für den nördlichen Abschnitt auf sich räumlich immer wieder verlagernde, aber anhaltende vulkanische Aktivität seit dem mittleren Eozän hin. Im Gegensatz zur südlichen ZEVP finden sich jedoch keine deutlichen Zusammenhänge zwischen Gesteinstypen und -altern. Auch fehlen paläozäne Vulkanite völlig und oberkretazische Vorkommen sind nur durch Trachyt-Xenolithe und camptonitische Ganggesteine im Vogelsberg repräsentiert (74–66 Ma; Bogaard & Wörner 2003, Martha et al. 2014, Schmitt et al. 2007). Diese Alter überlappen mit denen der wenigen Trachyt-Vorkommen der Untermainebene und der (phonolithischen) Haüynite/Noseanite und Haüyn-Nephelinite im Odenwald und Kraichgau. Auch die übrigen, Melilith-freien, primitiven nephelinitischen bis basanitischen Gesteine der alten Gruppe in der südlichen ZEVP prädatieren ansonsten alle weiteren Gesteine des nördlichen Teils der Provinz. Dort begann die känozoische Aktivität nach heutigem Kenntnisstand spätestens mit der Entstehung von Basaniten, Basalten sowie untergeordnet Latiten und Trachyten in der Hocheifel (~45–35 Ma). Darauf folgten für die nördliche ZEVP seltene, melilithitische bis nephelinitische Gesteine der Heldburger Gangschar (38–25 Ma; Pfänder et al. 2018), 7 Mio. Jahre später komplettiert durch Basanite und einen Phonolith-Stock (18–12 Ma; Abratis et al. 2007, 2015). Indessen entstanden in der Lausitz (Eger-Graben), im Siebengebirge, in der Wetterau, in der Osteifel, im Westerwald, in der Rhön und im Vogelsberg vom Oligozän bis ins Mittelmiozän (~35–14 Ma) Basanite und Basalte sowie Latite, Trachyte und Phonolithe als differenzierte Pendants ohne deutliche petrochronologische Verteilungsmuster (Abratis et al. 2007, Bogaard et al. 2001, Büchner et al. 2015, Kolb et al. 2012, Linthout et al. 2009, Mertz et al. 2007, Neuhaus 2010).

Im Gegensatz dazu sind aus der südlichen ZEVP für den gesamten Zeitraum zwischen dem mittleren Eozän und dem frühen Miozän (~47–19 Ma) bis auf die sporadischen Ausbrüche in Lothringen und im südlichen Oberrheingraben (~27–25 Ma) keine Eruptionen feststellbar. Parallel zur Aktivität im Vogelsberg und bei Heldburg sowie gegen Ende des Rhön-Vulkanismus trat jedoch im Süden schließlich die Hauptphase der

zweiten Periode ausgedehnter und wiederkehrender magmatischer Aktivität auf (~19–9 Ma: Uracher Vulkangebiet, Kaiserstuhl und übriger südlicher Oberrheingraben, Hegau). Während der dortige Vulkanismus damit sein vorläufiges Ende fand, kam es im Pliozän in der nördlichen ZEVP im Westerwald erneut zur Förderung basanitischer Magmen (~5 Ma; Schubert et al. 2015), bevor im Quartär der Vulkanismus in der Lausitz (370–170 ka; Mrlina et al. 2007, Wagner et al. 1998) sowie in der Eifel (~760–10 ka; Mertz et al. 2015, Schmitt et al. 2017, Shaw et al. 2010, Singer et al. 2008, Sirocko et al. 2013, van den Bogaard 1995) reaktiviert wurde.

Für die gesamte ZEVP sind keine offensichtlichen Beziehungen zwischen räumlicher, kompositioneller und zeitlicher Entwicklung des Vulkanismus wie progradierende Hot Spots, die auf Manteldiapirismus hindeuten würden, erkennbar. Gleichwohl finden sich für verschiedene Vulkanzentren innerhalb desselben Vulkangebiets vereinzelt zeitlich-kompositionelle und räumliche Zusammenhänge. In einigen Regionen mit bimodalem oder polygenetischem Vulkanismus folgten primitive auf stärker differenzierte Gesteine oder stark SiO_2-untersättigte auf weniger SiO_2-untersättigte oder andersherum, teilweise mit größerer zeitlicher Unterbrechung (vgl. Abratis et al. 2015, Bogaard & Wörner 2003, Pfänder et al. 2018, Lustrino & Wilson 2007). Andernorts in der ZEVP eruptierten nach differenzierten Magmen primitivere, die wiederum von differenzierteren abgelöst wurden (vgl. Büchner et al. 2015, Przybyla et al. 2018, Ulrych et al. 2011, 2013, 2016). Viele dieser Abfolgen werden auf Prä-, Syn- und Post-Rift-Phasen (z. B. Eger-Graben), auf komplexe subvulkanische Kammer- und Leitungssysteme (z. B. Siebengebirge; Przybyla et al. 2018) sowie auf verschiedene Quellen und Tiefen der Schmelzbildung zurückgeführt (z. B. Heldburg, Kaiserstuhl, Eger-Graben; Braunger et al. 2018, Ghobadi et al. 2022, Pfänder et al. 2018, Ulrych et al. 2016).

Wenngleich konvektionsbedingte Auftriebsprozesse und thermale Anomalien in der Asthenosphäre als Triebkraft der magmatischen Aktivität nicht ausgeschlossen werden können, so deuten doch die großen Unterschiede der südlichen ZEVP im Vergleich zu ihrem nördlichen Teil, wie die 20 Mio. Jahre währende eruptionslose Phase, der zumeist monogenetische Charakter der Vulkangebiete und die geringeren Magmavolumina auf eine strukturelle Kontrolle im Rahmen der Alpidischen Orogenese hin. Die zeitliche, räumliche und kompositionelle Variabilität innerhalb der südlichen ZEVP einerseits, aber große petrografische Gemeinsamkeiten zwischen gleichaltrigen Vorkommen andererseits unterstützen die Annahme eines heterogen zusammengesetzten subkontinentalen Mantels unter Mitteleuropa (Puziewicz et al. 2020). Der zeitliche

Trend von Melilith-freien nephelinitischen bis basanitischen Gesteinen hin zu Melilith-führenden Olivin-Nepheliniten und Olivin-Melilithiten könnte auf abnehmende Aufschmelzgrade, höhere Bildungstiefen, eine geringmächtigere Lithosphäre, eine zunehmend mit Karbonat angereicherte Quelle und/oder einen abnehmenden Einfluss von Assimilations- und Fraktionierungsprozessen hindeuten (z. B. Bogaard & Wörner 2003, Dunworth & Wilson 1998, Jung et al. 2006, Pfänder et al. 2018).

3.2. Petrogenese der Melilithite, Foidite und Basanite

Nachdem zwischen den Gesteinen der beiden Altersgruppen petrografisch bereits deutliche Variationen offensichtlich wurden, erfolgte eine detaillierte Charakterisierung ihrer geochemischen, mineralogischen und mineralchemischen Zusammensetzung, um zugrundeliegende Unterschiede in der Petrogenese identifizieren und interpretieren zu können. Die Ergebnisse (Binder et al., 2024b) sollen an dieser Stelle zusammengefasst werden.

Die oberkretazischen bis eozänen (~73–47 Ma) porphyrischen Olivin-Nephelinite, basanitischen Nephelinite und Nephelinbasanite zeichnen sich durch moderate bis hohe Gehalte von MgO (8–16 Gew.-%), CaO, Ni, Co, Cr, Nb und Ba sowie niedrige F- und SiO_2-Konzentrationen aus. Die Gesteine enthalten große Mengen Klinopyroxen, variable Anteile von Olivin-Makrokristallen und Nephelin, F-armen Phlogopit und Hydroxylapatit. Die weniger verbreiteten Apatit-reichen (phonolithischen) Haüynite/Noseanite und Haüyn-Nephelinite (~68–62 Ma) sind als entwickelte Pendants derselben Altersgruppe reich an Na_2O, K_2O, Al_2O_3, P_2O_5, Nb, Zn, REE sowie SO_3, während die Gehalte an MgO (4–6 Gew.-%), CaO, Ni, Co und Cr niedrig sind.

Im Gegensatz zu diesen beiden älteren Lithologien umfasst die oligozäne bis miozäne Serie (~27–9 Ma) porphyrische Olivin-Melilithite und Melilith-führende Olivin-Nephelinite, charakterisiert durch außerordentlich hohe MgO- (10–22 Gew.-%), CaO-, Ni-, Co-, Cr-, Nb- und Ba-Gehalte sowie hohe F-Konzentrationen bei sehr geringen SiO_2-Gehalten. Dies drückt sich unter anderem in der Präsenz von Melilith, Perowskit, reichlich Olivin, F-, Ba- und Mg-reichem Glimmer (Phlogopit und Kinoshitalit) sowie Fluorapatit neben Klinopyroxen und Nephelin aus.

In den nephelinitischen bis basanitischen Gesteinen der alten Gruppe finden sich regelmäßig *Grünkernpyroxene* (Duda & Schmincke 1985) und xenomorphe, in Klinopyroxen-Makrokristallen eingeschlossene Hydroxylapatit-Kristalle sowie gelegentlich Amphibol und Feldspat in der Matrix. Demgegenüber treten in den Melilith-führenden

Gesteinen der jungen Gruppe Cr-Diopsid-Kerne in Klinopyroxen-Makrokristallen sowie invers zonierte Olivin-Makrokristalle mit Forsterit-verarmtem und teilweise resorbiertem Kern auf. Grundsätzlich jedoch nehmen Mg- und Ni-Gehalte in den Olivinkristallen vom Zentrum zum Rand ab, wobei sie in den Melilith-führenden Gesteinen gegenüber den nephelinitischen bis basanitischen Gesteinen generell etwas höher sind. Daneben finden sich in den Vulkaniten beider Altersgruppen teilweise resorbierte, von Titanomagnetit-Säumen umhüllte, xenomorphe Mg-reiche Oxyspinell-Kristalle. Während diese in den oligozänen bis miozänen Vulkaniten Cr- und Al-akzentuiert sind, dominieren Al-reiche Endglieder in den oberkretazischen bis eozänen Vulkaniten. Mineralchemische Besonderheiten in den Haüyn/Nosean-reichen Gesteinen sind die hohen Cl-, SO_3- und Sr-Gehalte im Fluorapatit, die erhöhten Gehalte von Mn und Fe in Olivin und von Mn und Zn in Titanomagnetit sowie das Auftreten von Sanidin und dem Amphibol Fluorokatophorit in der Grundmasse.

3.2.1. Kristallisationsbedingungen

Klinopyroxen- und Gesamtgestein-basierte Geothermobarometrie ergibt für die beiden primitiven Gesteinsserien ununterscheidbare Bildungsdrücke von ~0,2–1,3 GPa und Bildungstemperaturen von ~1150–1350 °C (bzw. ~1100–1330 °C bei Berücksichtigung des H_2O-Gehalts im Gestein). Für Glimmer-reiche Nephelinbasanite und basanitische Nephelinite aus dem Odenwald und dem Kraichgau wurden durchschnittlich etwas geringere Drücke (<0,9 GPa) und Temperaturen (1080-1180 °C) ermittelt.

Die kombinierte Bestimmung von Temperatur, SiO_2-Aktivität und Sauerstofffugazität mittels der Software QUILF an spätmagmatischen Paragenesen (Olivinsäume, Cr-armer Oxyspinell, kogenetischer Klinopyroxen) ergibt Gleichgewichtstemperaturen von 820–1060 °C für die primitiven Vulkanite und 830–930 °C für die entwickelten (phonolithischen) Haüynite/Noseanite und Haüyn-Nephelinite, wobei diese als Solidus- bis Subsolidus-Temperaturen zu betrachten sind. Die Redoxbedingungen für die meisten Melilithite, Foidite und Basanite liegen bei einem ΔFMQ von etwa +2,5 bis +4; wenige Basanite und Nephelinite sowie die entwickelten Haüyn-reichen Gesteine sind tendenziell weniger oxidiert mit einem ΔFMQ ≥+1. Die SiO_2-Aktivität beträgt für die primitiven Vulkanite ~0,5–0,9, für die Haüyn/Nosean-reichen Gesteine ~0,4–0,7.

Da die geothermobarometrischen Ergebnisse und die Bestimmung der Redoxbedingungen keine deutlichen Unterschiede für die beiden primitiven Gesteinsgruppen ergeben, sondern weitgehend überlappen, ist auszuschließen, dass die verschiedenen

Gesteinstypen lediglich variable Druck-, Temperatur- und Redoxbedingungen während ihrer Entstehung und Entwicklung reflektieren. Vielmehr deuten die Ergebnisse auf individuelle Magmaquellen und damit auf unterschiedliche parentale Schmelzen hin. Um deren primäre Signaturen in den beprobten Vulkaniten identifizieren zu können, ist eine gesamtheitliche Interpretation der petrografischen Beobachtungen sowie geochemischen und mineralchemischen Zusammensetzungen notwendig. Dadurch können Nebengesteinsinteraktion, Assimilations-, Fraktionierungs- und Magmamischungsprozesse sowie spätmagmatische Modifizierungen herausgefiltert werden.

3.2.2. Kristallfracht als Schlüssel zum Verständnis von Schmelzentwicklung, Magmeninteraktion und Aufstiegsprozessen

Die untersuchten Proben enthalten unterschiedliche Anteile von Xenokristallen, Antekristallen und Phänokristallen sowie Mikrokristalle, welche die Grundmasse aufbauen. Während die beiden letztgenannten früh- bzw. spätmagmatisch aus der Schmelze kristallisierten, bildeten sich die Antekristalle im Gleichgewicht mit einem Vorläufermagma, das sich in seiner Zusammensetzung von der später kristallisierenden Schmelze aufgrund zwischenzeitlicher Modifizierung unterscheidet. Teilweise resorbierte Mg-Cr-Al-Spinell-Kerne, xenomorpher und geschert deformierter Mg- und Ni-reicher Olivin mit undulöser Auslöschung und wenige Orthopyroxen-Kristalle stellen Xenokristalle dar, die nach Desintegration von Mantellithologien vom Magma aufgenommen und mitgeführt wurden. Selten sind entsprechende Gesteine als mm³- bis cm³-große Xenolithe in den beprobten Gesteinen erhalten.

Die entwickelten xenomorphen, später von Diopsid-reichen Mänteln umwachsenen grünen Kerne einiger Klinopyroxene in den nephelinitischen bis basanitischen Gesteinen wurden während des Magmaaufstiegs partiell resorbiert und zeigen damit ein Ungleichgewicht gegenüber der Zusammensetzung des Wirtsmagmas an. Die meisten Grünkerne stammen wahrscheinlich aus einer Schmelze abweichender Zusammensetzung, was auf Mischungsprozesse zwischen primären primitiven Magmen und einer ebenfalls aus dem oberen Mantel stammenden differenzierten Schmelze intermediärer Zusammensetzung hinweist (z. B. Tephriphonolith; Dobosi & Fodor 1992, Jung & Hoernes 2000, Loges et al. 2019). Die periodische Infiltration neuer Magmapulse in diese Schmelzen könnte Grünkerne mit einem schwammartig kristallisierten inneren Bereich aufgrund von schneller Ungleichgewichtskristallisation erklären. Die weitere Kristallisation nach der Gleichgewichtseinstellung äußert sich im klaren einschluss-

freien äußeren Bereich. Wahrscheinlich akkumulierten die grünen Pyroxen-Kristalle als Kristallbrei in kleinen Gängen oder Schmelztaschen im oberen Mantel und/oder kleinen Magmakammern oder Gangnetzwerken in der Unterkruste, wie es unter anderem für Grünkernpyroxene aus der Westeifel vorgeschlagen wurde (Duda & Schmincke 1985). Die darauffolgende Aufnahme vor Kristallisation der gesamten entwickelten Schmelze durch das primitive nephelinitische bis basanitische Wirtsmagma erklärt die Resorptionstexturen der Grünkernpyroxene und das Fehlen vollständiger Xenolithe entwickelter Zusammensetzung in den Gesteinsproben. Trotz starker Unterschiede in der Zusammensetzung zwischen den Grünkernen und den Diopsid-reichen Mänteln fand kaum Diffusion zwischen den beiden Bereichen statt, was auf schnelles Abkühlen und damit auf eine Aufnahme durch das Wirtsmagma nicht lange vor dem Ausbruch hindeutet (Jankovics et al. 2016).

Vereinzelte farblose Cr-Diopsid-Kerne in Klinopyroxen-Kristallen beider primitiver Gesteinsgruppen repräsentieren entweder mitgerissene Xenokristalle oder aber Antekristalle, die durch Reaktion eines Vorgängermagmas mit Oxyspinell aus desintegrierten Mantellithologien mit Cr angereichert wurden (Dunworth & Wilson 1998, Ulianov et al. 2007). Sowohl korrodierte und resorbierte Oxyspinell-Xenokristalle als auch die Cr-Diopsid-Kerne weisen demnach auf Instabilität von Mg-Cr-Al-Spinell hin, was von Mantellithologien, die eine Metasomatose durch karbonatitische Schmelzen erfuhren, bekannt ist und auf die Präsenz von Karbonat während der Schmelzbildung und -entwicklung deutet (Ionov et al. 1994, 1996, Ulianov et al. 2007, Wiechert et al. 1997).

Auch die relativ Forsterit-verarmten (Fo_{77-85}), großen und teilweise resorbierten Olivin-Kerne in einigen Proben der jüngeren Gesteinsgruppe können als Antekristalle aufgefasst werden, die – ähnlich den Grünkernpyroxenen – aus einem Magma etwas anderer Zusammensetzung stammen und während kurzzeitiger Stagnations- und Mischungsprozesse in einem Magmareservoir aufgenommen worden sind (vgl. Sundermeyer et al. 2020). Alternative Erklärungsansätze für die umgekehrte Zonierung, welche Änderungen der Sauerstofffugazität während der Kristallisation bedingt durch CO-CO_2-Partitionierung und -Entmischung voraussetzen, erscheinen hingegen fragwürdig. Die Relevanz des Gleichgewichts $CO_2 = CO + ½\ O_2$ für das Fe^{3+}/Fe^{2+}-Verhältnis in Partialschmelzen des lithosphärischen bis oberasthenosphärischen Mantels wird vielfach angezweifelt (Cottrell & Kelley 2011, Iacono-Marziano et al. 2012, Lowenstern 2001, Mathez 1984, Morizet et al. 2010, Ni & Keppler 2013).

3.2.3. Frühmagmatische Kristallisation: Die unterschiedliche Rolle von CO_2 und Karbonaten in der Magmaquelle

Die Stammmagmen beider primitiver Gesteinsserien waren anfangs Olivin-gesättigt, in der älteren Gruppe begleitet von Klinopyroxen, in der jüngeren von Melilith, wobei sich auch hier später meist Klinopyroxen dazugesellte. Die konzentrische kontinuierliche Zonierung der Mehrheit der Olivin- und Klinopyroxen-Phänokristalle spiegelt Veränderungen der Zusammensetzung des Magmas während der Kristallisation wider und setzt polybare Kristallisation im Verlauf eines zügigen, adiabatischen Aufstiegs des Magmas voraus (z. B. Arzamastsev et al. 2009, Duda & Schmincke 1985, Dunworth & Wilson 1998). Mitunter mm³-große Melilith-Phänokristalle und höhere Durchschnittsgehalte von CaO und MgO bei geringeren SiO_2-Gehalten in der jüngeren Gesteinsgruppe bilden Unterschiede ihrer parentalen Magmen und derer Quelllithologien im Vergleich zur älteren Gruppe ab (vgl. Melluso et al. 2011, Mertes & Schmincke 1985). Neben anderen Faktoren wird die primäre Zusammensetzung einer Mantelschmelze durch den Umfang von gelöstem CO_2 in der silikatischen Schmelze (Dunworth & Wilson 1998, Seifert & Thomas 1995) sowie die Menge von $CaCO_3$ in der Mantellithologie der Magmaquelle beeinflusst. Die Präsenz von CO_2 und $CaCO_3$ ist vermutlich auf Karbonat-Metasomatose des Mantels zurückzuführen und in der Reaktion dolomitkarbonatitischer Schmelze mit Orthopyroxen begründet, wodurch es zur Wehrlitisierung des ursprünglich lherzolithisch zusammengesetzten oberen Mantels kommt (Seifert & Thomas 1995, Ulianov et al. 2007, Veksler & Lentz 2006).

$$5\ Mg_2[Si_2O_6] + 4\ CaMg(CO_3)_2 \leftrightarrow 6\ Mg_2[SiO_4] + 2\ CaMg[Si_2O_6] + 2\ CaCO_3 + 6\ CO_2 \quad (1)$$

Als Folge entstehen zusätzlicher Klinopyroxen und Olivin unter Bildung einer Ca-angereicherten Karbonatit-Schmelze, wobei in dieser CO_2 gelöst ist und/oder ein weiteres CO_2-reiches Fluid mit dieser koexistiert. Verringerte Schmelztemperaturen solcher Karbonatit-Wehrlit-Lithologien begünstigen ein anschließendes nicht-modales Aufschmelzen unter Bildung einer sekundären Dolomitkarbonatit-Schmelze durch In-situ-Reaktion der Ca- und CO_2-reichen Produkte aus Reaktion (1) mit Olivin (vgl. Ulianov et al. 2007).

$$2\ Mg_2[SiO_4] + 5\ CaCO_3 + CO_2 \leftrightarrow Ca_2Mg[Si_2O_7] + 3\ CaMg(CO_3)_2 \quad (2)$$

$$2\ Mg_2[SiO_4] + 4\ CaCO_3 + 2\ CO_2 \leftrightarrow CaMg[Si_2O_6] + 3\ CaMg(CO_3)_2 \quad (3)$$

Die beiden schematisierten Reaktionen (2) und (3) deuten an, dass in Abhängigkeit vom CaO-CO_2-Verhältnis der Karbonatitschmelze und ggf. des Fluids sowohl Melilith oder Klinopyroxen als auch beide Phasen aus einer Partialschmelze, die ihren

Ursprung in einer wehrlitischen Lithologie hat, zusätzlich zu Olivin kristallisieren können. Daneben kann Melilith-Bildung jedoch auch durch vorausgehende Reaktion der Ca-reichen Karbonatitschmelze mit Klinopyroxen im Wehrlit begünstigt werden:

$$CaMg[Si_2O_6] + CaCO_3 \leftrightarrow Ca_2Mg[Si_2O_7] + CO_2 \quad (4)$$

Aus der Reaktion wird ferner deutlich, dass partielles Aufschmelzen von SiO_2-armen Lithologien die anschließende Kristallisation von Melilith gegenüber Klinopyroxen bevorzugt, da mehr $CaCO_3$-Beteiligung an der Schmelzbildung gleichzeitig eine geringere SiO_2-Konzentration in diesen Magmen bedeutet. Daneben entscheiden selbstverständlich auch die silikatischen Komponenten der Quelle über SiO_2-Gehalt und SiO_2-Aktivität im Magma. All dies lässt sich gut mit einem Olivin- und Klinopyroxen-reichen wehrlitischen Ursprung für die SiO_2-ärmeren Melilith-führenden Gesteine vereinbaren.

Für die Melilith-freie nephelinitische bis basanitische Gruppe kommt hingegen eine Orthopyroxen-haltige und folglich SiO_2-reichere und Ca-ärmere lherzolithische Lithologie infrage, zumal in den Proben Mantel-Xenokristalle von Orthopyroxen auftreten, die von Klinopyroxen, einer der ersten kristallisierenden Phasen, umhüllt sind. Die frühmagmatische Kristallisation von Klinopyroxen und Olivin im Gegensatz zu Melilith aus Partialschmelzen solch eines Lherzoliths ist möglich, ohne dass CO_2, $CaCO_3$ bzw. karbonatitische Metasomatose und vorangehende Wehrlitisierung notwendig gewesen sein müssen. H_2O-haltige Minerale wie Amphibol und/oder Phlogopit in der Mantellithologie könnten in diesem Fall die Magmabildung erleichtert oder gar erst ermöglicht haben. Ein von zusätzlicher Ca-Anreicherung weitgehend unbeeinflusster Mantel erklärt neben dem Fehlen von Melilith auch niedrigere CaO- und höhere SiO_2-Gehalte in den Vulkaniten. Die durchschnittlich geringeren MgO-Gehalte in den älteren Gesteinen gegenüber den jüngeren können mindestens teilweise auf geringere Anteile von Olivin-Xenokristallen zurückgeführt werden. Dies macht beispielhaft deutlich, dass die geochemische Zusammensetzung des Gesamtgesteins ohne die Charakterisierung der Phänokristallfracht und ihrer mineralchemischen Zusammensetzung nur bedingt Rückschlüsse auf die Petrogenese porphyrischer Vulkanite zulässt.

Ein weiterer petrogenetischer Faktor ist das Verhältnis zwischen Orthopyroxen und Dolomitkarbonatit-Schmelze während der Wehrlitisierung. Reagiert Orthopyroxen abweichend von Reaktion (1) mit einer unzureichenden Menge Schmelze, so wird die spätere Kristallisation von Melilith aus einem zukünftigen Magma aus diesem Wehrlit erschwert, da nicht genügend Ca-reiche Karbonatitschmelze, ergo kein normativer

Calcit entsteht, wie Reaktion (5) demonstriert (vgl. Falloon & Green 1990, Ulianov et al. 2007, Yaxley et al. 2022). Folglich können anschließend weder Reaktion (2) oder (3) noch (4) auftreten.

$$2\,Mg_2[Si_2O_6] + CaMg(CO_3)_2 \leftrightarrow 2\,Mg_2[SiO_4] + CaMg[Si_2O_6] + 2\,CO_2 \qquad (5)$$

Nur effektive Metasomatose durch dolomitkarbonatitische Schmelzen führt zur Wehrlitisierung des lherzolithischen Mantels *und* zur Bildung von calcitkarbonatitischer Schmelze sowie von CO_2 als Fluid oder gelöst in der Schmelze (Reaktion 1). Die nachfolgende Reaktion von Olivin (Reaktionen 2 & 3) und/oder Klinopyroxen (Reaktion 4) mit dieser Schmelze verursachte nicht-modales Aufschmelzen des Wehrlits, wodurch Ca-reiche Magmen entstanden, aus denen schließlich die Melilith-führenden jungen Gesteine kristallisierten. Ihr variables Verhältnis von Melilith und Klinopyroxen (innerhalb der Regionen) ist auf Schwankungen in den CaO-CO_2-Verhältnissen während der Magmagenese (Reaktionen 2 & 3) und Unterschiede in den CaO-MgO-Verhältnissen der Magmaquelle zurückzuführen (Reaktionen 1 & 5). Das Fehlen von magmatischen Karbonaten in den untersuchten silikatischen Gesteinen resultiert vermutlich aus der Entmischung der hochmobilen karbonatreichen Fluide sowie gelöstem CO_2 aus dem System spätestens beim Erreichen von oberkrustalen Drücken. Auch eine räumlich voranschreitende Wehrlitisierung ohne Bildung weiterer Karbonate entsprechend der Reaktion 5 würde die durch Reaktionen 2 und 3 freigesetzten Dolomitkarbonatit-Schmelzen aufzehren, ohne weitere Karbonate zu bilden.

3.2.4. Spätmagmatische Entwicklung, die Bedeutung von Volatilen und Entgasung

Die anhaltende Kristallisation diopsidischen Pyroxens überdauerte das spätmagmatische Ende der Melilith- und Perowskit-Kristallisation in den jüngeren Gesteinen und mündete schließlich in die Bildung von Klinopyroxen mit zunehmend höheren Fe^{3+}-, Al- und Ti-Gehalten, was mit einer ansteigenden Tschermak-Substitution einherging. Dies wird allerdings auch in den älteren Melilith-freien Gesteinen beobachtet und ist auf einen beständigen Rückgang des SiO_2-Gehalts bei gleichzeitigem relativem Anstieg von Fe^{3+}-, Al- und Ti-Konzentrationen in der residualen Schmelze zurückzuführen, sodass in der Folge auch Titanomagnetit, Nephelin und Minerale der Sodalith-Gruppe kristallisierten.

Die Zusammensetzung dieser und anderer spätmagmatischer Phasen, darunter auch Apatit, Phlogopit/Kinoshitalit, Amphibol, Rhönit und Perowskit reflektiert im Wesentlichen die Na_2O/K_2O-Entwicklung, die Anreicherung mit LILE (Ba, Sr), LREE, TiO_2 und

Nb sowie die Verhältnisse und die Gehalte der Volatilen, besonders H_2O, F, Cl und S in den Magmen während der Kristallisation. Unterschiede zwischen den beiden primitiven Gesteinsgruppen in Bezug auf Mengen und Zusammensetzungen von Mineralen reich an volatilen Elementen (v. a. H_2O-F-Cl- und SO_3-Cl-Verhältnisse) können die Variabilität der Magmaquellen oder aber (auch) die relative Anreicherung während der magmatischen Entwicklung und unterschiedliche Zeitpunkte und Ausmaße des Entgasens während des Aufstiegs widerspiegeln. Bekannt ist, dass kontinuierliche Entmischung und Abgabe von CO_2 vor und während der Kristallisation der Grundmassephasen die Abwesenheit Karbonat-haltiger Minerale erklären und die Stabilität von Melilith gewährleisten, indem die Rückreaktion 4, also der spätmagmatische Abbau von Melilith durch Reaktion mit CO_2 zu Klinopyroxen und Calcit verhindert wird (vgl. Melluso et al. 2011, Veksler & Lentz 2006).

Die älteren, nephelinitischen bis basanitischen Gesteine sind gegenüber den jüngeren Vulkaniten neben der Abwesenheit von Melilith und Perowskit durch deutlich F-ärmeren Phlogopit und Apatit gekennzeichnet, was auf geringere F- und/oder höhere H_2O-Gehalte im spätmagmatischen Stadium dieser Schmelzen hindeutet. Die Melilith-führenden Gesteine enthalten dagegen meist auch Perowskit und zeigen hohe F-Gehalte in Phlogopit, Kinoshitalit und Apatit, sodass auf hohe CaO- bei niedrigeren H_2O- und SiO_2-Gehalten in der Schmelze geschlossen werden kann. Die spätmagmatische Kristallisation von Phlogopit bzw. Kinoshitalit und das Fehlen der Entstehung von Amphibol ist auf sukzessive abfallende Ca-Konzentrationen und Na-K-Verhältnisse in der Ba-, F- und/oder H_2O-angereicherten Restschmelze sowie möglicherweise partielle Resorption von Olivin zurückzuführen. Phlogopit-Präzipitation aus anfänglich sodischen Magmen und die moderate Kompatibilität von K in Nephelin und Haüyn erklären das weitgehende Fehlen weiterer K-reicher Silikate.

In einigen besonders CaO-reichen Gesteinen des Uracher Vulkangebiets tritt als spätmagmatische Phase jedoch mikrokristalliner Kalsilit auf. Dem liegen vergleichsweise geringe anfängliche Na_2O-K_2O-Verhältnisse und äußerst geringe SiO_2-Aktivitäten zu Grunde, was sich auch an der Präsenz von Perowskit zeigt. Daneben ist eine Anreicherung von K gegenüber Na in den Melilith-reichen Gesteinen auch während der frühmagmatischen Schmelzentwicklung möglich, da das mit relevanten Anteilen auftretende Melilith-Endglied Alumoåkermanit dem Magma Na, nicht aber K entzieht. Kalsilit-führende Gesteine weisen ferner nur geringe Gehalte an Glimmer auf, welcher zudem F- und Ba-reich ist (Fluoro- und Oxykinoshitalit). Dies zeigt, dass die Bildung von Kal-

silit durch sehr geringe Wassergehalte in der residualen Schmelze und eine hohe Konkurrenz von K durch Ba auf der Glimmer-Zwischenschicht unterstützt wird. In weniger stark SiO_2-untersättigten Nephelinbasaniten der oberkretazischen bis eozänen Gruppe sind mitunter geringe Mengen interstitiellen Sanidins zu finden. Dies dürfte ebenfalls in erhöhten K-Gehalten und der Hemmung weiterer Glimmerbildung in der durch Entgasung an H_2O- und F-verarmten residualen Schmelzen begründet liegen.

3.2.5. Der geringe Einfluss von fraktionierter Kristallisation, Magmamischung und Nebengesteinsinteraktion in den primitiven Gesteinen

Größtenteils kontinuierlich abnehmende MgO-, Ni- und Cr-Gehalte sowie variierende Al_2O_3- und SiO_2-Gehalte im Zuge der magmatischen Entwicklung beider Gesteinsgruppen können teilweise durch Fraktionierung Cr-reichen Oxyspinells und Mg- und Ni-reichen Olivins erklärt werden. Nennenswerte Klinopyroxen-Fraktionierung ist dagegen unwahrscheinlich, da eine erhebliche Abnahme von CaO und Sc nicht festzustellen ist (Embey-Isztin et al. 1993, Jung & Masberg 1998, Pfänder et al. 2018, Schubert et al. 2015). Besonders hohe MgO-, Cr- und Ni-Gehalte in einigen Magmen (vor allem im Uracher Vulkangebiet) sind auf hohe Olivin-Gehalte, Cr-reiche Oxyspinell-Xenokristalle und Cr-führende Klinopyroxen-Kerne zurückzuführen (vgl. Arzamastsev et al. 2009, Dunworth & Wilson 1998).

Die niedrigen SiO_2- und K_2O-Gehalte, das Fehlen einer Eu-Anomalie sowie hohe MgO-Gehalte und Ce/Pb-Verhältnisse schließen signifikante Assimilation von felsischen krustalen Lithologien aus, da in diesem Fall schwächer SiO_2-untersättigte Gesteine, Alkalien- und Pb-Anreicherung und bedeutend mehr Alkalifeldspat-Kristallisation zu erwarten wären (Bogaard et al. 2001, Haase et al. 2004, Jung & Hoernes 2000, Kolb et al. 2012). Allerdings zeigen die Grünkernpyroxene in den nephelinitischen bis basanitischen Gesteinen, dass Magmamischung bzw. die Aufnahme von bereits kristallisierendem Magma innerhalb der Kruste und/oder dem obersten Erdmantel regional eine Rolle spielte (vgl. Duda & Schmincke 1985, Jung & Hoernes 2000; Jung et al. 2012). Der Roßberg-Nephelinit (Untermainebene) führt große Mengen Cl-reichen Sodaliths und weist bei ansonsten primitiver Signatur hohe Mn-Gehalte im Gesamtgestein auf, was auf Assimilation von Zechstein-Evaporiten und Zechstein-Dolomit mit Mn-Oxid-Horizonten hindeutet. Die Präsenz solcher Ablagerungen in der Sedimentationsfolge der Untermainebene und des Odenwalds im Gegensatz zum übrigen Untersuchungsgebiet ist seit langem bekannt (Becker 1904, Klemm & Fazakas 1975, Ramdohr 1975).

Die jüngeren Melilith-haltigen Gesteine enthalten bis auf wenige Ausnahmen keine Grünkernpyroxene und weisen im Durchschnitt höhere Mg-, Cr-, Ni- und Co-Gehalte sowie niedrige Ca-Ni-Verhältnisse in Olivin-Kernen ähnlich solchen des Erdmantels auf (vgl. Bussweiler et al. 2015, Foley et al. 2013), was einen geringen Einfluss von fraktionierter Kristallisation und Kontaminationsprozessen zeigt. Dennoch belegen die Forsterit-verarmten Olivin-Kerne in einigen Proben, dass auch diese Gesteinsgruppe nicht völlig unberührt von Stagnation und Magmamischung im oberen lithosphärischen Erdmantel ist. Dies wird durch die – wenngleich einzigen – Vorkommen der jüngeren Gesteinsserie mit Grünkernpyroxenen (Eisenrüttel, Buggingen) untermauert. Im Fall des Eisenrüttels lassen große Mengen von Mineralen reich an volatilen Elementen sowie überdurchschnittlich hohe Sr-, Nb-, Ta-, Th- und REE-Gehalte in Haüyn, Apatit und Perowskit für seine Entstehung zusätzlich Fraktionierungsprozesse vermuten.
Insgesamt deuten geochemische und mineralchemische Zusammensetzung sowie die Kristallfracht auf quantitativ nachrangige Kontaminations-, fraktionierte Kristallisations- und Magmamischungsprozesse in der Unterkruste und im oberstem Erdmantel hin, die jedoch regional und lokal spürbar variieren können. Mineralbestand und Spurenelementmuster der primitiven Gesteine dürften demnach sowohl die Schmelzentwicklung als auch die Heterogenität der Magmaquellen sowie den partiellen Aufschmelzgrad widerspiegeln (vgl. Bogaard et al. 2001, Kolb et al. 2012, Mayer et al. 2013).

3.2.6. Petrogenese der entwickelten Haüyn/Nosean-reichen Gesteine

Die oberkretazischen bis paläozänen (phonolithischen) Haüynite/Noseanite und Haüyn-Nephelinite des Odenwalds und des Kraichgaus repräsentieren als Folge der Fraktionierung größerer Mengen Olivin, Klinopyroxen und Oxyspinell gegenüber den beiden primitiven Gesteinsgruppen deutlich stärker entwickelte Magmen. Die Chondrit-normierten REE-Muster der Gesteine unterstützen diesen Befund, da sie abgesehen vom höheren Anreicherungsfaktor aller Seltener Erden denen der primitiveren Glimmer-reichen Nephelinbasanite und basanitischen Nephelinite aus derselben Region gleichen. Im Mineralbestand drückt sich die magmatische Entwicklung durch geringe Gehalte (<10 Vol.-%) und kleine, unzonierte Forsterit-verarmte Kristalle von Olivin aus. Die erhebliche Abweichung der Mn- und Ni-Gehalte vom Kristallisationstrend für Olivin in den primitiven Gesteinen des Odenwalds und des Kraichgaus, die hohen Mn-Gehalte im Gesamtgestein und das Auftreten von Mn- und Zn-führendem Oxyspinell sowie Alkalifeldspat weisen jedoch auch auf nennenswerte Nebengesteinsinteraktion

hin, wobei dafür die unterlagernde ~2 km mächtige karbonische bis triassische Sedimentabfolge des Kraichgau-Beckens (Rupf & Nitsch 2008) in Frage kommt.
Hohe Konzentrationen von Wasser und weiteren volatilen Elementen in den Gesteinen spiegeln sich in Mineralbestand und Mineralchemie wider (Haüyn/Nosean, zahlreiche SO_3- und Cl-führende Apatit-Phänokristalle, Fluorokatophorit) und deuten auf Zufuhr dieser Elemente aus salinaren Formationswässern während des Aufstiegs und/oder abgeschwächte Entgasung des Magmas hin. Möglicherweise hielt die Retention von Volatilen bis in die spätmagmatische Entwicklung hinein die Solidus-Temperaturen niedrig und könnte so die zügige Kristallisation verhindert, aber Fraktionierungsprozesse und Nebengesteinsinteraktion gefördert haben, wodurch die flüchtigen Elemente im Residuum wiederum aufkonzentriert wurden (vgl. ähnliche Lithologien im Eger-Graben; Vaněčková et al. 1993).

3.2.7. Magmaquelle(n) und Aufschmelzgrade

Die bisher beschriebenen Variationen bei der Magmaentwicklung der beiden primitiven Gesteinsgruppen genügen nicht, um alle Unterschiede zwischen den oberkretazischen bis eozänen und den oligozänen bis miozänen Vulkaniten zu erklären. Ein größerer Einfluss von fraktionierter Kristallisation, wie er für die älteren Gesteine gegenüber den jüngeren angenommen wird, würde beispielweise zu einer relativen Anreicherung inkompatibler Elemente (Ti, Nb, Zr) in den jeweiligen Schmelzen führen. Allerdings werden höhere Gehalte dieser Elemente in den Melilith-führenden, jungen Gesteinen beobachtet, also genau das Gegenteil, was sich in Nb-haltigem Perowskit, höheren Titanomagnetit-Gehalten und dem gelegentlichen Auftreten Ti-reichen Amphibols äußert und eindeutig auf Unterschiede in der geochemischen Zusammensetzung der Magmaquellen hindeutet. Ebenso wenig können die unterschiedlich angereicherten inkompatiblen Spurenelemente allein über Variationen des partiellen Aufschmelzgrades erklärt werden, da damit einhergehende Konzentrationsunterschiede durch Verdünnung alle inkompatiblen Elemente in ähnlicher Weise betreffen würden (Jung & Hoernes 2000).
Die starke Anreicherung der leichten gegenüber den schweren REE und Y in beiden primitiven Gruppen weist auf eine Mantelquelle mit Pyrop-dominiertem Granat als residuale Phase hin, zumal dieser neben Y und schweren im Vergleich zu leichten REE auch Al deutlich gegenüber Ca anreichert (Bogaard et al. 2001, Haase et al. 2004, Jung et al. 2006, Kolb et al. 2012, Schubert et al. 2015). Dadurch sind die CaO-Al_2O_3-

Verhältnisse in partiellen Schmelzen aus Lithologien mit residualem Granat höher als in solchen aus Spinell-führenden Peridotiten. Die höheren durchschnittlichen CaO-Gehalte und damit ebenfalls höheren CaO-Al_2O_3-Verhältnisse sowie die niedrigeren SiO_2-Gehalte in den Melilith-führenden Gesteinen können jedoch auch durch eine intensivere Wehrlitisierung ihrer Magmaquellen durch Dolomitkarbonatit-Schmelzen erklärt werden (vgl. Reaktionen 1–4). Das zeitliche Zusammentreffen des karbonatitischen und alkalischen Magmatismus im Kaiserstuhl mit den Melilith-führenden Vulkaniten in der südlichen ZEVP (Binder et al. 2023, Ghobadi et al. 2022) ist ein weiteres Indiz für den stärkeren Einfluss Ca-reicher Karbonate und höhere Konzentrationen inkompatibler Elemente (z. B. Ba, Sr, Nb) in der Quelle der jüngeren Vulkanite gegenüber jener der oberkretazischen bis eozänen Magmen. Die niedrigen Al_2O_3- und SiO_2-Gehalte in den oligozänen bis miozänen Gesteinen, besonders im Uracher Vulkangebiet, weisen außerdem auf höhere Bildungsdrücke (Sun & Dasgupta 2020) und geringere Aufschmelzgrade hin (Jung & Hoernes 2000, Jung & Masberg 1998).

Geringere La-Lu- und höhere Y-Ho-Verhältnisse belegen für die Melilith-freien, älteren Gesteine eine weniger ausgeprägte Verarmung von schweren REE und Y. Gemeinsam mit höheren SiO_2- und Al_2O_3-Gehalten bei niedrigeren MgO-Konzentrationen deutet dies auf einen höheren Anteil von aufschmelzendem gegenüber residualem Granat hin, was höhere Aufschmelzgrade der Quelle implizieren würde (Jung & Hoernes 2000, Jung et al. 2006, Kolb et al. 2012). Auch ein niedrigerer Granat-Gehalt zu Gunsten von Spinell in der Quelle könnte die weniger effektive Fraktionierung von schweren REE und Y gegenüber leichten und Al gegenüber Ca erklären (Haase et al. 2004). Beide Optionen würden geringere Tiefen für die Magmagenese der Nephelinite und Basanite gegenüber den Melilith-führenden Gesteinen nahelegen, wenngleich das Aufschmelzen einer lherzolithischen anstatt einer wehrlitischen Quelle zumindest die niedrigeren durchschnittlichen CaO-Al_2O_3-Verhältnisse und höhere SiO_2-Gehalte allein erklären könnte. Eine H_2O-dominierte Metasomatose mit geringem Einfluss von Karbonat und CO_2 in der Quelle der älteren Magmen steht im Einklang mit höheren Gehalten wasserhaltiger Minerale in diesen Gesteinen.

Die Variationen in den Al_2O_3-, TiO_2- und SiO_2-Gehalten innerhalb der beiden primitiven Gesteinsgruppen spiegeln die Spannbreite der Mineralogie der Quelle, insbesondere die Schwankungen der Granat-, Amphibol-, Phlogopit- und Orthopyroxen-Gehalte, und/oder des Aufschmelzgrads wider, da dieser die Anteile und Verhältnisse der Beteiligung der genannten Minerale an der Partialschmelze maßgeblich beeinflusst. Nega-

tive K- und Pb-Anomalien im auf den primitiven Mantel normierten Spurenelementmuster sowie charakteristische K-La, Ce-Pb-, Ba-La- und Ba-Rb-Verhältnisse deuten auf residualen Amphibol ± Phlogopit in der Magmaquelle beider primitiver Gesteinsgruppen hin (Adam & Green 2006, Haase et al. 2004, Hegner et al. 1995, LaTourrette et al. 1995, Mayer et al. 2013). Der überwiegend sodische Charakter der untersuchten Gesteine zeigt ferner, dass umfängliches Aufschmelzen von Phlogopit unwahrscheinlich ist (Bogaard & Wörner 2003, Foley 1988, Harangi 2001, Jung et al. 2005, Mertes & Schmincke 1985). Jedoch kann besonders für einige Melilith-reiche Gesteine aus dem Uracher Vulkangebiet und dem Hegau mit etwas höheren K_2O-Gehalten, Ba- und F-reichem Glimmer sowie seltenem Kalsilit die Präsenz von geringeren Mengen Phlogopit neben Amphibol in der Magmaquelle nicht ausgeschlossen werden. Das Ausmaß und das Verhältnis der Beteiligung von Amphibol und Phlogopit am Aufschmelzprozess könnten die lokalen Unterschiede im Na_2O-K_2O-Verhältnis erklären und eine inhomogene Metasomatose des Mantels auf lokalem Maßstab reflektieren.
Die Anwendung nicht-modaler *Batch-Melting*-Modelle (Haase et al. 2004, Jung et al. 2006, Kolb et al. 2012, Mertz et al. 2015), welche für ähnliche Vulkanite aus dem nördlichen Teil der ZEVP entwickelt wurden, impliziert bei einer Granat-führenden Magmaquelle für die Melilith-führenden Gesteine einen Aufschmelzgrad von weniger als 3,5 %, während sich für die weniger Granat-reiche Quelle der nephelinitischen bis basanitischen Gesteine ein Aufschmelzgrad von 1–6 % ergibt. Die Glimmer-reichen Nephelinbasanite und basanitischen Nephelinite zeigen mit 2,5–6 % die höchsten Aufschmelzgrade, was mit niedrigeren Liquidustemperaturen aufgrund der erhöhten Wassergehalte dieser Magmen vereinbar ist.

3.2.8. Magmagenese im Rahmen der regionalen geodynamischen Entwicklung

Die Präsenz von Granat und Amphibol gilt in den Mantelquellen beider Gesteinsserien nach den zuvor benannten geochemischen Charakteristika als gesichert, sodass basierend auf dem überlappenden Anteil ihrer Stabilitätsbereiche (Falloon & Green 1990, Foley 1991, Green & Ringwood 1967, Inoue et al. 1998, Klemme 2004, Nagayoshi et al. 2016, Pintér et al. 2021, Trønnes 2002, Ziberna et al. 2013) Manteltiefen von ~70–115 km und Temperaturen von bis zu ~1350 °C für die Magmagenese angenommen werden können. Als Minimalabschätzung dienen die Kristallisationstemperaturen der frühesten Klinopyroxen-Phänokristalle in Höhe von 1250–1350 °C, was

die Schmelzbildung auf ein Intervall von <100 K eingrenzt und mit gewöhnlichen Manteltemperaturen sowie einem weitgehend adiabatischen Magmaaufstieg vereinbar ist. In der Oberkreide und im Paläozän wird von einer Lithosphärenmächtigkeit von ~80–100 km im in der Entstehung begriffenen Alpenvorland ausgegangen (Dèzes et al. 2004, Ziegler et al. 2004). Aufgrund der angenommenen Aufschmelztiefen und der beobachteten Magmazusammensetzungen ist daher für die nephelinitischen bis basanitischen Gesteine eine Magmaquelle in der unteren Lithosphäre in der thermalen Grenzschicht oder in der obersten Asthenosphäre wahrscheinlich. Dabei handelt es sich vermutlich um einen Lherzolith, der nur schwach durch Karbonate modifiziert, dafür aber von einer wässrigen Metasomatose mit niedrigem $CO_2/(CO_2+H_2O)$-Verhältnis erfasst wurde. Im Gegensatz dazu liegt die heutige Grenze zwischen Lithosphäre und Asthenosphäre in einer flacheren Tiefe von 60 ± 5 km unter dem Oberrheingraben, dem Schwarzwald und dem Odenwald, und 78 ± 5 km südwestlich und südöstlich des Oberrheingrabens unter der Schwäbischen Alb und den Vogesen (Seiberlich et al. 2013). In diesen Gebieten traten zuvor erhöhte Extension und Transtension, topografische Hebung und Erosion in Kombination mit asthenosphärischem Auftrieb und einer Ausdünnung des lithosphärischen Mantels auf. Die ursächlichen Prozesse begannen im frühen Oligozän und verstärkten sich während des Miozäns (Ziegler & Dèzes 2005). Da die jüngeren Melilith-führenden Gesteine in der südlichen ZEVP größtenteils exakt an die obengenannten Regionen gebunden sind, zapften ihre parentalen Schmelzen bei Berücksichtigung der ermittelten Tiefen für die Magmagenese eine Quelle in der oberen Asthenosphäre an, die mit metasomatisch überprägten Anteilen der Lithosphäre kontaminiert war. Eine vorherige Wehrlitisierung durch karbonatreiche Fluide in solchen Tiefenbereichen wurde z. B. für den Kaiserstuhl aber auch andernorts vorgeschlagen (Beard et al. 2007, Gorring & Kay 2000, Kargin 2021, Rehfeldt et al. 2008, Soltys et al. 2016, Ulianov et al. 2007, Yaxley et al. 2022, Xu et al. 1996).

Beide vulkanischen Episoden sind wahrscheinlich mit der mechanischen Verbindung zwischen dem Alpinen Orogen und dessen Vorland während Perioden erhöhten Subduktionswiderstands verknüpft. In diesen Zeiträumen wurden Kompressionsspannungen weit in die Vorlandbereiche übertragen, was auch dort zur starken Deformation der Lithosphäre wie Faltung, Überschiebungen und Reaktivierung tiefgreifender variszischer bis permischer Großstörungen führte (Dèzes et al. 2004, Grimmer et al. 2017, Ziegler & Dèzes 2005). Daraus resultierten isostatische Ausgleichsbewegungen, die sich in Hebung, Erosion und damit Ausdünnung der Lithosphäre äußerten (Eynatten

et al. 2020, Voigt et al. 2021). Sie wurden zur Zeit der oligozänen bis miozänen vulkanischen Aktivität von komplexen horizontalen, O-W-orientierten trans- und extensionalen Ausweichbewegungen (*passive Grabenbildung*) gegen die NW-gerichtete Stauchung der Alpen sowie gegen interferierende, nordwärts gerichtete Kompressionsspannungen infolge der Pyrenäen-Kollision begleitet (Ring & Gerdes 2016, Schumacher 2002). Die starke Interaktion zwischen Lithosphäre und Asthenosphäre, d. h. thermale Ausdünnung und Aufnahme metasomatisch überprägter Bereiche der unteren Lithosphäre durch die Asthenosphäre könnte eine Folge der tektonischen Deformationsprozesse sein und maßgeblich zur partiellen Schmelzbildung beigetragen haben (vgl. Eynatten et al. 2020, Jung & Hoernes 2000, Jung et al. 2005, Kolb et al. 2012, Mertz et al. 2015, Pfänder et al. 2018, Puziewicz et al. 2020, Schubert et al. 2015).

Wässrige als auch Karbonat-Metasomatose und Wehrlitisierung in der unteren Lithosphäre erfolgten vermutlich bevor EKRiS-assoziierte Hebungs- und Grabenbildungsprozesse einsetzten und als die Grenze zwischen Lithosphäre und Asthenosphäre noch tiefer lag (~100–120 km; Seiberlich et al. 2013, Ziegler & Dèzes 2005). Die metasomatischen Fluide resultierten wahrscheinlich aus der kontinuierlichen Entwässerung und partiellen Rückführung von Teilen der subduzierten variszischen Kruste in den Mantel, was die Abgabe von Ca, CO_2, H_2O und weiteren volatilen sowie inkompatiblen Elementen in die Asthenosphäre und untere Lithosphäre umfasste. Dadurch können die Anreicherung der Magmen und ihrer peridotitischen Quellen mit CaO, Nb, Sr, Ba, LREE, U und Th im Vergleich zum primitiven Mantel sowie die Präsenz von CO_2; H_2O und F und damit von wässrigen, LILE-haltigen Phasen wie Amphibol und ggf. Phlogopit erklärt werden (vgl. Blusztajn & Hegner 2002, Jung et al. 2006, Loges et al. 2019, Mertes & Schmincke 1985, Ulrych et al. 2008). Über Anzahl und Dauer metasomatischer Ereignisse in der südlichen ZEVP kann zurzeit nur spekuliert werden, wobei verschiedene Signaturen der beiden Gesteinsgruppen eine zeitliche und/oder räumliche Heterogenität der Überprägung voraussetzen. Xenolithe aus dem lithosphärischen Mantel unter Mitteleuropa weisen darauf hin, dass der verarmte orogene Mantel sowohl durch karbonatisierte alkalische Schmelzen aus subduzierter Lithosphäre als auch durch primäre asthenosphärische Schmelzen (wieder)angereichert worden sein könnte (Puziewicz et al. 2020).

Die thermodynamischen Bedingungen führten jedenfalls nicht unmittelbar nach der Metasomatose zur Schmelzbildung und Magmamobilisierung. Erst Aufwölbung der Asthenosphäre und Ausdünnung der Lithosphäre bedingt durch die geodynamische

Entwicklung ab der Oberkreide gewährleisteten wirksame Wärmezufuhr in metasomatisch veränderten Bereichen und lösten vulkanische Aktivität aus (Blusztajn & Hegner 2002, Eynatten et al. 2020, Harangi et al. 2015, Wilson et al. 1995). Im Verlauf der weiteren Entwicklung des EKRiS setzte sich die Hebung der Asthenosphäre fort (Ziegler & Dèzes 2005), wodurch die Lithosphäre abermals ausgedünnt, thermisch erodiert, partiell aufgeschmolzen und in die Asthenosphäre eingearbeitet wurde, was den oligozänen bis miozänen Vulkanismus zur Folge hatte. Eine Entwicklung von Lithosphäre- zu Asthenosphäre-dominierten Magmaquellen wird auch für andere Regionen in der ZEVP sowie für das Französische Zentralmassiv und das Pannonische Becken vorgeschlagen, wenngleich innerhalb kürzerer Zeitabschnitte (Bogaard & Wörner 2003, Dautria et al. 2010, Harangi & Lenkey 2007, Jung & Masberg 1998, Seghedi & Downes 2011). Im Untersuchungsgebiet könnte dieser Prozess durch Relaxation von Intraplattenspannungen infolge der Reaktivierung der Subduktion im Alpengürtel sowie Perioden erhöhter Subsidenz und verminderter Hebung zwischen 47 und 27 Ma verzögert worden sein.

Weder ein übermäßig heißer Mantel noch eine thermische Anomalie oder vom tiefen Mantel ausgehende Konvektionsströme sind notwendig (*aktive Grabenbildung*), um den oberkretazischen bis miozänen Vulkanismus in der südlichen ZEVP zu erklären. Vielmehr genügen lokale oder regionale, räumlich und zeitlich variierende Hebungen der Grenze zwischen Lithosphäre und Asthenosphäre, um das Aufschmelzen der metasomatisch überprägten Domains durch thermische und kompositionelle Interaktion zwischen Lithosphäre und Asthenosphäre zu ermöglichen. Ob konvektive Prozesse in der oberen Asthenosphäre und konduktiver Wärmetransfer an die darüberliegende Lithosphäre die Dynamik der Kruste kontrollieren oder vielmehr eine Antwort auf diese sind, kann jedoch nicht abschließend beantwortet werden.

3.3. Entstehung der Nosean-Phonolithe im Hegau als Folge von Differentiationsprozessen

Als eine der wenigen Regionen mit Vorkommen von sowohl primitiven melilithitischen bis nephelinitischen Vulkaniten (~12–9 Ma) als auch hochentwickelten SiO_2-untersättigten alkalischen Gesteinen in Form von Nosean-Phonolithen (~14–11 Ma) ist der Hegau besonders geeignet, um der Frage nachzugehen, ob und unter welchen Bedingungen intrakontinentale wenig differenzierte Mantelschmelzen der ZEVP zu felsischen Magmen fraktionieren und ob zusätzliche Assimilationsprozesse dafür unabdingbar sind (Binder et al. 2024a). Die Nosean-Phonolithe sind durch hohe Na_2O-, K_2O-, Al_2O_3-, SiO_2-, Rb-, Nb-, Zr-, U-, Pb-, S- und niedrige MgO-, CaO-, Fe_2O_3-, TiO_2-, P_2O_5-, Ba-, Ni- und V-Gehalte gekennzeichnet. Sie enthalten große Mengen von Ba-haltigen Alkalifeldspat- und Nosean-Haüyn-Sodalith-Phänokristallen (primär $Nsn_{48-65}Hyn_{28-45}Sdl_{6-10}$) und daneben Ägirin-Augit sowie akzessorisch Apatit ($F_{24-89}OH_{11-74}Cl_{0-2}$-Ap), Nb- und Zr-haltigen Titanit, Zirkon und Pyrochlor. Die Grundmasse besteht ebenfalls hauptsächlich aus Alkalifeldspat, Nosean ($Nsn_{89-100}Hyn_{0-11}Sdl_{0-1}$), Nephelin und Ägirin-Augit. Ferner enthalten alle vulkanischen Gesteine des Hegaus cm³-große, grobkörnige Einschlüsse von (Nephelin-)Syenit, die sich aus idiomorphem bis hypidiomorphem Alkalifeldspat, Nephelin und Ägirin-Augit in jeweils variablen Mengen sowie etwas Dunkelglimmer zusammensetzen. Daneben kommen interstitiell Karbonat und akzessorisch Apatit, Titanit, Pyrochlor, Zirkon, Thorit und Thorianit vor, wobei Apatit in einzelnen Proben mit bis zu 30 Vol.-% eines der Hauptminerale darstellt. Anhand des Klinopyroxen-Gehaltes lassen sich eine leukokrate und eine mesokrate Varietät von (Nephelin-)Syenit unterscheiden, die im selben Einschluss zu finden sein können.

Ausschließlich in den primitiven melilithitischen bis nephelinitischen Magmen treten grobkörnige ijolithische Schlieren auf, die durch eine wenige Millimeter breite Übergangszone vom feinkörnigen Gesteinskörper abgegrenzt sind und sich im Gegensatz zu diesem durch das Fehlen von Olivin und höhere Gehalte von Nephelin, Klinopyroxen, Fluorapatit, Titanomagnetit sowie Nb-, Na-, Sr- und REE-reichen Perowskit auszeichnen. Die beiden letztgenannten Minerale sind sehr häufig durch skeletale Kristalle und Kristallgruppen charakterisiert, während zonierter Klinopyroxen, Apatit und mitunter Nephelin ein hohes Maß an Eigengestalt zeigen.

3.3.1. Ijolithische Schlieren als Folge von In-situ-Differentiation: ein Bindeglied zwischen melilithitischen bis nephelinitischen und phonolithischen Magmen?

Die grobkörnigen schlierenartigen Texturen in Melilith-führenden Olivin-Nepheliniten bzw. Olivin-Melilithiten des Hegaus deuten auf In-situ-Differentiationsprozesse hin. Ihre geochemische Zusammensetzung ist entwickelter als die der vulkanischen Wirtsgesteine, wie sich an höheren Na_2O-, K_2O- und Al_2O_3- bei niedrigeren MgO- und Fe_2O_3-Gehalten zeigt, die sich alle in Richtung der Zusammensetzung der Nosean-Phonolithe entwickeln. SiO_2, CaO, TiO_2 und P_2O_5 spiegeln den Entwicklungstrend in diesem Stadium noch nicht wider. Insgesamt ist die geochemische Zusammensetzung der Ijolithe konsistent mit den Veränderungen im Mineralbestand, die sich im Fehlen von Olivin und Melilith und der Zunahme von Klinopyroxen, Nephelin, Titanomagnetit, Perowskit und Apatit gegenüber dem Wirtsgestein bemerkbar machen. Während die Kernzusammensetzungen von Klinopyroxen-Kristallen Diopsid-dominiert sind, weisen die Ränder hohe Ägirin- und Hedenbergit-Anteile und Ti-Gehalte auf, die der Zusammensetzung von Klinopyroxen in den Nosean-Phonolithen und (Nephelin-)Syeniten stark ähneln. Außerdem zeigt Perowskit in den Ijolithen eine kontinuierliche Anreicherung von inkompatiblen Elementen (Nb, Ta, Na, Sr, Th, REE) gegenüber Perowskit in den melilithitischen bis nephelinitischen Vulkaniten. Dasselbe gilt für Cl und H_2O in Apatit und Mn und V in Magnetit. Die Beobachtungen unterstützen die Annahme der Anreicherung dieser Elemente in kleinräumigen, wahrscheinlich cm^3- bis dm^3-großen residualen Schmelztaschen und damit des Auftretens lokal begrenzter In-situ-Differentiation, auch wenn ein Anstieg des SiO_2-Gehaltes und Alkalifeldspat-Sättigung für eine weiterreichende Entwicklung hin zu einer phonolithischen Zusammensetzung fehlen. Wahrscheinlich verhinderten die Kristallisation unter annähernden Gleichgewichtsbedingungen ohne ausreichenden Entzug von Kristallen, also der Mangel an Fraktionierung, und die schnelle Abkühlung eine intensivere Differentiation zu SiO_2-reicheren und CaO-, TiO_2 und P_2O_5-verarmten Phonolithen oder Nephelin-Syeniten. Diese These wird durch die zahlreichen Skelettkristalle von Perowskit und Magnetit unterstützt, die auf schnelles Wachstum durch starke Übersättigung der entsprechenden Elemente aufgrund zügiger Unterkühlung der eingeschlossenen Restschmelze hindeuten (vgl. Gornitz 1981).

3.3.2. Fraktionierte Kristallisation melilithitischer bis nephelinitischer Schmelzen ermöglicht die Entwicklung zu Nosean-Phonolithen

Die Alter der primitiven und der entwickelten vulkanischen Gesteine des Hegaus überlappen, wenngleich der phonolithische Vulkanismus früher einsetzte und die auch in den melilithitischen bis nephelinitischen Magmen auftretenden (Nephelin-)Syenit-Einschlüsse zeigen, dass zum Zeitpunkt der Eruptionen bereits entwickelte Magmatite in der Kruste existierten. Sie können als Kumulatgesteine gedeutet werden, die aufgrund der variablen Anteile von Nephelin und Klinopyroxen – teilweise innerhalb desselben Fragments – auf eine geschichtete Anordnung mesokrater und leukokrater Lithologien innerhalb einer Magmakammer hindeuten, welche Konvektion und periodischen Magmanachschub erfuhr. Allerdings repräsentieren sämtliche Kumulatfragmente ein bereits stark differenziertes, SiO_2- und Alkalien-reiches Magma, sodass sie allein keine Auskunft geben, ob die parentalen Schmelzen der Nosean-Phonolithe der Zusammensetzung der primitiven melilithitischen bis nephelinitischen Magmen entsprechen. In diesem Fall wären die älteren Phonolith-Staukuppen nach erheblicher Fraktionierung solch primitiver Schmelzen in der Kruste entstanden, während die jüngeren Vulkanite in der Folge des Transports des Magmas vom Mantel direkt an die Oberfläche eruptiert wurden. Dafür sprechen das Auftreten von Mineralen der Sodalith-Gruppe in beiden Gesteinstypen und die kontinuierliche Entwicklung der Klinopyroxen-Zusammensetzung von Diopsid–Hedenbergit in Richtung Ägirin, was eine Veränderung der Magmazusammensetzung in Richtung sehr niedriger MgO- und CaO- sowie hoher Na_2O-Gehalte und Fe^{3+}-Fe^{2+}-Verhältnisse widerspiegelt. Die hohen Konzentrationen von Na_2O, K_2O, Al_2O_3 und SiO_2 äußern sich in den Nosean-Phonolithen vor allem durch große Mengen Alkalifeldspat, Nephelin und die Kristallisation von Titanit anstelle von Perowskit. Die Abnahme der CaO-Gehalte bei gleichzeitiger Zunahme der K_2O-Gehalte lässt sich außerdem an der Zusammensetzung der Minerale der Sodalith-Gruppe ablesen, die in den Nosean-Phonolithen K-reich und faktisch Ca-frei sind, während sie in den Melilithiten und Nepheliniten Ca-reich und K-arm sind.

Die REE-Muster, Zr-Hf- und Nb-Ta-Fraktionierung, die auffallend negativen Ti- und P-Anomalien in der Mantel-normierten Spurenelementverteilung und die niedrigen CaO-, TiO_2- und P_2O_5-Gehalte in den Nosean-Phonolithen weisen deutlich auf Titanit- und Apatit- sowie möglicherweise Pyrochlor-Fraktionierung während der Schmelzentwicklung hin. All diese Minerale treten in bedeutenden Mengen in den (Nephelin-)Syeniten auf, was auf ihre partielle Separation von der residualen Phonolith-Schmelze und

Anreicherung in den Kumulatgesteinen schließen lässt. Das übrige Spurenelementmuster spiegelt die relative Anreicherung bestimmter inkompatibler Elemente (z. B. Cs, Th, U, Ta, Nb, Hf, Zr) während der Differentiation und deren Verteilung auf die Mineralphasen im (nephelin-)syenitischen Kumulat und in der phonolithischen Restschmelze wider. Dabei sind vor allem die Akzessorien Zirkon, Titanit und Pyrochlor sowie der Zr-Gehalt in Klinopyroxen relevant. Hohe Ba-Konzentrationen im Feldspat sind auf bereits hohe Ba-Gehalte in den melilithitischen bis nephelinitischen Schmelzen und die weitere Anreicherung während der Fraktionierung zurückzuführen, wie es typisch für Phonolithe ist, die aus nephelinitischen Schmelzen hervorgehen (Le Bas 1987). Die sehr geringen Cl-Gehalte im Apatit in den Nosean-Phonolithen im Vergleich zu den primitiven Gesteinen und den Ijolithen erklären sich durch die großen Mengen von Nosean-Haüyn-Sodalith in den entwickelten Gesteinen, welche den größten Teil des Chlors aufgenommen haben.

Fraktionierte Kristallisationsmodellierung mit der Software-Plattform MELTS unterstützt die Schlussfolgerungen aus geochemischen, mineralogischen und mineralchemischen Ergebnissen. Sie zeigt, dass die fraktionierte Kristallisation von 11–19 % Oxyspinell, 4–10 % Olivin, 42–57 % Klinopyroxen, ~2 % Apatit, <3 % Glimmern, <9 % Foiden, und <8 % Feldspat (einsetzend in der genannten Reihenfolge) aus Magmen mit der Zusammensetzung der primitiven Hegau-Vulkanite zu phonolithischen Restschmelzen führen kann. Ihre prognostizierten geochemischen und mineralogischen Zusammensetzungen entsprechen weitgehend denen der Nosean-Phonolithe und auf ihrem Differentiationspfad dorthin denen der Nephelin-Syenite. Die bestmögliche Annäherung wird bei oberkrustalen Drücken von 200 MPa sowie solchen melilithitischen bis nephelinitischen Magmen mit den niedrigeren Alkaliengehalten erreicht. Dabei zeigt sich, dass das phonolithische Residuum nach der Differentiation über basanitische/tephritische (seltener trachybasaltische oder basaltische), phonotephritische und tephriphonolithische (seltener Alkalien-reiche foiditische) Zusammensetzungen noch ~12–35 Masse-% der primitiven Ausgangsschmelzen repräsentiert.

Die Ergebnisse deuten ferner auf ein ausgedehntes Kristallisationsintervall hin, welches zwischen ~1050 und 800 °C zur Bildung der (Nephelin-)Syenit-Kumulate führte. Die Extraktion der phonolitischen Schmelzen erfolgte bei nicht weniger als 900 °C und die vollständige Erstarrung bei spätestens 750 °C. Die großen Temperaturintervalle sind mit dem porphyrischen Gefüge, welches auf kontinuierliche Kristallisation während der Abkühlung hinweist, sowie mit möglicher partieller Kumulatremobilisierung,

-wiederaufschmelzung und Aufnahme von Kumulatkristallen durch Magmakonvektion und -nachschub vereinbar (vgl. Sliwinski et al. 2015, Wörner & Wright 1984). Für die Kristallisation phonolithischer Gesteine in der übrigen ZEVP andernorts wurden vergleichbare Temperaturen und ebenfalls große Temperaturintervalle ermittelt (vgl. Berndt et al. 2001, Bourdon et al. 1994, Braunger et al. 2018, Ginibre et al. 2004, Mann et al. 2006, Panina et al. 2000, Schmitt et al. 2010, Sharygin et al. 2005, Sliwinski et al. 2015, Wörner & Wright 1984).

Merkliche Krustenassimilation während der fraktionierten Kristallisation ist nicht erforderlich, um die geochemischen, mineralogischen und mineralchemischen Eigenschaften der Nosean-Phonolithe zu erklären. Die leicht positive Pb-Anomalie im Vergleich zur stark negativen in den primitiven Gesteinen, niedrige Ce-Pb-Verhältnisse und stark variierende Nb-U-Verhältnisse könnten auf die Assimilation kontinentaler Kruste hindeuten; jedoch wären für Nachweis und Quantifizierung Isotopendaten notwendig.

3.3.3. Die Bunsen-Daly-Lücke und Konsequenzen für die vulkanische Entwicklung

Oberkrustale Differentiationsprozesse (15–11 Ma; Alter der Nephelinsyenite und Syenite) kulminierten im zentralen Ost-Hegau in der Platznahme von Phonolith-Staukuppen (14–11 Ma), während weitgehend undifferenzierte melilithitische bis nephelinitische Laven (12–9 Ma) im nördlichen und westlichen Hegau dominieren. Die kompositionelle Lücke zwischen primitiven und entwickelten Gesteinen bei bimodalem Vulkanismus wird als *Bunsen-Daly-Lücke* bezeichnet. Sie ist im Fall des Hegaus auf die größtenteils zeitlich separierte Kristallisation und Abtrennung von zunächst fast ausschließlich mafischen und anschließend vornehmlich felsischen Mineralen sowie auf den bevorzugten Zeitpunkt der Magmaextraktion zurückzuführen. Diese Beobachtung wird auch durch die Ergebnisse der MELTS-Modellierung abgebildet, die für den Temperaturbereich oberhalb von ~1050–1100 °C überwiegend Fraktionierung von Oxyspinell, Olivin, Klinopyroxen und geringen Mengen Apatit vorhersagt, wodurch die Restschmelze auf etwa 30–50 % des ursprünglichen Volumens reduziert wird. Entsprechende olivinpyroxenitisch bis wehrlitisch zusammengesetzte Kumulatgesteinsfragmente sind aus den Phonolithen des Hegaus nicht überliefert. Dies könnte jedoch sowohl an der effektiven gravitativen Trennung der dichten mafischen Kumuluskristalle vom leichteren intermediären bis felsischen Residuum als auch an der vollständigen Auflösung solcher Lithologien durch das starke Ungleichgewicht zu der mittlerweile stark entwickelten Restschmelze liegen.

Die Klinopyroxen- und Apatit-Kristallisation setzt sich in geringerem Umfang noch bis ~900 °C herab fort, während zwischen 1050 und 950 °C die Bildung von Glimmer, Feldspat und Foiden beginnt, die sich bis zur Erstarrung der Phonolithe fortsetzt. Diese Fraktionierungsperiode lässt sich gut an der Makrokristallfracht der Nosean-Phonolithe und an den variabel zusammengesetzten Kumulatfragmenten nachvollziehen. Sie sind durch eine kontinuierliche Entwicklung von mesokraten (Nephelin-)Syeniten mit bis zu 30 Vol.-% Klinopyroxen, 5 Vol.-% Dunkelglimmer ± Apatit sowie akzessorisch Titanit und Zirkon zu leukokraten (Nephelin-)Syeniten mit Alkalifeldspat, Dunkelglimmer ± Nephelin sowie akzessorisch Karbonat, Titanit, Pyrochlor, Zirkon, Thorit und Thorianit gekennzeichnet. Möglicherweise hat Magmanachschub intermediärer Zusammensetzung die Extraktion und Eruption der phonolithischen Schmelzen inklusive der Mitnahme von Kumulatfragmenten ausgelöst. Dies muss zu einem Zeitpunkt erfolgt sein, als Klinopyroxen und Apatit noch kristallisierten, also bei >900 °C. Verwandte Modelle zur Erklärung von bimodalem alkalischen Vulkanismus auf den Kanarischen Inseln und im Äthiopischen Grabenbruch basieren ebenfalls auf einer zeitlich getrennten Kristallisation mafischer und felsischer Minerale sowie einer bevorzugten Magmamobilisierung zu bestimmten Zeitpunkten. Dafür werden einerseits das Überschreiten des intermediären Entwicklungsstadiums innerhalb eines engen Temperaturintervalls mit einer entsprechend geringen Kristallisationsrate (Peccerillo et al. 2003) und andererseits der optimale Zeitpunkt der Schmelzextraktion aus einem Kristallbrei bei mittlerer Kristallinität (d. h. ~30–60 % Feststoff; Sliwinski et al. 2015) verantwortlich gemacht. Demzufolge begünstigen in diesem Zeitabschnitt die rheologischen Bedingungen und die freigesetzte Kristallisationswärme, welche die Kristallisationsrate absenkt, eine effektive Kristall-Magma-Separation und vereinfachen dadurch die anschließende Magmamobilisierung.

Für die räumliche und zumindest phasenweise zeitliche Trennung der entwickelten von den primitiven Vulkangebäuden im Hegau sind wahrscheinlich Unterschiede in der Dichte und der Plastizität der verschiedenen Grundgebirgseinheiten die Ursache. Außerdem könnten die flach einfallenden Grenzflächen von Überschiebungen den Auftrieb mafischer Schmelzen beeinträchtigt und dadurch ihren Aufstieg verzögert und Differentiationsprozesse ermöglicht haben (z. B. Büchner et al. 2015). Eine zeitliche Separation primitiver melilithitischer bis nephelinitischer Gesteine von stärker entwickelten Vulkaniten wird unter anderem auch im Eger-Graben und im Siebengebirge beobachtet, wo erstere Magmen hauptsächlich im Laufe der Vorphase und unterge-

ordnet in der Spätphase der Grabenbildung beim Vorherrschen eines kompressiven Spannungsfeldes auftreten, wogegen differenzierte Magmen während der extensionalen Hauptphase dominieren (Ulrych et al. 2011, Przybyla et al. 2018). An Grabensysteme gebundene, primitive vulkanische Gesteine sind demnach häufig mit bedeutenden Verwerfungen assoziiert, während das Auftreten entwickelter Lithologien weniger durch Bruchtektonik kontrolliert wird, was den langsameren Aufstieg und die dadurch erleichterte Differentiation erklären könnte.

Auch im Hegau dürften Differentiation, Magmaaufstieg, Eruptionen und Platznahme durch die regionale geotektonische Entwicklung gesteuert worden sein. Der spätestmögliche Beginn oberkrustaler Differentiationsprozesse wird durch die ältesten bekannten Nephelinsyenit-Alter (~15 Ma; Hohenstoffeln) markiert und erstreckte sich über große Bereiche des Hegaus, wie sich an den flächenhaft verbreiteten und in zahlreichen Vulkaniten vorkommenden Kumulatfragmenten zeigt. Auch eine durch Fernerkundung und GIS erfasste, ausgedehnte ringförmige magmatische Struktur im Untergrund stützt diese Annahme (Theilen-Willige 2011). Ausgeprägte Hebung im Vogesisch-Schwäbischen Bogen am südlichen Ende der Süddeutschen Blockscholle, die zu intensiver Erosion in der Schwäbischen Alb führte (Ring & Bolhar 2020), ist ein Anzeichen für die Ausdünnung der Lithosphäre, wodurch die magmatische Aktivität möglicherweise eingeleitet wurde. Hebung und Erosion setzten sich im späten Miozän und frühen Pliozän fort und bewirkten Überschiebungen und eine deutliche Faltung des Juras und des Molassebeckens vor 12–10 Ma (Becker 2000, Hagke et al. 2012), was sich mit dem Alter der jüngeren, primitiven Vulkanite im Hegau deckt. Intensivierte Hebung und einsetzende Grabenbildung führten also zunächst zur Entwicklung größerer oberkrustaler Magmakammern und entsprechenden Differentiationsprozessen, aus welchen die (Nephelin-)Syenit-Kumulate und phonolithische Schmelzen hervorgingen. Fortgesetzte und fortschreitende Grabenbildung, verbunden mit dem Auseinanderbrechen der Oberkruste, verursachte die Reaktivierung tiefreichender Störungssysteme und vereinfachte damit den zügigen Magmaaufstieg, sodass die melilithitischen bis nephelinitischen Schmelzen und mafische Tuffe ohne vorherige nennenswerte Fraktionierung eruptierten. Die teilweise zeitliche Überlappung der verschiedenen Formen des Hegau-Vulkanismus reflektiert kontinuierliche Aktivität mit einem schrittweisen Wechsel von entwickeltem zu primitivem Vulkanismus, vermutlich begünstigt durch die räumliche Heterogenität der deformierten Kruste.

4. Fazit

Diese Arbeit konnte mithilfe der Kombination geochronologischer, petrografischer, geochemischer und mineralchemischer systematischer Untersuchungen an vulkanischen Alkaligesteinen aus zehn Regionen der südlichen ZEVP erstmals zeigen, dass sich deren magmatische Aktivität auf zwei klar voneinander getrennte Zeiträume verteilt, die zwei kompositionell und räumlich deutlich unterscheidbare Gesteinsserien hervorbrachten. Die primitiven 73–47 Ma alten Olivin-Nephelinite, basanitischen Nephelinite und Nephelinbasanite sind auf Taunus, Bonndorfer Graben und Freiburger Bucht, Vogesen, Pfälzerwald, Untermainebene sowie Odenwald und Kraichgau beschränkt. Nur dort finden sich mit (phonolithischen) Haüyniten/Noseaniten und Haüyn-Nepheliniten (68–62 Ma) auch Differentiate dieser Gesteine. Ebenfalls primitive Olivin-Melilithite und Melilith-führende Olivin-Nephelinite sind mit 27–9 Ma hingegen bedeutend jünger und beschränken sich auf Lothringen, den südlichen Oberrheingraben, das Uracher Vulkangebiet und den Hegau. Die Aktivität fällt mit der Entstehung des polygenetischen Vulkankomplexes des Kaiserstuhls (19–15 Ma) zusammen und brachte entwickelte Gesteine ansonsten lediglich in Form der Nosean-Phonolithe im Hegau hervor, der damit einzigen Region mit klassischem bimodalen Vulkanismus in der südlichen ZEVP.

Die kompositionellen Differenzen zwischen den beiden primitiven Gesteinsgruppen gehen aufgrund des zügigen, weitgehend adiabatischen Magmaaufstiegs und trotz einiger Variationen während der magmatischen Entwicklung größtenteils auf unterschiedliche Mantelquellen und auf die daraus hervorgegangenen partiellen Schmelzen zurück. Die älteren nephelinitischen bis basanitischen Magmen reflektieren bis zu 6 % Aufschmelzgrad eines Amphibol-führenden Granat(-Spinell)-Lherzoliths aus der Basis der Lithosphäre, welcher die Signatur einer Metasomatose durch wasserhaltige Schmelzen/Fluide trägt. Hingegen stammen die jüngeren Melilith-führenden Vulkanite aus einem Ca-reicheren sowie durch karbonatreiche Fluide überprägten, Amphibol- ± Phlogopit-führenden Granat-Wehrlit der in geringerem Umfang aufgeschmolzenen (<3,5 %) oberen Asthenosphäre. Eine entsprechende Metasomatose steht wahrscheinlich im Zusammenhang mit variszischen Subduktionsprozessen und war durch Schmelzen/Fluide mit hohen CaO-MgO- und CO_2-(CO_2+H_2O)-Verhältnissen gekennzeichnet. Wenngleich die Speicherung von Ca, CO_2, H_2O sowie weiteren volatilen und inkompatiblen Elementen nach Abgabe aus ozeanischer Kruste in den Mantel durch kontinuierliches Recycling vermutlich in der unteren Lithosphäre erfolgte, führte deren

Ausdünnung spätestens mit Beginn des jüngeren Magmatismus zur teilweisen Inkorporation dieser Bereiche durch die sich aufwölbende Asthenosphäre.
Die vulkanischen Episoden können in existierende geodynamische Modelle zur Alpidischen Orogenese und der damit einhergehenden Entwicklung des EKRiS integriert werden, was auf eine größtenteils strukturelle Kontrolle des Magmatismus hindeutet. Mit zunehmendem Abstand vom Alpenbogen und dessen nördlichem Vorland verringern sich die Auswirkungen dazugehöriger Krustendeformation auf den darunterliegenden Mantel, was erklären könnte, warum in der nördlichen ZEVP keine zwei zeitlich diskreten Phasen vulkanischer Aktivität zu beobachten sind. Dort könnten sowohl tiefere Mantelprozesse als auch zusätzliche lithosphärische Vorgänge den Anteil der Alpenbildung am Vulkanismus überlagern und beeinflussen. Im südlichen Teil der ZEVP weisen die Magmazusammensetzungen, nur schwach magmatisch geprägte Grabenstrukturen, vulkanische Aktivität außerhalb von Gräben und die beträchtliche topografische Hebung darauf hin, dass auch Konvektion und Aufwölbung der Asthenosphäre und ihre Wechselwirkung mit der unteren Lithosphäre sowie konduktiver Wärmetransport zum Magmatismus beigetragen haben. Jedoch können all diese Prozesse als Reaktion auf die Dynamik der Lithosphäre interpretiert werden, zumal die Ergebnisse dieser Arbeit weder auf die Notwendigkeit noch auf die Existenz eines übermäßig heißen Mantels, einer thermischen Anomalie oder vom tiefen Mantel ausgehender Konvektionsströme hindeuten, wenngleich ein Einfluss asthenosphärischer Triebkräfte nicht völlig auszuschließen ist.

Literaturverzeichnis

Abratis M, Mädler J, Hautmann S, Leyk H-J, Meyer R, Lippolt HJ, Viereck-Götte L (2007) Two distinct Miocene age ranges of basaltic rocks from the Rhön and Heldburg areas (Germany) based on $^{40}Ar/^{39}Ar$ step heating data. Chem. Erde – Geochem. 67(2):133–150

Abratis M, Munsel D, Viereck-Götte L (2009) Melilithite und Melilith-führende Magmatite des sächsischen Vogtlands: Petrographie und Mineralchemie. J. Geol. Sci. 37(1–2):41–79

Abratis M, Viereck L, Pfänder JA, Hentschel R (2015) Geochemical composition, petrography and $^{40}Ar/^{39}Ar$ age of the Heldburg phonolite: implications on magma mixing and mingling. Int. J. Earth Sci. 104(8):2033–2055

Adam J, Green T (2006) Trace element partitioning between mica- and amphibole-bearing garnet lherzolite and hydrous basanitic melt: 1. Experimental results and the investigation of controls on partitioning behaviour. Contrib. Mineral. Petrol. 152:1–17

Albers M, Christensen UR (1996) The excess temperature of plumes rising from the core-mantle boundary. Geophys. Res. Lett. 23(24):3567–3570

Andersen DJ, Lindsley DH, Davidson PM (1993) QUILF: A pascal program to assess equilibria among Fe–Mg–Mn–Ti oxides, pyroxenes, olivine, and quartz. Comput. Geosci. 19(9):1333–1350

Arzamastsev AA, Arzamastseva LV, Bea F, Montero P (2009) Trace elements in minerals as indicators of the evolution of alkaline ultrabasic dike series: LA-ICP-MS data for the magmatic provinces of northeastern Fennoscandia and Germany. Petrology 17(1):46–72

Baranyi I, Lippolt HJ, Todt W (1976) Kalium-Argon-Altersbestimmungen an tertiären Vulkaniten des Oberrheingraben-Gebietes: II Die Alterstraverse vom Hegau nach Lothringen. Oberrh. geol. Abh. 25(1):41–62

Beard AD, Downes H, Mason PRD, Vetrin VR (2007) Depletion and enrichment processes in the lithospheric mantle beneath the Kola Peninsula (Russia): Evidence from spinel lherzolite and wehrlite xenoliths. Lithos 94:1–24

Becker A (2000) The Jura Mountains — an active foreland fold-and-thrust belt? Tectonophysics 321(4):381–406

Becker E (1904) Der Rossbergbasalt bei Darmstadt und seine Zersetzungsprodukte. Inaugural-Dissertation, Vereinigte Friedrichs-Universität Halle-Wittenberg

Berndt J, Holtz F, Koepke J (2001) Experimental constraints on storage conditions in the chemically zoned phonolitic magma chamber of the Laacher See volcano. Contrib. Mineral. Petrol. 140(4):469–486

Binder T, Marks MAW, Friedrichsen B-E, Walter BF, Wenzel T, Markl G (2024a) Bimodal volcanism in the Hegau region (SW Germany): Differentiation of primitive melilititic to nephelinitic rocks produces evolved nosean phonolites. Lithos 472-473:107565

Binder T, Marks MAW, Walter BF, Wenzel T, Markl G (2024b) Two Distinct Metasomatized Mantle Sources Produced Two Groups of Alkaline SiO_2-Undersaturated Rocks in the Southern Central European Volcanic Province. J. Petrol. 65(7):1–29

Binder T, Marks MAW, Walter BF, Wenzel T, Markl G, Gerdes A, Grimmer J, Beranoaguirre A (2023) Two distinct age groups of melilitites, foidites, and basanites from the southern Central European Volcanic Province reflect lithospheric heterogeneity. Int. J. Earth Sci. 112(3):881–905

Blanckenburg F von, Davies JH (1995) Slab breakoff: a model for syncollisional magmatism and tectonics in the Alps. Tectonics 14:120–131

Blusztajn J, Hegner E (2002) Osmium isotopic systematics of melilitites from the Tertiary Central European Volcanic Province in SW Germany. Chem. Geol. 189(1-2):91–103

Bogaard PJ, Wörner G, Henjes-Kunst F (2001) Chemical stratigraphy and origin of volcanic rocks from the drill-core “Forschungsbohrung Vogelsberg 1996”. In: Hoppe A, Schulz R (Hrsg.) Die Forschungsbohrung Vogelsberg 1996. Einblicke in einen miozänen Vulkankomplex. Hessisches Landesamt für Umwelt und Geologie, Wiesbaden, S. 69–99

Bogaard PJF, Wörner G (2003) Petrogenesis of Basanitic to Tholeiititic Volcanic Rocks from the Miocene Vogelsberg, Central Germany. J. Petrol. 44(3):569–602

Bourdon B, Zindler A, Wörner G (1994) Evolution of the Laacher See magma chamber: Evidence from SIMS and TIMS measurements of U-Th disequilibria in minerals and glasses. Earth Planet. Sci. Lett. 126(1-3):75–90

Braunger S, Marks MAW, Walter BF, Neubauer R, Reich R, Wenzel T, Parsapoor A, Markl G (2018) The Petrology of the Kaiserstuhl Volcanic Complex, SW Germany: The Importance of Metasomatized and Oxidized Lithospheric Mantle for Carbonatite Generation. J. Petrol. 59(9):1731–1762

Buchner E, Schwarz WH, Schmieder M, Trieloff M (2010) Establishing a 14.6 ± 0.2 Ma age for the Nördlinger Ries impact (Germany)—A prime example for concordant isotopic ages from various dating materials. Meteorit. Planet. Sci. 45(4):662–674

Büchner J, Tietz O, Viereck L, Suhr P, Abratis M (2015) Volcanology, geochemistry and age of the Lausitz Volcanic Field. Int. J. Earth Sci. 104(8):2057–2083

Bussweiler Y, Foley SF, Prelević D, Jacob DE (2015) The olivine macrocryst problem: New insights from minor and trace element compositions of olivine from Lac de Gras kimberlites, Canada. Lithos 220-223:238–252

Cottrell E, Kelley KA (2011) The oxidation state of Fe in MORB glasses and the oxygen fugacity of the upper mantle. Earth Planet. Sci. Lett. 305(3-4):270–282

Dautria J-M, Liotard J-M, Bosch D, Alard O (2010) 160 Ma of sporadic basaltic activity on the Languedoc volcanic line (Southern France): A peculiar case of lithosphere–asthenosphere interplay. Lithos 120(1-2):202–222

Dèzes P, Schmid SM, Ziegler PA (2004) Evolution of the European Cenozoic Rift System: interaction of the Alpine and Pyrenean orogens with their foreland lithosphere. Tectonophysics 389(1-2):1–33

Dielforder A, Frasca G, Brune S, Ford M (2019) Formation of the Iberian-European Convergent Plate Boundary Fault and Its Effect on Intraplate Deformation in Central Europe. Geochem. Geophys. Geosyst. 20:2395–2417

Dobosi G, Fodor RV (1992) Magma fractionation, replenishment, and mixing as inferred from green-core clinopyroxenes in Pliocene basanite, southern Slovakia. Lithos 28(133-150)

Duda A, Schmincke H-U (1985) Polybaric differentiation of alkali basaltic magmas: evidence from green-core clinopyroxenes (Eifel, FRG). Contrib. Mineral. Petrol. 91(4):340–353

Dunworth EA, Wilson M (1998) Olivine Melilitites of the SW German Tertiary Volcanic Province: Mineralogy and Petrogenesis. J. Petrol. 39(10):1805–1836

Embey-Isztin A, Downes H, James DE, Upton BGJ, Dobosi G, Ingram GA, Harmon RS, Scharbert HG (1993) The Petrogenesis of Pliocene Alkaline Volcanic Rocks from the Pannonian Basin, Eastern Central Europe. J. Petrol. 34(2):317–343

Eynatten H von, Kley J, Dunkl I, Hoffmann V-E, Simon A (2020) Late Cretaceous to Paleogene exhumation in Central Europe – localized inversion vs. large-scale domal uplift. Solid Earth 12(4):935–958

Falloon TJ, Green DH (1990) Solidus of carbonated fertile peridotite under fluid-saturated conditions. Geology 18(3):195

Fekiacova Z, Mertz DF, Renne PR (2007) Geodynamic Setting of the Tertiary Hocheifel Volcanism (Germany), Part I: $^{40}Ar/^{39}Ar$ geochronology. In: Ritter JR, Christensen UR (Hrsg.) Mantle Plumes. A Multidisciplinary Approach, 1. Aufl. Springer, Berlin, Heidelberg, S. 185–206

Fichtner A, Villaseñor A (2015) Crust and upper mantle of the western Mediterranean – Constraints from full-waveform inversion. Earth Planet. Sci. Lett. 428:52–62

Foley S (1991) High-pressure stability of the fluor- and hydroxy-endmembers of pargasite and K-richterite. Geochim. Cosmochim. Acta 55(9):2689–2694

Foley SF (1988) The Genesis of Continental Basic Alkaline Magmas-- An Interpretation in Terms of Redox Melting. J. Petrol. Spec. Vol.(1):139–161

Foley SF, Prelevic D, Rehfeldt T, Jacob DE (2013) Minor and trace elements in olivines as probes into early igneous and mantle melting processes. Earth Planet. Sci. Lett. 363:181–191

Ghiorso MS, Gualda GAR (2015) An H_2O–CO_2 mixed fluid saturation model compatible with rhyolite-MELTS. Contrib. Mineral. Petrol. 169(6)

Ghiorso MS, Hirschmann MM, Reiners PW, Kress VC (2002) The pMELTS: A revision of MELTS for improved calculation of phase relations and major element partitioning related to partial melting of the mantle to 3 GPa. Geochem. Geophys. Geosyst. 3(5):1–35

Ghiorso MS, Sack RO (1995) Chemical mass transfer in magmatic processes IV. A revised and internally consistent thermodynamic model for the interpolation and extrapolation of liquid-solid equilibria in magmatic systems at elevated temperatures and pressures. Contrib. Mineral. Petrol. 119(2-3):197–212

Ghobadi M, Brey GP, Gerdes A, Höfer HE, Keller J (2022) Accessories in Kaiserstuhl carbonatites and related rocks as accurate and faithful recorders of whole rock age and isotopic composition. Int. J. Earth Sci. 111(2):573–588

Ginibre C, Wörner G, Kronz A (2004) Structure and Dynamics of the Laacher See Magma Chamber (Eifel, Germany) from Major and Trace Element Zoning in Sanidine: a Cathodoluminescence and Electron Microprobe Study. J. Petrol. 45:2197–2223

Goes S, Spakman W, Bijwaard H (1999) A Lower Mantle Source for Central European Volcanism. Science 286(5446):1928–1931

Gornitz V (1981) Skeletal crystals. In: Frye K (Hrsg.) The Encyclopedia of Mineralogy. Hutchinson Ross Publishing Company, Boston, MA, S. 469–473

Gorring ML, Kay SM (2000) Carbonatite metasomatized peridotite xenoliths from southern Patagonia: implications for lithospheric processes and Neogene plateau magmatism. Contrib. Mineral. Petrol. 140:55–72

Granet M, Wilson M, Achauer U (1995) Imaging a mantle plume beneath the French Massif Central. Earth Planet. Sci. Lett. 136(3-4):281–296

Green DH (2015) Experimental petrology of peridotites, including effects of water and carbon on melting in the Earth's upper mantle. Phys. Chem. Miner. 42:95–122

Green DH, Ringwood AE (1967) The stability fields of aluminous pyroxene peridotite and garnet peridotite and their relevance in upper mantle structure. Earth Planet. Sci. Lett. 3:151–160

Grimmer JC, Ritter JRR, Eisbacher GH, Fielitz W (2017) The Late Variscan control on the location and asymmetry of the Upper Rhine Graben. Int. J. Earth Sci. 106(3):827–853

Haase KM, Goldschmidt B, Garbe-Schönberg C-D (2004) Petrogenesis of Tertiary Continental Intra-plate Lavas from the Westerwald Region, Germany. J. Petrol. 45(5):883–905

Hagke C von, Cederbom CE, Oncken O, Stöckli DF, Rahn MK, Schlunegger F (2012) Linking the northern Alps with their foreland: The latest exhumation history resolved by low-temperature thermochronology. Tectonics 31(5):1-25

Harangi S (2001) Neogene to Quaternary volcanism of the Carpathian–Pannonian Region—a review. Acta Geol. Hung. 44(2):223–258

Harangi S, Jankovics MÉ, Sági T, Kiss B, Lukács R, Soós I (2015) Origin and geodynamic relationships of the Late Miocene to Quaternary alkaline basalt volcanism in the Pannonian basin, eastern–central Europe. Int. J. Earth Sci. 104(8):2007–2032

Harangi S, Lenkey L (2007) Genesis of the Neogene to Quaternary volcanism in the Carpathian-Pannonian region: Role of subduction, extension, and mantle plume. In: Beccaluva L, Bianchini G, Wilson M (Hrsg.) Cenozoic Volcanism in the Mediterranean Area, S. 67–92

Hegner E, Vennemann TW (1997) Role of fluids in the origin of Tertiary European intraplate volcanism: Evidence from O, H, and Sr isotopes in melilitites. Geology 25(11):1035–1038

Hegner E, Walter HJ, Satir M (1995) Pb-Sr-Nd isotopic compositions and trace element geochemistry of megacrysts and melilitites from the Tertiary Urach volcanic field: source composition of small volume melts under SW Germany. Contrib. Mineral. Petrol. 122(3):322–335

Hoffmann M (2017) Young tectonic evolution of the Northern Alpine Foreland Basin, southern Germany, based on linking geomorphology and structural geology. Dissertation, Ludwig-Maximilians-Universität München

Horn P, Lippolt HJ, Todt W (1972) Kalium-Argon-Altersbestimmungen an tertiären Vulkaniten des Oberrheingrabens. I. Gesamtgesteinsalter. Eclogae Geol. Helv. 65(1):131–156

Iacono-Marziano G, Morizet Y, Le Trong E, Gaillard F (2012) New experimental data and semi-empirical parameterization of H_2O–CO_2 solubility in mafic melts. Geochim. Cosmochim. Acta 97:1–23

Inoue T, Irifune T, Yurimoto H, Miyagi I (1998) Decomposition of K-amphibole at high pressures and implications for subduction zone volcanism. Phys. Earth Planet. Inter. 107:221–231

Ionov DA, Hofmann AW, Shimizu N (1994) Metasomatism-induced Melting in Mantle Xenoliths from Mongolia. J. Petrol. 35:753–785

Ionov DA, O'Reilly SY, Genshaft YS, Kopylova MG (1996) Carbonate-bearing mantle peridotite xenoliths from Spitsbergen: phase relationships, mineral compositions and trace-element residence. Contrib. Mineral. Petrol. 125:375–392

Jankovics ME, Taracsák Z, Dobosi G, Embey-Isztin A, Batki A, Harangi S, Hauzenberger CA (2016) Clinopyroxene with diverse origins in alkaline basalts from the western Pannonian Basin: Implications from trace element characteristics. Lithos 262:120–134

Jung C, Jung S, Hoffer E, Berndt J (2006) Petrogenesis of Tertiary Mafic Alkaline Magmas in the Hocheifel, Germany. J. Petrol. 47(8):1637–1671

Jung S, Hoernes S (2000) The major- and trace-element and isotope (Sr, Nd, O) geochemistry of Cenozoic alkaline rift-type volcanic rocks from the Rhön area

(central Germany): petrology, mantle source characteristics and implications for asthenosphere–lithosphere interactions. J. Volcanol. Geotherm. Res. 99(1-4):27–53

Jung S, Masberg P (1998) Major- and trace-element systematics and isotope geochemistry of Cenozoic mafic volcanic rocks from the Vogelsberg (central Germany) Constraints on the origin of continental alkaline and tholeiitic basalts and their mantle sources. J. Volcanol. Geotherm. Res. 86:151–177

Jung S, Mezger K, Hauff F, Pack A, Hoernes S (2013) Petrogenesis of rift-related tephrites, phonolites and trachytes (Central European Volcanic Province, Rhön, FRG): Constraints from Sr, Nd, Pb and O isotopes. Chem. Geol. 354:203–215

Jung S, Pfänder JA, Brauns M, Maas R (2011) Crustal contamination and mantle source characteristics in continental intra-plate volcanic rocks: Pb, Hf and Os isotopes from central European volcanic province basalts. Geochim. Cosmochim. Acta 75(10):2664–2683

Jung S, Pfänder JA, Brügmann G, Stracke A (2005) Sources of primitive alkaline volcanic rocks from the Central European Volcanic Province (Rhön, Germany) inferred from Hf, Os and Pb isotopes. Contrib. Mineral. Petrol. 150(5):546–559

Jung S, Vieten K, Romer RL, Mezger K, Hoernes S, Satir M (2012) Petrogenesis of Tertiary Alkaline Magmas in the Siebengebirge, Germany. J. Petrol. 53(11):2381–2409

Kargin AV (2021) Multistage Mantle Metasomatism during the Generation of Kimberlite Melts: Evidence from Mantle Xenoliths and Megacrysts of the Grib Kimberlite, Arkhangelsk, Russia. Petrology 29(3):221–245

Keller J, Kraml M, Henjes-Kunst F (2002) $^{40}Ar/^{39}Ar$ single crystal laser dating of early volcanism in the Upper Rhine Graben and tectonic implications. Schweiz. Mineral. Petrogr. Mitt. 82:121–130

Klemm DD, Fazakas H (1975) Die Schwerspatvorkommen des Odenwaldes. In: Amstutz GC, Meisl S, Nickel E (Hrsg.) Mineralien und Gesteine im Odenwald. Beiträge zum heutigen Forschungsstand, Heidelberg, S. 263–266

Klemme S (2004) The influence of Cr on the garnet–spinel transition in the Earth's mantle: experiments in the system $MgO–Cr_2O_3–SiO_2$ and thermodynamic modelling. Lithos 77(1-4):639–646

Kolb M, Paulick H, Kirchenbaur M, Münker C (2012) Petrogenesis of Mafic to Felsic Lavas from the Oligocene Siebengebirge Volcanic Field (Germany): Implications for the Origin of Intracontinental Volcanism in Central Europe. J. Petrol. 53(11):2349–2379

Kraml M, Keller J, Henjes-Kunst F (1995) New K-Ar, ^{40}Ar-^{39}Ar step heating and ^{40}Ar-^{39}Ar laser fusion dates for the Kaiserstuhl volcanic complex. Eur. J. Mineral. 7(Beih. 1):142

Kraml M, Keller J, Henjes-Kunst F (1999) Time constraints for the carbonatic intrusions of the Kaiserstuhl volcanic complex, Upper Rhine Graben, Germany. Terra Nova Abstract Supplement 10(1)

Kramm U, Wedepohl KH (1990) Tertiary basalts and peridotite xenoliths from the Hessian Depression (NW Germany), reflecting mantle compositions low in radiogenic Nd and Sr. Contrib. Mineral. Petrol. 106(1):1–8

Kröchert JS, Theye T, Buchner E (2009) Considerations on the age of the Urach volcanic field (Southwest Germany). J. Appl. Reg. Geol. 160(4):325–331

LaTourrette T, Hervig R, Holloway JR (1995) Trace element partitioning between amphibole, phlogopite, and basanite melt. Earth Planet. Sci. Lett. 135:13–30

Le Bas MJ (1987) Nephelinites and carbonatites. Geol. Soc. Lond. Spec. Publ. 30:53–83

Le Maitre RW, Streckeisen A, Zanettin B, Le Bas MJ, Bonin B, Bateman P, Bellieni G, Dudek A, Efremov S, Keller J, Lameyre J, Sabine PA, Schmid R, Sørensen H, Woolley AR (2002) Igneous Rocks. A Classification and Glossary of Terms, 2. Aufl. Cambridge University Press, Cambridge

Lenz OK, Wilde V, Mertz DF, Riegel W (2015) New palynology-based astronomical and revised 40Ar/39Ar ages for the Eocene maar lake of Messel (Germany). Int. J. Earth Sci. 104(3):873–889

Linthout K, Paulick H, Wijbrans JR (2009) Provenance of basalt blocks from Roman sites in Vleuten-De Meern (the Netherlands) traced to the Tertiary Siebengebirge (Germany): a geoarchaeological quest using petrological and geochemical methods. Neth. J. Geosci. 88(1):55–74

Lippolt HJ (1983) Distribution of volcanic activity in space and time. In: Fuchs K, Gehlen K von, Mälzer H, Murawski, H, Semmel, A (Hrsg.) Plateau Uplift. The Rhenish Shield—a case history, 1. Aufl. Springer, Berlin, S. 112–120

Lippolt HJ, Baranyi I, Todt W (1975) Die Kalium-Argon-Alter der postpermischen Vulkanite des nord-östlichen Oberrheingrabens. In: Amstutz GC, Meisl S, Nickel E (Hrsg.) Mineralien und Gesteine im Odenwald. Beiträge zum heutigen Forschungsstand, Heidelberg, S. 205–212

Lippolt HJ, Gentner W, Wimmenauer W (1963) Altersbestimmungen nach der Kalium-Argon-Methode an tertiären Eruptivgesteinen Südwestdeutschlands. Jahresh. Geol. Landesamts Baden-Württ. 6:507–538

Lippolt HJ, Horn P, Todt W (1976) Kalium-Argon-Altersbestimmungen an tertiären Vulkaniten des Oberrheingraben-Gebietes: IV. Kalium-Argon-Alter von Mineralien und Einschlüssen der Basalt-Vorkommen Katzenbuckel und Roßberg. J. Mineral. Geochem. 127(3):242–260

Loges A, Schultze D, Klügel A, Lucassen F (2019) Phonolitic melt production by carbonatite Mantle metasomatism: evidence from Eger Graben xenoliths. Contrib. Mineral. Petrol. 174(11)

Lowenstern J (2001) Carbon dioxide in magmas and implications for hydrothermal systems. Miner. Depos. 36(6):490–502

Lustrino M, Carminati E (2007) Phantom plumes in Europe and the circum-Mediterranean region. Geol. Soc. America Spec. Pap. 430:723–745

Lustrino M, Wilson M (2007) The circum-Mediterranean anorogenic Cenozoic igneous province. Earth-Sci. Rev. 81(1-2):1–65

Lutz H, Lorenz V, Engel T, Häfner F, Haneke J (2013) Paleogene phreatomagmatic volcanism on the western main fault of the northern Upper Rhine Graben (Kisselwörth diatreme and Nierstein–Astheim Volcanic System, Germany). Bull. Volcanol. (Bulletin of Volcanology) 75:741

Mader S, Ritter JRR, Reicherter K (2021) Seismicity and seismotectonics of the Albstadt Shear Zone in the northern Alpine foreland. Solid Earth 12(6):1389–1409

Mahfoud RF, Beck JN (1989) Alkaline basalt-phonolite rocks from the Singen area, Hegau, southern F.R.G. Chem. Geol. 74(3-4):217–227

Mann U, Marks MA, Markl G (2006) Influence of oxygen fugacity on mineral compositions in peralkaline melts: The Katzenbuckel volcano, Southwest Germany. Lithos 91(1-4):262–285

Martha SO, Zulauf G, Dörr W, Nesbor H-D, Petschick R, Prinz-Grimm P, Gerdes A (2014) The Saxothuringian-Rhenohercynian boundary underneath the Vogelsberg volcanic field: evidence from basement xenoliths and U-Pb zircon data of trachyte. J. Appl. Reg. Geol. 165(3):373–394

Mathez EA (1984) Influence of degassing on oxidation states of basaltic magmas. Nature 310:371–375

Mayer B, Jung S, Romer RL, Pfänder JA, Klügel A, Pack A, Gröner E (2014) Amphibole in alkaline basalts from intraplate settings: implications for the petrogenesis of alkaline lavas from the metasomatised lithospheric mantle. Contrib. Mineral. Petrol. 167(3):989

Mayer B, Jung S, Romer RL, Stracke A, Haase KM, Garbe-Schönberg C-D (2013) Petrogenesis of Tertiary Hornblende-bearing Lavas in the Rhön, Germany. J. Petrol. 54(10):2095–2123

Melluso L, Le Roex AP, Morra V (2011) Petrogenesis and Nd-, Pb-, Sr-isotope geochemistry of the Cenozoic olivine melilitites and olivine nephelinites ("ankaratrites") in Madagascar. Lithos 127(3-4):505–521

Merle O (2011) A simple continental rift classification. Tectonophysics 513(1-4):88–95

Mertes H, Schmincke H-U (1985) Mafic potassic lavas of the Quaternary West Eifel volcanic field. Contrib. Mineral. Petrol. 89(4):330–345

Mertz DF, Löhnertz W, Nomade S, Pereira A, Prelević D, Renne PR (2015) Temporal–spatial evolution of low-SiO_2 volcanism in the Pleistocene West Eifel volcanic field (West Germany) and relationship to upwelling asthenosphere. J. Geodyn. 88:59–79

Mertz DF, Renne PR, Wuttke M, Mödden C (2007) A numerically calibrated reference level (MP28) for the terrestrial mammal-based biozonation of the European Upper Oligocene. Int. J. Earth Sci. 96(2):353–361

Mertz DF, Swisher CC, Franzen JL, Neuffer FO, Lutz H (2000) Numerical dating of the Eckfeld maar fossil site, Eifel, Germany: a calibration mark for the Eocene time scale. Naturwissenschaften 87(6):270–274

Morizet Y, Paris M, Gaillard F, Scaillet B (2010) C–O–H fluid solubility in haplobasalt under reducing conditions: An experimental study. Chem. Geol. 279(1-2):1–16

Mrlina J, Kämpf H, Geissler WH, van den Bogaard P (2007) Assumed Quaternary maar structure at the Czech/German boundary between Mýtina and Neualbenreuth (western Eger Rift, Central Europe): geophysical, petrochemical and geochronological indications. J. Geol. Sci. 35(4-5):213–230

Nagayoshi M, Kubo T, Kato T (2016) Experimental investigation of the kinetics of the spinel-to-garnet transformation in peridotite: A preliminary study. Am. Mineral. 101(9):2020–2028

Neave DA, Putirka KD (2017) A new clinopyroxene-liquid barometer, and implications for magma storage pressures under Icelandic rift zones. Am. Mineral. 102(4):777–794

Neuhaus S (2010) New age for Paleogene/Neogene clastics at the northern termination of the Upper Rhine Graben (Hesse, Germany). J. Appl. Reg. Geol. 161(3):303–322

Ni H, Keppler H (2013) Carbon in Silicate Melts. Rev. Mineral. Geochem. 75(1):251–287

Panina LI, Sharygin VV, Keller J (2000) Olivine nephelinite, tephrite, essexite, phonolite, and tinguaite from Kaiserstuhl, Germany: Evidence from melt inclusions in pyroxene. Geochem. Int. 38(4):343–352

Peccerillo A, Barberio MR, Yirgu, G., Ayalew, D., Barbieri M, Wu TW (2003) Relationships between Mafic and Peralkaline Silicic Magmatism in Continental Rift Settings: a Petrological, Geochemical and Isotopic Study of the Gedemsa Volcano, Central Ethiopian Rift. J. Petrol. 44(11):2003–2032

Pfänder JA, Jung S, Klügel A, Münker C, Romer RL, Sperner B, Rohrmüller J (2018) Recurrent Local Melting of Metasomatised Lithospheric Mantle in Response to Continental Rifting: Constraints from Basanites and Nephelinites/Melilitites from SE Germany. J. Petrol. 59(4):667–694

Pfänder JA, Jung S, Münker C, Stracke A, Mezger K (2012) A possible high Nb/Ta reservoir in the continental lithospheric mantle and consequences on the global Nb budget – Evidence from continental basalts from Central Germany. Geochim. Cosmochim. Acta 77:232–251

Pintér Z, Foley SF, Yaxley GM, Rosenthal A, Rapp RP, Lanati AW, Rushmer T (2021) Experimental investigation of the composition of incipient melts in upper mantle peridotites in the presence of CO_2 and H_2O. Lithos 396-397:106224

Przybyla T, Pfänder JA, Münker C, Kolb M, Becker M, Hamacher U (2018) High-resolution 40Ar/39Ar geochronology of volcanic rocks from the Siebengebirge (Central Germany)—Implications for eruption timescales and petrogenetic evolution of intraplate volcanic fields. Int. J. Earth Sci. 107(4):1465–1484

Putirka KD (2008) Thermometers and Barometers for Volcanic Systems. Rev. Mineral. Geochem. 69(1):61–120

Puziewicz J, Matusiak-Małek M, Ntaflos T, Grégoire M, Kaczmarek M-A, Aulbach S, Ziobro M, Kukuła A (2020) Three major types of subcontinental lithospheric mantle beneath the Variscan orogen in Europe. Lithos 362-363:105467

Ramdohr P (1975) Die Lagerstätten des Odenwaldes. In: Amstutz GC, Meisl S, Nickel E (Hrsg.) Mineralien und Gesteine im Odenwald. Beiträge zum heutigen Forschungsstand, Heidelberg, S. 235–236

Rasser MW, Bechly G, Böttcher R, Ebner M, Heizmann E, Höltke O, Joachim C, Kern AK, Kovar-Eder J, Nebelsick JH, Roth-Nebelsick A, Schoch RR, Schweigert G, Ziegler R (2013) The Randeck Maar: Palaeoenvironment and habitat differentiation of a Miocene lacustrine system. Palaeogeogr. Palaeoclimatol. Palaeoecol. 392:426–453

Rehfeldt T, Foley SF, Jacob DE, Carlson RW, Lowry D (2008) Contrasting types of metasomatism in dunite, wehrlite and websterite xenoliths from Kimberley, South Africa. Geochim. Cosmochim. Acta 72(23):5722–5756

Ring U, Bolhar R (2020) Tilting, uplift, volcanism and disintegration of the South German block. Tectonophysics 795:228611

Ring U, Gerdes A (2016) Kinematics of the Alpenrhein-Bodensee graben system in the Central Alps: Oligocene/Miocene transtension due to formation of the Western Alps arc. Tectonics 35(6):1367–1391

Ritter JR, Jordan M, Christensen UR, Achauer U (2001) A mantle plume below the Eifel volcanic fields, Germany. Earth Planet. Sci. Lett. 186(1):7–14

Rosenbaum G, Lister GS, Duboz C (2002) Relative motion of Africa, Iberia and Europe during Alpine orogeny. Tectonophysics 359:117–129

Rupf I, Nitsch E (2008) Das Geologische Landesmodell von Baden-Württemberg: Datengrundlagen, technische Umsetzung und erste geologische Ergebnisse. LGRB-Inf. 21:1–82

Schmitt AK (2006) Hochauflösende U-Pb Datierung von Zirkonen des Sporneiche-Trachyts. Geol. Jahrb. Hess. 133:75–81

Schmitt AK, Klitzke M, Gerdes A, Schäfer C (2017) Zircon Hafnium–Oxygen Isotope and Trace Element Petrochronology of Intraplate Volcanic Rocks from the Eifel (Germany) and Implications for Mantle versus Crustal Origins of Zircon Megacrysts. J. Petrol. 58(9):1841–1870

Schmitt AK, Marks MA, Nesbor HD, Markl G (2007) The onset and origin of differentiated Rhine Graben volcanism based on U-Pb ages and oxygen isotopic composition of zircon. Eur. J. Mineral. 19(6):849–857

Schmitt AK, Wetzel F, Cooper KM, Zou H, Wörner G (2010) Magmatic Longevity of Laacher See Volcano (Eifel, Germany) Indicated by U–Th Dating of Intrusive Carbonatites. J. Petrol. 51(5):1053–1085

Schubert S, Jung S, Pfänder JA, Hauff F, Garbe-Schönberg D (2015) Petrogenesis of Tertiary continental intra-plate lavas between Siebengebirge and Westerwald, Germany: Constraints from trace element systematics and Nd, Sr and Pb isotopes. J. Volcanol. Geotherm. Res. 305:84–99

Schumacher ME (2002) Upper Rhine Graben: Role of preexisting structures during rift evolution. Tectonics 21(1):6-1–6-17

Seghedi I, Downes H (2011) Geochemistry and tectonic development of Cenozoic magmatism in the Carpathian–Pannonian region. Gondwana Res. 20(4):655–672

Seiberlich C, Ritter J, Wawerzinek B (2013) Topography of the lithosphere–asthenosphere boundary below the Upper Rhine Graben Rift and the volcanic Eifel region, Central Europe. Tectonophysics 603:222–236

Seifert W, Thomas R (1995) Silicate-carbonate immiscibility: a melt inclusion study of olivine melilitite and wehrlite xenoliths in tephrite from the Elbe Zone, Germany. Chem. Erde – Geochem. 55:263–279

Sharygin VV, Di Muro A, Madyukov I. A. (2005) Crystallization temperature of haüyne from phonolite (ULST, E.Eifel, Germany) and haüynophyre (Vulture volcano, Italy): evidence from silicate melt inclusions. Abstr. E-book ECROFI 18

Shaw CS (2004) The temporal evolution of three magmatic systems in the West Eifel volcanic field, Germany. J. Volcanol. Geotherm. Res. 131(3-4):213–240

Shaw CSJ, Woodland AB, Hopp J, Trenholm ND (2010) Structure and evolution of the Rockeskyllerkopf Volcanic Complex, West Eifel Volcanic Field, Germany. Bull. Volcanol. (Bulletin of Volcanology) 72(8):971–990

Singer BS, Hoffman KA, Schnepp E, Guillou H (2008) Multiple Brunhes Chron excursions recorded in the West Eifel (Germany) volcanics: Support for long-held mantle control over the non-axial dipole field. Phys. Earth Planet. Inter. 169(1-4):28–40

Sirocko F, Dietrich S, Veres D, Grootes PM, Schaber-Mohr K, Seelos K, Nadeau M-J, Kromer B, Rothacker L, Röhner M, Krbetschek M, Appleby P, Hambach U, Rolf C, Sudo M, Grim S (2013) Multi-proxy dating of Holocene maar lakes and Pleistocene dry maar sediments in the Eifel, Germany. Quat. Sci. Rev. 62:56–76

Skála R, Ulrych J, Ackerman L, Krmíček L, Fediuk F, Balogh K, Hegner E (2015) Upper Cretaceous to Pleistocene melilitic volcanic rocks of the Bohemian Massif: petrology and mineral chemistry. Geol. Carp. 66(3):197–216

Sliwinski JT, Bachmann O, Ellis BS, Dávila-Harris P, Nelson BK, Dufek J (2015) Eruption of shallow crystal cumulates during explosivephonolitic eruptions on Tenerife, Canary Islands. J. Petrol. 56:2173–2194

Soltys A, Giuliani A, Phillips D, Kamenetsky VS, Maas R, Woodhead J, Rodemann T (2016) In-situ assimilation of mantle minerals by kimberlitic magmas — Direct evidence from a garnet wehrlite xenolith entrained in the Bultfontein kimberlite (Kimberley, South Africa). Lithos 256-257:182–196

Sun C, Dasgupta R (2020) Thermobarometry of CO2-rich, silica-undersaturated melts constrains cratonic lithosphere thinning through time in areas of kimberlitic magmatism. Earth Planet. Sci. Lett. 550:116549

Sundermeyer C, Gätjen J, Weimann L, Wörner G (2020) Timescales from magma mixing to eruption in alkaline volcanism in the Eifel volcanic fields, western Germany. Contrib. Mineral. Petrol. 175(8):77

Theilen-Willige B (2011) Remote Sensing and GIS Studies of the Hegau Volcanic Area in SW Germany. Photogramm. Fernerkund. Geoinform. 2011(5):361–372

Trønnes RG (2002) Stability range and decomposition of potassic richterite and phlogopite end members at 5-15 GPa. Mineral. Petrol. 74(2-4):129–148

Ulianov A, Müntener O, Ulmer P, Pettke T (2007) Entrained Macrocryst Minerals as a Key to the Source Region of Olivine Nephelinites: Humberg, Kaiserstuhl, Germany. J. Petrol. 48(6):1079–1118

Ulrych J, Ackerman L, Balogh K, Hegner E, Jelínek E, Pécskay Z, Přichystal A, Upton BG, Zimák J, Foltýnová R (2013) Plio-Pleistocene basanitic and melilititic series of the Bohemian Massif: K-Ar ages, major/trace element and Sr–Nd isotopic data. Chem. Erde – Geochem. 73(4):429–450

Ulrych J, Dostal J, Adamovič J, Jelínek E, Špaček P, Hegner E, Balogh K (2011) Recurrent Cenozoic volcanic activity in the Bohemian Massif (Czech Republic). Lithos 123(1-4):133–144

Ulrych J, Dostal J, Hegner E, Balogh K, Ackerman L (2008) Late Cretaceous to Paleocene melilitic rocks of the Ohře/Eger Rift in northern Bohemia, Czech Republic: Insights into the initial stages of continental rifting. Lithos 101(1-2):141–161

Ulrych J, Krmíček L, Tomek Č, Lloyd FE, Ladenberger A, Ackerman L, Balogh K (2016) Petrogenesis of Miocene alkaline volcanic suites from western Bohemia: whole rock geochemistry and Sr–Nd–Pb isotopic signatures. Chem. Erde – Geochem. 76(1):77–93

van den Bogaard P (1995) $^{40}Ar/^{39}Ar$ ages of sanidine phenocrysts from Laacher See Tephra (12,900 yr BP): Chronostratigraphic and petrological significance. Earth Planet. Sci. Lett. 133(1-2):163–174

Vaněčková M, Holub FV, Souček J, Bowes DR (1993) Geochemistry and petrogenesis of the tertiary alkaline volcanic suite of the Labe tectonovolcanic zone, Czech Republic. Mineral. Petrol. 48(1):17–34

Veksler IV, Lentz D (2006) Parental Magmas of Plutonic Carbonatites, Carbonate-Silicate immiscibility and Decarbonation Reactions: Evidence from Melt and Fluid Inclusions. In: Webster JD (Hrsg.) Melt Inclusions in Plutonic Rocks, Montreal, S. 123–150

Voigt T, Kley J, Voigt S (2021) Dawn and dusk of Late Cretaceous basin inversion in central Europe. Solid Earth 12(6):1443–1471

Wagner GA, Gögen K, Jonckheere R, Kämpf H, Wagner I, Woda C (1998) The age of Quaternary volcanoes Železná Hůrka and Komorní Hůrka (Western Eger Rift), Czech Republic: alpha-recoil track, TL, ESR and fission track chronometry. In: Cajz V, Adomoviè J, Ulrych J (Hrsg.) Magma and Rift Basin Evolution—Excursion Guide, Prague, S. 95–96

Wedepohl KH, Baumann A (1999) Central European Cenozoic plume volcanism with OIB characteristics and indications of a lower mantle source. Contrib. Mineral. Petrol. 136(3):225–239

Wiechert U, Ionov DA, Wedepohl KH (1997) Spinel peridotite xenoliths from the Atsagin-Dush volcano, Dariganga lava plateau, Mongolia: a record of partial melting and cryptic metasomatism in the upper mantle. Contrib. Mineral. Petrol. 126:345–364

Wilson M, Downes H, Cebriá J-M (1995) Contrasting Fractionation Trends in Coexisting Continental Alkaline Magma Series; Cantal, Massif Central, France. J. Petrol. 36(6):1729–1753

Witt-Eickschen G, Kramm U (1998) Evidence for the multiple stage evolution of the subcontinental lithospheric mantle beneath the Eifel (Germany) from pyroxenite and composite pyroxenite/peridotite xenoliths. Contrib. Mineral. Petrol. 131(2-3):258–272

Wörner G, Wright TL (1984) Evidence for magma mixing within the Laacher See magma chamber (East Eifel, Germany). J. Volcanol. Geotherm. Res. 22(3-4):301–327

Wörner G, Zindler A, Staudigel H, Schmincke H-U (1986) Sr, Nd, and Pb isotope geochemistry of Tertiary and Quaternary alkaline volcanics from West Germany. Earth Planet. Sci. Lett. 79:107–119

Xu Y, Mercier J-CC, Menzies MA, Ross JV, Harte B, Lin C, Shi L (1996) K-rich glass-bearing wehrlite xenoliths from Yitong, Northeastern China: petrological and chemical evidence for mantle metasomatism. Contrib. Mineral. Petrol. 125:406–420

Yaxley GM, Anenburg M, Tappe S, Decree S, Guzmics T (2022) Carbonatites: Classification, Sources, Evolution, and Emplacement. Annu. Rev. Earth Planet. Sci. 50:261–293

Ziberna L, Klemme S, Nimis P (2013) Garnet and spinel in fertile and depleted mantle: insights from thermodynamic modelling. Contrib. Mineral. Petrol. 166(2):411–421

Ziegler PA, Bertotti G, Cloetingh S (2002) Dynamic processes controlling foreland development: the role of mechanical (de)coupling of orogenic wedges and forelands. EGU Stephan Mueller Spec. Publ. Ser. 1:17–56

Ziegler PA, Dèzes P (2005) Evolution of the lithosphere in the area of the Rhine Rift System. Int. J. Earth Sci. 94(4):594–614

Ziegler PA, Schumacher ME, Dèzes P, van Wees J-D, Cloetingh S (2004) Post-Variscan evolution of the lithosphere in the Rhine Graben area: constraints from subsidence modelling. Geol. Soc. Lond. Spec. Publ. 223:289–317

Anlage I

Akzeptierte Publikation

Arbeit 1

Binder T, Marks MAW, Gerdes A, Walter BF, Grimmer J, Beranoaguirre A, Wenzel T, Markl G (2023) Two distinct age groups of melilitites, foidites, and basanites from the southern Central European Volcanic Province reflect lithospheric heterogeneity. Int. J. Earth Sci. 112:881–905. https://doi.org/10.1007/s00531-022-02278-y.

International Journal of Earth Sciences (2023) 112:881–905
https://doi.org/10.1007/s00531-022-02278-y

ORIGINAL PAPER

Two distinct age groups of melilitites, foidites, and basanites from the southern Central European Volcanic Province reflect lithospheric heterogeneity

Thomas Binder[1] · Michael A. W. Marks[1] · Axel Gerdes[2,3] · Benjamin F. Walter[4,5] · Jens Grimmer[4] · Aratz Beranoaguirre[2,3,4,5] · Thomas Wenzel[1] · Gregor Markl[1]

Received: 21 December 2021 / Accepted: 22 November 2022 / Published online: 4 December 2022

Abstract

Petrographic observations and in situ U–Pb ages of melilitites, foidites, basanites, phonolites, and trachytes from the southern part of the Central European Volcanic Province (CEVP) and related plutonic inclusions therein reveal two distinct age groups separated by a gap of ~ 20 Myr. A late Cretaceous to early Eocene group (~ 73–47 Ma; Taunus, Lower Main plain, Odenwald and Kraichgau area, Bonndorfer Graben and Freiburger Bucht area, Vosges and Pfälzerwald) is characterized by nephelinites and basanites mostly devoid of melilite and perovskite, and by rare haüynites, and trachytes. In contrast, a late Oligocene to late Miocene group (~ 27–9 Ma; Lorraine, southern Upper Rhine Graben, Urach, Hegau area) is dominated by melilitites, melilite-bearing nephelinites (both carrying perovskite), and phonolites. Both magmatic episodes are related to domal topographic uplift, erosion, and formation of major angular unconformities in the Upper Rhine Graben, suggesting an association with dynamic topography interrupted by phases of subsidence (or abatements of uplift). The investigated rocks in the southern CEVP (south of a line Eifel–Vogelsberg–Rhön–Heldburg), except for the Kaiserstuhl volcanic complex, mostly comprise small and isolated occurrences or monogenetic volcanic fields, whereas the northern CEVP is dominated by large volcanic complexes and dyke swarms, which are mostly SiO_2-saturated to weakly SiO_2-undersaturated. In the northern CEVP, evidence of spatially varying but recurrent volcanic activity exists since the Eocene, lacking the distinct 20 Myr gap as documented from the southern CEVP. While the temporal and spatial distribution of volcanism are a result of the Cretaceous to Miocene tectonic evolution in Central Europe, further studies are needed to explain the petrographic differences between the two age groups in the south.

Keywords In situ U–Pb dating · Central European Volcanic Province · Upper Rhine Graben · Foidites · Olivine melilitites · Geochronology of volcanic rocks

✉ Thomas Binder
thomas.binder@uni-tuebingen.de

[1] Department of Geosciences, Eberhard Karls Universität Tübingen, Schnarrenbergstraße 94–96, 72076 Tübingen, Germany

[2] Frankfurt Isotope and Element Research Center (FIERCE), Goethe-Universität Frankfurt, Altenhöferallee 1, 60438 Frankfurt am Main, Germany

[3] Department of Geosciences, Goethe-Universität Frankfurt, Altenhöferallee 1, 60438 Frankfurt am Main, Germany

[4] Institute of Applied Geosciences, Karlsruhe Institute of Technology, Adenauerring 20b, 76131 Karlsruhe, Germany

[5] Laboratory for Environmental and Raw Material Analysis (LERA), Adenauerring 20b, 76131 Karlsruhe, Germany

Introduction

The late Cretaceous–Holocene Central European Volcanic Province (CEVP; Fig. 1, Table 1) is part of the Circum-Mediterranean Anorogenic Cenozoic Igneous province (CiMACI; Lustrino and Wilson 2007) and comprises several volcanic regions in eastern France, western, central, and southern Germany, western Poland, and the Czech Republic (e.g., Lustrino and Wilson 2007; Schmitt et al. 2007; Sirocko et al. 2013). Many of these regions are characterized by polygenetic, others by monogenetic igneous activities. Some of them comprise large-scale lava sheets or pyroclastic deposits, while others consist of accumulations of vents, stocks, or dykes. The volcanic products investigated in the studied area (Table 1) comprise basalts, basanites, tephrites,

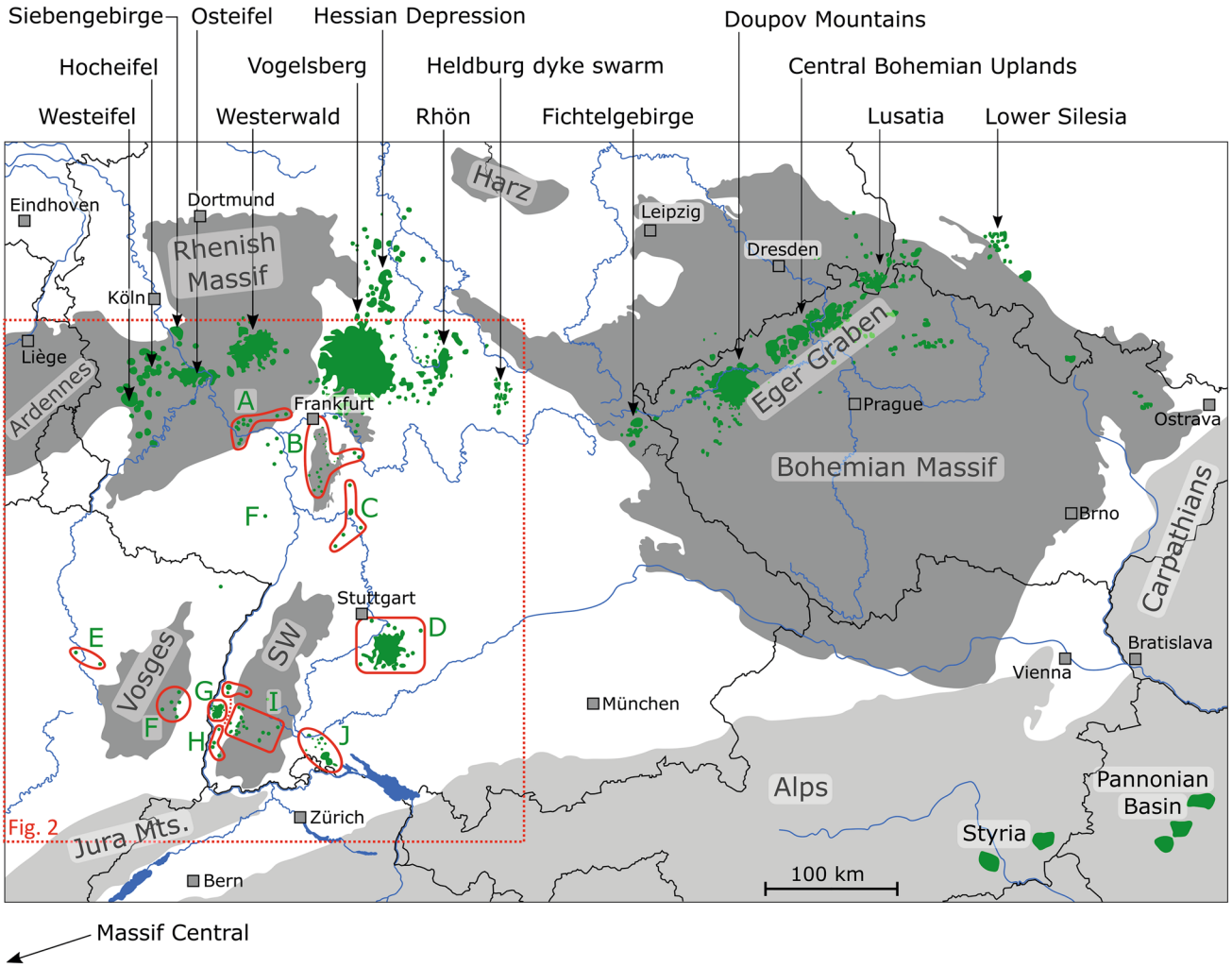

Fig. 1 Map showing the Central European Volcanic Province (CEVP) with their volcanic fields and complexes in green. Variscan basement rocks are shown in dark grey, rocks affected by the Alpine orogeny in light grey. The study areas of this work are outlined in red. *A* Taunus, *B* Lower Main plain, *C* Odenwald and Kraichgau area, *D* Urach, *E* Lorraine, *F* Vosges and Pfälzerwald, *G* Kaiserstuhl, *H* Southern Upper Rhine Graben, *I* Bonndorfer Graben and Freiburger Bucht area, *J* Hegau area

Table 1 Geomorphological characteristics and number of known localities within the regions in the southern CEVP (study area)

Region	Plugs/necks	Dykes	Tuff diatremes	*n*
Hegau area (J)	++	+	o	~30 and extensive tuff
Urach (D)	+	+	++	>400
Kaiserstuhl (G)	Stratovolcanic complex			
Southern URG (H)	+	+	+	13
Lorraine (E)	++	o	o	2
Vosges and Pfälzerwald (F)	++	o	+	10
Taunus (A)	++		+	~15
Bonndorfer Graben and Freiburger Bucht (I)	++	+	+	~30
Odenwald and Kraichgau area (C)	++	o	o	8
Lower Main plain (B)	++	o	+	~30

n number of known occurrences; ++ abundant; + present; o: absent; letters in brackets refer to the areas illustrated in Figs. 1, 2, 4, 7, and 8)

latites, trachytes, phonolites, nephelinites, haüynites, melilitites, and carbonatites (e.g., Abratis et al. 2009; Bogaard and Wörner 2003; Braunger et al. 2018; Büchner et al. 2015; Dunworth and Wilson 1998; Jung and Hoernes 2000; Jung et al. 2005, 2006, 2011; Kolb et al. 2012; Kramm and Wedepohl 1990; Schubert et al. 2015; Skála et al. 2015; Ulrych et al. 2016; Wörner et al. 1986).

The volcanic activity in the CEVP is closely related to the evolution of the European Cenozoic Rift System (ECRiS; e.g., Dèzes et al. 2004; Merle 2011), in particular to the changes in the Alpine foreland stress field and the local reactivation of Variscan-age lithosphere-scale faults (Dèzes et al. 2004; Goes et al. 1999). The relationship between uplift, rifting, and volcanism in Central Europe is controversial, and several competing and complementary models of melt generation and melt sources have been proposed (e.g., Goes et al. 1999; Lustrino and Wilson 2007; Pfänder et al. 2018 and references therein). Explanations range from asthenospheric mantle upwelling caused by thermal instabilities (active upwelling) to melt formation by lithospheric deformation and thinning (passive rifting), both resulting in decompression melting (Lustrino and Wilson 2007; Pfänder et al. 2018; Ulrych et al. 2013). For the former case, an active large-scale mantle plume system, anchored near the core–mantle boundary layer (e.g., Albers and Christensen 1996; Goes et al. 1999), or several smaller (finger-like) plumes sourced in the asthenosphere or the transition zone have been proposed as the cause for magmatism (e.g., Dèzes et al. 2004; Goes et al. 1999; Granet et al. 1995; Haase et al. 2004; Hegner et al. 1995; Mertz et al. 2015; Ritter et al. 2001; Wedepohl and Baumann 1999). Opposing concepts that reject the dominant influence of mantle plumes invoke a partly metasomatized upper mantle beneath the CEVP that interacted with fluids and/or melts derived from subducted ancient oceanic and continental lithosphere, resulting in the presence of (low-melting) hydrous and partly carbonate-bearing mantle domains (Blusztajn and Hegner 2002; Jung et al. 2005; Pfänder et al. 2018; Ulrych et al. 2008). Such models assume that decompression and subsequent melt formation are primarily caused by passive asthenospheric upwelling as a result of lithospheric thinning, uplift, and erosion (Eynatten et al. 2021; Fichtner and Villaseñor 2015; Lustrino and Carminati 2007).

Considering the variable composition, the different ages and magma volumes, and the occasional lack of spatial correlation between volcanism, graben structures, and thinned lithosphere for CEVP volcanic activity (Dunworth and Wilson 1998; Goes et al. 1999; Pfänder et al. 2018), it seems likely that a single general model alone cannot explain the petrogenesis of all the occurrences (Eynatten et al. 2021; Lustrino and Wilson 2007; Mertz et al. 2015). Rather, the spatial chemical heterogeneity of the lower lithospheric mantle, the formation depth and origin of the magmas, and the varying position of the lithosphere–asthenosphere boundary must be integrated into a comprehensive geodynamic scenario (Lustrino and Carminati 2007; Lustrino and Wilson 2007; Puziewicz et al. 2020).

In the northern part of the CEVP, numerous occurrences of volcanic rocks have been dated by modern $^{40}Ar/^{39}Ar$ techniques (e.g., Abratis et al. 2007; Büchner et al. 2015; Linthout et al. 2009; Mayer et al. 2014; Mertz et al. 2000, 2007, 2015; Pfänder et al. 2018; Przybyla et al. 2018; Schubert et al. 2015; Shaw et al. 2010; Singer et al. 2008; van den Bogaard 1995). In the southern CEVP, however, modern geochronological studies are rare (Fekiacova et al. 2007; Keller et al. 2002; Schmitt et al. 2007) and precise ages for many regions and individual localities in the southern CEVP are still lacking and existing ages mostly represent old K–Ar whole-rock data (Baranyi et al. 1976; Horn et al. 1972; Lippolt et al. 1963, 1973, 1975; Lippolt 1983), which have been shown to be erroneous or at least imprecise in several cases (e.g., Baranyi et al. 1976; Keller et al. 2002; Lippolt et al. 1963).

Here, we present a detailed study on primitive to evolved, mostly SiO_2-undersaturated rocks of the southern CEVP applying in situ U–Pb dating of the magmatic phases perovskite, apatite, titanite, zircon, and pyrochlore using LA-ICP-MS analyses on samples carefully studied petrographically. Considering the observed spatial and compositional variations, the present study not only contributes to understanding the chronology of magmatism in the CEVP, but provides also inferences on the driving forces responsible for the volcanic activity, regarding its close link to the preceding melting processes in the upper mantle.

Geological setting

The northern part of the CEVP comprises larger volcanic fields and dyke swarms of the Eifel, Siebengebirge, Westerwald, Vogelsberg, Hessian Depression, Rhön, Heldburg region, Fichtelgebirge, Doupov Mountains, Central Bohemian Uplands, Lusatia, and Lower Silesia (Fig. 1). The focus of the present study is the southern part of the CEVP encompassing volcanic rocks in the Taunus, Lower Main plain, Odenwald and Kraichgau area, Bonndorfer Graben and Freiburger Bucht area, Vosges and Pfälzerwald, Lorraine, southern Upper Rhine Graben (URG), at Urach, and in the Hegau area (Fig. 1, Online Resource 1). The volcanic rocks of Urach, the Hegau area, the southern URG, and Lorraine are strongly SiO_2-undersaturated and comprise primitive olivine melilitites, melilite-bearing olivine nephelinites, and evolved phonolites, contrasting with melilite-free olivine nephelinites, basanitic nephelinites, nepheline basanites, haüynites, and trachytes in the remaining regions (Figs. 2 and 3).

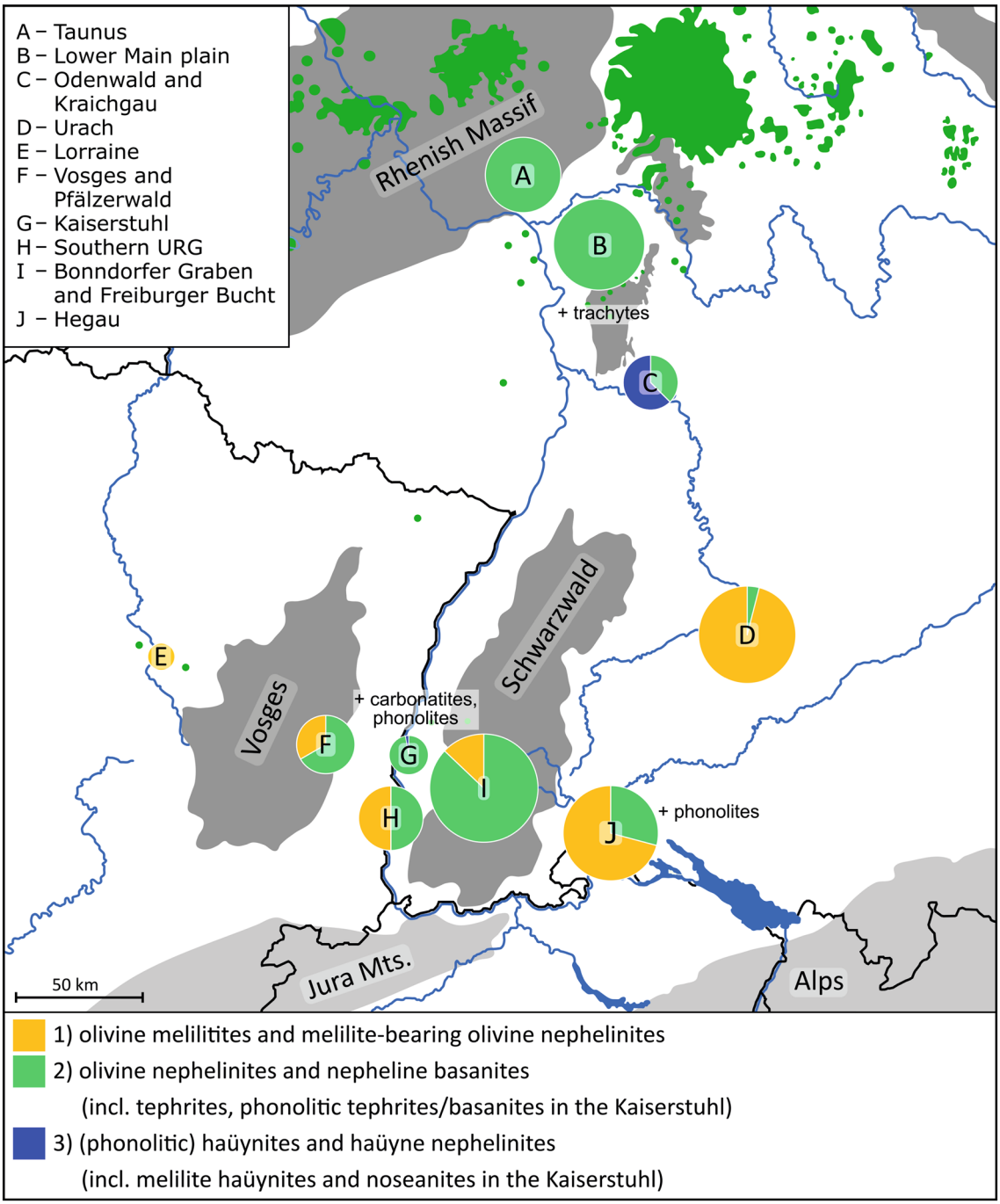

Fig. 2 Map of SW Germany and E France showing the study areas of this work as circular diagrams representing the semi-quantitative distribution of groups of SiO_2-undersaturated rock types in each region determined by number of known occurrences. The circle size roughly correlates with the number of described occurrences (Lorraine: $n = 2$, Bonndorfer Graben and Freiburger Bucht area: $n = 31$), except for the Kaiserstuhl, for which surface coverage percentages are used. The rock types were determined by microscopy of 215 thin sections from approx. 120 localities in the southern CEVP. For regions that also contain strongly evolved rocks, these are additionally stated

Most of the studied occurrences are tied to obvious tectonic structures (Fig. 4): the Kaiserstuhl volcanic complex and several isolated stocks and diatremes are located within the URG between the Variscan massifs of the Vosges and the Schwarzwald. The volcanic dykes and vents in these massifs occur on the flanks of the URG (e.g., Freiburger Bucht) and in the WNW-trending Bonndorfer Graben, merging eastwards into the Hegau Graben that hosts additional dykes, plugs, domes, and larger tuff deposits. The Albstadt shear zone is a seismically active, few km wide, deformation zone

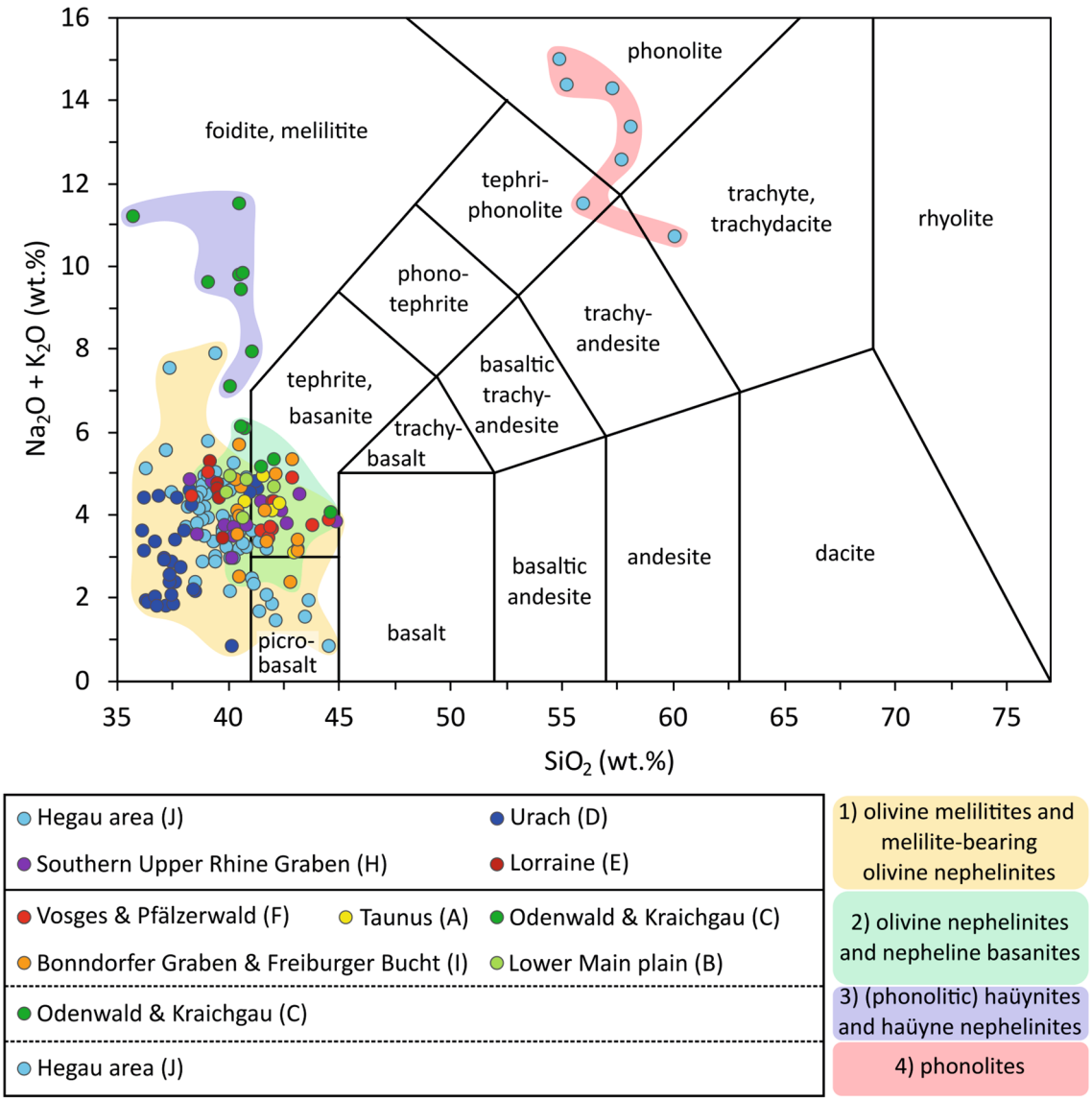

Fig. 3 TAS diagram for the investigated rocks in the southern CEVP. Thirty-four new analyses performed according to the XRF method reported in Braunger et al. (2018) were supplemented by literature data from Dunworth and Wilson (1998), Frenzel (1975), Hegner et al. (1995), Hurrle (1976), Keller et al. (1990), Krause and Weiskirchner (1981), Neumann et al. (1992), Staesche (1995), Stähle and Koch (2003), and Stellrecht and Emmermann (1970). All data have been renormalized to a volatile-free composition. Note that the naming of the rocks in the petrography chapter was done based on the mineral composition, which is why the position in the TAS diagram may differ from the assigned rock name. No whole-rock analyses are available for the trachytes of the Lower Main plain

(Mader et al. 2021) that trends parallel to the URG and connects the Hegau Graben with the westernmost margin of the Urach volcanic field, which is delimited by several minor faults (Fig. 4; Ring and Bolhar 2020). The volcanic rocks of the Lower Main plain occur along the eastern flank of the URG (Sprendlinger Horst), those from Forst (Pfälzerwald) and the more southerly Vosges along the western flank. The basanites and nephelinites in the Taunus trend parallel to the South Hunsrück–Taunus border fault, while the volcanic rocks in the Odenwald and Kraichgau area and Lorraine are not associated with any obvious structure.

The study area comprises some of the most primitive melilitites and nephelinites of the entire CEVP (Fig. 3). However, while several studies on the petrogenesis of such rocks exist for the northern part of the CEVP (e.g., Duda and Schmincke 1985; Harmon et al. 1987; Jung et al. 2006; Pfänder et al. 2018; Skála et al. 2015; Ulrych et al. 2008, 2011, 2013, 2016), similar occurrences in the southern CEVP have been much less investigated (Blusztajn and Hegner 2002; Dunworth and Wilson 1998; Hegner et al. 1995; Hegner and Vennemann 1997) and comparative work involves SiO_2-saturated, basaltic and evolved rocks (e.g.,

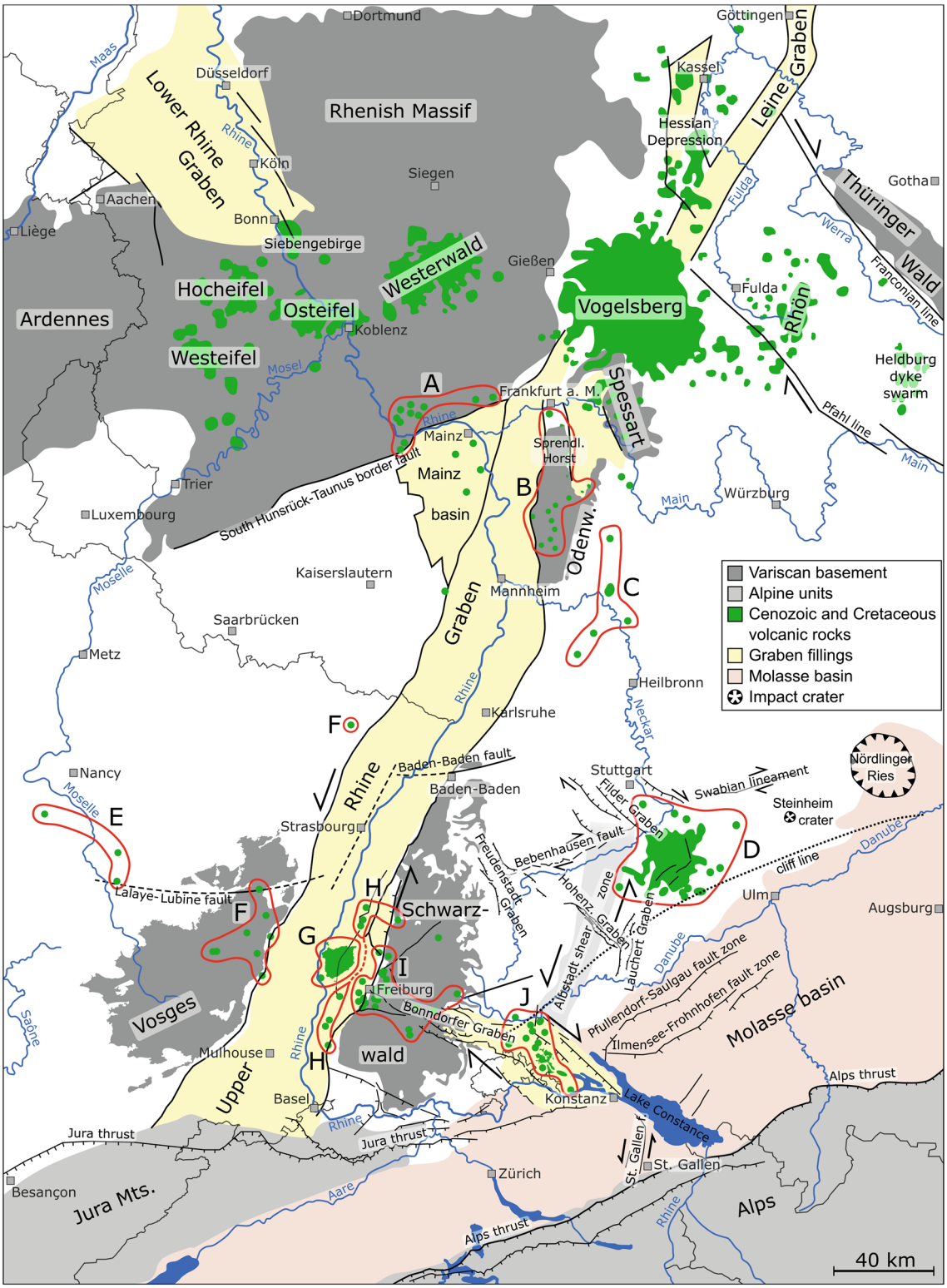

Fig. 4 Simplified geologic map of SW Germany and E France showing major tectonic structures, geological main units, and occurrences of late Cretaceous to Holocene volcanic rocks (modified after Egli et al. 2017; Ring and Bolhar 2020). *A* Taunus, *B* Lower Main plain, *C* Odenwald and Kraichgau area, *D* Urach, *E* Lorraine, *F* Vosges and Pfälzerwald, *G* Kaiserstuhl, *H* Southern Upper Rhine Graben, *I* Bonndorfer Graben and Freiburger Bucht area, *J* Hegau area

Lustrino and Wilson 2007; Wedepohl et al. 1994; Wedepohl and Baumann 1999; Wilson and Downes 1992; Wörner et al. 1986).

Petrogenetic models explaining the diversity of volcanic rocks in the CEVP

Previous studies from the Urach and Hegau areas suggested that melilititic rocks crystallized from very low-degree, volatile- and trace-element-rich partial melts that originated in the sub-lithospheric mantle (> 100 km depth; dolomite–garnet peridotite stability field) and infiltrated and metasomatized the overlying lithospheric mantle (~ 75 km; Dunworth and Wilson 1998), or in some cases directly erupted at the surface. Other models, however, locate the melt generation of melilite-bearing rocks in the CEVP at the base of the lithosphere (Blusztajn and Hegner 2002), possibly in the thermal boundary layer (TBL; Heldburg region; Pfänder et al. 2018). Despite the timing, origin, and processes of metasomatic overprint are not yet well constrained, previous modifications to ancient subduction processes are widely accepted as the major forces for metasomatic overprinting of the mantle (e.g., Blusztajn and Hegner 2002; Hegner and Vennemann 1997; Lustrino and Wilson 2007; Puziewicz et al. 2020; Ulrych et al. 2011; Witt-Eickschen and Kramm 1998). According to Pfänder et al. (2018), prolonged subduction of oceanic and continental lithosphere with successive dehydration during Variscan Orogeny generates aqueous to supercritical fluids enriched in volatiles and other trace elements, causing metasomatism at great depths (> 125 km) in the thickened lithosphere. This process results in the formation of a carbonated, phlogopite-bearing garnet lherzolite that is later partially melted during evolution of the ECRiS in response to perturbation of the TBL and decompression associated with lithospheric thinning (< 85 km). For instance, Hegner and Vennemann (1997) identified an influence of recycled seawater that overprinted the lithospheric mantle prior to melt formation at Urach and in the Hegau area. However, the asthenospheric mantle is often considered as another major melt source component in melilite-bearing rocks, interacting and mixing with lithospheric domains (Jung et al. 2006; Lustrino and Wilson 2007; Skála et al. 2015; Ulrych et al. 2008, 2013, 2016).

For melilite-free nephelinitic to basanitic rocks, slightly higher degrees of partial melting and shallower depths of extraction (spinel peridotite stability field or transition zone to garnet stability field) are assumed (Mertz et al. 2015; Pfänder et al. 2018; Schubert et al. 2015; Ulrych et al. 2013). Further, Ulrych et al. (2013) and Pfänder et al. (2018) suppose a less metasomatized lithospheric source for basanites than for the melilite-bearing rocks of the Heldburg region and the Eger Graben, without excluding an asthenospheric component. For basanites and nephelinites from the Westeifel, Vogelsberg, and Westerwald, Jung et al. (2011), Mertz et al. (2015), and Schubert et al. (2015) favor an asthenospheric source coupled with thermal erosion of strongly metasomatized lithosphere and/or intense asthenosphere–lithosphere interaction. The less primitive nature of some of these rocks was explained by temporary stagnation and early polybaric fractionation of olivine, clinopyroxene, and chromium spinel combined with contamination and mixing processes in the upper lithosphere, apparently consistent with frequent occurrence of resorbed green-core pyroxenes in the Westeifel and Hocheifel (Duda and Schmicke 1985; Jung et al. 2006).

Evolved phonolites from the Hegau have been suggested to represent differentiates of primitive foiditic magmas (Mahfoud and Beck 1989). Abratis et al. (2015) showed that (tephri)phonolites in the Heldburg dyke swarm were derived from a nephelinitic parental magma, but subsequently modified during stagnation and fractionation by mixing and mingling with basanitic melts, producing intermediate compositions. For trachytes and phonolites from the Rhön and the Lower Main Plain, assimilation of crustal rocks is suggested as another contribution to their formation (Jung et al. 2013; Schmitt 2006a).

In summary, some models for the CEVP invoke the involvement of mantle plumes or at least active diapiric upwelling (Dunworth and Wilson 1998; Haase et al. 2004; Hegner et al. 1995; Jung et al. 2006; Mertz et al. 2015; Schubert et al. 2015), whereas other studies doubt the necessity of mantle plumes and explain partial melting by earlier metasomatism in the mantle source (Blusztajn and Hegner 2002; Jung et al. 2005, 2011; Pfänder et al. 2018; Ulrych et al. 2008). Given the widely varying definitions of mantle plumes in terms of formation depth and thermodynamic properties, many of the modern models can be considered hybrid concepts. These do not attribute melting and volcanism exclusively to thermal or compositional anomalies of an uplifted asthenosphere, nor alone to metasomatism followed later by extensional–transtensional lithospheric thinning and uplift (Lustrino and Wilson 2007). However, deep-seated active asthenospheric upwelling causing a thermal anomaly below or in the TBL (mantle plumes in the narrower sense) is meanwhile mostly rejected for the formation of the CEVP (e.g., Fichtner and Villaseñor 2015).

Materials and methods

For this study, thin sections of 232 rock samples from approximately 130 localities in the CEVP were prepared for petrographic examination (Fig. 2), with a special focus on mineralogy, textures, and alteration state to classify them according to Le Maitre et al. (2002). Most samples originate

from various collections in Germany (University of Tübingen, Goethe University Frankfurt, University of Mainz, LGBR Freiburg, HLNUG Wiesbaden) and France (Terrae Genesis, Le Syndicat), supplemented by resampling of several localities. Based on the presence of datable minerals (perovskite, apatite, titanite, zircon, and/or pyrochlore) of adequate grain size, 56 thin sections from 45 localities were selected for U–Pb dating and supplemented by mounted heavy mineral concentrates from five localities (Online Resource 1).

U–Pb age data, supported by ~ 3000 spot analyses, were collected on a Thermo Scientific Element XR sector field ICP-MS coupled with a Resonetics RESOLution 193 nm ArF Excimer laser (CompexPro 102) at FIERCE (Goethe-Universität Frankfurt am Main) using a slightly modified method as previously described in Gerdes and Zeh (2006, 2009). The ICP-MS was tuned for maximum sensitivity while keeping the oxide formation (UO/U < 0.2%) and element fractionation (i.e., Th/U ~ 1) low. Analytical details are reported in the metadata tables of each sequence (Online Resource 2–13). Raw data were corrected offline using an in-house VBA Microsoft Excel© spreadsheet program (Gerdes and Zeh 2006, 2009). The $^{207}Pb/^{206}Pb$ and $^{206}Pb/^{238}U$ ratios were corrected for mass biases, including drift over time for each of the 11 sequences measured, using the primary reference material SRM-NIST 612. An additional correction was applied on the $^{206}Pb/^{238}U$ ratios to account for compositional differences using Durango apatite (31.44 Ma; McDowell et al. 2005), in-house Nama titanite (999 Ma; TIMS data, Wolfgang Dörr, pers. comm.), GJ-1 zircon (Jackson et al. 2004; 603 Ma; TIMS data, Wolfgang Dörr, pers. comm.), and Ice River perovskite (361 Ma; Tappe and Simonetti 2012). Ages were calculated using Isoplot 4.15 (Ludwig 2009) and are plotted within the Tera–Wasserburg space (Tera and Wasserburg 1972). All uncertainties are reported at the 2σ level and were calculated following the guidelines provided by Horstwood et al. (2016).

Results

Petrography

Based on mineralogy and textures, five groups of volcanic rock types that differ in spatial distribution are distinguished in the study area (Fig. 2): (1) olivine melilitites and melilite-bearing olivine nephelinites, (2) olivine nephelinites and nepheline basanites, (3) (phonolitic) haüynites and haüyne nephelinites, (4) phonolites, and (5) trachytes. Detailed information on the modal mineralogy of all rock types in the investigated regions is presented in Table 2, complemented by a TAS diagram (Fig. 3).

Olivine melilitites and melilite-bearing olivine nephelinites predominate at Urach, in the Hegau area, and in Lorraine and represent half of the occurrences in the southern URG but occur only rarely and often strongly altered in the Bonndorfer Graben and the Freiburger Bucht area and in the Vosges (Fig. 2). These are porphyritic rocks characterized by macrocrysts of melilite (< 2 mm; av. ~ 0.5 mm), olivine (< 10 mm; av. ~ 1 mm), and occasional clinopyroxene (< 2.5 mm; av. ~ 0.5 mm) set in a fine-grained groundmass of clinopyroxene, opaque phases, interstitial nepheline, melilite, biotite, betimes haüyne, and small amounts of subhedral to euhedral perovskite and apatite (Fig. 5a, b).

Olivine nephelinites and nepheline basanites, in contrast to the latter group, are melilite- and mostly perovskite-free. They are composed of macrocrysts of olivine (< 12 mm; av. ~ 1 mm) and clinopyroxene (< 10 mm; av. 1 mm) embedded in a very fine-grained or hyaline groundmass containing clinopyroxene, nepheline, and occasional haüyne. Such rocks are typical of the Vosges and Pfälzerwald, the Bonndorfer Graben and Freiburger Bucht area, the Taunus, the Lower Main plain, and parts of the Kaiserstuhl (Fig. 2). Two textural types of clinopyroxene macrocrysts can be distinguished: Type I is represented by beige to yellowish or pale brownish euhedral to subhedral crystals under polarized light. Type II (so-called green-core pyroxene, e.g., Duda and Schmincke 1985) consists of rounded greenish cores, surrounded by a fringe of Type I clinopyroxene. Some of these green-core pyroxenes enclose anhedral, stocky rounded apatite (Fig. 5c). Several samples with groundmass plagioclase and minor alkali feldspar are classified as basanitic nephelinites or nepheline basanites. Odenwald and Kraichgau samples may contain high amounts of biotite (Fig. 5d). In the Hegau area and the southern URG, some melilite-free olivine nephelinites occur as well (Fig. 2), but they lack green-core pyroxenes, contain betimes perovskite, and their texture is similar to the melilite-bearing rocks from these regions.

Haüynites to *phonolitic haüynites, and haüyne nephelinites to phonolitic haüyne nephelinites* are limited to few occurrences in the Odenwald and the Kraichgau area (Fig. 2). Medium-grained euhedral haüyne, Ti magnetite, and apatite phenocrysts surrounded by a fine-grained groundmass of nepheline, clinopyroxene, alkali feldspar, and amphibole are abundant. Subhedral poikiloblastic clinopyroxene macrocrysts (< 6 mm; av. 2 mm) form glomerules with inclusions of euhedral apatite and Ti magnetite crystals (Fig. 5e). Rare small subhedral olivine crystals are embedded in the groundmass. Further, evolved clinopyroxene-, nepheline-, and perovskite-bearing haüyne-melilititic to melilite-haüynitic dykes without any olivine occur in the Kaiserstuhl.

Phonolites in the eastern Hegau area are characterized by phenocrysts of alkali feldspar (< 5 mm; av. 1–2 mm), haüyne (< 3 mm; av. 0.5 mm), or their alteration products,

Table 2 Modal mineralogy of investigated rocks in the southern CEVP

Rock series/region	Ol	Cpx	Spl/Usp	Bt/Phl	Mll	Nph + Zeo	Hyn/Nsn/Sdl	Pl	Afs	Acc
Olivine melilitites and melilite-bearing nephelinites										
Hegau area	*20–40*	10–35	10–15	< 5	*< 20*	*< 20*	< 5	–	–	**prv,** ap
Urach	*20–50*	< 30	~ 15	< 5	*< 40*	*< 10*	< 5	–	–	**prv**, ap
Southern URG	*20–30*	25–30	< 20	< 5	*< 20*	*10–25*	Acc	–	–	**prv**, ap, grt
Lorraine	*25–35*	~ 30	10–15	Acc	*5–10*	*< 10*	Acc	–	–	**prv**
Vosges[a]	*~ 30*	~ 10	10–15	Acc	*15–20*	*< 5*	Acc	–	–	ap
Olivine nephelinites and nepheline basanites										
Vosges and Pfälzerwald	*20–30*	*40–55*	5–15	< 5	–	*5–20*	Acc	–	–	ap
Taunus	*10–35*	*35–50*	5–15	< 10	–	*< 20*	Acc	< 10	< 5	**ap**, ttn
Bonndorfer Graben and Freiburger Bucht	*10–40*	*20–60*	5–15	< 10	–	*< 20*	< 10	–	–	**ap**
Odenwald and Kraichgau area	*15–30*	*15–35*	10–20	*< 25*	–	*5–10*	< 5	< 15	< 5	ap
Lower Main plain	*20–25*	*30–35*	10–15	< 5	–	*20–25*	< 5	–	–	ap
Southern URG and Hegau area	*20–35*	*20–50*	10–15	< 5	–	*10–25*	Acc	–	–	**ap**, prv
(Phonolitic) haüynites and haüyne nephelinites										
Odenwald and Kraichgau area	< 10	*10–30*	15–20	< 10	–	< 10	*10–20*	–	< 10	***ap*** *(< 10)*
Kaiserstuhl[a]	–	5–20	5–10	< 5	*10–35*	5–10	*25–35*			***ap, prv****, grt*
Ijolites										
Hegau area[a]	–	*~ 30*	~ 10	Acc	–	*50–60*	–	–	–	**prv, ap**
Urach[a]	–	*~ 35*	~ 5	Acc	–	*~ 45*	–	–	–	**prv, ap**
Syenites and nepheline syenites										
Hegau area	–	*< 25*	Acc	< 5	–	*< 35*	–	–	*50–65*	**ttn, ap, zrn, pcl,** thn
Phonolites										
Hegau area	–	*10–20*	Acc	Acc	–	*15–30*	*15–25*	–	*40–50*	**ttn, ap,** zrn, pcl
Trachytes										
Lower Main plain	–	–	5–10	Acc	–	–	–	< 10	*85–95*	**zrn, ap,** ttn

Distinctive values are in italics, characteristic accessories are in bold

Ol olivine, *Cpx* clinopyroxene, *Spl* spinel group (including magnetite), *Usp* ulvöspinel, *Bt* biotite, *Phl* phlogopite, *Mll* melilite, *Nph* nepheline, *Zeo* zeolites, *Hyn* haüyne, *Nsn* nosean, *Sdl* sodalite, *Pl* plagioclase, *Afs* alkali feldspar, *Acc* accessory minerals, *ap* apatite, *prv* perovskite, *grt* garnet, *ttn* titanite, *zrn* zircon, *pcl* pyrochlore, *xtm* xenotime, *thn* thorianite

[a]The difference to 100% results from optically not resolvable mineral phases due to alteration or microcrystalline matrix minerals

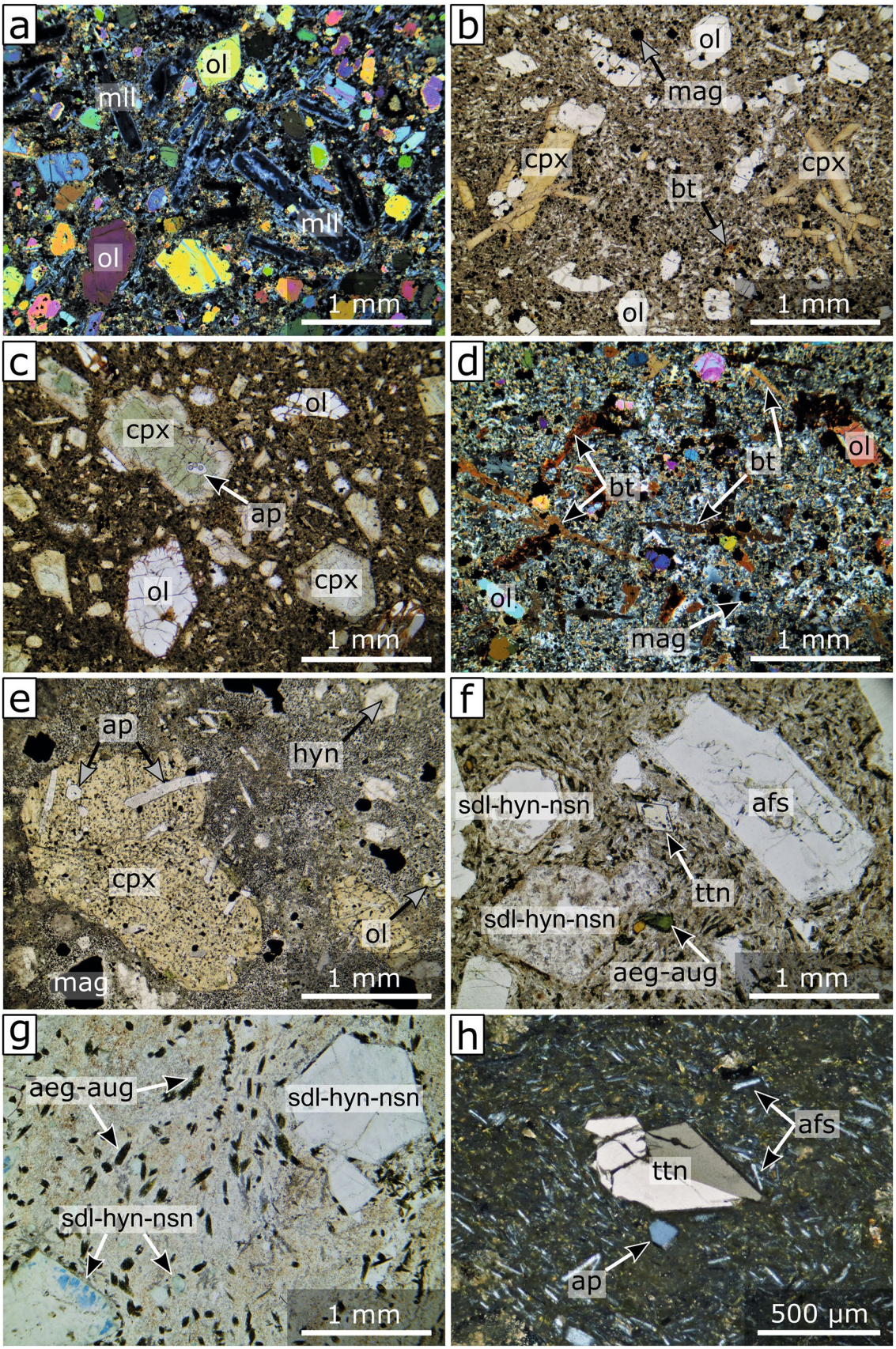
a
ol
mll
mll
ol
1 mm
b
ol
mag
cpx
cpx
bt
ol
1 mm
c
ol
cpx
ap
ol
cpx
1 mm
d
bt
bt
ol
ol
mag
1 mm
e
ap
hyn
cpx
ol
mag
1 mm
f
sdl-hyn-nsn
afs
ttn
sdl-hyn-nsn
aeg-aug
1 mm
g
aeg-aug
sdl-hyn-nsn
sdl-hyn-nsn
1 mm
h
afs
ttn
ap
500 µm

◂**Fig. 5** Microstructure and mineral textures in melilitites, foidites, basanites, and phonolites of the southern CEVP. **a** Olivine melilitite with olivine (ol) macrocrysts and melilite (mll) phenocrysts, crossed polarization (Hohenbol, Urach). **b** Nepheline-bearing olivine melilitite with olivine macrocrysts and agglomerations of clinopyroxene (cpx) in a groundmass of fine-grained clinopyroxene, melilite, nepheline, magnetite (mag), and little biotite (bt) (Hohenstoffeln, Hegau area). **c** Olivine nephelinite with olivine macrocrysts, clinopyroxene phenocrysts and resorbed green-core pyroxenes, containing an inclusion of anhedral apatite (ap), embedded in a cryptocrystalline groundmass (Rotteckruhe, Freiburger Bucht). **d** Phonolitic phlogopite-nepheline basanite with lath-shaped, large phlogopite and medium-grained olivine crystals in a groundmass of clinopyroxene, magnetite, nepheline, plagioclase, and minor alkali feldspar (Steinsberg, Kraichgau). **e** Olivine-bearing nepheline haüynite with poikiloblastic clinopyroxene enclosing euhedral apatite and haüyne (hyn), magnetite, and olivine phenocrysts in a groundmass of nepheline, clinopyroxene, and minor alkali feldspar (Neckarbischofsheim, Kraichgau). **f** Phonolite with phenocrysts of alkali feldspar (afs), a strongly altered sodalite group mineral (sdl–hyn–nsn), titanite (ttn) and aegirine-augite (aeg-aug) in a groundmass of alkali feldspar, aegirine-augite, and nepheline (Hohentwiel, Hegau area). **g** Phonolite with altered sodalite group minerals showing exsolution textures in a groundmass of aegirine-augite, alkali feldspar, nepheline, and sodalite group minerals (Hohenkrähen, Hegau area). **h** Phonolite with a phenocrystal of titanite and small apatite in a fine-grained groundmass of aegirine-augite, alkali feldspar, and nepheline (Hohentwiel, Hegau area)

and occasional aegirine-augite (< 1 mm) embedded in a groundmass of alkali feldspar, haüyne, nepheline, and aegirine–augite (Fig. 5f, g). Euhedral apatite, titanite, zircon, and rare pyrochlor are typical accessories (Fig. 5h). Some samples contain few biotite xenocrysts. *Trachytes* in the Lower Main plain (Hoher Berg near Heusenstamm and Sporneiche) consist of alkali feldspar phenocrysts (< 3 mm) and microcrysts along with minor amounts of opaque minerals, biotite, titanite, and zircon (Fig. 6a).

Additionally, two groups of coarse-grained magmatic rocks have been investigated: *ijolitic* veins and schlieren occur within the melilite-bearing rocks at Urach (Sternberg) and in the Hegau area (Hohenstoffeln). They are composed of euhedral, commonly sector-zoned, greenish clinopyroxene and subhedral, tabular nepheline and its alteration products, complemented by squat or skeletal, medium-grained Ti magnetite and euhedral apatite needles. Perovskite is abundant and forms either anhedral brownish grains (Urach, Fig. 6b) or purple skeletal crystals and crystal groups (Hegau area, Fig. 6c). *Syenitic to nepheline syenitic* fragments consisting of alkali feldspar, nepheline, and clinopyroxene, plus small amounts of biotite and opaque phases are enclosed in augite-hornblende-phlogopite tuffs, melilite-bearing olivine nephelinites, and phonolites from the Hegau area. Common accessory minerals are titanite, apatite, zircon (Fig. 6d), pyrochlore, and thorianite.

U–Pb geochronology

In situ U–Pb ages obtained on perovskite, apatite, titanite, zircon, and pyrochlore are listed and illustrated along with their 2σ errors, the number of measurement points (n), and the mean square weighted deviation (MSWD) in Tables 3 and 4 and in Fig. 7. The results reveal a late Cretaceous to early Eocene and a late Oligocene to late Miocene group separated by a ~ 20 Myr age gap. These age differences correlate with mineralogical differences and show systematic distribution patterns (Fig. 2): late Cretaceous to late Paleocene melilite-free olivine nephelinites and nepheline basanites occur in the Taunus (~ 68–55 Ma) and the Bonndorfer Graben and Freiburger Bucht area (~ 67–58 Ma), late Cretaceous to early Paleocene trachytes and haüynites are localized in the Lower Main plain (~ 73–65 Ma) and the Odenwald and Kraichgau area (~ 68–62 Ma). Late Oligocene to late Miocene perovskite-bearing olivine melilitites and melilite-bearing olivine nephelinites are restricted to Lorraine (~ 26 Ma), the southern URG (~ 26–25 Ma and 17–16 Ma), Urach (~ 19–12 Ma), and the Hegau area (12–9 Ma). Ages for ijolitic veins and schlieren therein (Hegau and Urach) are in good agreement with the host rock ages. Additionally, phonolites from five Hegau localities were dated to ~ 14–12 Ma and syenitic inclusions therein (Gönnersbohl) reveal ages of ~ 14–11 Ma. Nepheline syenitic xenoliths in tuffs and in melilite-bearing olivine nephelinites encompass a similar age range (~ 15–11 Ma), an augite-hornblende-phlogopite tuff yields ages of 14.5 ± 1.1 Ma and 12.5 ± 1.6 Ma, respectively. An exception from all these rock type–age relations is the polygenetic Kaiserstuhl, with melilite-rich rocks, melilite-free nephelinites, (phonolitic) tephrites/basanites, carbonatites, haüynites, phonolites, and noseanites, all of which erupted during the Miocene (~ 19–15 Ma; this study; Ghobadi et al. 2021).

Discussion

Timing and duration of volcanism in the southern CEVP

Using in situ U–Pb geochronology, we have dated numerous volcanic rocks of the southern CEVP for the first time, giving precise age constrains for several localities previously dated mostly by the K–Ar method on whole-rock samples (Baranyi et al. 1976; Horn et al. 1972; Kraml et al. 1995, 1999; Lippolt et al. 1963, 1973, 1975; Lippolt 1983). In comparison with previous literature data, the results of this dating approach, supplemented with published ages applying different modern methods, show two age groups in the southern CEVP (Figs. 7 and 8). Discrepancies and former uncertainties result from known problems of the K–Ar

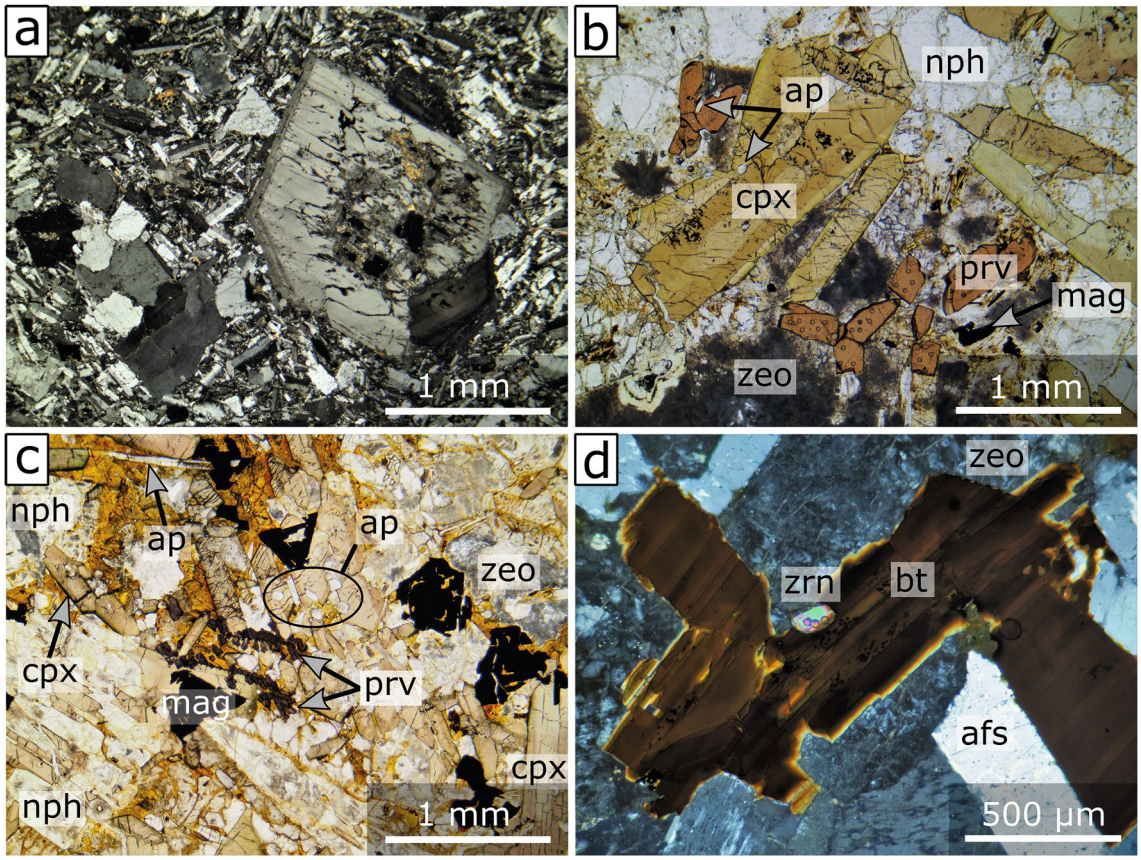

Fig. 6 Microstructure and mineral textures in trachytes, ijolites, and nepheline syenites of the southern CEVP. **a** Trachyte with a phenocryst of a sericitic altered, perthitic alkali feldspar and an accumulation of anhedral alkali feldspar in a groundmass of lath-shaped sanidine (Sporneiche, Lower Main plain). **b** Ijolite with euhedral sector-zoned clinopyroxene, tabular nepheline (nph), zeolite (zeo), and anhedral perovskite (prv) (Sternberg, Urach). **c** Ijolite with skeletal magnetite and perovskite surrounded by subhedral to euhedral clinopyroxene, nepheline, zeolite, and minor apatite (Hohenstoffeln, Hegau area). **d** Nepheline syenite xenolith with an anhedral zircon grain next to a tabular biotite crystal surrounded by alkali feldspar and zeolite (2 km E Weil, Hegau area)

method (e.g., Baranyi et al. 1976; Horn et al. 1972), such as loss of ^{40}Ar due to devitrification of rocks and alteration, particularly on small grains, or excess ^{40}Ar caused by inheritance during magma formation and/or ascent (e.g., wall rock contamination, presence of xenocrysts). Low closure temperatures for certain K-rich minerals and alteration-related K loss can also lead to erroneous age determinations. The old K–Ar ages are discussed in Online Resource 14.

Crystallization and cooling during ascent and emplacement of subvolcanic to volcanic rocks have no significant influence on the determined mineral ages, since 2σ uncertainties are generally larger than the duration of such processes (Schmitt 2006b; Schmitt et al. 2010; Sundermeyer et al. 2020). Thus, resolvable age differences between texturally distinct minerals in the same sample, between different samples of similar rock types from the same locality, and between plutonic cumulates and their volcanic host rocks allow for deciphering time spans of several Myr relevant for transcrustal plumbing systems at local and regional scales. Mineral ages in xenoliths may potentially suffer from thermal overprint by the host magma during ascent, which would result in partial reset of the original age if closure temperatures of the dated minerals are below those of the xenolith-transporting magma. Closure temperatures for the U–Pb system vary considerably between minerals, depending on grain size and cooling rate and increase from ~ 350–550 °C for apatite, via ~ 570–700 °C for titanite and ~ 660–950 °C for perovskite, to ~ 740–1010 °C for zircon (Carlson 2019; Chew and Spikings 2015; Flowers et al. 2007; Heaman and Parrish 1991; Spear and Parrish 1996; Wu et al. 2010). In the present study, several xenoliths of the same occurrence have been dated with different crystals and several different mineral phases (apatite, pyrochlore, titanite, zircon), with ages consistent within analytical uncertainty (Table 4). Thus, we consider them to represent crystallization ages of the xenoliths.

Our data (Tables 3 and 4) indicate that the oldest volcanic rocks in the southern CEVP formed in the late Cretaceous

Table 3 U–Pb ages of the late Cretaceous to early Eocene group

Sample	Locality	Rock type	Mineral	Age (Ma)	±2σ	*n*	MSWD
Taunus (A)							
75	Naurod (Erbsenacker)	ON	Ttn	55.38	0.91	34	0.91
75	Naurod (Erbsenacker)	ON	Ap	65.68	2.42	17	0.61
75-3	Naurod (Erbsenacker)	ON	Ap	68.13	2.41	32	0.96
Bonndorfer Graben and Freiburger Bucht area (I)							
N 119	Berghäuser Kapelle	Hyn b. ON	Ap	62.08	0.48	44	0.80
N 604	Berghäuser Kapelle	Hyn b. ON	Ap	59.13	2.22	27	1.09
N 604	Berghäuser Kapelle	Hyn b. ON	Zrn	59.55	1.35	18	1.79
N 251	Erentrudiskapelle Munzingen	Foiditic tuff	Ap	60.63	1.22	26	0.87
N 308	Heuweiler	Bt b. ON	Ap	66.54	2.92	11	1.16
N 46	Rautebacher Höfe	Hyn b. ON	Ap	62.81	0.87	57	1.21
N 104	Rotteckruhe	ON	Ap	59.86	0.96	11	0.62
N 96	St. Ottilien	Hyn, Bt b. ON	Ap	61.21	1.72	8	1.16
N 311	Tannengrund	ON	Ap	63.85	8.47	4	0.45
N 47	Uhlberg	Bt b. ON	Ap	64.57	1.18	12	1.10
Lower Main plain (B)							
HBH 1	Hoher Berg quarry near Heusenstamm	Trachyte	Ap	64.96	4.64	10	0.59
HBH 1	Hoher Berg quarry near Heusenstamm	Trachyte	Zrn	72.41	1.20	11	0.91
EPM 1	Sporneiche	Trachyte	Ap	66.83	6.43	18	0.59
GM 36	Sporneiche	Trachyte	Ap	68.51	6.27	18	0.89
GM 36	Sporneiche	Trachyte	Ttn	72.21	2.00	12	1.33
GM 36	Sporneiche	Trachyte	Zrn	72.60	1.46	6	0.79
Odenwald and Kraichgau area (C)							
N 595	Geisberg, Diedesheim	Bt b. NH	Ap	67.36	5.24	24	0.86
N 20	Hamberg near Neckarelz	Ol, Nph b. H	Ap	65.65	7.52	19	1.80
N 15	Neckarbischofsheim	ONH	Ap	67.71	8.65	54	0.63
I 20	Waldbrunn	Ol b. NH	Ap	62.32	4.27	52	0.94

b. bearing, *Bt* biotite, *Hyn* haüyne, *Nph* nepheline, *Ol* olivine, *NH* nepheline haüynite, *ON* olivine nephelinite, *ONH* olivine nepheline haüynite, *Ap* Apatite, *Ttn* titanite, *Zrn* zircon, *n* number of measurement spots, *MSWD* mean squared weighted deviation

and represent strongly evolved trachytes and haüyne-rich rocks from the Lower Main plain (~ 73–65 Ma) and the Odenwald and Kraichgau area (~ 70–62 Ma) in the east of the northern URG, consistent with U–Pb zircon ages in the same region for the Sporneiche trachyte (68.6 ± 1.9 Ma; Schmitt 2006a) and the Katzenbuckel phonolite (69.6 ± 1.9 Ma; Schmitt et al. 2007). A similar age range (~ 67–58 Ma) determined for the Freiburger Bucht and the Bonndorfer Graben area on the eastern flank of the URG coincides with the eruption of the Trois Épis olivine melilitite in the Vosges on the opposite graben shoulder with an amphibole $^{40}Ar/^{39}Ar$ age of 60.9 ± 0.6 Ma (Keller et al. 2002). For the Taunus, a new titanite age for Naurod (55.4 ± 0.9 Ma) is very similar to a $^{40}Ar/^{39}Ar$ age for Rabenkopf (58.7 ± 0.4 Ma; Fekiacova et al. 2007). However, significantly older ages for apatite inclusions in titanite (65.7 ± 2.4 Ma) and apatite in a second sample from Naurod (68.1 ± 2.4 Ma) reveal prolonged magmatic activity in this area started at least 10 Myr earlier, potentially revealing discontinuous magma replenishment events. During the early Eocene (~ 56–47 Ma), volcanism in the southern CEVP was basaltic to nephelinitic and restricted to the Lower Main plain and the Pfälzerwald (Forstberg, Messel maar, Stetteritz, Forst, and Kisselwörth; Fekiacova et al. 2007; Lenz et al. 2015; Lutz et al. 2013).

After a volcanic gap of ~ 20 Ma, the oldest known olivine melilitites of the younger series erupted in the late Oligocene (~ 26–25 Ma) near Essey-la-Côte in Lorraine and at the Buggingen potash salt deposit in the southern URG (Table 4). Subsequently, no magmatism is documented until a phase of intense volcanism represented at Urach (~ 19–12 Ma), in the Hegau area (~ 15–9 Ma), and the remaining southern URG (~ 17–16 Ma; Mahlberg, Herbolzheim) including the Kaiserstuhl volcanic complex (~ 19–15 Ma), whose activity is well constrained by recent dating of numerous rock types using U–Pb, $^{40}Ar/^{39}Ar$, Rb–Sr, (U-Th)/He, and fission track (Ghobadi et al. 2021 and references therein; Kraml et al. 1995, 1999), confirmed by our apatite and perovskite U–Pb ages for a haüyne melilitite from the Kaiserstuhl. The

Table 4 U–Pb ages of the late Oligocene to late Miocene group

Sample	Locality	Rock type	Mineral	Age (Ma)	±2σ	*n*	MSWD
Lorraine (E)							
LM 455	Essey-la-Côte	Nph b. OM	Prv	26.16	1.03	38	3.72
Southern URG (H)							
M 110	Buggingen	OM	Ap	24.68	1.80	41	1.23
M 110	Buggingen	OM	Prv	25.56	0.64	44	1.81
HERB	Herbolzheim	Foiditic tuff	Ap	16.75	0.84	120	1.00
2018-001	Mahlberg	ON	Prv	16.09	0.37	16	0.87
Kaiserstuhl (G)							
HTAC 1332	Horberig	HM	Ap	16.17	0.50	40	0.94
HTAC 1332	Horberig	HM	Prv	17.16	1.38	31	0.57
Urach (D)							
U 006	Am Hofwald	Bt b. OM	Prv	15.38	0.78	22	1.44
W 42	Autmuthbach	OM	Prv	12.30	1.09	14	1.64
U 028	Bölle	OM	Prv	13.29	4.56	25	2.16
U 018	Dietenbühl	Bt b. MON	Prv	13.53	1.38	27	0.90
M 10	Donnstetten	Nph b. OM	Prv	15.75	0.87	35	1.23
N 469	Eisenrüttel	Hyn b. ON	Prv	15.53	1.60	12	0.94
U 015	Eisenrüttel	Hyn b. ON	Prv	17.28	0.55	29	0.94
U 009	Floriansberg	Hyn b. OM	Prv	19.06	1.76	47	1.45
U 026	Floriansberg	Bt b. OM	Prv	14.18	0.36	10	0.90
U 005	Gaisbühl	OM	Prv	15.77	0.77	31	1.41
U 021	Götzenbrühl	Nph b. OM	Prv	14.66	1.18	35	0.89
833	Hohenbol near Owen	Nph b. OM	Prv	15.94	0.26	37	1.63
U 027	Hohenbol near Owen	OM	Prv	15.39	3.44	27	0.60
U 030	Hohenbol near Owen	Nph b. OM	Prv	15.49	2.64	27	0.58
U 031	Jusi	OM	Prv	18.90	2.70	13	1.29
U 032	Metzinger Weinberg	Nph b. OM	Prv	13.61	0.65	42	1.01
U 025	Schopfloch	OM	Prv	12.97	1.22	45	1.16
U 001	Sternberg	Ijolite	Ap	11.95	6.61	43	0.88
U 001	Sternberg	Ijolite	Prv	12.65	0.45	60	1.63
U 016	Sternberg	OM	Prv	13.95	2.32	21	0.82
U 022	Sulzburg	OM	Prv	14.02	1.68	27	0.67
U 010	Wittlinger Steige	OM	Prv	14.42	0.99	22	0.78
Hegau area (J)							
N 374	Blauer Stein (Steinröhren)	Mll b. ON	Prv	9.93	0.96	9	0.93
HEG 17	Hohenhewen	Mll b. ON	Prv	10.28	0.41	33	1.40
HEG 02	Hohenstoffeln	Ijolite	Prv	11.04	0.32	64	1.47
HEG 02	Hohenstoffeln	Ijolite	Ap	11.11	0.86	59	1.39
HEG 05	Hohenstoffeln	Ijolite	Prv	10.23	0.23	58	1.23
HEG 05	Hohenstoffeln	Ijolite	Ap	9.77	0.75	57	0.62
HEG 15	Neuhewen	Mll b. ON	Prv	11.67	0.38	34	1.15
GB-2	Gönnersbohl	Phonolite	Ap	12.83	0.95	29	0.71
GB-2	Gönnersbohl	Phonolite	Ttn	12.93	0.48	15	1.24
GB-2	Gönnersbohl	Syenite	Ap	11.85	1.95	30	0.83
GB-2	Gönnersbohl	Syenite	Ttn	11.60	1.35	28	1.18
2020-07	Gönnersbohl	Syenite	Ap	12.06	2.42	75	0.86
2020-07	Gönnersbohl	Syenite	Ttn	13.48	0.38	171	1.24
2020-07	Gönnersbohl	Syenite	Zrn	13.19	0.24	20	1.63
HK-2	Hohenkrähen	Phonolite	Ap	13.13	0.98	8	0.84
HK-2	Hohenkrähen	Phonolite	Ttn	12.77	0.32	25	1.17
HW 2a	Hohentwiel	Phonolite	Ap	12.70	0.65	30	0.85

Table 4 (continued)

Sample	Locality	Rock type	Mineral	Age (Ma)	±2σ	*n*	MSWD
HW 2a	Hohentwiel	Phonolite	Ttn	12.79	0.32	20	0.85
HW 2a	Hohentwiel	Phonolite	Zrn	12.91	0.21	24	0.90
MB-1	Mägdeberg	Phonolite	Ap	13.26	1.17	27	1.39
MB-1	Mägdeberg	Phonolite	Ttn	12.85	0.30	32	1.16
ST-1	Staufen	Phonolite	Ap	13.36	0.70	34	0.70
ST-1	Staufen	Phonolite	Ttn	12.35	0.30	31	1.41
HEG 09	Twiel SW, Elisabethenberg	Aug–Hbl–Phl tuff	Ap	12.49	1.57	47	1.18
H 7	Twiel SW, Elisabethenberg	Aug–Hbl–Phl tuff	Ap	14.51	1.11	30	1.13
HEG 06	Hohenstoffeln	NS	Ttn	13.56	0.46	43	0.80
HEG 06	Hohenstoffeln	NS	Zrn	14.43	1.20	7	0.38
N 248	2 km E Weil	NS	Pcl	11.79	0.34	31	1.54
N 248	2 km E Weil	NS	Zrn	12.85	0.32	16	1.62
E 403	2 km E Weil	NS	Pcl	12.42	0.32	26	0.84
E 403	2 km E Weil	NS	Zrn	12.90	0.24	44	1.70

b. bearing, *Aug* augite, *Bt* biotite, *Hbl* hornblende, *Hyn* haüyne, *Mll* melilite, *Nph* nepheline, *Ol* olivine, *Phl* phlogopite, *HM* haüyne melilitite, *MON* melilite olivine nephelinite, *NS* nepheline syenite, *OM* olivine melilitite, *ON* olivine nephelinite, *Ap* Apatite, *Pcl* pyrochlore, *Prv* perovskite, *Ttn* titanite, *Zrn* zircon, *n* number of measurement spots, *MSWD* mean squared weighted deviation

repeatedly stated hypothesis that volcanism at Urach was triggered by the Ries impact (e.g., Ring and Bolhar 2020) must be rejected, as several volcanic rocks (Table 4) and biostratigraphic evidence from Randeck maar sediments (14.8–17.0 Ma; Rasser et al. 2013) provide significantly older ages (Table 4) than the Ries impactites (e.g., $^{40}Ar/^{39}Ar$ age of 14.6 ± 0.2 Ma; Buchner et al. 2010). The igneous activity at Urach persisted ~ 7 Myr, significantly longer than the 2 Myr recently assumed by Kröchert et al. (2009) and Ring and Bolhar (2020). Towards the end of volcanism at Urach, relocation of magmatic activity from the northern to the southern tip of the Albstadt shear zone (Fig. 4) is expressed by phonolitic domes in the eastern Hegau (~ 14–11 Ma) and primitive melilititic to nephelinitic eruptions in the western Hegau (~ 12–9 Ma), representing the last magmatic signal in the southern CEVP. Age data from evolved nepheline syenitic xenoliths in tuffs and melilititic to nephelinitic rocks (~ 15–11 Ma) match those of the Hegau phonolites and syenitic autoliths therein. Thus, there is no age gap between the emplacement of primitive and evolved rocks, suggesting a close genetic relationship between both rock types and differentiation and storage processes over such time scales in the upper crust. The spatial separation of melilite-bearing nephelinites in the west and phonolites in the east may suggest that minor structural differences in the nature of the upper lithosphere led in some cases to prolonged stagnation and evolution in a magma chamber and in other cases to direct eruption. The ijolitic schlieren from the Hohenstoffeln are interpreted as in situ differentiation products accumulating and crystallizing from the surrounding magma, consistent with their identical age within the uncertainty compared to that of the nephelinitic host rock.

Chronological and petrographic relations within the CEVP

Compared to the northern part of the CEVP, where volcanic rocks are mostly represented by extensive polygenetic or diversely composed complexes and dyke swarms, those in the study area occur as small stocks, vents, or dykes either isolated (e.g., Taunus, Odenwald and Kraichgau area) or as larger fields (e.g., Urach, Hegau; Figs. 1 and 4, Table 1), with the Kaiserstuhl being a prominent exception. The northern volcanic rocks are only mildly SiO_2-undersaturated or SiO_2-saturated, forming basanitic to basaltic and more evolved rocks. Nevertheless, foidites and melilitites do occur as integral part of some volcanic regions in the northern CEVP such as Hessian Depression, Eifel, Rhön, Eger Graben, and Heldburg dyke swarm, too (Abratis et al. 2007, 2009, 2015; Büchner et al. 2015; Jung et al. 2006; Kramm and Wedepohl 1990; Mertz et al. 2015; Pfänder et al. 2018; Skála et al. 2015; Ulrych et al. 2016). Conversely, evolved rocks are rare in the study area, comprising phonolites in the eastern Hegau area, diverse Kaiserstuhl rocks, and trachytes in the Lower Main plain.

The age distribution for the northern and southern CEVP based on literature and our new data, disregarding K–Ar whole-rock ages (Fig. 8), indicates continuous volcanism since the middle Eocene at varying locations. In contrast to the southern part (Fig. 2), however, no obvious correlation between rock types and ages in the northern CEVP exists. The only evidence for late Cretaceous igneous activity in the northern CEVP are trachytic xenoliths and camptonitic dykes at the Vogelsberg, (~ 74–66 Ma; Bogaard and Wörner 2003; Martha et al. 2014; Schmitt et al. 2007). This

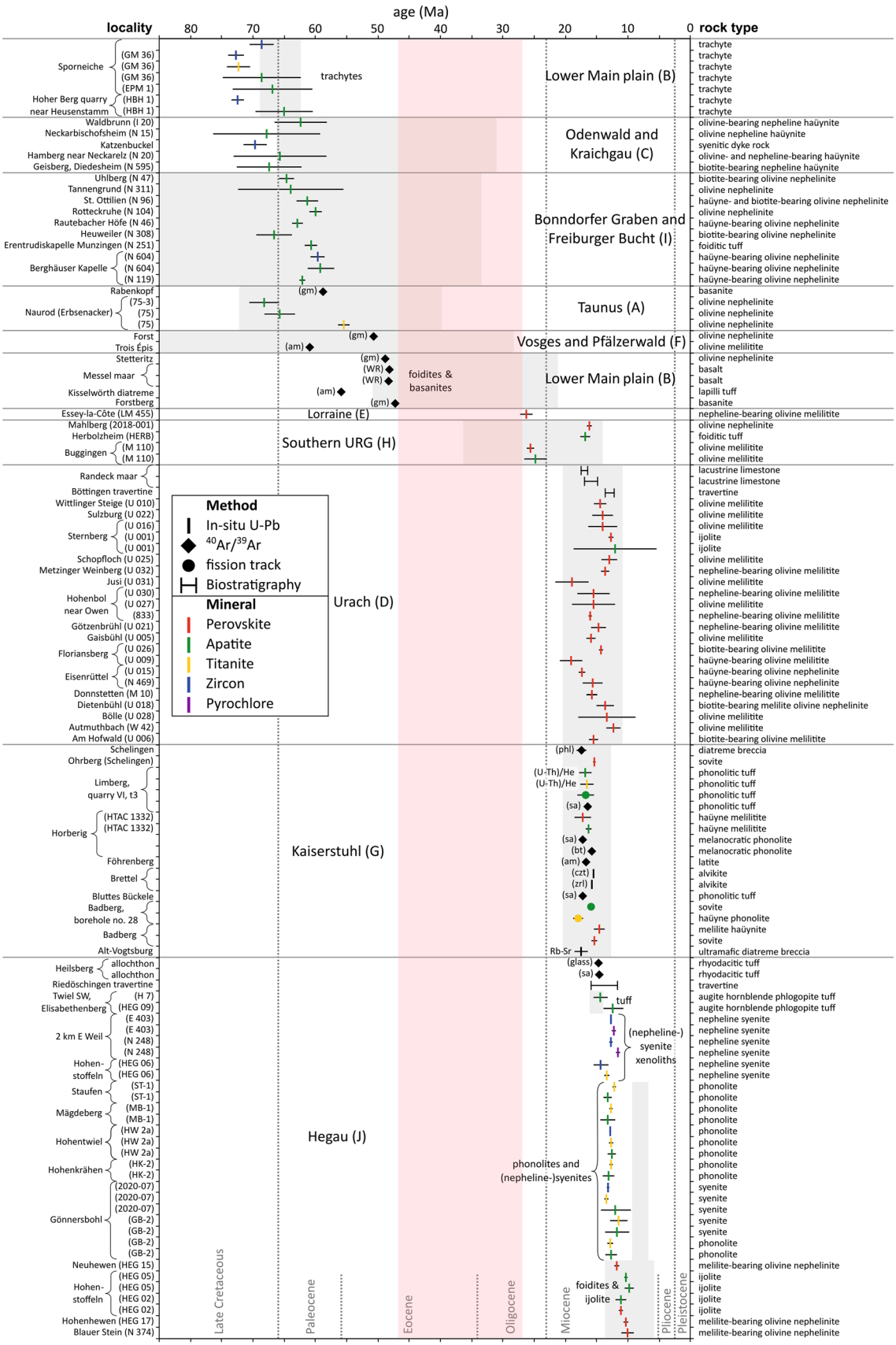
age (Ma)
locality
rock type
80
70
60
50
40
30
20
10
0
Sporneiche (GM 36) (GM 36) (GM 36)
Hoher Berg quarry near Heusenstamm (EPM 1) (HBH 1) (HBH 1)
trachytes
Lower Main plain (B)
trachyte
Waldbrunn (I 20)
Neckarbischofsheim (N 15)
Katzenbuckel
Hamberg near Neckarelz (N 20)
Geisberg, Diedesheim (N 595)
Odenwald and Kraichgau (C)
olivine-bearing nepheline haüynite
olivine nepheline haüynite
syenitic dyke rock
olivine- and nepheline-bearing haüynite
biotite-bearing nepheline haüynite
Uhlberg (N 47)
Tannengrund (N 311)
St. Ottilien (N 96)
Rotteckruhe (N 104)
Rautebacher Höfe (N 46)
Heuweiler (N 308)
Erentrudiskapelle Munzingen (N 251)
Berghäuser Kapelle (N 604) (N 604) (N 119)
Bonndorfer Graben and Freiburger Bucht (I)
biotite-bearing olivine nephelinite
olivine nephelinite
haüyne- and biotite-bearing olivine nephelinite
olivine nephelinite
haüyne-bearing olivine nephelinite
biotite-bearing olivine nephelinite
foiditic tuff
haüyne-bearing olivine nephelinite
haüyne-bearing olivine nephelinite
haüyne-bearing olivine nephelinite
Rabenkopf (gm)
Naurod (Erbsenacker) (75-3) (75) (75)
Taunus (A)
basanite
olivine nephelinite
olivine nephelinite
olivine nephelinite
Forst (gm)
Trois Épis (am)
Vosges and Pfälzerwald (F)
olivine nephelinite
olivine melilitite
Stetteritz (gm)
Messel maar (WR) (WR)
Kisselwörth diatreme (am)
Forstberg (gm)
foidites & basanites
Lower Main plain (B)
olivine nephelinite
basalt
basalt
lapilli tuff
basanite
Essey-la-Côte (LM 455)
Lorraine (E)
nepheline-bearing olivine melilitite
Mahlberg (2018-001)
Herbolzheim (HERB)
Buggingen (M 110) (M 110)
Southern URG (H)
olivine nephelinite
foiditic tuff
olivine melilitite
olivine melilitite
Randeck maar
Böttingen travertine
Wittlinger Steige (U 010)
Sulzburg (U 022)
Sternberg (U 016) (U 001) (U 001)
Schopfloch (U 025)
Metzinger Weinberg (U 032)
Jusi (U 031)
Hohenbol near Owen (U 030) (U 027) (833)
Götzenbrühl (U 021)
Gaisbühl (U 005)
Floriansberg (U 026) (U 009)
Eisenrüttel (U 015) (N 469)
Donnstetten (M 10)
Dietenbühl (U 018)
Bölle (U 028)
Autmuthbach (W 42)
Am Hofwald (U 006)
Urach (D)
lacustrine limestone
lacustrine limestone
travertine
olivine melilitite
olivine melilitite
olivine melilitite
ijolite
ijolite
olivine melilitite
nepheline-bearing olivine melilitite
olivine melilitite
nepheline-bearing olivine melilitite
olivine melilitite
nepheline-bearing olivine melilitite
nepheline-bearing olivine melilitite
olivine melilitite
biotite-bearing olivine melilitite
haüyne-bearing olivine melilitite
haüyne-bearing olivine nephelinite
haüyne-bearing olivine nephelinite
nepheline-bearing olivine melilitite
biotite-bearing melilite olivine nephelinite
olivine melilitite
olivine melilitite
biotite-bearing olivine melilitite
Method
In-situ U-Pb
40Ar/39Ar
fission track
Biostratigraphy
Mineral
Perovskite
Apatite
Titanite
Zircon
Pyrochlore
Schelingen
Ohrberg (Schelingen)
Limberg, quarry VI, t3
Horberg (HTAC 1332) (HTAC 1332)
Föhrenberg
Brettel
Bluttes Bückele
Badberg, borehole no. 28
Badberg
Alt-Vogtsburg
Kaiserstuhl (G)
(phl)
(U-Th)/He
(U-Th)/He
(sa)
(sa)
(bt)
(am)
(czt)
(zrl)
(sa)
Rb-Sr
diatreme breccia
sovite
phonolitic tuff
phonolitic tuff
phonolitic tuff
phonolitic tuff
haüyne melilitite
haüyne melilitite
melanocratic phonolite
melanocratic phonolite
latite
alvikite
alvikite
phonolitic tuff
sovite
haüyne phonolite
melilite haüynite
sovite
ultramafic diatreme breccia
Heilsberg allochthon allochthon
Riedöschingen travertine
Twiel SW, Elisabethenberg (H 7) (HEG 09)
2 km E Weil (E 403) (E 403) (N 248) (N 248)
Hohen-stoffeln (HEG 06) (HEG 06)
Staufen (ST-1) (ST-1)
Mägdeberg (MB-1) (MB-1)
Hohentwiel (HW 2a) (HW 2a) (HW 2a)
Hohenkrähen (HK-2) (HK-2)
Gönnersbohl (2020-07) (2020-07) (2020-07) (GB-2) (GB-2) (GB-2) (GB-2)
Neuhewen (HEG 15)
Hohen-stoffeln (HEG 05) (HEG 05) (HEG 02) (HEG 02)
Hohenhewen (HEG 17)
Blauer Stein (N 374)
Hegau (J)
(glass)
(sa)
tuff
(nepheline-) syenite xenoliths
phonolites and (nepheline-)syenites
foidites & ijolite
rhyodacitic tuff
rhyodacitic tuff
travertine
augite hornblende phlogopite tuff
augite hornblende phlogopite tuff
nepheline syenite
nepheline syenite
nepheline syenite
nepheline syenite
nepheline syenite
nepheline syenite
phonolite
phonolite
phonolite
phonolite
phonolite
phonolite
phonolite
phonolite
phonolite
syenite
syenite
syenite
syenite
syenite
phonolite
phonolite
melilite-bearing olivine nephelinite
ijolite
ijolite
ijolite
ijolite
melilite-bearing olivine nephelinite
melilite-bearing olivine nephelinite
Late Cretaceous
Paleocene
Eocene
Oligocene
Miocene
Pliocene
Pleistocene

◂**Fig. 7** Overview of all new in situ U–Pb age data amended by existing $^{40}Ar/^{39}Ar$, fission track, (U-Th)/He, Rb–Sr, and biostratigraphical results. The previous age distributions for the different regions based on old K–Ar age data are shown in light grey (Baranyi et al. 1976; Horn et al. 1972; Lippolt et al. 1963, 1973, 1975; Lippolt 1983). The current data indicates that there was no continuous primitive SiO_2-undersaturated volcanism in SW Germany and E France since the late Cretaceous, but two phases of activity separated by a middle Eocene to early Oligocene gap (shown in pink). This contrasts with previous K–Ar data. Age data from this work were supplemented with results from Aziz et al. (2010), Fekiacova et al. (2007), Ghobadi et al. (2021), Gregor (2003), Keller et al. (2002), Koban and Schweigert (1993), Kraml et al. (1995, 1999), Kraml et al. (2006), Lenz et al. (2015), Lutz et al. (2013), Rasser et al. (2013), Schleicher et al. (1990), Schmitt (2006a), Schmitt et al. (2007), and Wagner (1976). Note that for some $^{40}Ar/^{39}Ar$ and U–Pb ages, the published error range is smaller than the symbol size. *gm* groundmass, *WR* whole-rock, *am* amphibole, *phl* phlogopite, *sa* sanidine, *bt* biotite, *czt* calzirtite, *zrl* zirconolite

volcanic activity overlaps with the formation of trachytes in the Lower Main plain, haüyne-rich foidites in the Odenwald and Kraichgau area (Fig. 8), and an apatite inclusion age at Naurod (Taunus). The basaltic to nephelinitic rocks in the Lower Main plain and Pfälzerwald (~ 56–47 Ma) indicate the end of early magmatic activity in the southern CEVP.

In the Hocheifel region, basanites, basalts, and minor evolved rocks (latites, trachytes) erupted in the Eocene between ~ 45–35 Ma (Fekiacova et al. 2007; Mertz et al. 2000) and mark the beginning of Cenozoic magmatism in the northern CEVP. About 10 Myr later, trachytic tuffs were emplaced in the Osteifel (~ 25.5 Ma; Mertz et al. 2007). Subsequently, volcanic activity did not occur again in the Osteifel and in the Westeifel until the Quaternary (~ 760–10 ka; Mertz et al. 2015; Schmitt et al. 2017; Shaw et al. 2010; Singer et al. 2008; Sirocko et al. 2013; van den Bogaard 1995), producing both strongly SiO_2-undersaturated, primitive rocks such as basanites, tephrites, nephelinites, melilitites, and more evolved rocks like phonolite and trachytes, and minor carbonatites (Mertz et al. 2015; Schmitt et al. 2010; Sundermeyer et al. 2020; Wörner et al. 1986). Recurrent melilititic to nephelinitic volcanism formed parts of the Heldburg dyke swarm between ~ 38–25 Ma, complemented by basanites and a phonolite ~ 7 Myr later (~ 18–12 Ma; Abratis et al. 2007, 2015; Pfänder et al. 2018).

Basanites, alkaline basalts, and tholeiites formed throughout the Oligocene and the early Miocene in Lusatia (Eger Graben; ~ 35–27 Ma), the Siebengebirge (~ 31–22 Ma), the Westerwald (~ 25 Ma), the Rhön (24–18 Ma), and the Vogelsberg (~ 17–14 Ma), occasionally associated with latites, trachytes, and phonolites without a clear chronological sequence (Abratis et al. 2007; Bogaard et al. 2001; Büchner et al. 2015; Kolb et al. 2012; Linthout et al. 2009; Mayer et al. 2014; Mertz et al. 2007; Przybyla et al. 2018). Trachytic tuffs are also reported for the Wetterau in the northernmost Cenozoic successions of the URG (~ 26 Ma; Neuhaus 2010). Unlike the north, there is no evidence of volcanism in the southern CEVP for the middle Eocene to early Oligocene until sporadic eruptions of the second magmatic phase occurred ~ 26–25 Ma ago and were followed ~ 6 Myr later by recurrent, partly long-lasting volcanism at Urach, in the Kaiserstuhl, the southern URG, and the Hegau area (> 9 Ma), overlapping the Miocene activity of the Rhön, Vogelsberg, and Heldburg dyke swarm. In contrast to these regions, in the southern CEVP, mainly melilite-bearing nephelinites, melilitites, and subordinately basanites/tephrites, haüynites, phonolites, noseanites, and carbonatites (Kaiserstuhl, Hegau) were emplaced. The magmatic history coincides with increased hydrothermal activity around the URG (Walter et al. 2018) with U–Pb ages of hydrothermal carbonates indicating a late Cretaceous phase (~ 74–60 Ma) and a main Miocene to recent phase (< 20 Ma). However, increased hydrothermal activity from 40–28 Ma falls in a period of volcanic quiescence, and thus cannot be straightforwardly correlated with magmatism in the southern CEVP.

Pliocene volcanic rocks in Germany are only reported for the Westerwald, with a basanite dated to 5.0 ± 0.2 Ma (Schubert et al. 2015). Furthermore, a new phase of volcanic activity occurred in Lusatia in the Pleistocene (~ 370–170 ka; Mrlina et al. 2007; Wagner et al. 1998), coinciding with the Eifel volcanism. In the French Massif Central (~ 14 Ma–5 ka) and the Pannonian Basin (~ 18.5 Ma–8 ka), on the other hand, the main phase of volcanism dates back to the middle Miocene and has continued with short interruptions until today, the spectrum of erupted magmas ranging from basanites to rhyolites (Harangi et al. 2010, 2015; Hurai et al. 2013; Lexa et al. 2010; Lukács et al. 2018; Molnár et al. 2019; Nowell et al. 2006; Riisager et al. 2000; Seghedi and Downes 2011; Wijbrans et al. 2007).

Considering the entire CEVP, there are no obvious correlations between spatial, compositional, and temporal evolution of volcanism like propagating hot-spot tracks that would support a plume-like mantle anomaly (Lustrino and Wilson 2007). Although thermal asthenospheric upwelling cannot be ruled out as driving force, the most striking differences of the southern CEVP compared to the northern one, i.e., the ~ 20 Ma age gap, the more pronounced SiO_2-undersaturation of the rocks, and the usually monogenetic character, indicate a structural control on the occurrence of volcanism linked to the geodynamic evolution of Europe. However, there are some spatial variations at same times and temporal variations within same areas. For instance, in some regions with bimodal or polygenetic volcanism, primitive rocks follow more differentiated ones and/or strongly SiO_2-undersaturated rocks follow less SiO_2-undersaturated or SiO_2-saturated ones (e.g., Hegau, Vogelsberg; this study; Bogaard and Wörner 2003), sometimes vice versa (e.g., Heldburg; Abratis et al. 2015;

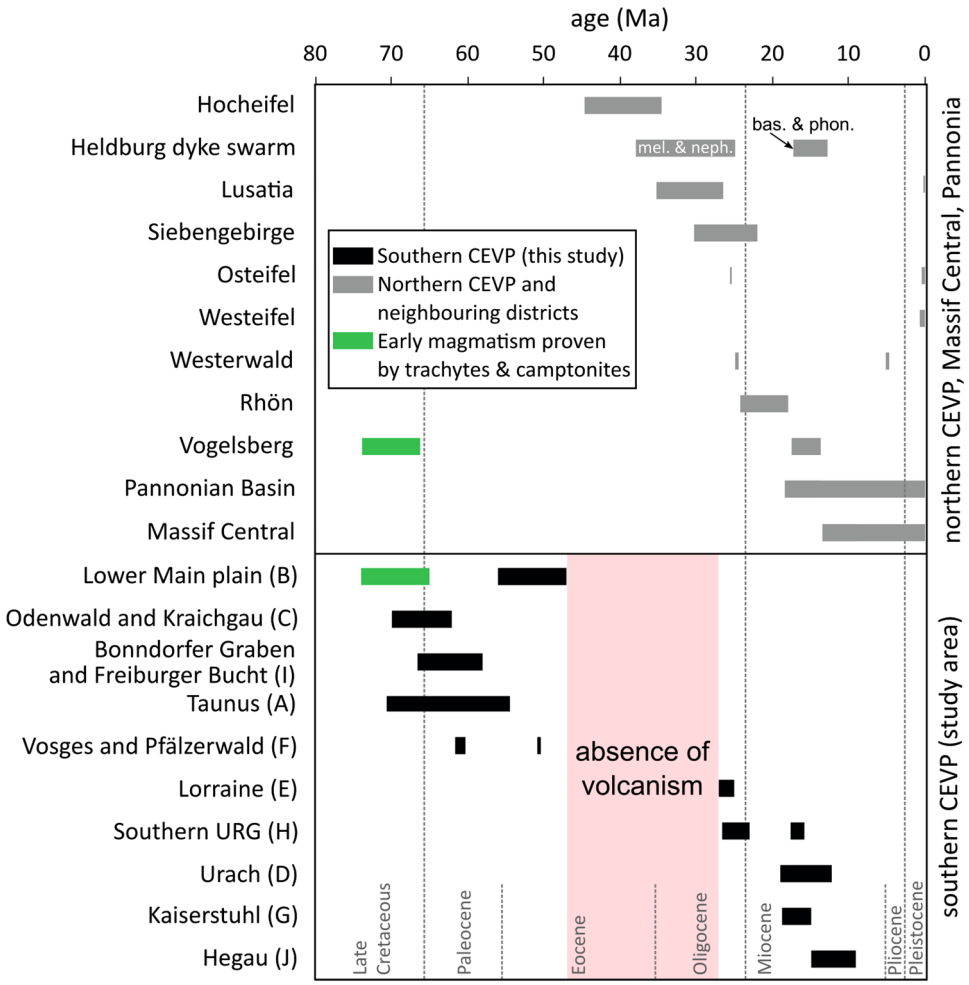

Fig. 8 Age distribution of igneous rocks in the Central European Volcanic Province. The data of this work are amended by literature data (except for K–Ar data; Abratis et al. 2007; Aziz et al. 2010; Büchner et al. 2015; Fekiacova et al. 2007; Ghobadi et al. 2021; Gregor 2003; Harangi et al. 2010; Harangi et al. 2015; Hurai et al. 2013; Keller et al. 2002; Koban and Schweigert 1993; Kraml et al. 1995, 1999; Kraml et al. 2006; Lenz et al. 2015; Lexa et al. 2010; Linthout et al. 2009; Lukács et al. 2018; Lutz et al. 2013; Mayer et al. 2014; Mertz et al. 2000; Mertz et al. 2007; Mertz et al. 2015; Molnár et al. 2019; Nowell et al. 2006; Pfänder et al. 2018; Przybyla et al. 2018; Rasser et al. 2013; Riisager et al. 2000; Schleicher et al. 1990; Schmitt 2006a; Schmitt et al. 2007; Schubert et al. 2015; Shaw et al. 2010; Singer et al. 2008; van den Bogaard 1995; Wagner 1976; Wagner et al. 1998; Wijbrans et al. 2007). Continuous magmatism throughout the province can be traced back to the late Cretaceous. However, primitive, strongly SiO_2-undersaturated volcanism in the southern CEVP is restricted to two periods: from the late Cretaceous to the early Eocene and from the late Oligocene to the late Miocene. *mel.* melilitites, *neph.* nephelinites, *bas.* basanites, *phon.* phonolites

Pfänder et al. 2018), and sometimes with age gaps as in the Eifel (Lustrino and Wilson 2007). In other regions, primitive rocks follow more differentiated ones, in turn succeeding primitive rocks (Büchner et al. 2015; Przybyla et al. 2018; Ulrych et al. 2011, 2013, 2016). Such compositional sequences have been attributed to pre-, syn-, and post-rift stages (e.g., Eger Graben; Ulrych et al. 2011), differentiation due to magmatic plumbing systems (e.g., Siebengebirge; Przybyla et al. 2018), and/or different sources and depths of melt generation (e.g., Heldburg region, Kaiserstuhl, Eger Graben; Braunger et al. 2018; Ghobadi et al. 2021; Pfänder et al. 2018; Ulrych et al. 2016). Likewise in the southern CEVP, the high temporal, spatial, and compositional variability of the individual regions on the one hand, and the compositional similarities of coeval occurrences on the other hand, refer to heterogeneities in the sub-lithospheric mantle beneath Central Europe (Puziewicz et al. 2020). The temporal trend for primitive rocks in the southern CEVP from melilite-free nephelinitic–basanitic rocks to melilite-bearing olivine nephelinites and olivine melilitites may indicate decreasing partial melting degrees, greater formation depths, a thicker lithosphere, a more carbonate-accentuated source, and/or a reduced influence of assimilation and fractional crystallization for the latter (e.g., Bogaard and Wörner

2003; Dunworth and Wilson 1998; Jung et al. 2006; Pfänder et al. 2018).

Implications for the geological evolution in the southern CEVP area

The older volcanic rocks of the southern CEVP (~ 73–47 Ma) postdate the late Cretaceous (~ 95–75 Ma) inversion tectonics in Central Europe (Voigt et al. 2021) and predate Upper Rhine Graben formation (< 47 Ma; Grimmer et al. 2017). Late Cretaceous to early Eocene volcanic activity in the southern CEVP overlaps in time with the ~ 75–55 Ma topographic uplift in Central Germany (Eynatten et al. 2021). The late Cretaceous inversion and the late Cretaceous to Eocene doming and respective magnitudes of shortening and uplift in the southern CEVP area are yet—due to the lack of Cretaceous sedimentary rocks—only inferred from apatite fission track and U–Th/He thermochronological data from the rift flanks of the URG (Link 2010). Time–temperature modeling of apatite fission track length distributions indicates late Cretaceous rapid cooling of crystalline basement rocks along both the western and eastern rift flanks of the URG (Link 2010), similarly to what documented in the Odenwald, Harz, and Thüringer Wald (Wagner et al. 1989; Eynatten et al. 2019, 2021; Thomson and Zeh 2000). A major portion of apatite fission track data in the Schwarzwald and Odenwald displays late Cretaceous to Eocene ages predating rift-related Cenozoic uplift and cooling (e.g., Link 2010; Wagner et al. 1989). A well-defined erosional angular unconformity recording a > 100 Myr hiatus in the subcrop of the URG documents this pre-Eocene uplift and erosion (e.g., Grimmer et al., 2017). In the northern URG, removal of the entire Mesozoic succession indicates that a zone of major uplift was probably located in the Taunus–Odenwald area, where numerous late Cretaceous to early Eocene volcanic rocks are documented as well. The dynamic topography concept of Eynatten et al. (2021) considers that thermally induced uplift of the lithosphere–asthenosphere boundary (LAB) and regional-scale doming terminated the late Cretaceous inversion at ~ 75 Ma in Central Germany. On the other hand, SW–NE shortening was probably ongoing until ~ 42 Ma along the western European continental margin (> 1000 km to the NW in Ireland), as indicated by calcite twinning analysis (Craddock et al. 2022). Eynatten et al. (2021) suggest that late Cretaceous to Eocene LAB uplift caused a dynamic topography of ~ 1 km and concomitant erosion of up to ~ 4 km. The formation of low-percentage melts that translocated to upper crustal levels appears to be controlled by interfering processes such as LAB shallowing and decompression, metasomatism, and deep-rooted faults such as the URG boundary fault system and the Albstadt shear zone. Dynamic topography can be induced by either convection-induced LAB uplift and subsequent cooling (or an abatement of LAB shallowing) or by translocation of continental lithosphere over upward convecting asthenospheric domains (e.g., Braun et al. 2013). Domal uplift terminated late Cretaceous shortening at ~ 75 Ma in western Central Europe. Late Cretaceous to early Eocene volcanic rocks occur around and possibly in the subcrop of the northern URG, where major uplift is considered for the Odenwald and southern Taunus, but also in the southern Schwarzwald (Bonndorfer Graben and Freiburger Bucht; Figs. 1 and 8; Table 3). Dykes strike NW, N, and NE as documented from maps, geophysical anomalies, and field observations (e.g., Mäussnest 1975; Stellrecht and Emmermann 1970). The ~ 47–27 Ma volcanic age gap temporarily overlaps with the early Eocene to Oligocene syn-rift phase of the URG during (W)NW-extension (e.g., Schumacher 2002).

A major change in deformation characterized by (E)NE-trending extension and transtension is considered to have started ~ 18 Ma (Schumacher 2002) or earlier (~ 25 Ma; Grimmer et al. 2017), associated with major activity of the NNW-trending Ludwigshafen hinge zone and the onset of distinct early Miocene subsidence of the Heidelberg basin (e.g., Grimmer et al. 2017). U–Pb ages of calcite fibers from NNE-trending Alpenrhein graben boundary faults yield 25.3 ± 5.6 Ma to 21.8 ± 3.4 Ma, interpreted with the initial phase of graben formation postdating Helvetic nappe emplacement (Ring and Gerdes 2016). The NNE-trending phonolitic Heldburg dyke (Fig. 1), yielding 17–14 Ma ($^{40}Ar/^{39}Ar$-ages; Abratis et al. 2015), and U–Pb ages of NW-striking calcite veins of 15.3–2.3 Ma from Miocene domal uplift (Ring and Bolhar 2020) indicate that (E)NE-extension was initiated at that time and persisted during Miocene domal uplift, volcanism, and erosion, and hence throughout the Neogene. Apparent conformable sedimentation in the URG from ~ 47 Ma to ~ 18–16 Ma was interrupted by uplift and erosion, resulting in a rift-wide, angular unconformity that separates conformably deposited older graben filling sediments in the footwall from younger, i.e., Pliocene to Quaternary graben fillings (e.g., Grimm 2011). The late Oligocene to late Miocene volcanic activity (~ 27–9 Ma; Table 4) temporarily overlaps with middle to late Miocene domal uplift in the southern CEVP as documented by the Burdigalian cliff (~ 20–18 Ma) elevated to > 900 m a.s.l. in the WSW and to < 400 m a.s.l. in the ENE of the Swabian Alb (Hoffmann 2017; Fig. 4), and by Miocene apatite fission track data in the southern Schwarzwald (Timar-Geng et al. 2006). East of the southern Schwarzwald, the Upper Miocene younger Juranagelfluh in the Hegau area comprises a late Miocene unroofing sequence, documenting erosion of an uplifted area in the W to NW of the Hegau area (Schreiner 1965). Dykes and elongated plugs show variable trends in the Hegau and Urach areas (e.g., Mäussnest 1974), indicating that pre-existing, shallow-rooted structures were used for the emplacement of melts, either locally along pre-existing

structures or during variations between strike-slip and normal faulting in the northern foreland of the Alps (Egli et al. 2017; Grimmer et al. 2017; Ring & Bolhar 2020; Craddock et al. 2022). In summary, though several details and processes still need to be clarified and quantified, it appears that since ~ 75–70 Ma dynamic topography has exerted major control on deformation, structural, and sedimentological development of the URG area and correlates temporally with the volcanic activity in the southern CEVP until today.

Conclusion

Based on new U–Pb mineral ages (perovskite, apatite, titanite, zircon, pyrochlor) for volcanic rocks and related plutonic inclusions from nine regions in the southern CEVP and complemented by existing age data, two distinct periods of volcanism are identified, with an age gap of ~ 20 Ma in between: a late Cretaceous to early Eocene (~ 73–47 Ma) group and a late Oligocene to late Miocene (~ 27–9 Ma) group. These two groups also differ in terms of mineralogy and spatial distribution coinciding with topographically uplifted areas. The older group occurs in the Lower Main plain, the Odenwald and Kraichgau area, the Taunus, the Bonndorfer Graben and Freiburger Bucht area, the Vosges and the Pfälzerwald and mostly comprises nephelinites, basanites, haüynites, and trachytes. The young group is mainly represented by perovskite-bearing olivine melilitites, melilite-bearing olivine nephelinites, and phonolites of Lorraine, the southern URG, Urach, and the Hegau area. As an exception, the Kaiserstuhl comprises basanites, tephrites, melilitites, nephelinites, haüynites, carbonatites, phonolites, and noseanites, all of which are of Miocene age.

Magmatism in both periods is linked to dynamic topography and the tectonic evolution in Central Europe, expressed in its age and location, reflecting large-scale stress field changes in the interplay of Pyrenean and Alpine orogeny interrupted by phases of subsidence causing a volcanic hiatus. The older volcanic rocks tend to occur in or along NE–SW striking structures and/or in the periphery of or on the shoulders of present-day graben structures (Fig. 4). They postdate late Cretaceous inversion tectonics (NE shortening; > 73 Ma) and, together with erosion of Permo-Mesozoic units, possibly reflect late Cretaceous to Eocene doming, shortening and uplift in the southern CEVP. The temporal and spatial coincidence of the 47–27 Ma volcanic gap with the initial phase of the URG development suggests a lithosphere-scale event such as cooling-induced regional subsidence and/or an abatement of asthenospheric uplift following the 75–55 Ma period considered for dynamic topography in Central Germany. The younger volcanic rocks are bound to Cenozoic N–S striking fault zones that developed with the ongoing formation of the ECRiS during Neogene (E) NE-extension–transtension (< 25 Ma). Again, this partly coincides with doming, uplift, and erosion in the southern CEVP and the URG from the middle to late Miocene, followed by subsidence during the Pliocene and Quaternary.

Evolved phonolites and (nepheline) syenite xenoliths in the melilite-bearing nephelinites of the Hegau area show that felsic alkaline magmatism beneath the Hegau area was already active before ~ 15 Ma, predating the first melilititic to nephelinitic eruptions (~ 12 Ma ago). The onset of volcanism is possibly related to the simultaneous attenuation, extinction, and relocation of Urach volcanic activity (19–12 Ma) at the northern tip of the Albstadt shear zone. Volcanism at Urach was not caused by the Ries impact (14.6 ± 0.2 Ma).

Magmatism in the northern part of the CEVP differs from the igneous activity in the southern sectors studied here. The generally mildly SiO_2-undersaturated volcanic rocks of the northern CEVP cover larger areas mostly forming voluminous, diversely composed complexes and are often more evolved than the isolated and low-volume, primitive nephelinites and melilitites in the southern CEVP. Even though volcanism in the northern CEVP has been recurrently active since the middle Eocene and the 20 Myr gap is absent, some temporal parallels with activity in the southern CEVP are apparent. Altogether, a spatial heterogeneous sub-lithospheric mantle source, varying lithospheric and crustal thicknesses, different depths of melt formation and degrees of partial melting, differentiation processes, and crustal contamination combined with the tectonic evolution in Central Europe can explain the different compositions of volcanic rocks and the magmatic evolution in the CEVP. The petrography and new age data do not provide evidence for a large-scale and deep-routed active asthenospheric upwelling beneath Central Europe. However, to delimit, determine, and describe these possible causes more precisely, detailed geochemical and petrological studies are in progress.

Supplementary Information The online version contains supplementary material available at https://doi.org/10.1007/s00531-022-02278-y.

Acknowledgements We thank Simone Schafflick, Philip Werner, and Alexander Rettenberger for sample preparation (University of Tübingen). We also thank Horst Marschall and Peter Prinz-Grimm (Goethe University Frankfurt) as well as Udo Neumann (University of Tübingen), D. Nesbor, L. Behr (HLNUG) and Kirsten Grimm (University of Mainz) for providing samples used in this study. We would especially like to thank Cyrille Delange and Luc Jaillard (Terrae Genesis) and Klaus Brauch (terratec Geophysical Services), who contributed with sampling in the field for us. Constructive comments by Dr. Jörg A. Pfänder, an anonymous reviewer, and the Editor-in-Chief Dr. Ulrich Riller greatly improved the manuscript and are gratefully acknowledged. FIERCE would like to acknowledge the financial support by the Wilhelm and Else Heraeus Foundation and the Deutsche Forschungsgemeinschaft (DFG). This is FIERCE contribution No. 117.

Author contributions Writing—original draft: TB, JG, AB. Writing—review and editing: MAWM, GM, TB, BFW, JG, TW. Visualization: TB. Investigation: TB, AG, AB, TW. Formal analysis: AB, AG, TB,

TW. Validation: AG. Conceptualization: MAWM, GM, TB. Project administration: GM, MAWM. Resources: GM, AG. Funding acquisition: MAWM, BFW, GM. Supervision: GM.

Funding Open Access funding enabled and organized by Projekt DEAL. This work was funded by the Deutsche Forschungsgemeinschaft (DFG)—Grant MA 2563/19 and WA 3116/6.

Data availability All research data are provided in Supplemental Information of the online version.

Declarations

Conflict of interest The authors declare that they have no known competing financial interests or personal relationships that could have appeared to influence the work reported in this paper.

References

Abratis M, Mädler J, Hautmann S, Leyk H-J, Meyer R, Lippolt HJ, Viereck-Götte L (2007) Two distinct Miocene age ranges of basaltic rocks from the Rhön and Heldburg areas (Germany) based on $^{40}Ar/^{39}Ar$ step heating data. Geochemistry 67(2):133–150. https://doi.org/10.1016/j.chemer.2006.03.003

Abratis M, Munsel D, Viereck-Götte L (2009) Melilithite und Melilithführende Magmatite des sächsischen Vogtlands: petrographie und Mineralchemie. Z Geol Wiss 37(1–2):41–79

Abratis M, Viereck L, Pfänder JA, Hentschel R (2015) Geochemical composition, petrography and $^{40}Ar/^{39}Ar$ age of the Heldburg phonolite: implications on magma mixing and mingling. Int J Earth Sci (geol Rundsch) 104(8):2033–2055. https://doi.org/10.1007/s00531-015-1207-x

Albers M, Christensen UR (1996) The excess temperature of plumes rising from the core-mantle boundary. Geophys Res Lett 23(24):3567–3570. https://doi.org/10.1029/96GL03311

Aziz HA, Böhme M, Rocholl A, Prieto J, Wijbrans JR, Bachtadse V, Ulbig A (2010) Integrated stratigraphy and $^{40}Ar/^{39}Ar$ chronology of the early to middle Miocene Upper Freshwater Molasse in western Bavaria (Germany). Int J Earth Sci (geol Rundsch) 99(8):1859–1886. https://doi.org/10.1007/s00531-009-0475-8

Baranyi I, Lippolt HJ, Todt W (1976) Kalium-Argon-Altersbestimmungen an tertiären Vulkaniten des Oberrheingraben-Gebietes: II Die Alterstraverse vom Hegau nach Lothringen. Oberrh Geol Abh 25(1):41–62

Blusztajn J, Hegner E (2002) Osmium isotopic systematics of melilitites from the Tertiary Central European Volcanic Province in SW Germany. Chem Geol 189(1–2):91–103. https://doi.org/10.1016/S0009-2541(02)00143-2

Bogaard PJF, Wörner G, Henjes-Kunst F (2001) Chemical stratigraphy and origin of volcanic rocks from the drill-core "Forschungsbohrung Vogelsberg 1996". In: Hoppe A, Schulz R (eds) Die Forschungsbohrung Vogelsberg 1996. Einblicke in einen miozänen Vulkankomplex, vol 107, Wiesbaden, pp 69–99

Bogaard PJF, Wörner G (2003) Petrogenesis of Basanitic to Tholeiititic Volcanic Rocks from the Miocene Vogelsberg. Central Germany J Petrol 44(3):569–602. https://doi.org/10.1093/petrology/44.3.569

Braun J, Robert X, Simon-Labric T (2013) Eroding dynamic topography. Geophys Res Lett 40(8):1494–1499. https://doi.org/10.1002/grl.50310

Braunger S, Marks MAW, Walter BF, Neubauer R, Reich R, Wenzel T, Parsapoor A, Markl G (2018) The Petrology of the Kaiserstuhl Volcanic Complex, SW Germany: the Importance of Metasomatized and Oxidized Lithospheric Mantle for Carbonatite Generation. J Petrol 59(9):1731–1762. https://doi.org/10.1093/petrology/egy078

Buchner E, Schwarz WH, Schmieder M, Trieloff M (2010) Establishing a 14.6 ± 0.2 Ma age for the Nördlinger Ries impact (Germany)—a prime example for concordant isotopic ages from various dating materials. Meteorit Planet Sci 45(4):662–674. https://doi.org/10.1111/j.1945-5100.2010.01046.x

Büchner J, Tietz O, Viereck L, Suhr P, Abratis M (2015) Volcanology, geochemistry and age of the Lausitz Volcanic Field. Int J Earth Sci (geol Rundsch) 104(8):2057–2083. https://doi.org/10.1007/s00531-015-1165-3

Carlson RW (2019) Absolute age determinations: radiometric. In: Gupta HK (eds) Encyclopedia of solid earth geophysics. Encyclopedia of Earth Sciences Series. Springer, Cham, pp 1–8. https://doi.org/10.1007/978-3-030-10475-7_69-1

Chew DM, Spikings RA (2015) Geochronology and thermochronology using apatite: time and temperature, lower crust to surface. Elements 11(3):189–194. https://doi.org/10.2113/gselements.11.3.189

Craddock JP, Ring U, Pfiffner OA (2022) Deformation of the European Plate (58–0 Ma): evidence from Calcite Twinning Strains. Geosciences 12(6):254. https://doi.org/10.3390/geosciences12060254

Dahl PS (1997) A crystal-chemical basis for Pb retention and fission-track annealing systematics in U-bearing minerals, with implications for geochronology. Earth Planet Sci Lett 150(3–4):277–290. https://doi.org/10.1016/S0012-821X(97)00108-8

Dèzes P, Schmid SM, Ziegler PA (2004) Evolution of the European Cenozoic Rift System: interaction of the Alpine and Pyrenean orogens with their foreland lithosphere. Tectonophysics 389(1–2):1–33. https://doi.org/10.1016/j.tecto.2004.06.011

Duda A, Schmincke H-U (1985) Polybaric differentiation of alkali basaltic magmas: evidence from green-core clinopyroxenes (Eifel, FRG). Contrib Mineral Petrol 91(4):340–353. https://doi.org/10.1007/BF00374690

Dunworth EA, Wilson M (1998) Olivine Melilitites of the SW German Tertiary Volcanic Province: mineralogy and Petrogenesis. J Petrol 39(10):1805–1836. https://doi.org/10.1093/petroj/39.10.1805

Egli D, Mosar J, Ibele T, Madritsch H (2017) The role of precursory structures on Tertiary deformation in the Black Forest—Hegau region. Int J Earth Sci (geol Rundsch) 106(7):2297–2318. https://doi.org/10.1007/s00531-016-1427-8

Fekiacova Z, Mertz DF, Renne P (2007) Geodynamic Setting of the Tertiary Hocheifel Volcanism (Germany), Part I: $^{40}Ar/^{39}Ar$ geochronology. In: Ritter JR, Christensen UR (eds) Mantle Plumes A Multidisciplinary Approach, 1st edn. Springer, Berlin, pp 185–206. https://doi.org/10.1007/978-3-540-68046-8_6

Fichtner A, Villaseñor A (2015) Crust and upper mantle of the western Mediterranean—constraints from full-waveform inversion. Earth Planet Sci Lett 428:52–62. https://doi.org/10.1016/j.epsl.2015.07.038

Flowers RM, Shuster DL, Wernicke BP, Farley KA (2007) Radiation damage control on apatite (U-Th)/He dates from the Grand Canyon region. Colorado Plateau Geol 35(5):447. https://doi.org/10.1130/G23471A.1

Frenzel G (1975) Die Nephelingesteinsparagenese des Katzenbuckels im Odenwald. Aufschluß Sonderband 27:213–228

Gerdes A, Zeh A (2006) Combined U-Pb and Hf isotope LA-(MC-) ICP-MS analyses of detrital zircons: Comparison with SHRIMP and new constraints for the provenance and age of an Armorican metasediment in Central Germany. Earth Planet Sci Lett 249(1–2):47–61. https://doi.org/10.1016/j.epsl.2006.06.039

Gerdes A, Zeh A (2009) Zircon formation versus zircon alteration—new insights from combined U-Pb and Lu–Hf in-situ LA-ICP-MS analyses, and consequences for the interpretation of Archean zircon from the Central Zone of the Limpopo Belt. Chem Geol 261(3–4):230–243. https://doi.org/10.1016/j.chemgeo.2008.03.005

Ghobadi M, Brey GP, Gerdes A, Höfer HE, Keller J (2021) Accessories in Kaiserstuhl carbonatites and related rocks as accurate and faithful recorders of whole rock age and isotopic composition. Int J Earth Sci (geol Rundsch). https://doi.org/10.1007/s00531-021-02130-9

Goes S, Spakman W, Bijwaard H (1999) A lower mantle source for central european volcanism. Science 286(5446):1928–1931. https://doi.org/10.1126/science.286.5446.1928

Granet M, Wilson M, Achauer U (1995) Imaging a mantle plume beneath the French Massif Central. Earth Planet Sci Lett 136(3–4):281–296. https://doi.org/10.1016/0012-821X(95)00174-B

Gregor H-J (2003) Miocene macroflora of Randecker Maar (Germany). PANGAEA. https://doi.org/10.1594/PANGAEA.104847

Griesshaber E, O'Nions RK, Oxburgh ER, (1992) Helium and carbon isotope systematics in crustal fluids from the Eifel, the Rhine Graben and Black Forest, F.R.G. Chem Geol 99(4):213–235. https://doi.org/10.1016/0009-2541(92)90178-8

Grimm KI (2011) Stratigraphie von Deutschland IX. Tertiär, Teil 1: Oberrheingraben und benachbarte Tertiärgebiete. Schriftenreihe der Deutschen Gesellschaft für Geowissenschaften, vol 75. Schweizerbart, Stuttgart

Grimmer JC, Ritter JRR, Eisbacher GH, Fielitz W (2017) The Late Variscan control on the location and asymmetry of the Upper Rhine Graben. Int J Earth Sci (geol Rundsch) 106(3):827–853. https://doi.org/10.1007/s00531-016-1336-x

Haase KM, Goldschmidt B, Garbe-Schönberg C-D (2004) Petrogenesis of Tertiary continental Intra-plate Lavas from the Westerwald Region. Germany J Petrol 45(5):883–905. https://doi.org/10.1093/petrology/egg115

Harangi S, Molnár M, Vinkler AP, Kiss B, Jull AJT, Leonard AG (2010) Radiocarbon dating of the last volcanic eruptions of Ciomadul Volcano, southeast Carpathians. Eastern-Central Europe Radiocarb 52(3):1498–1507. https://doi.org/10.1017/S0033822200046580

Harangi S, Lukács R, Schmitt AK, Dunkl I, Molnár K, Kiss B, Seghedi I, Novothny Á, Molnár M (2015) Constraints on the timing of Quaternary volcanism and duration of magma residence at Ciomadul volcano, east–central Europe, from combined U-Th/He and U–Th zircon geochronology. J Volcanol Geotherm Res 301:66–80. https://doi.org/10.1016/j.jvolgeores.2015.05.002

Harmon RS, Hoefs J, Wedepohl KH (1987) Stable isotope (O, H, S) relationships in Tertiary basalts and their mantle xenoliths from the Northern Hessian Depression, W. Germany. Contrib Mineral Petrol 95(3):350–369. https://doi.org/10.1007/BF00371849

Heaman L, Parrish RR (1991) U-Pb geochronology on accessory minerals. In: Ludden JN (ed) Heaman L. Applications of radiogenic isotope systems to problems in geology, Toronto, pp 59–102

Hegner E, Vennemann TW (1997) Role of fluids in the origin of Tertiary European intraplate volcanism: Evidence from O, H, and Sr isotopes in melilitites. Geol 25(11):1035. https://doi.org/10.1130/0091-7613(1997)025%3c1035:ROFITO%3e2.3.CO;2

Hegner E, Walter HJ, Satir M (1995) Pb-Sr-Nd isotopic compositions and trace element geochemistry of megacrysts and melilitites from the Tertiary Urach volcanic field: source composition of small volume melts under SW Germany. Contrib Mineral Petrol 122(3):322–335. https://doi.org/10.1007/s004100050131

Heidbach O, Custodio S, Kingdon A, Mariucci MT, Montone P, Müller B, Pierdominici S, Rajabi M, Reinecker J, Reiter K, Tingay M, Williams J, Ziegler M (2016) Stress map of the mediterranean and central Europe 2016. GFZ Data Services. https://doi.org/10.5880/WSM.Europe2016

Hoffmann M (2017) Young tectonic evolution of the Northern Alpine Foreland Basin, southern Germany, based on linking geomorphology and structural geology, Dissertation, Ludwig Maximilian University of Munich. https://edoc.ub.uni-muenchen.de/21123/1/Hoffmann_Markus.pdf

Horn P, Lippolt HJ, Todt W (1972) Kalium-Argon-Altersbestimmungen an tertiären Vulkaniten des Oberrheingrabens. Teil I, Gesamtgesteinsalter. Eclogae Geol Helv 65(1):131–156

Horstwood MSA, Košler J, Gehrels G, Jackson SE, McLean NM, Paton C, Pearson NJ, Sircombe K, Sylvester P, Vermeesch P, Bowring JF, Condon DJ, Schoene B (2016) Community-derived standards for LA-ICP-MS U-(Th-)Pb geochronology—uncertainty propagation, age interpretation and data reporting. Geostand Geoanal Res 40(3):311–332. https://doi.org/10.1111/j.1751-908X.2016.00379.x

Hurai V, Danišík M, Huraiová M, Paquette J-L, Ádám A (2013) Combined U/Pb and (U–Th)/He geochronometry of basalt maars in Western Carpathians: implications for age of intraplate volcanism and origin of zircon metasomatism. Contrib Mineral Petrol 166(4):1235–1251. https://doi.org/10.1007/s00410-013-0922-1

Hurrle H (1976) Ocelli- und Mandelbildung der ultrabasischen Basalte im Kalisalzlager Buggingen und im Kristallin des Schwarzwaldes. Jahresh Geol Landesamt Baden-Wurtt 18:19–37

Jackson SE, Pearson NJ, Griffin WL, Belousova EA (2004) The application of laser ablation-inductively coupled plasma-mass spectrometry to in situ U-Pb zircon geochronology. Chem Geol 211(1–2):47–69. https://doi.org/10.1016/j.chemgeo.2004.06.017

Jung S, Hoernes S (2000) The major- and trace-element and isotope (Sr, Nd, O) geochemistry of Cenozoic alkaline rift-type volcanic rocks from the Rhön area (central Germany): petrology, mantle source characteristics and implications for asthenosphere–lithosphere interactions. J Volcanol Geotherm Res 99(1–4):27–53. https://doi.org/10.1016/S0377-0273(00)00156-6

Jung S, Pfänder JA, Brügmann G, Stracke A (2005) Sources of primitive alkaline volcanic rocks from the Central European Volcanic Province (Rhön, Germany) inferred from Hf, Os and Pb isotopes. Contrib Mineral Petrol 150(5):546–559. https://doi.org/10.1007/s00410-005-0029-4

Jung C, Jung S, Hoffer E, Berndt J (2006) Petrogenesis of Tertiary Mafic Alkaline Magmas in the Hocheifel. Germany J Petrol 47(8):1637–1671. https://doi.org/10.1093/petrology/egl023

Jung S, Pfänder JA, Brauns M, Maas R (2011) Crustal contamination and mantle source characteristics in continental intra-plate volcanic rocks: Pb, Hf and Os isotopes from central European volcanic province basalts. Geochim Cosmochim Acta 75(10):2664–2683. https://doi.org/10.1016/j.gca.2011.02.017

Jung S, Mezger K, Hauff F, Pack A, Hoernes S (2013) Petrogenesis of rift-related tephrites, phonolites and trachytes (Central European Volcanic Province, Rhön, FRG): Constraints from Sr, Nd, Pb and O isotopes. Chem Geol 354:203–215. https://doi.org/10.1016/j.chemgeo.2013.06.026

Keller J, Kraml M, Henjes-Kunst F (2002) $^{40}Ar/^{39}Ar$ single crystal laser dating of early volcanism in the Upper Rhine Graben and tectonic implications. Schweiz Mineral Petrogr Mitt 82:121–130

Keller J, Brey GP, Lorenz V, Sachs P (1990) IAVCEI 1990 pre-conference excursion 2A: volcanism and petrology of the Upper Rhinegraben (Urach-Hegau-Kaiserstuhl), Mainz

Koban CG, Schweigert G (1993) Microbial Origin of Travertine Fabrics - Two Examples from Southern Germany (Pleistocene Stuttgart Travertines and Miocene Riedöschingen Travertine). Facies 29:251–264. https://doi.org/10.1007/BF02536931

Kolb M, Paulick H, Kirchenbaur M, Münker C (2012) Petrogenesis of Mafic to Felsic Lavas from the Oligocene Siebengebirge Volcanic Field (Germany): implications for the origin of intracontinental volcanism in Central Europe. J Petrol 53(11):2349–2379. https://doi.org/10.1093/petrology/egs053

Kraml M, Keller J, Henjes-Kunst F (1999) Time constraints for the carbonatic intrusions of the Kaiserstuhl volcanic complex, Upper Rhine Graben. Germany J Conf Abstr 4:322

Kraml M, Pik R, Rahn M, Selbekk R, Carignan J, Keller J (2006) A New Multi-Mineral Age Reference Material for $^{40}Ar/^{39}Ar$, (U-Th)/He and Fission Track Dating Methods: the Limberg t3 Tuff. Geostand Geoanalyt Res 30(2):73–86. https://doi.org/10.1111/j.1751-908X.2006.tb00914.x

Kraml M, Keller J, Henjes-Kunst F (1995) New K-Ar, ^{40}Ar-39Ar step heating and ^{40}Ar-^{39}Ar Iaser fusion dates for the Kaiserstuhl volcanic complex. Eur. J. Mineral. (Ber. Dtsch. mineral. Ges.) 7(Beih. 1):142

Kramm U, Wedepohl KH (1990) Tertiary basalts and peridotite xenoliths from the Hessian Depression (NW Germany), reflecting mantle compositions low in radiogenic Nd and Sr. Contrib Mineral Petrol 106(1):1–8. https://doi.org/10.1007/BF00306404

Krause O, Weiskirchner W (1981) Die Olivin-Nephelinite des Hegaus. Jahresh Geol Landesamt Baden-Wurtt 23:87–130

Kröchert JS, Theye T, Buchner E (2009) Considerations on the age of the Urach volcanic field (Southwest Germany). Z Dtsch Ges Geowiss 160(4):325–331. https://doi.org/10.1127/1860-1804/2009/0160-0325

Lenz OK, Wilde V, Mertz DF, Riegel W (2015) New palynology-based astronomical and revised $^{40}Ar/^{39}Ar$ ages for the Eocene maar lake of Messel (Germany). Int J Earth Sci (geol Rundsch) 104(3):873–889. https://doi.org/10.1007/s00531-014-1126-2

Lexa J, Seghedi I, Németh K, Szakács A, Konečny V, Pécskay Z, Fülöp A, Kovacs M (2010) Neogene-Quaternary Volcanic forms in the Carpathian-Pannonian Region: a review. Open Geosci. https://doi.org/10.2478/v10085-010-0024-5

Link K (2010) Die thermo-tektonische Entwicklung des Oberrheingraben-Gebietes seit der Kreide. Dissertation, University of Freiburg

Linthout K, Paulick H, Wijbrans JR (2009) Provenance of basalt blocks from Roman sites in Vleuten-De Meern (the Netherlands) traced to the Tertiary Siebengebirge (Germany): a geoarchaeological quest using petrological and geochemical methods. Neth J Geosci 88(1):55–74. https://doi.org/10.1017/S0016774600000998

Lippolt HJ, Gentner W, Wimmenauer W (1963) Altersbestimmungen nach der Kalium-Argon-Methode an tertiären Eruptivgesteinen Südwestdeutschlands. Jahresh Geol Landesamt Baden-Wurtt 6:507–538

Lippolt HJ, Todt W, Baranyi I (1973) K-Ar ages of basaltic rocks from the Urach volcanic district, SW Germany. Fortschr Mineral Beih 50(3):101–102

Lippolt HJ, Baranyi I, Todt W (1975) Die Kalium-Argon-Alter der postpermischen Vulkanite des nord-östlichen Oberrheingrabens. Aufschluß Sonderbd 27:205–212

Lippolt HJ (1983) Distribution of volcanic activity in space and time. In: Fuchs K, Gehlen K von, Mälzer H, Murawski H, Semmel A (eds) Plateau Uplift. The Rhenish Shield—a case history, 1st edn. Springer, Berlin, pp 112–120

Ludwig KR (2009) Isoplot Version 3.71, a Geochronological Toolkit for Microsoft Excel, 4. Berkeley Geochronol Cent Spec Publ 70

Lukács R, Harangi S, Guillong M, Bachmann O, Fodor L, Buret Y, Dunkl I, Sliwinski J, von Quadt A, Peytcheva I, Zimmerer M (2018) Early to Mid-Miocene syn-extensional massive silicic volcanism in the Pannonian Basin (East-Central Europe): eruption chronology, correlation potential and geodynamic implications. Earth-Sci Rev 179:1–19. https://doi.org/10.1016/j.earscirev.2018.02.005

Lustrino M, Carminati E (2007) Phantom plumes in Europe and the circum-Mediterranean region. In: Foulger GR, Jurdy DM (eds) Plates, plumes, and planetary processes: Geological Society of America Special Paper, vol 430, pp 723–745. https://doi.org/10.1130/2007.2430(33)

Lustrino M, Wilson M (2007) The circum-Mediterranean anorogenic Cenozoic igneous province. Earth-Sci Rev 81(1–2):1–65. https://doi.org/10.1016/j.earscirev.2006.09.002

Lutz H, Lorenz V, Engel T, Häfner F, Haneke J (2013) Paleogene phreatomagmatic volcanism on the western main fault of the northern Upper Rhine Graben (Kisselwörth diatreme and Nierstein-Astheim Volcanic System. Bull Volcanol, Germany). https://doi.org/10.1007/s00445-013-0741-2

Mader S, Ritter JRR, Reicherter K, AlpArray Working Group (2021) Seismicity and seismotectonics of the Albstadt Shear Zone in the northern Alpine foreland. Solid Earth 12(6):1389–1409. https://doi.org/10.5194/se-12-1389-2021

Mahfoud RF, Beck JN (1989) Alkaline basalt-phonolite rocks from the Singen area, Hegau, southern F.R.G. Chem Geol 74(3–4):217–227. https://doi.org/10.1016/0009-2541(89)90033-8

Le Maitre RW, Streckeisen A, Zanettin B, Le Bas MJ, Bonin B, Bateman P, Bellieni G, Dudek A, Efremov S, Keller J, Lameyre J, Sabine PA, Schmid R, Sørensen H, Woolley AR (2002) Igneous rocks. A classification and glossary of terms, 2nd edn. Cambridge University Press, Cambridge. https://doi.org/10.1017/CBO9780511535581

Martha SO, Zulauf G, Dörr W, Nesbor H-D, Petschick R, Prinz-Grimm P, Gerdes A (2014) The Saxothuringian–Rhenohercynian boundary underneath the Vogelsberg volcanic field: evidence from basement xenoliths and U-Pb zircon data of trachyte. Z Dtsch Ges Geowiss 165(3):373–394. https://doi.org/10.1127/1860-1804/2014/0079

Mäussnest O (1974) Die Eruptionspunkte des Schwäbischen Vulkans – Teil I. Z Dtsch Ges Geowiss 125:23–54

Mäussnest O (1975) Die Anomalien des erdmagnetischen Feldes im Gebiet des Katzenbuckels. Aufschluß 27:229–234

Mayer B, Jung S, Romer RL, Pfänder JA, Klügel A, Pack A, Gröner E (2014) Amphibole in alkaline basalts from intraplate settings: implications for the petrogenesis of alkaline lavas from the metasomatised lithospheric mantle. Contrib Mineral Petrol. https://doi.org/10.1007/s00410-014-0989-3

McDowell FW, McIntosh WC, Farley KA (2005) A precise ^{40}Ar–^{39}Ar reference age for the Durango apatite (U–Th)/He and fission-track dating standard. Chem Geol 214(3–4):249–263. https://doi.org/10.1016/j.chemgeo.2004.10.002

Meier L, Eisbacher GH (1991) Crustal kinematics and deep structure of the northern Rhine Graben. Germany Tectonics 10(3):621–630. https://doi.org/10.1029/91TC00142

Merle O (2011) A simple continental rift classification. Tectonophysics 513(1–4):88–95. https://doi.org/10.1016/j.tecto.2011.10.004

Mertz DF, Swisher CC, Franzen JL, Neuffer FO, Lutz H (2000) Numerical dating of the Eckfeld maar fossil site, Eifel, Germany: a calibration mark for the Eocene time scale. Sci Nat (die Naturwissenschaft) 87(6):270–274. https://doi.org/10.1007/s001140050719

Mertz DF, Renne PR, Wuttke M, Mödden C (2007) A numerically calibrated reference level (MP28) for the terrestrial mammal-based biozonation of the European Upper Oligocene. Int J Earth Sci (geol Rundsch) 96(2):353–361. https://doi.org/10.1007/s00531-006-0094-6

Mertz DF, Löhnertz W, Nomade S, Pereira A, Prelević D, Renne PR (2015) Temporal–spatial evolution of low-SiO2 volcanism in the Pleistocene West Eifel volcanic field (West Germany) and relationship to upwelling asthenosphere. J Geodyn 88:59–79. https://doi.org/10.1016/j.jog.2015.04.002

Molnár K, Lukács R, Dunkl I, Schmitt AK, Kiss B, Seghedi I, Szepesi J, Harangi S (2019) Episodes of dormancy and eruption of the Late Pleistocene Ciomadul volcanic complex (Eastern Carpathians, Romania) constrained by zircon geochronology. J Volcanol Geotherm Res 373:133–147. https://doi.org/10.1016/j.jvolgeores.2019.01.025

Mrlina J, Kämpf H, Geissler WH, van den Bogaard P (2007) Assumed Quaternary maar structure at the Czech/German boundary between Mýtina and Neualbenreuth (western Eger Rift, Central Europe): geophysical, petrochemical and geochronological indications. Z Geol Wiss 35(4–5):213–230

Neuhaus S (2010) New age for Paleogene/Neogene clastics at the northern termination of the Upper Rhine Graben (Hesse, Germany). Z Dtsch Ges Geowiss 161(3):303–322. https://doi.org/10.1127/1860-1804/2010/0161-0303

Neumann U, Metz P, Westphal F (1992) Vulkanismus der Schwäbischen Alb. Beih Eur J Mineral 4(2):1–37

Nowell DAG, Jones MC, Pyle DM (2006) Episodic Quaternary volcanism in France and Germany. J Quat Sci 21(6):645–675. https://doi.org/10.1002/jqs.1005

Pfänder JA, Jung S, Münker C, Stracke A, Mezger K (2012) A possible high Nb/Ta reservoir in the continental lithospheric mantle and consequences on the global Nb budget—evidence from continental basalts from Central Germany. Geochim Cosmochim Acta 77:232–251. https://doi.org/10.1016/j.gca.2011.11.017

Pfänder JA, Jung S, Klügel A, Münker C, Romer RL, Sperner B, Rohrmüller J (2018) Recurrent local melting of metasomatised lithospheric mantle in response to continental rifting: constraints from Basanites and Nephelinites/Melilitites from SE Germany. J Petrol 59(4):667–694. https://doi.org/10.1093/petrology/egy041

Przybyla T, Pfänder JA, Münker C, Kolb M, Becker M, Hamacher U (2018) High-resolution $^{40}Ar/^{39}Ar$ geochronology of volcanic rocks from the Siebengebirge (Central Germany)—implications for eruption timescales and petrogenetic evolution of intraplate volcanic fields. Int J Earth Sci (geol Rundsch) 107(4):1465–1484. https://doi.org/10.1007/s00531-017-1553-y

Puziewicz J, Matusiak-Małek M, Ntaflos T, Grégoire M, Kaczmarek M-A, Aulbach S, Ziobro M, Kukuła A (2020) Three major types of subcontinental lithospheric mantle beneath the Variscan orogen in Europe. Lithos 362–363:105467. https://doi.org/10.1016/j.lithos.2020.105467

Rasser MW, Bechly G, Böttcher R, Ebner M, Heizmann E, Höltke O, Joachim C, Kern AK, Kovar-Eder J, Nebelsick JH, Roth-Nebelsick A, Schoch RR, Schweigert G, Ziegler R (2013) The Randeck Maar: palaeoenvironment and habitat differentiation of a Miocene lacustrine system. Palaeogeogr Palaeoclimatol Palaeoecol 392:426–453. https://doi.org/10.1016/j.palaeo.2013.09.025

Riisager J, Perrin M, Riisager P, Ruffet G (2000) Paleomagnetism, paleointensity and geochronology of Miocene basalts and baked sediments from Velay Oriental. French Massif Central J Geophys Res 105(B1):883–896. https://doi.org/10.1029/1999JB900337

Ring U, Bolhar R (2020) Tilting, uplift, volcanism and disintegration of the South German block. Tectonophysics 795:228611. https://doi.org/10.1016/j.tecto.2020.228611

Ring U, Gerdes A (2016) Kinematics of the Alpenrhein-Bodensee graben system in the Central Alps: Oligocene/Miocene transtension due to formation of the Western Alps arc. Tectonics 35(6):1367–1391. https://doi.org/10.1002/2015TC004085

Ritter JR, Jordan M, Christensen UR, Achauer U (2001) A mantle plume below the Eifel volcanic fields. Germany Earth Planet Sci Lett 186(1):7–14. https://doi.org/10.1016/S0012-821X(01)00226-6

Rupf I, Nitsch E (2008) Das Geologische Landesmodell von Baden-Württemberg: Datengrundlagen, technische Umsetzung und erste geologische Ergebnisse. LGRB-Inf 21:1–81

Schleicher H, Keller J, Kramm U (1990) Isotope studies on alkaline volcanics and carbonatites from the Kaiserstuhl, Federal Republic of Germany. Lithos 26:21–35. https://doi.org/10.1016/0024-4937(90)90038-3

Schmitt AK (2006a) Hochauflösende U-Pb Datierung von Zirkonen des Sporneiche Trachyts. Geol Jahrb Hess 133:75–81

Schmitt AK (2006b) Laacher See revisited: high-spatial-resolution zircon dating indicates rapid formation of a zoned magma chamber. Geol 34(7):597. https://doi.org/10.1130/G22533.1

Schmitt AK, Marks MA, Nesbor HD, Markl G (2007) The onset and origin of differentiated Rhine Graben volcanism based on U-Pb ages and oxygen isotopic composition of zircon. Eur J Mineral 19(6):849–857. https://doi.org/10.1127/0935-1221/2007/0019-1776

Schmitt AK, Wetzel F, Cooper KM, Zou H, Wörner G (2010) Magmatic longevity of Laacher See Volcano (Eifel, Germany) indicated by U-Th dating of intrusive carbonatites. J Petrol 51(5):1053–1085. https://doi.org/10.1093/petrology/egq011

Schmitt AK, Klitzke M, Gerdes A, Schäfer C (2017) Zircon Hafnium-oxygen isotope and trace element petrochronology of intraplate volcanic rocks from the Eifel (Germany) and implications for Mantle versus crustal origins of zircon megacrysts. J Petrol 58(9):1841–1870. https://doi.org/10.1093/petrology/egx075

Schreiner A (1965) Die Juranagelfluh im Hegau. Jahreshefte Des Geologischen Landesamtes Baden-Württemberg 7:303–354

Schubert S, Jung S, Pfänder JA, Hauff F, Garbe-Schönberg D (2015) Petrogenesis of Tertiary continental intra-plate lavas between Siebengebirge and Westerwald, Germany: constraints from trace element systematics and Nd, Sr and Pb isotopes. J Volcanol Geotherm Res 305:84–99. https://doi.org/10.1016/j.jvolgeores.2015.08.023

Schumacher ME (2002) Upper Rhine Graben: role of preexisting structures during rift evolution. Tectonics 21(1):1006. https://doi.org/10.1029/2001TC900022

Seghedi I, Downes H (2011) Geochemistry and tectonic development of Cenozoic magmatism in the Carpathian–Pannonian region. Gondwana Res 20(4):655–672

Shaw CSJ, Woodland AB, Hopp J, Trenholm ND (2010) Structure and evolution of the Rockeskyllerkopf Volcanic Complex, West Eifel Volcanic Field. Germany Bull Volcanol 72(8):971–990. https://doi.org/10.1007/s00445-010-0380-9

Singer BS, Hoffman KA, Schnepp E, Guillou H (2008) Multiple Brunhes Chron excursions recorded in the West Eifel (Germany) volcanics: support for long-held mantle control over the non-axial dipole field. Phys Earth Planet Inter 169(1–4):28–40. https://doi.org/10.1016/j.pepi.2008.05.001

Sirocko F, Dietrich S, Veres D, Grootes PM, Schaber-Mohr K, Seelos K, Nadeau M-J, Kromer B, Rothacker L, Röhner M, Krbetschek M, Appleby P, Hambach U, Rolf C, Sudo M, Grim S (2013) Multi-proxy dating of Holocene maar lakes and Pleistocene dry maar sediments in the Eifel, Germany. Quat Sci Rev 62:56–76. https://doi.org/10.1016/j.quascirev.2012.09.011

Skála R, Ulrych J, Ackerman L, Krmíček L, Fediuk F, Balogh K, Hegner E (2015) Upper Cretaceous to Pleistocene melilitic volcanic rocks of the Bohemian Massif: petrology and mineral chemistry. Geol Carp 66(3):197–216. https://doi.org/10.1515/geoca-2015-0020

Spear FS, Parrish RR (1996) Petrology and cooling rates of the Valhalla complex, British Columbia. Canada J Petrol 37(4):733–765. https://doi.org/10.1093/petrology/37.4.733

Staesche A (1995) Der genetische Zusammenhang zwischen Melilithiten und Phonolithen des Hegaus, SW-Deutschland. Diploma thesis, University of Tübingen

Stähle V, Koch M (2003) Primary and secondary pseudobrookite minerals in volcanic rocks from the Katzenbuckel Alkaline Complex, southwestern Germany. Swiss Bull Mineral Petrol 83(2):145–158

Stellrecht R, Emmermann R (1970) Das Olivinnephelinit-Vorkommen von Forst/Pfalz. Oberrh Geol Abh 19:29–41

Sundermeyer C, Gätjen J, Weimann L, Wörner G (2020) Timescales from magma mixing to eruption in alkaline volcanism in the Eifel volcanic fields, western Germany. Contrib Mineral Petrol. https://doi.org/10.1007/s00410-020-01715-y

Tappe S, Simonetti A (2012) Combined U-Pb geochronology and Sr–Nd isotope analysis of the Ice River perovskite standard, with implications for kimberlite and alkaline rock petrogenesis. Chem Geol 304–305:10–17. https://doi.org/10.1016/j.chemgeo.2012.01.030

Tera F, Wasserburg GJ (1972) U-Th-Pb systematics in three Apollo 14 basalts and the problem of initial Pb in lunar rocks. Earth Planet Sci Lett 14(3):281–304. https://doi.org/10.1016/0012-821X(72)90128-8

Thomson SN, Zeh A (2000) Fission-track thermochronology of the Ruhla Crystalline Complex: new constraints on the post-Variscan thermal evolution of the NW Saxo-Bohemian Massif. Tectonophysics 324(1–2):17–35. https://doi.org/10.1016/S0040-1951(00)00113-X

Timar-Geng Z, Fügenschuh B, Wetzel A, Dresmann H (2006) Low-temperature thermochronology of the flanks of the southern Upper Rhine Graben. Int J Earth Sci (geol Rundsch) 95(4):685–702. https://doi.org/10.1007/s00531-005-0059-1

Ulrych J, Dostal J, Hegner E, Balogh K, Ackerman L (2008) Late Cretaceous to Paleocene melilitic rocks of the Ohře/Eger Rift in northern Bohemia, Czech Republic: Insights into the initial stages of continental rifting. Lithos 101(1–2):141–161. https://doi.org/10.1016/j.lithos.2007.07.012

Ulrych J, Dostal J, Adamovič J, Jelínek E, Špaček P, Hegner E, Balogh K (2011) Recurrent Cenozoic volcanic activity in the Bohemian Massif (Czech Republic). Lithos 123(1–4):133–144. https://doi.org/10.1016/j.lithos.2010.12.008

Ulrych J, Ackerman L, Balogh K, Hegner E, Jelínek E, Pécskay Z, Přichystal A, Upton BG, Zimák J, Foltýnová R (2013) Plio-Pleistocene basanitic and melilititic series of the Bohemian Massif: K-Ar ages, major/trace element and Sr–Nd isotopic data. Geochemistry 73(4):429–450. https://doi.org/10.1016/j.chemer.2013.02.001

Ulrych J, Krmíček L, Tomek Č, Lloyd FE, Ladenberger A, Ackerman L, Balogh K (2016) Petrogenesis of Miocene alkaline volcanic suites from western Bohemia: whole rock geochemistry and Sr–Nd–Pb isotopic signatures. Geochemistry 76(1):77–93. https://doi.org/10.1016/j.chemer.2015.11.003

van den Bogaard P (1995) $^{40}Ar/^{39}Ar$ ages of sanidine phenocrysts from Laacher See Tephra (12,900 yr BP): chronostratigraphic and petrological significance. Earth Planet Sci Lett 133:163–174. https://doi.org/10.1016/0012-821X(95)00066-L

Voigt T, Kley J, Voigt S (2021) Dawn and dusk of Late Cretaceous basin inversion in central Europe. Solid Earth 12(6):1443–1471. https://doi.org/10.5194/se-12-1443-2021

von Eynatten H, Dunkl I, Brix M, Hoffmann V-E, Raab M, Thomson SN, Kohn B (2019) Late Cretaceous exhumation and uplift of the Harz Mountains, Germany: a multi-method thermochronological approach. Int J Earth Sci (geol Rundsch) 108(6):2097–2111. https://doi.org/10.1007/s00531-019-01751-5

von Eynatten H, Kley J, Dunkl I, Hoffmann V-E, Simon A (2021) Late Cretaceous to Paleogene exhumation in Central Europe—localized inversion vs. large-scale domal uplift. Solid Earth 12:935–958. https://doi.org/10.5194/se-12-935-2021

Wagner GA (1976) Spaltspurendatierungen an Apatit und Titanit aus den Subvulkaniten des Kaiserstuhls. N Jahrb Mineral Monatshefte 9:389–393

Wagner GA, Gögen K, Jonckheere R, Kämpf H, Wagner I, Woda C (1998) The age of Quaternary volcanoes Železná Hůrka and Komurni Hůrka (western Eger Rift), Czech Republic Republic: Alpha-recoil Track, TL, ESR and Fission Track chronometry. In: Cajz V, Adomoviè J (eds) Ulrych J. Magmatism and rift basin evolution, Prague, pp 95–96

Wagner GA, Michalski I, Zaun P (1989) Apatite fission track dating of the Central European basement. Postvariscan Thermo-Tectonic Evolution. In: Emmermann R, Wohlenberg J (eds) The German continental deep drilling program (KTB). Site-selection Studies in the Oberpfalz and Schwarzwald. Springer, Berlin, Heidelberg, pp 481–500

Walter BF, Gerdes A, Kleinhanns IC, Dunkl I, von Eynatten H, Kreissl S, Markl G (2018) The connection between hydrothermal fluids, mineralization, tectonics and magmatism in a continental rift setting: fluorite Sm-Nd and hematite and carbonates U-Pb geochronology from the Rhinegraben in SW Germany. Geochim Cosmochim Acta 240:11–42. https://doi.org/10.1016/j.gca.2018.08.012

Wedepohl KH, Baumann A (1999) Central European Cenozoic plume volcanism with OIB characteristics and indications of a lower mantle source. Contrib Mineral Petrol 136(3):225–239. https://doi.org/10.1007/s004100050534

Wedepohl KH, Gohn E, Hartmann G (1994) Cenozoic alkali basaltic magmas of western Germany and their products of differentiation. Contrib Mineral Petrol 115(3):253–278. https://doi.org/10.1007/BF00310766

Wijbrans J, Németh K, Martin U, Balogh K (2007) $^{40}Ar/^{39}Ar$ geochronology of Neogene phreatomagmatic volcanism in the western Pannonian Basin. Hung J Volcanol Geotherm Res 164(4):193–204. https://doi.org/10.1016/j.jvolgeores.2007.05.009

Wilson M, Downes H (1992) Mafic alkaline magmatism associated with the European Cenozoic rift system. Tectonophysics 208:173–182. https://doi.org/10.1016/B978-0-444-89912-5.50014-4

Witt-Eickschen G, Kramm U (1998) Evidence for the multiple stage evolution of the subcontinental lithospheric mantle beneath the Eifel (Germany) from pyroxenite and composite pyroxenite/peridotite xenoliths. Contrib Mineral Petrol 131(2–3):258–272. https://doi.org/10.1007/s004100050392

Wörner G, Zindler A, Staudigel H, Schmincke H-U (1986) Sr, Nd, and Pb isotope geochemistry of Tertiary and Quaternary alkaline volcanics from West Germany. Earth Planet Sci Lett 79:107–119. https://doi.org/10.1016/0012-821X(86)90044-0

Wu F-Y, Yang Y-H, Mitchell RH, Li Q-L, Yang J-H, Zhang Y-B (2010) In situ U-Pb age determination and Nd isotopic analysis of perovskites from kimberlites in southern Africa and Somerset Island. Canada Lithos 115(1–4):205–222. https://doi.org/10.1016/j.lithos.2009.12.010

Anlage II

Akzeptierte Publikation

Arbeit 2

Binder T, Marks MAW, Walter BF, Wenzel T, Markl G (2024b) Two Distinct Metasomatized Mantle Sources Produced Two Groups of Alkaline SiO_2-Undersaturated Rocks in the Southern Central European Volcanic Province. J. Petrol. 65(7):1–29. https://doi.org/10.1093/petrology/egae070.

THOMAS BINDER[1], MICHAEL A. W. MARKS[1], BENJAMIN F. WALTER[1], THOMAS WENZEL[1] & GREGOR MARKL[1]

Two Distinct Metasomatized Mantle Sources Produced Two Groups of Alkaline SiO_2-undersaturated Rocks in the Southern Central European Volcanic Province

[1] Department of Geosciences, Eberhard Karls Universität Tübingen, Schnarrenbergstraße 94–96, 72076 Tübingen, Germany

Corresponding author: Thomas Binder

E-mail address: thomas.binder@uni-tuebingen.de

Telephone: +49-7071-29-73488

ABSTRACT

Upper Cretaceous–Miocene alkaline SiO_2-undersaturated volcanic rocks in the southern Central European Volcanic Province (CEVP) comprise two distinct rock series: (i) Upper Cretaceous–Eocene (~73-47 Ma) olivine nephelinites, basanitic nephelinites, and nepheline basanites have moderate to high MgO (8-16 wt.%), CaO, Ni, Co, Cr, Nb, and Ba, coupled with low F and SiO_2 concentrations. These rocks contain abundant clinopyroxene and variable amounts of olivine macrocrysts as well as nepheline, K-dominated F-poor mica, and hydroxyapatite. Evolved and less common apatite-rich (phonolitic) haüynites/noseanites and haüyne nephelinites (~68-62 Ma) represent differentiated counterparts within this older group, showing higher alkali, Al_2O_3, P_2O_5, Nb, Zn, REE, and SO_3 concentrations at low MgO (4-6 wt.%), CaO, Ni, Co, and Cr contents. (ii) Oligocene–Miocene (~27-9 Ma) olivine melilitites and melilite-bearing olivine nephelinites are characterized by even higher MgO (10-22 wt.%), CaO, Ni, Co, Cr, Nb, Ba, and high F contents at lower SiO_2 concentrations, as reflected by the presence of abundant olivine macrocrysts, melilite, perovskite, Cr-rich spinel, F- and Ba-rich mica, and fluorapatite in addition to clinopyroxene and nepheline.

Distinct mineral assemblages, crystallization trends, and various xenocrysts indicate different melt sources, a varying extent of enrichment, retention, and loss of volatiles (including timing of H_2O and CO_2 saturation), and limited wall-rock interaction for the two rock groups. Partly resorbed, Fo-depleted olivine cores in the younger rocks and green-core pyroxenes in the older ones suggest early magma mixing. The nephelinitic–basanitic magmas derived from up to 6 % partial melting of amphibole-bearing garnet/spinel lherzolite at or just above the lithosphere-asthenosphere boundary. This source was metasomatized involving hydrous melts or fluids. On the other hand, the melilite-bearing rocks probably originated in the upper asthenosphere by less than 3.5 % partial melting of amphibole ±phlogopite-bearing garnet wehrlite, previously generated by subduction-related metasomatism with high

CaO/MgO and $CO_2/(CO_2+H_2O)$ ratios. Infiltration and storage of the metasomatic agents occurred in the former lower lithosphere, following continuous recycling of oceanic crust, comprising the release of Ca, CO_2, H_2O, further volatiles, and incompatible elements.

Both volcanic episodes coincide with topographic uplift, erosion, rifting, and reactivation of lithosphere-scale faults, probably related to phases of strong mechanical coupling between Alpine orogen and European foreland. The first period overlapped with an era of prolonged N-directed intraplate compressional stress due to the Adriatic-Eurasian collision, provoking large-scale deformation, isostatic compensation, erosion, and consequent lithosphere thinning in the future CEVP. The second period is associated with the Oligocene–Miocene main stage of the European Cenozoic Rift System. Onset of volcanism was accompanied by a change in deformation in the Upper Rhine Graben from (W)NW extension to (E)NE extension and transtension by a complex interplay of evasive movements responding to shortening in Alps and Jura. Magma compositions, barely magmatic graben structures, volcanic activity outside rifts, and extensive exhumation suggest that in response to rifting, passive asthenospheric doming also contributed to magmatism by causing strong lithosphere-asthenosphere interaction and providing heat.

Keywords: Central European Volcanic Province; foidite; mantle upwelling; mineral chemistry; olivine melilitite

INTRODUCTION

Origin and evolution of alkaline SiO_2-undersaturated intraplate magmas are controversially discussed. Studies on such compositions occurring in the Central European Volcanic Province (CEVP) mostly focussed on whole-rock geochemistry or geochronology, especially from its northern sector (e.g., Wedepohl, 1985; Wörner *et al.*, 1986; Jung & Hoernes, 2000; Bogaard & Wörner, 2003; Haase *et al.*, 2004; Jung *et al.*, 2006; Schubert *et al.*, 2015; Ulrych *et al.*, 2016; Pfänder *et al.*, 2018). Petrological studies are rare and only available for the Eifel, Katzenbuckel, Hegau and Urach regions, the Kaiserstuhl and other scattered Upper Rhine Graben (URG) volcanoes, and for the Eger Graben (Hegner *et al.*, 1995; Seifert & Thomas, 1995; Dunworth & Wilson, 1998; Stähle & Koch, 2003; Shaw, 2004; Mann *et al.*, 2006; Ulrych *et al.*, 2008; Keller & Wimmenauer, 2015; Braunger *et al.*, 2018, 2021; Sundermeyer *et al.*, 2020). Many occurrences in the southern CEVP (Fig. 1a) have not been studied by modern methods and comprise primitive alkaline rocks in the Taunus, Lower Main plain, Vosges and Pfälzerwald, Bonndorfer Graben and Freiburger Bucht, Lorraine, and Odenwald and Kraichgau regions (Wimmenauer, 1952; Stellrecht & Emmermann, 1970; Horn *et al.*, 1972; Velde & Thiebaut, 1973; Frenzel, 1975).

To explain the igneous activity in the southern CEVP, complementary but also mutually contradictory models have been proposed. The petrogenetic models range from mantle plumes, meaning deep upwelling and subsequent melting induced by thermal instabilities originated at the core-mantle boundary (e.g., Goes *et al.*, 1999; Ritter *et al.*, 2001) to passive asthenospheric doming in response to lithospheric deformation, uplift, and erosion with partial melting supported by recycling of subducted lithologies (e.g., Lustrino & Carminati, 2007; Fichtner & Villaseñor, 2015; Przybyla *et al.*, 2018). Many studies suggest a link to changes of the central European stress field in the Alpine foreland (Braun et al., 2013;

Egli et al., 2017; Grimmer et al., 2017; Eynatten et al., 2021; Ring & Bolhar, 2020; Voigt et al., 2021).

Primitive CEVP rocks are mostly SiO_2-undersaturated and show relatively high Ni, Co, and Cr contents, depletion of K, Pb, and Hf, variable enrichment of volatiles (H_2O, F, Cl, CO_2, S), large-ion lithophile elements (LILE), high-field-strength elements (HFSE), and enrichment of light rare-earth elements (LREE) over heavy ones (HREE; e.g., Wedepohl & Baumann, 1999; Jung & Hoernes, 2000; Lustrino & Wilson, 2007). To explain such compositions, partial melting either in the asthenosphere (e.g., Hegner *et al.*, 1995; Jung *et al.*, 2006; Schubert *et al.*, 2015) or the lithospheric mantle has been proposed (e.g., Blusztajn & Hegner, 2002); other studies suggest strong lithosphere-asthenosphere interaction with thermal erosion of the base of the lithosphere (e.g., Wilson *et al.*, 1995; Jung & Masberg, 1998; Jung *et al.*, 2005; Kolb *et al.*, 2012; Ulrych *et al.*, 2013; Mertz *et al.*, 2015; Braunger *et al.*, 2018; Pfänder *et al.*, 2018). Partial melting occurred in the dolomite-garnet stability field, the garnet-spinel transition zone, and/or the spinel stability field (Wedepohl, 1985; Harmon *et al.*, 1987; Hegner & Vennemann, 1997; Jung & Masberg, 1998; Jung & Hoernes, 2000; Bogaard *et al.*, 2001; Blusztajn & Hegner, 2002; Jung *et al.*, 2012; Kolb *et al.*, 2012; Mayer *et al.*, 2013; Schubert *et al.*, 2015; Pfänder *et al.*, 2018; Puziewicz *et al.*, 2020). In any case, the mantle lithologies are considered likely modified by ancient subduction-related metasomatism (e.g., Wilson *et al.*, 1995; Wedepohl & Baumann, 1999; Lustrino & Wilson, 2007; Pfänder *et al.*, 2012; Green, 2015; Yaxley *et al.*, 2022).

We present a detailed petrological study on melilititic, foiditic, and basanitic rocks in the southern CEVP to decipher and compare their melt sources, melting and crystallization conditions. Combined with previous U-Pb age data (Binder et al., 2023), the volcanic history in the study area is reconstructed in the context of the evolution of the European Cenozoic Rift System (ECRiS; e.g., Dèzes et al., 2004) and its precursors. The comparison of volcanic

regions from two time periods within the southern CEVP unveils yet obscured spatial and temporal mantle heterogeneities and differences in melt formation and evolution.

GEOLOGICAL SETTING

The study area comprises volcanic fields and individual volcanic structures in southwestern Germany and eastern France in the southern part of the Upper Cretaceous–Holocene CEVP (Fig. 1). The northern segment of the CEVP consists of polygenetic and minor monogenetic volcanic regions in central Germany, the Czech Republic, and western Poland, specifically Eifel, Siebengebirge, Westerwald, Vogelsberg, Hessian Depression, Rhön, Heldburg region, Fichtelgebirge, Doupovské hory Mts., České středohoří Mts., Central Bohemian Uplands, Lusatia, and Lower Silesia. In contrast, the volcanic regions in the southern CEVP, except for the polygenetic Kaiserstuhl and the Hegau and Odenwald phonolites (Mann *et al.*, 2006; Binder *et al.*, 2024), comprise mostly primitive melilititic, nephelinitic, and basanitic sodic rocks, plus rare evolved (phonolitic) haüyne nephelinites and haüynites/noseanites (Fig. 1a; Binder *et al.*, 2023 and references therein):

- Upper Cretaceous–Eocene (~73-47 Ma) melilite-free nephelinitic–basanitic rocks occur mainly in the Taunus, the Lower Main plain, the Odenwald and Kraichgau region, the Vosges and Pfälzerwald, and the Bonndorfer Graben and Freiburger Bucht region, with evolved haüyne- and nosean-rich rocks being restricted to the Odenwald and Kraichgau region. These occurrences are mostly found mostly on the URG flanks, within Variscan massifs and/or along ~E-W striking unconformities (Fig. 1b).
- Oligocene–Miocene (~27-9 Ma) perovskite-bearing olivine melilitites and melilite-bearing olivine nephelinites dominate in the Hegau region, at Urach, in the southern URG, and in Lorraine; they are mainly linked to N-S trending faults like the Albstadt shear zone (Fig. 1b).

For both magmatic periods, a relationship to crustal dynamics in combination with the reactivation of major faults is assumed (*passive rifting*; Schumacher, 2002; Dèzes *et al.*, 2004; Grimmer *et al.*, 2017; Binder *et al.*, 2023). Nevertheless, the limited amount of lithospheric extension in the Alpine foreland, some barely magmatic Cenozoic graben structures, and volcanism far from rifts (Fig. 1b) are quoted as evidence that active asthenospheric flow and upwelling due to convective instabilities are also necessary to cause sufficient decompression, weakening, and thinning of the lithosphere for igneous activity (Wilson *et al.*, 1995; Lustrino & Wilson, 2007; Grimmer *et al.*, 2017; Ring & Bolhar, 2020; Eynatten *et al.*, 2021).

Early volcanism followed late Cretaceous thrusting and crustal thickening caused by the convergence of Iberia and Europe (~95-70 Ma; Dielforder *et al.*, 2019; Eynatten *et al.*, 2021; Voigt *et al.*, 2021). The magmatic activity coincided with a phase of prolonged Paleocene intraplate compressional stress resulting from the collision of the Adriatic and Eurasian plates, which provoked large-scale deformation, isostatic uplift, and subsequent erosion and thinning of the central European lithosphere (Dèzes *et al.*, 2004; Ziegler & Dèzes, 2005). The ~20 Myr volcanic hiatus between the two episodes coincides with periods of subsidence or reduced uplift in the study area (Dèzes *et al.*, 2004; Eynatten *et al.*, 2021; Binder *et al.*, 2023), probably linked to the resumption of subduction of European lithosphere beneath the Alpine orogenic wedge (~52-35 Ma; Ziegler *et al.*, 2002; Ziegler & Dèzes, 2005), which caused mechanical decoupling of the Central European from Alpine lithosphere.

After extensive widening and subsidence of the Molasse basin in the late Eocene, increasing subduction resistance reactivated N-directed intraplate compressional stresses in the Alpine foreland, controlling the subsequent ECRiS evolution and forwarding the early rifting phase of the URG by *collisional foreland splitting* (Ring & Gerdes, 2016) with strike-slip deformation and transtensional reactivation of Variscan and Permian discontinuities (Bergerat, 1987; Schumacher, 2002; Dèzes *et al.*, 2004; Ziegler & Dèzes, 2005; Ring &

Bolhar, 2020). During the Oligocene, compressive deformation resulting from the NW-directed convergence between the Adriatic and Eurasian Plates and from N-directed stresses in the Pyrenean collision zone provoked complex evasive movements in the northern Alpine foreland, which governed the E-W extensional stage of the ECRiS and subsidence of the URG (*constructive interference*; Schumacher, 2002; Dèzes *et al.*, 2004; Ziegler & Dèzes, 2005, Ring & Gerdes, 2016). At the onset of the second magmatic period, deformation in the URG shifted from (W)NW to (E)NE extension and transtension, accompanied by regional uplift (~25-18 Ma). This reflected a significant change in the interplay between ECRiS evolution and NW-directed shortening in the Alps and Jura Mts. (Schumacher, 2002; Ring & Gerdes, 2016; Grimmer *et al.*, 2017). Concomitant southward tilting of the South German block, uplift, and subsequent erosion in the study area initiated at ~18-16 Ma and persisted throughout the Neogene (Ziegler & Dèzes, 2005; Hoffmann, 2017; Ring & Bolhar, 2020).

METHODS

For petrographic examination and classification according to Le Maitre *et al.* (2002), 170 thin sections from >100 localities (Supplementary data, Table A1) were studied by polarization and scanning electron microscopy (*Phenom XL, Thermo Fisher Scientific*). Considering the alteration state, 83 thin sections from 60 localities were selected for electron probe microanalysis (EPMA, Table 1) and 34 samples from 27 localities for whole-rock analyses (Supplementary data, File 1), including most of the samples used for the geochronological study by Binder *et al.* (2023). For details on the application of clinopyroxene-based geothermobarometry according to Putirka (2008) and Neave & Putirka (2017) and the quantification of temperature, oxygen fugacity (fO_2), and $aSiO_2$ according to Andersen et al. (1993), see Supplementary data, File 2.

EPMA

Mineral compositions were analysed using a *JEOL JXA 8230* electron probe microanalyzer in wave-length dispersive mode at the Department of Geosciences, University of Tübingen. The specific sensitivities of the mineral surfaces to the probe current depend on the chemical composition and were a critical factor in adjusting the configurations (given in Supplementary data, Table A2). Peak count times were fixed at 10 s for light and volatile elements (e.g., Na, F), 16 s for the other major elements and 30 s for minor elements, with background count time being each half of peak count time. Calibration was carried out by synthetic and natural standards, and several peak overlap corrections (Cr-V, V-Ti, F-Fe, F-Ce, Ce-Ba, Pr-La, Ba-Ti). An internal φ(ρz) raw data correction was performed for all analyses except the oxyspinel analyses, for which ZAF correction was applied. Specific parameters for the analytical protocols are given in Supplementary data, Tables A3-10, details of mineral formula and end-member calculations in Supplementary data, File 2, and all analytical results in File 3.

Whole-rock geochemistry

Whole-rock analyses (major, minor, and trace elements) were performed at the Laboratory of Environmental and Raw Materials Analysis, Karlsruhe Institute of Technology using wavelength dispersive XRF (*S4 Explorer, Bruker AXS*) and ICP-MS (*iCap RQ, Thermo Fisher Scientific*). To determine the mass loss on ignition, one gram of the powdered sample was heated to 950 °C for 3 h. For XRF, fused beads were prepared with a Li tetraborate/metaborate mixture (*Spectroflux 110, Alfa Aesar*) as flux. The certified standards AGV-1 (andesite), GS-N (granite), SY-2 and SY-3 (syenites) were measured intermittently as reference materials (Govindaraju, 1994; CRM-TMDW-A, *High-Purity standards, Inc.*), yielding an accuracy in the range of 2 % for most elements and 10 % for Ti and Mn. For

ICP-MS, 100 mg of powdered rock was treated by HNO_3-HF-$HClO_4$ acid digestion. A sample was heated together with 65 % HNO_3 (subboiled), 40 % HF (Suprapur®), and 65 % $HClO_4$ (Normatom®) in a closed Teflon vessel for 16 h at 120 °C, ensuring total silicate decomposition. After evaporating the acids to incipient dryness, the residue was redissolved in 65 % HNO_3 (sub-boiled) and evaporated three times again for purification. The final residue was dissolved in 50 ml of ultrapure H_2O. Certified reference materials SY-2 and SY-3 (Govindaraju, 1994), an in-house phonolite standard, and two blank samples were included in the analyses for quality assurance. Accuracy was 10 % for most trace elements, except for Sc, Zr, Cs, Hf, W, and some HREE (25 %). The contents of C_{tot} and S_{tot} were determined by combusting powdered material in an O_2 flow with an induction furnace at 2000 °C (*CS 2000, Eltra*). The reference materials steel (n = 7) and cast Fe (n = 2) were used for calibration and quality control. Accuracy was in the range 1 %; the 1σ was 0.7 % for steel and 2.5 % for cast iron. For more details see Supplementary data, File 1.

RESULTS

Petrography

Based on mineralogy and microstructure, two primitive and one evolved magma series with varying abundances in the different regions of the study area are distinguished (Fig. 1a, Tables 2 & 3).

Olivine nephelinites and nepheline basanites

These predominantly Upper Cretaceous–Eocene (~73-47 Ma) rocks contain variable amounts of olivine and clinopyroxene macrocrysts, embedded in a groundmass (50-80 vol.%) with clinopyroxene, oxyspinel, interstitial nepheline, minor amounts of anhedral dark mica, and accessory apatite in most samples (Figs. 2a-c). Olivine comprises varying proportions of both

euhedral–subhedral and subhedral–anhedral, rounded, partly sheared, ruptured macrocrysts, the latter occasionally exhibiting wavy extinction (Figs. 2b-c). Euhedral clinopyroxene macrocrysts are beige to pale-brownish or yellowish and show concentric, sometimes hourglass sector zoning, and/or twinning (Fig. 2a-d). In some samples, they enclose rounded cores of greenish clinopyroxene, a feature known as green-core pyroxenes (Duda & Schmincke, 1985). Some of these cores include anhedral apatite (Fig. 2a), others are zoned, with a spongy inner domain rich in melt and fluid inclusions, overgrown by a green and largely inclusion-free outer part (Fig. 2e). In addition, partly resorbed pale cores occur, distinguishable from the surrounding crystal by lack of zoning, different interference colour, or varying extinction angle (Fig. 2b). Rarely, euhedral–subhedral clinopyroxene macrocrysts enclose corroded orthopyroxene crystals (Fig. 2d). In many samples, brown, yellow, or green oxyspinel exhibits resorption and corrosion textures with anhedral crystals overgrown by fringes of magnetite-ulvöspinel$_{ss}$ (Figs. 2f-g), sometimes displaying diffusion-affected contacts and/or porous labyrinthine–spongy structures (Fig. 2g). Depending on region and locality, further characteristic minerals such as dark mica (<25 %; Fig. 2h), plagioclase (<15 %), alkali feldspar (<5 %), haüyne-nosean-sodalite$_{ss}$ (<10 %), and accessory perovskite may occur (Table 2).

(Phonolitic) haüynites, noseanites and haüyne nephelinites

Upper Cretaceous–Paleocene (~68-62 Ma) haüyne/nosean-rich (phonolitic) foidites are restricted to the Odenwald and Kraichgau region and contain abundant subhedral poikilitic macrocrysts of beige–yellowish clinopyroxene enclosing euhedral magnetite-ulvöspinel$_{ss}$ and apatite (Fig. 2i). Crystals of euhedral haüyne-nosean-sodalite$_{ss}$, apatite, subhedral–euhedral olivine, and magnetite-ulvöspinel$_{ss}$ (often showing exsolution lamellae of ilmenite) are surrounded by a groundmass of beige–greenish clinopyroxene needles, anhedral

magnetite-ulvöspinel$_{ss}$, nepheline, sanidine, apatite, and minor amounts of interstitial amphibole and dark mica.

Olivine melilitites and melilite-bearing olivine nephelinites

Late Oligocene–Miocene (~27-9 Ma) porphyritic olivine melilitites contain variable proportions of euhedral, subhedral, and anhedral olivine macrocrysts embedded in a groundmass (50-70 vol.%) of euhedral clinopyroxene, magnetite-ulvöspinel$_{ss}$, melilite, olivine, perovskite, apatite, and interstitial nepheline ± dark mica (Fig. 3a). Larger crystals of magnetite-ulvöspinel$_{ss}$ occasionally enclose Cr-rich oxyspinel cores. Particularly in melilite-rich rocks, euhedral melilite crystals approach the size of olivine macrocrysts (Fig. 3b). Some samples contain reversely zoned olivine macrocrysts (Fig. 3c), small- to medium-grained haüyne-nosean$_{ss}$ (Fig. 3d), and clinopyroxene macrocrysts (Figs. 3d-e), and/or macrocryst glomerules (Fig. 3f). Few mica-poor olivine melilitites from Urach contain accessory kalsilite microcrysts (Fig. 3g), and only the melilititic rocks from Buggingen carry green-core pyroxenes and accessory garnet (Braunger et al., 2021). Melilite-bearing olivine nephelinites contain lower amounts of melilite, coinciding with higher portions of nepheline and clinopyroxene.

Mineral chemistry

Olivine

Olivine has a composition in the Fo$_{73-93}$ range, typically with core-to-rim decreasing Fo (normal zoning). In most samples, the composition of the olivine macrocrysts is independent of their shape-based classification, which sometimes makes a clear petrogenetic distinction difficult (cf. Dunworth & Wilson, 1998). Rarely, olivine crystals in melilite-bearing rocks show relatively Fo-poor cores (Fo$_{77-85}$) overgrown by Fo-rich rims (reverse zoning; Figs. 3c &

4a). Subtle differences in olivine chemistry between the various rock groups can be observed (Fig. 4): In olivine crystals from the younger melilite-bearing rocks, Fo decreases from ~Fo_{90-92} (core) to ~Fo_{83-88} (rim); in the older nephelinitic–basanitic rocks, olivine evolves towards more Fe-rich compositions (~Fo_{89-93} to ~Fo_{77-88}). Olivine from haüyne/nosean-rich and mica-rich rocks has a composition of ~Fo_{73-83}. The Ca content in olivine increases from the core (<0.005 apfu) towards the rim to ~0.035 apfu in melilite-bearing rocks, ~0.02 apfu in nephelinitic–basanitic rocks, and usually <0.01 apfu in haüyne/nosean-rich rocks (Fig. 4a). Also, Mn contents generally increase from the centre towards the rim of crystals (~0.002 to 0.015 apfu), with some of the evolved haüyne/nosean-rich rocks showing remarkably high Mn contents off the trend (<0.035 apfu; Fig. 4b).

In most melilitites, nephelinites, and basanites, Ni contents decrease from ~0.008 apfu (cores) to ~0.001 apfu (rims), while olivine from haüyne/nosean-rich and mica-rich rocks is relatively Ni-poor (<0.004 apfu; Fig. 4c). In the olivine cores, Ni decreases with increasing Ca content; their Ca-Ni ratio in the melilite-bearing rocks often corresponds to the typical ratio reported for olivine in mantle peridotite (Fig. 4d; e.g., Foley *et al.*, 2013; Bussweiler *et al.*, 2015), whereas this does not apply to the melilite-free nephelinitic–basanitic rocks, except for olivine in peridotite xenoliths and their disaggregated relics.

Pyroxenes

Clinopyroxene in all rock types is dominated by the quadrilateral end-members (mostly Di+Hd), with tschermakitic proportions (CaFeTs, CaTiTs, CaAlTs, CrAlTs) reaching <45 % and Na end-members (Aeg, Ti-Aeg, Jd) <10 % (Fig. 5a). Most macrocrysts show concentric zoning, characterized by varying ratios of tschermakitic and quadrilateral end-members. Green-core pyroxenes are comparatively Di-poor but Hd- and Aeg-rich compared to the euhedral macrocrysts; few samples contain minor Aeg-dominated groundmass clinopyroxenes

(Fig. 5b). Rare orthopyroxene ($En_{86-94}Fs_{6-14}$) occurs exclusively as (disaggregated) lherzolite xenoliths and anhedral macrocrysts (Supplementary data, Fig. A1).

In several clinopyroxene crystals, hourglass zoning is an important factor (Fig. 3f), with the opposite sectors being rich in Al and Ti or poor in Al and Ti, respectively. Regardless of this, the Al (<0.6 apfu) and Ti (<0.22 apfu) contents within the sectors and in sector-free clinopyroxene generally increase from core to rim, whereas Mg and Si decrease (Fig. 5c). Few macrocrysts are relatively Cr-rich (<0.04 apfu; Fig. 6a) like clinopyroxenes from mantle xenoliths (Witt-Eickschen & O'Neill, 2005; this study). The comparatively Mg-poor green-core pyroxenes are off-trend and reach only moderate Ti contents (Fig. 6b), and Aeg-rich clinopyroxene shows considerable scatter (0.04-0.21 apfu).

Oxyspinel

The oxyspinel group comprises magnetite-ulvöspinel$_{ss}$ (all samples; 0-65 mol% ulvöspinel; Supplementary data, Fig. A2a) and chromite-spinel$_{ss}$ (restricted to primitive magmas; Fig. 6c). Magnetite-ulvöspinel$_{ss}$ exhibits varying contents of Al, Mg, and Cr, in turn forming a continuous solid solution series with chromite, magnesiochromite, hercynite, and spinel. However, compositions intermediate between magnetite-ulvöspinel$_{ss}$ and Mg-Cr-Al spinel are restricted to the blurred domain between resorbed relict crystals and Fe-Ti-dominated overgrowth rims. In basanites and nephelinites, the Mg-Cr-Al-rich cores (X_{Cr} = 0.07-0.72) show greater compositional variations and reach a higher average Mg spinel component (X_{Mg} = 0.23-0.84, mainly >0.60) than in the melilite-bearing rocks (X_{Cr} = 0.22-0.73; X_{Mg} = 0.41-0.73; Fig. 6c). The Mn content is generally very low, except for groundmass oxyspinel from Buggingen (southern URG) and Waldbrunn (Odenwald and Kraichgau region; <35 % jacobsite; Supplementary data, Fig. A2b), where Mn-rich olivine also occurs.

Melilite

Melilite is åkermanite-rich (~48-71 %), with <37 % sodic melilite, <20 % ferro-åkermanite, and <12 % gehlenite components. The highest åkermanite contents were found in Urach samples (Supplementary data, Fig. A3a). The low Sr content (<0.03 apfu) decreases with increasing Mg, and correlates with Na (Supplementary data, Fig. A3b-c).

Haüyne-nosean-sodalite$_{ss}$

Rare unaltered crystals of sodalite group minerals in the Urach and Hegau rocks are haüyne-nosean$_{ss}$ with a maximum of 18 % sodalite component, whereas in Odenwald and Kraichgau rocks, they cover almost the entire range of the sodalite group (Fig. 7a), with the Cl content tending to increase towards the crystal rims (especially at Waldbrunn). In one olivine nephelinite (Roßberg), only sodalite with a haüyne-nosean$_{ss}$ proportion of 13-49 % occurs. All data reveal Na predominance over K and Ca (Fig. 7b) and generally low Sr contents (<0.08 apfu), except for haüyne from the in many respects peculiar Eisenrüttel occurrence (up to 0.22 apfu; Fig. 7c).

Mica

Predominantly Mg-rich mica occurs as common mica (K-dominated, i.e., phlogopite) plus minor brittle mica (Ba-dominated, i.e., kinoshitalite; Fig. 7d) and encompasses hydroxy-, fluoro-, and oxy-micas (Supplementary data, Fig. A4a). It differs between the two age groups, regions, and individual localities: Oligocene–Miocene melilite-bearing rocks mostly contain very Mg- and F-rich mica (except for Buggingen), whereas in Upper Cretaceous–Eocene rocks, mica is less Mg-rich and relatively F-poor (Fig. 7d). Further, mica in melilite-bearing rocks contains up to 0.65 apfu Ba, while mica in melilite-free rocks is generally low in Ba (<0.20 apfu), except for the Lower Main plain. Increasing Ba contents roughly correlate with

increasing F and Ti contents (Figs. 7e-f). Similar Ba, Ti, and F-rich mica is known from nephelinites and melilititeselsewhere (Ba <0.58 apfu; Dunworth & Wilson, 1998; Melluso *et al.*, 2011; Lakroud *et al.*, 2020). Na, Cl, and Ti contents decrease with increasing X_{Mg} (Supplementary data, Figs. A4b-d), partly with significant scatter though.

Accessory minerals

Apatite comprises fluorapatite–hydroxyapatite$_{ss}$, the latter occurring exclusively in the melilite-free Upper Cretaceous–Eocene rocks, especially as inclusions in clinopyroxene crystals (Figs. 2a & 8a). The chlorapatite component reaches ~11 % in the primitive rocks and ~18 mol% in the haüyne/nosean-rich ones. The contents of Sr+Ba (<0.25 apfu), Na+K (<0.20 apfu), REE (<0.08 apfu) and SO_4^{2-} (<0.02 apfu) are low in apatite from the primitive rocks, while in the haüyne/nosean-rich rocks, it shows on average elevated Sr, Ba, Na and K contents and increased values for SO_4^{2-} (<0.10 apfu; Figs. 8b-c).

Perovskite is generally restricted to the Oligocene–Miocene rocks. Contents of Na (<0.1 apfu), REE (<0.07 apfu), Nb (<0.08 apfu), Ta (<0.003 apfu), Sr (<0.05 apfu), and Th (<0.005 apfu) are variable and lowest for the Urach rocks, except for the locality Eisenrüttel, which has some of the highest Na, Sr, REE, and Th contents in the study area (Supplementary data, Fig. A5).

Amphibole occurs only in some samples and is mostly represented by Ti-rich calcic amphibole, the majority of which is kaersutite (Supplementary data, Fig. A6). Subordinately, ferrokaersutite, magnesiohastingsite, hastingsite, and ferroedenite are present. F-rich sodic-calcic amphibole (magnesiokatophorite, fluorokatophorite) occurs in the groundmass of the phonolitic nepheline noseanite from Waldbrunn. The F content in all amphiboles increases with increasing $Mg/(Mg+Fe^{2+})$ ratio, while Cl and Ba contents (each <0.04 apfu) decrease, and K contents are 0.20-0.36 apfu.

Whole-rock geochemistry

Most Oligocene–Miocene melilite-bearing rocks plot in the foidite/melilitite field in the TAS diagram (Fig. 9). The Upper Cretaceous–Eocene nephelinitic–basanitic rocks have on average higher SiO_2, while the haüyne/nosean-rich rocks from the Odenwald and Kraichgau region have remarkably high Na_2O+K_2O contents. Few samples plot in the basalt field, coinciding with numerous inclusions of country rocks like quartzites, phyllites, gneisses, granitoids, and siliciclastic rocks in these samples (Naurod, Taunus) or considerable argillization, zeolitization, serpentinization, and chloritization (Buggingen, southern URG; Hurrle, 1976).

Major oxide and trace element compositions (Figs. 10-13; Supplementary data, File 1) overlap among the primitive rock groups. Melilite-rich rocks reach the highest MgO and CaO contents, while haüyne/nosean-rich rocks have the lowest values. Melilite-free rocks show higher average contents of Na_2O+K_2O, Al_2O_3, and SiO_2 than melilite-bearing ones (Figs. 10a-e). The Na_2O/K_2O ratios vary little in haüyne/nosean-rich rocks (~1.8-3.2) but show larger scatter in the primitive rocks (~0.4-8.7, mostly ~0.9-4.5; Fig. 10f). P_2O_5 ranges from 0.5-1.4 wt.%, except for haüyne/nosean-rich rocks and the sodalite-rich Roßberg occurrence (Lower Main plain), where higher values are reached (1.4-2.8 wt.%; Fig. 10g), consistent with their elevated amount of modal apatite. The TiO_2 contents are mostly confined in the ~2-3 wt.% range; some Hegau and Odenwald and Kraichgau samples show higher contents of up to 9 wt.% (Fig. 10h).

The Ni concentrations of the two primitive rock series largely overlap (~120-600 µg/g), albeit melilite-free rocks have higher contents than melilite-bearing rocks at a given MgO (Fig. 11a). The melilite-free rocks have lower average and maximum Ni, Co, Cr, and V contents than melilite-bearing ones (Figs. 11a-d), while the haüyne/nosean-rich rocks show remarkably low concentrations for these elements. Differences for Nb are likewise

evident, with concentrations of 20-120 µg/g in the primitive older rocks and 70-160 µg/g in the younger ones (Fig. 11e). The primitive rocks show moderate variability in Zn, Ce, and Y contents, while the haüyne/nosean-rich rocks show a wide range with high average concentrations for these elements and Nb (Figs. 11e-h).

Compared to the CI chondrite composition, the investigated rocks are highly enriched in LREE (La: ~160-850 times), but only moderately in HREE (Lu: ~4-25 times), with the highest enrichment in the haüyne/nosean-rich Odenwald and Kraichgau rocks (Fig. 12a). The REE pattern of these latter rocks is similar to that of all other samples, except for the strikingly flat trend between La and Nd, resembling the mica-rich nepheline basanites and basanitic nephelinites from the same region. Primitive mantle-normalized element patterns show a decreasing enrichment with increasing mantle compatibility in the rocks of all the investigated regions except for K, Pb, Hf, Zr (and sometimes Rb and Ta), exhibiting variable negative K and Pb anomalies (Fig. 12b). Mobile elements (e.g., Cs, Rb, Ba, U) show large concentration differences, also within the same region. The haüyne/nosean-rich rocks and mica-rich nepheline basanites and basanitic nephelinites in the Odenwald and Kraichgau have negative K, Pb, and Hf anomalies but show higher enrichment factors for most trace elements.

Crystallization conditions

Clinopyroxene-based geothermometry (Eqn. 33 in Putirka, 2008) and geobarometry (Neave & Putirka, 2017) for the two primitive magma series (Supplementary data, Fig. A7) yields indistinguishable P (~0.2-1.3 GPa) and T (~1150-1350 °C). The temperature estimate is slightly lower (~1100-1330 °C) when considering H_2O contents of the whole rock. For mica-rich nepheline basanites and basanitic nephelinites, P <0.9 GPa and T of ~1080-1180 °C are indicated. The results are similar to P-T estimates for related rocks in other CEVP regions (Supplementary data, File 2).

Combined T – $aSiO_2$ – fO_2 estimates (QUILF; Supplementary data, Fig. A8a & File 4) yield lower equilibrium temperatures of 820-1060 °C (primitive magmas) and 830-930 °C (evolved magmas), considered to represent near-solidus to sub-solidus conditions for the corresponding assemblage (see Supplementary data, File 2). Redox conditions for most basanites, foidites, and melilitites are oxidized (ΔFMQ = +2.5 to +4), with few basanites, foidites, and evolved rocks indicating less oxidized conditions (down to ΔFMQ ≈ +1); $aSiO_2$ are ~0.5-0.9 for the primitive, ~0.4-0.7 for the evolved magmas (Supplementary data, Fig. A8b).

DISCUSSION

Given the similar geothermobarometric estimates, it is unlikely that the two primitive magma series simply reflect different *P-T* conditions during magmatic evolution. Rather, the characteristic mineral assemblages, mineral and whole-rock compositions of both rock series (Fig. 1a; Tables 2 & 3) provide evidence for different magma sources and a distinct melt evolution, including fractional crystallization, interaction with host rocks, magma mixing events, and the volatile behaviour (fluid exsolution, degassing) during ascent and emplacement.

Unravelling crystal load and mineral chemistry: Clues to melt formation, evolution, ascent and emplacement

The investigated rocks contain variable proportions of xenocrysts, antecrysts, phenocrysts, and groundmass microcrysts. While the latter two crystallized directly from the magma during early- and late-magmatic stages, respectively, antecrysts formed from a magma of different composition and have been entrained during ascent (Fig. 14). Xenocrysts from mantle lithologies include anhedral and partly sheared olivine (Figs. 2b-c), rare orthopyroxene

(Fig. 2d), and partly resorbed and decomposed spinel cores (Figs. 2f g & 6c). Sporadic Cr diopside cores (Figs. 3e & 6a) are also mantle xenocrysts or they resemble antecrysts that were enriched in Cr by reaction of a precursor magma with oxyspinel xenocrysts from disintegrated mantle lithologies (Fig. 14a; Dunworth & Wilson, 1998; Ulianov et al., 2007). Such textures are known from mantle lithologies that underwent carbonatitic metasomatism (Ionov et al., 1994; 1996; Wiechert et al., 1997; Ulianov et al., 2007) and suggest the presence of carbonate during melt formation and evolution.

Green-core pyroxenes in the older rocks (Figs. 2a & e) suggest limited mixing with mantle-derived melts of intermediate to evolved compositions (e.g., Duda & Schmincke, 1985; Dobosi & Fodor, 1992; Jung & Hoernes, 2000; Loges *et al.*, 2019). Such clinopyroxene crystals probably accumulated in dyke networks or small intrusions in the upper mantle or lower crust (Duda & Schmincke, 1985). While scant diffusion despite strong compositional differences between the green cores and the phenocrystic rims indicates fast cooling and thus entrainment not long before eruption, the provenance of green-core pyroxenes remains controversial (Jankovics et al., 2016).

Relatively Fo-depleted and partly resorbed olivine cores (Figs. 3c & 4) in some of the younger rocks are interpreted as antecrysts, incorporated during stagnation and mixing processes in a magma reservoir (e.g., Sundermeyer *et al.*, 2020). Alternative explanations for the reverse zonation assume changes in fO_2 during crystallization but are frequently doubted (see Supplementary data, File 2; Mathez 1984, Lowenstern 2001, Morizet et al. 2010, Cottrell & Kelley 2011, Iacono-Marziano et al. 2012, Ni & Keppler 2013).

Early magmatic crystallization: The variable role of CO_2 and carbonate in the source

The parental melts of both primitive magma suites were initially saturated with olivine, accompanied by clinopyroxene in the older group (Figs. 2a-c) and with melilite in the younger group (Figs. 3b & g), joined by clinopyroxene in most cases (Figs. 3d & f). Continuous compositional zoning of most olivine and clinopyroxene phenocrysts reflects changes in the composition of the crystallizing magma pointing to polybaric crystallization during magma ascent (cf. Duda & Schmincke, 1985; Dunworth & Wilson, 1998; Arzamastsev *et al.*, 2009). Abundant melilite (Fig. 3b) and higher average CaO and MgO contents at lower SiO_2 contents (Figs. 10b & d) in the younger rock group compared to the older one indicate differences between their parental magmas and mantle sources (cf. Mertes & Schmincke, 1985; Melluso *et al.*, 2011). Initial melt composition is controlled, among other factors, by CO_2 dissolution in a silicate melt and the amount of $CaCO_3$ in the mantle assemblage (Seifert & Thomas, 1995; Dunworth & Wilson, 1998). Both CO_2 and $CaCO_3$ probably originate from carbonatitic mantle metasomatism by reaction of a dolomite-carbonatitic melt with orthopyroxene in a lherzolitic assemblage resulting in wehrlitization and formation of a Ca-enriched carbonatite melt in which CO_2 is dissolved and/or with which an additional CO_2-rich fluid coexists (reaction 1; Seifert & Thomas, 1995; Dunworth & Wilson, 1998; Veksler & Lenz, 2006; Ulianov *et al.*, 2007):

$$5\,Mg_2[Si_2O_6] + 4\,CaMg(CO_3)_2 \leftrightarrow 6\,Mg_2[SiO_4] + 2\,CaMg[Si_2O_6] + 2\,CaCO_3 + 6\,CO_2 \quad (1)$$

Opx + dolomite-carbonatitic melt ←→ Ol + Cpx + calcio-carbonatitic melt + CO_2-rich fluid

Subsequent reaction with olivine or clinopyroxene will then produce a dolomite-carbonatitic melt ± fluid, melilite and/or clinopyroxene, depending on the CaO/CO_2 ratio of the carbonatite melt ± fluid:

$$2\,Mg_2[SiO_4] + 5\,CaCO_3 + CO_2 \leftrightarrow Ca_2Mg[Si_2O_7] + 3\,CaMg(CO_3)_2 \quad (2)$$

Ol + calcio-carbonatitic melt + CO_2 ←→ Mll + dolomite-carbonatitic melt

$$2\,Mg_2[SiO_4] + 4\,CaCO_3 + 2\,CO_2 \leftrightarrow CaMg[Si_2O_6] + 3\,CaMg(CO_3)_2 \quad (3)$$

Ol + calcio-carbonatitic melt + CO_2 ←→ Cpx + dolomite-carbonatitic melt

$$CaMg[Si_2O_6] + CaCO_3 \leftrightarrow Ca_2Mg[Si_2O_7] + CO_2 \quad (4)$$

Cpx + calcio-carbonatitic melt ←→ Mll + CO_2-rich fluid

Partial melting of SiO_2-poor lithologies favours the subsequent crystallization of melilite over clinopyroxene, as $CaCO_3$ contribution to melt formation also means a lower SiO_2 concentration in such magmas. Obviously, the silicate components of the source also determine the SiO_2 content in the magma, which can be reconciled with an olivine- and clinopyroxene-rich wehrlitic origin of the SiO_2-poor melilititic rocks. Further, the amounts of dolomite-carbonatitic melt relative to orthopyroxene during wehrlitization critically influence the potential for melilite-crystallization from a future melt: If no or insufficient Ca-rich carbonatite melt is produced (reaction 5), melilite cannot form by reactions 2 or 4 (Falloon & Green, 1990; Ulianov *et al.*, 2007; Yaxley *et al.*, 2022).

$$2\,Mg_2[Si_2O_6] + CaMg(CO_3)_2 \leftrightarrow 2\,Mg_2[SiO_4] + CaMg[Si_2O_6] + 2\,CO_2 \quad (5)$$

Opx + dolomite-carbonatitic melt ←→ Ol + Cpx + CO_2-rich fluid

Thus, intense dolomite-carbonatitic metasomatism, causing both wehrlitization of the lherzolitic mantle *and* formation of calcite-carbonatitic melts (reaction 1), followed by their reaction with olivine and/or clinopyroxene (reactions 2-4) are required to allow non-modal melting of the wehrlite. This resulted in Ca-rich magmas, which eventually formed the melilite-bearing rocks in the southern CEVP, consistent with the temporal coincidence of carbonatitic volcanism in the Kaiserstuhl (Ghobadi *et al.*, 2022; Binder *et al.*, 2023). Elevated Nb/Ta ratios, correlating positively with the Lu/Hf ratios, and low Zr/Nb ratios also indicate the involvement of carbonatite melts in the formation of the younger magmas, albeit Zr/Hf ratios resemble those in ocean island basalts (OIB) and in the older rock group (Fig. 13). Carbonatites are known to have superchondritic Nb/Ta, and Lu/Hf >0.1 at very low Zr/Nb

ratios but Zr and Hf concentrations close to those in alkaline intraplate rocks (Pfänder *et al.*, 2012), explaining the observed trace element ratios. The lack of carbonates in the investigated silicate rocks is probably due to the escape of highly mobile carbonate-rich melts/fluids from the system and the exhaustion of dolomite-carbonatitic melt (generated by reactions 2 & 3) by progressing wehrlitization without further carbonate production (reaction 5).

For the melilite-free nephelinitic–basanitic group, however, an orthopyroxene-bearing and thus more SiO_2- and less Ca-rich lherzolitic source lithology is suggested, in line with orthopyroxene xenocrysts enveloped by clinopyroxene in some of the melilite-free rocks (Fig. 2d). Early-magmatic crystallization of clinopyroxene and olivine from lherzolite-derived partial melts is possible without the need for CO_2 and $CaCO_3$ input, consistent with the lower CaO at higher SiO_2 contents (Figs. 10b, d) and more OIB-like Nb/Ta, Lu/Hf, Zr/Hf, Zr/Nb, and La/Nb ratios in the corresponding rocks (Fig. 13). Magma generation in such mantle lithologies that probably experienced hydrous but no (or less) carbonatitic metasomatism is then facilitated by the presence of hydrous phases like amphibole and phlogopite.

Late-magmatic evolution and the importance of volatiles and degassing

In both groups, prolonged diopside-hedenbergite$_{ss}$ formation was followed by crystallization of clinopyroxene with a higher Tschermak's substitution and slightly elevated aegirine component, reflected in higher Fe^{3+}, Ti, and Al contents (Figs. 5a-c & 6b) at lower Si contents. This is probably due to the continuous relative enrichment of Fe^{3+}, Ti, and Al and a persistent SiO_2 decrease in the evolving melt, eventually resulting in magnetite-ulvöspinel$_{ss}$, nepheline, and haüyne-nosean-sodalite$_{ss}$ crystallization (Figs. 3a & d). Diverse compositions of these and other late-magmatic phases, including apatite, phlogopite/kinoshitalite, amphibole, and perovskite mirror the Na_2O/K_2O evolution, enrichment of LILE (Ba, Sr), HFSE (Ti, Nb), and LREE, and the behaviour of volatiles (particularly H_2O, F, Cl, S) in the

investigated magmas. Different amounts of volatile-rich minerals (apatite, phlogopite/kinoshitalite, amphibole, haüyne-nosean-sodalite$_{ss}$) and their compositions (e.g., H_2O/F/Cl and SO_3/Cl ratios; Figs. 7a, d & 8a) in the two rock groups (Fig. 14b) highlight different source characteristics, the relative enrichment during magmatic evolution, and the different timing and extent of degassing during ascent. Exsolution and continuous release of CO_2 before and during crystallization of groundmass phases could explain the absence of carbonate-bearing minerals and contribute to prevent a late-magmatic decomposition reaction of melilite with CO_2 to clinopyroxene and calcite (reverse reaction 4; Veksler & Lentz, 2006; Melluso *et al.*, 2011).

The high F/H_2O ratios in phlogopite/kinoshitalite and apatite (Figs. 7d-e & 8a) and the presence of melilite and perovskite in the young rocks (Figs. 3a-b) indicate higher CaO and F at low SiO_2 and H_2O concentrations in their parental melts, reflecting the carbonate- and CO_2-dominated metasomatism in the magma source of these rocks. In contrast, the predominance of H_2O over F in phlogopite, apatite, and amphibole (Figs. 7e & 8a, Supplementary data, Fig. A6f) and the lack of the Ca-rich phases melilite and perovskite in the older rocks display a source lithology affected by more hydrous metasomatism. Late-magmatic phlogopite/kinoshitalite crystallization and largely suppressed amphibole formation in both rock groups is related to successively declining CaO concentration and Na_2O/K_2O ratio in the Ba-, F-, and/or H_2O-bearing residual melt, and possibly the partial resorption of olivine (Figs. 2b & 3a).

The crystallization of phlogopite from initially sodic magmas (Fig. 10f) and moderate compatibility of K in nepheline and haüyne (Fig. 7b) explain the scarcity of other K-rich silicates. However, few CaO-rich Urach rocks (two samples) contain late-magmatic kalsilite (Fig. 3g). This may be due to comparatively low initial Na_2O/K_2O ratios (~1.4-2.2), a very low aSiO_2 (evidenced by perovskite crystallization), and stronger enrichment of K over Na in

the evolving melt by early crystallization of abundant melilite (20-40 vol.%; Fig. 3b) with a significant sodic melilite portion (20-30 mol%; Supplementary data, Fig. A3a). Mica in these rocks is exceptionally rare and largely composed of Ba-rich fluoro- and oxy-mica components. This demonstrates a low H_2O content in the melt residue as well as strong rivalry for K within the mica interlayer due to significant incorporation of Ba (Fig. 7e) driven by the incompatibility of this element for cogenetic minerals, both of which promote kalsilite formation. A few less SiO_2-undersaturated nepheline basanites of the old rock group contain small amounts of interstitial sanidine, likewise indicating excess K and inhibition of further mica crystallization in the evolving melts depleted of H_2O and F by degassing.

The limited role of fractional crystallization, magma mixing and wall-rock interaction in the primitive rocks

Decreasing Ni and Cr concentrations with decreasing MgO contents and varying Al_2O_3 and SiO_2 contents in both primitive rock groups (Figs. 10c-d, 11a & c) can be explained by minor fractionation of oxyspinel and olivine. Extensive clinopyroxene segregation is considered unlikely, since this would cause a perceptible decrease in CaO and Sc (Bédard et al., 1994), which is not observed (Fig. 10b; Supplementary data, File 1). Particularly high MgO (>18 wt.%), Cr, and Ni contents in some rocks are attributed to inherited olivine, xenocrystic Cr-rich spinel and clinopyroxene cores (Figs. 3e & 6a; Dunworth & Wilson, 1998; Arzamastsev *et al.*, 2009), and green-core pyroxenes in the nephelinitic–basanitic rocks demonstrate that magma mixing or entrainment of crystal mush within the lower crust and possibly the uppermost mantle occurred regionally.

Low SiO_2 and alkali contents (Fig. 9), the lack of Eu anomalies (Fig. 12a), and high MgO contents and Ce/Pb ratios (>20; Supplementary data, Figs. A9a-b) exclude notable assimilation of felsic crustal lithologies (e.g., Jung & Hoernes, 2000; Bogaard *et al.*, 2001;

Haase *et al.*, 2004; Kolb *et al.*, 2012). Only the Roßberg nephelinite (Lower Main Plain), which carries abundant Cl-rich sodalite (Fig. 7a) and shows high Mn contents in the olivine rims despite an otherwise primitive signature (Fig. 4b), may have assimilated Zechstein evaporites with Mn oxide horizons, present in the subsurface of the Lower Main plain and Odenwald region (Becker, 1904; Klemm & Fazakas, 1975; Ramdohr, 1975) but absent in the remaining regions.

The melilite-bearing rocks show higher average Mg, Cr, Ni, and Co contents (Figs. 11a-c) as well as low Ca/Ni ratios in olivine cores similar to those in mantle peridotites (Fig. 4d), which suggests a lower, subordinate influence of fractional crystallization and contamination processes. However, the rare Fo-depleted olivine cores in some samples (Figs. 3c & 4a-c) disclose that even the most primitive magmas are not entirely unaffected by stagnation and magma mixing in the upper lithospheric mantle. This is corroborated by the only occurrences of the younger rock series with green-core pyroxenes (Eisenrüttel, Buggingen). For the Eisenrüttel locality, large quantities of volatile-bearing minerals (up to 10 vol.% haüyne and 5 vol.% phlogopite) and high Sr, Nb, Ta, Th, and REE concentrations in haüyne, apatite, and perovskite compared to the other Urach rocks additionally indicate fractionation processes during its evolution (Figs. 7c, 8b, Supplementary data, Fig. A5). The garnet-, titanite-, mica-, and haüyne-bearing olivine melilitites from the Buggingen potash salt deposit are compositionally unique in the southern CEVP (e.g., Supplementary data, Figs. A2, A4 & A5) and underwent modification by late- or post-magmatic fluid and wall-rock interaction (Braunger *et al.*, 2021). Thus, they are not discussed when constraining source lithologies and melting conditions.

In summary, mineral assemblages and whole-rock compositions reflect locally variable but only limited fractional crystallization, contamination, and magma mixing processes in the crust and uppermost mantle. Hence, the different mineralogy and

incompatible trace element patterns of the two primitive rock groups must also reflect heterogeneous magma sources and their degree of partial melting.

Formation of the evolved rocks

Only the relatively evolved rocks of the Odenwald and Kraichgau region indicate higher degrees of fractional crystallization, confirmed by low contents of compatible elements (Ni, Cr, Co, V), considerable enrichment of alkalis and incompatible elements (Figs. 9-11), and low contents of olivine (<10 vol.%) with rather evolved composition (Figs. 2i & 4b-c). The deviation of Mn and Ni from the olivine trend for more primitive rocks of the same region, high whole-rock MnO contents (Supplementary data, File 1), the occurrence of Mn-rich and Zn-bearing oxyspinel (Supplementary data, Fig. A2b-c), and alkali feldspar additionally indicate significant wall-rock interaction, e.g., with the ~2 km thick Carboniferous–Triassic sedimentary sequence of the Kraichgau region (Rupf & Nitsch, 2008). High volatile contents in the magmas of these rocks, reflected in the mineral inventory and its chemistry (Figs. 7a-c & 8; haüyne-nosean-sodalite$_{ss}$, abundant SO_4- and Cl-bearing apatite phenocrysts, fluorokatophorite), suggest additional supply of volatiles by interaction with formation water/brines during ascent through the crust and/or only late, attenuated degassing processes (Fig. 14). Such retention of volatiles until the late-magmatic stage maintained the solidus temperature of the melt low and may have enabled prolonged fractionation processes and wall-rock interaction that in turn promoted further enrichment (cf. similar Eger Graben magmas; Vaněčková *et al.*, 1993).

Mantle source(s) and partial melting

A slightly higher degree of fractionation of the older compared to the younger primitive magmas (Fig. 14) cannot explain the geochemical differences between the two rock groups (Table 3), as this would suggest a relative enrichment of incompatible elements (Ti, Nb, Zr) in the older group. The opposite, however, is observed (Figs. 10h & 11e), with high Ti and Nb concentrations in the melilite-bearing rocks reflected by Nb-bearing perovskite, higher amounts of magnetite-ulvöspinel$_{ss}$, and Ti-bearing mica (Fig. 7f). Further, the variation in incompatible trace element enrichment between melilite-bearing and melilite-free rocks cannot be solely attributed to the degree of partial melting, as concentration decreases resulting from dilution would be recorded for all incompatible elements (Jung & Hoernes, 2000).

Strong enrichment of LREE over HREE+Y (Fig. 12a) suggests that both magma types derived from a garnet-bearing mantle source (Bogaard *et al.*, 2001; Haase *et al.*, 2004; Jung *et al.*, 2006; Kolb *et al.*, 2012; Schubert *et al.*, 2015). Higher La/Lu and lower Y/Ho ratios in the melilite-bearing rocks (Supplementary data, Figs. A9c-d) indicate a higher proportion of residual garnet in their source. This could imply a higher initial garnet content (at the expense of spinel) in the mantle lithology and/or a lower amount of garnet joining the melt, meaning a slightly greater depth of formation and/or a lower degree of partial melting for the melilite-bearing rocks compared to the nephelinitic–basanitic ones (e.g., Jung & Hoernes, 2000; Jung *et al.*, 2006; Kolb *et al.*, 2012). This is consistent with lower Al_2O_3 and SiO_2 contents in the younger rocks, especially in those from Urach, both of which likewise reflect higher formation *P* (e.g., Harangi *et al.*, 2015; Sun & Dasgupta, 2020) and lower melting degrees (e.g., Jung & Masberg, 1998; Jung & Hoernes, 2000).

Negative K and Pb anomalies, Rb depletion relative to Ba, low K/La (mostly <220), high Ce/Pb (mostly 25-45), and moderate Ba/La ratios (mostly 9-17; Supplementary data,

Figs. A9a-b & A10) indicate residual potassic amphibole ± subordinate phlogopite in the magma source of both primitive rock groups (LaTourrette *et al.*, 1995; Blusztajn & Hegner, 2002; Adam & Green, 2006; Lustrino & Wilson, 2007; Kolb *et al.*, 2012; Mayer *et al.*, 2013; Pfänder *et al.*, 2018). The predominantly sodic character of the investigated rocks shows that extensive melting of phlogopite is unlikely (Fig. 10f; Mertes & Schmincke, 1985; Foley, 1988; Harangi, 2001; Bogaard & Wörner, 2003; Jung *et al.*, 2005). However, especially for some melilite-bearing rocks from Urach and the Hegau region with slightly higher K_2O contents, F-rich phlogopite/kinoshitalite (Fig. 7e), and rare kalsilite (Fig. 3g), the presence of phlogopite alongside amphibole in the magma source is possible. Both the extent of amphibole and phlogopite involvement in partial melting and the corresponding ratio could explain local differences in Na_2O/K_2O ratios (Fig. 10f) and may reflect local-scale inhomogeneous mantle metasomatism.

Semi-quantitative non-modal batch melting models developed for similar northern CEVP rocks (Supplementary data, Fig. A10; Haase *et al.*, 2004; Jung *et al.*, 2006; Kolb *et al.*, 2012; Mertz *et al.*, 2015) suggest less than 3.5 % partial melting of a garnet-bearing source for the melilite-bearing rocks, while formation of the nephelinitic–basanitic rocks is reconcilable with 1-6 % partial melting of a less garnet-rich lithology. The sources of the mica-rich nepheline basanites and basanitic nephelinites probably experienced the highest degrees of melting (2.5-6 %), consistent with a lower liquidus temperature due to the high H_2O content in their magmas (indicated by abundant F-poor phlogopite in these rocks; Figs. 2h & 7d). For a critical evaluation of possible contributions of the classical mantle end-members to melt formation, see Supplementary Data, File 2.

Melting conditions and geodynamic implications

Based on the overlapping portion of the stability ranges of garnet and amphibole (Green & Ringwood, 1967; Falloon & Green, 1990; Foley, 1991; Inoue *et al.*, 1998; Trønnes, 2002; Klemme, 2004; Ziberna *et al.*, 2013; Nagayoshi *et al.*, 2016; Pintér *et al.*, 2021), mantle depths of ~70-115 km and temperatures of up to ~1350 °C can be assumed for magma genesis. The crystallization temperatures of the earliest clinopyroxene phenocrysts at 1250-1350 °C provide a minimum estimate, which constrains melt formation to an interval of <100 K and is consistent with ordinary mantle temperatures and a largely adiabatic magma ascent. For details on melting temperature estimates based on experimental data on amphibole and phlogopite stability in the mantle, see Supplementary Data, File 2.

In the late Cretaceous–Paleocene, a lithospheric thickness of ~80-100 km is inferred for the emerging Alpine foreland (Dèzes *et al.*, 2004; Ziegler *et al.*, 2004). Considering the proposed melting depth and magma compositions, the nephelinitic–basanitic magmas likely originated at or just above the lithosphere-asthenosphere boundary (LAB) from a lherzolite that was only weakly modified by carbonates but affected by more hydrous metasomatism. In contrast, the present-day LAB is located at a shallower depth of 60 ± 5 km beneath the URG, Schwarzwald, and Odenwald, and 78 ± 5 km SW and SE of the URG beneath Schwäbische Alb and Vosges (Seiberlich *et al.*, 2013). Previously, these areas experienced increased rifting-induced extension and transtension, uplift, and erosion, which resulted in lithosphere thinning (Ziegler & Dèzes 2005). As the younger melilite-bearing rocks in the southern CEVP are largely restricted to exactly those regions, their parental melts probably tapped a source in the upper asthenosphere contaminated with metasomatized lithospheric portions (Fig. 15). Strong lithosphere-asthenosphere interaction, i.e., thermal thinning and erosion of metasomatically overprinted areas of the lower lithosphere by the asthenosphere contributed significantly to partial mantle melting (Fig. 15; cf. Jung & Hoernes, 2000; Jung *et al.*, 2005;

Kolb *et al.*, 2012; Mertz *et al.*, 2015; Schubert *et al.*, 2015; Pfänder *et al.*, 2018; Puziewicz *et al.*, 2020; Eynatten *et al.*, 2021).

Hydrous as well as carbonate metasomatism and wehrlitization in the lower lithosphere probably occurred before the Alpine orogeny and ECRiS-associated uplift and rifting processes initiated, when the LAB was still situated at a deeper level (~100-120 km; Ziegler & Dèzes, 2005; Seiberlich *et al.*, 2013). The metasomatic fluids probably derived from the continuous dehydration and partial recycling of the subducted Variscan crust, including the release of Ca, CO_2, H_2O and other volatile and incompatible elements into the upper mantle (Fig. 15). This would explain the enrichment of the studied magmas with CaO, Nb, Sr, Ba, LREE, U, and Th compared to the primitive mantle (Figs. 10b, 11e & 12) as well as the supply of CO_2, H_2O, and F, accounting for the presence of carbonates and hydrous, LILE-bearing phases such as amphibole and possibly phlogopite (e.g., Mertes & Schmincke, 1985; Blusztajn & Hegner, 2002; Jung *et al.*, 2006; Ulrych *et al.*, 2008; Loges *et al.*, 2019). Conclusions on the number and duration of metasomatic events in the southern ZEVP remain speculative, though various trace element signatures of the two rock groups (Fig. 13) presuppose a temporal and/or spatial (stratified) heterogeneity of overprinting. Xenoliths from the lithospheric mantle beneath Central Europe indicate that the depleted orogenic mantle could have been (re)enriched by both carbonated alkaline melts from subducted lithosphere and primary asthenospheric melts (Puziewicz *et al.*, 2020; details on the possible nature of mantle metasomatism in Supplementary data, File 2).

In any case, the thermodynamic conditions did not lead to melt formation and magma mobilization immediately after metasomatism, but only asthenospheric uplift and thinning of the lithosphere in response to the geodynamic processes in Central Europe from the Upper Cretaceous onwards ensured effective heat flux in the metasomatized domains and triggered volcanic activity (Wilson *et al.*, 1995; Blusztajn & Hegner, 2002; Harangi *et al.*, 2015;

Eynatten *et al.*, 2020). An observed shift from more lithosphere-dominated magma sources during the early volcanic phase to more asthenosphere-dominated ones during the younger period (Fig. 15) has been similarly reported for other CEVP regions, the French Massif Central, and the Pannonian Basin, albeit on shorter time scales (Bogaard & Wörner 2003, Dautria et al. 2010, Harangi & Lenkey 2007, Jung & Masberg 1998, Seghedi & Downes 2011). The delay in the progression of asthenospheric uplift and lithospheric thinning in the study area, evident from the volcanic hiatus (47–27 Ma), was probably caused by relaxation of intraplate stresses following the reactivation of subduction in the Alpine belt (Ziegler *et al.*, 2002; Ziegler & Dèzes, 2005), resulting in periods of increased subsidence or at least reduced uplift (Binder *et al.*, 2023).

Neither an excessively hot mantle nor a thermal anomaly or convection from the deep mantle (mantle plumes) are necessary to explain the alkaline volcanism in the study area. Rather, local or regional, spatially and temporally varying elevation of the LAB caused partial melting of metasomatized mantle domains by thermal and compositional interaction between lithosphere and asthenosphere. Whether convective processes in the ductile upper asthenosphere and conductive heat transfer to the overlying continental lithosphere control crustal dynamics or are merely a response to them cannot yet be definitively answered.

CONCLUSIONS

In the southern CEVP, Upper Cretaceous–Eocene (~73-47 Ma) olivine nephelinites, basanitic nephelinites, and nepheline basanites that are rarely accompanied by evolved (phonolitic) haüynites, noseanites, and haüyne nephelinites (~68-62 Ma) can be distinguished from mostly Oligocene–Miocene (27-9 Ma) olivine melilitites and melilite-bearing olivine nephelinites.

Melt formation for both groups occurred in a depth range of ~70-115 km at temperatures of ~1250-1350 °C. Both rocks series derived from partial melting of a garnet-

bearing mantle lithology with residual amphibole ± minor phlogopite, with a higher amount of garnet entering the liquid phase (indicating higher melting degrees) and/or a lower initial garnet content in favour of spinel in the source (indicating slightly lower melting pressures) of the older melilite-free magmas. The melt source for the older rock series (amphibole-bearing garnet(-spinel) lherzolite) was affected by hydrous metasomatism, whereas that for the younger magmas (carbonated amphibole- ± phlogopite-bearing garnet wehrlite) formed by prior interaction with dolomite-carbonatitic melts.

Metasomatism of the involved mantle lithologies occurred before uplift and rifting processes emerged from the Upper Cretaceous onwards, when the LAB was deeper (100-120 km). The composition of the metasomatic agents was influenced by recycling of subducted Variscan lithosphere, explaining the significant enrichment of CaO, Nb, Sr, Ba, LREE, U, and Th compared to the primitive mantle, and of CO_2, H_2O, and F, reflected by hydrous LILE-bearing phases ± carbonates in the mantle lithologies.

Both volcanic episodes were accompanied by uplift, erosion, lithospheric thinning, and reactivation of major faults, all of which were a consequence of crustal dynamics mainly governed by the Alpine orogeny. Partial melting was supported by lithosphere-asthenosphere interaction, i.e., thermal erosion and incorporation of metasomatized lithosphere by the asthenosphere. A thicker lithosphere (~80-100 km) is assumed during Upper Cretaceous–Eocene volcanism than during Oligocene–Miocene activity when doming continued (~60-80 km). Given the estimated melting depths, this suggests that the older rocks originated at or just above the LAB, while the younger ones developed in the upper asthenosphere.

FUNDING

This work was supported by the Deutsche Forschungsgemeinschaft (DFG) [grant MA 2563/19 & WA 3116/6].

ACKNOWLEDGEMENTS

We are grateful to the Deutsche Forschungsgemeinschaft (DFG) for financial support for the acquisition of the electron probe microanalyzer [grant: INST 37/1026-1 FUGG]. We thank the Landesamt für Geologie, Rohstoffe und Bergbau (LGRB, Freiburg im Breisgau), Horst Marschall and Peter Prinz-Grimm (Goethe University Frankfurt), Udo Neumann (University of Tübingen), D. Nesbor and L. Behr (HLNUG), and Kirsten Grimm (University of Mainz) for providing samples used in this study. We would especially like to thank Cyrille Delangle and Luc Jaillard (Terrae Genesis) and Klaus Brauch (terratec Geophysical Services), who contributed with sampling in the field for us. Thanks also to Simone Schafflick and Philip Werner for sample preparation (University of Tübingen) and Michele Lustrino for providing the Excel spreadsheet for geothermobarometric calculations after Sun & Dasgupta (2020). Moreover, we thank Elisabeth Eiche, Claudia Mößner, and Janine Wagner (LERA, KIT) for their support in the whole-rock analyses. Constructive comments by Andreas Klügel, Stefan Jung, and three anonymous reviewers greatly improved the manuscript and are gratefully acknowledged. We further acknowledge editorial handling by Valentin Troll.

SUPPLEMENTARY DATA

Supplementary data are available at Journal of Petrology online.

DATA AVAILABILITY

The data underlying this article are available in the article and in its online supplementary material. Whole-rock geochemistry was supplemented by literature data from Becker (1904), Freudenberg (1906), Wimmenauer (1952), Krause (1969), Stellrecht & Emmermann (1970), Velde & Thibaut (1973), Wimmenauer (1974), Frenzel (1975), Hurrle (1976), Berg & Weiskirchner (1979), Krause & Weiskirchner (1981), Alibert *et al.* (1983), Butchereit (1990),

Keller *et al.* (1990), Stock (1990), Neumann *et al.* (1992), Walter (1994), Hegner *et al.* (1995), Staesche (1995), Dunworth & Wilson (1998), and Stähle *et al.* (2002) and mineral chemistry data for Buggingen volcanic rocks are from Braunger *et al.* (2021).

REFERENCES

Adam, J. & Green, T. (2006). Trace element partitioning between mica- and amphibole-bearing garnet lherzolite and hydrous basanitic melt: 1. Experimental results and the investigation of controls on partitioning behaviour. *Contributions to Mineralogy and Petrology* **152**, 1–17.

Alibert, C., Michard, A. & Albarède, F. (1983). The Transition from Alkali Basalts to Kimberlites: Isotope and Trace Element Evidence from Melilitites. *Contributions to Mineralogy and Petrology* **82**, 176–186.

Andersen, D. J., Lindsley, D. H. & Davidson, P. M. (1993). QUILF: A pascal program to assess equilibria among Fe–Mg–Mn–Ti oxides, pyroxenes, olivine, and quartz. *Computers & Geosciences* **19**, 1333–1350.

Arzamastsev, A. A., Arzamastseva, L. V., Bea, F. & Montero, P. (2009). Trace elements in minerals as indicators of the evolution of alkaline ultrabasic dike series: LA-ICP-MS data for the magmatic provinces of northeastern Fennoscandia and Germany. *Petrology* **17**, 46–72.

Becker, E. (1904). Der Rossbergbasalt bei Darmstadt und seine Zersetzungsprodukte. Inaugural-Dissertation. Halle (Saale): Vereinigte Friedrichs-Universität Halle-Wittenberg.

Bédard, J. H. (1994). A procedure for calculating the equilibrium distribution of trace elements among the minerals of cumulate rocks, and the concentration of trace elements in the coexisting liquids. *Chemical Geology* **118**, 143–153.

Berg, U. & Weiskirchner, W. (1979). Petrographische Untersuchungen an vulkanischen Gesteinen des Jusi (Schwäbische Alb). *Jahresberichte und Mitteilungen des Oberrheinischen Geologischen Vereins* **61**, 337–346.

Bergerat, F. (1987). Stress fields in the European platform at the time of Africa-Eurasia collision. *Tectonics* **6**, 99–132.

Binder, T., Marks, M. A. W., Gerdes, A., Walter, B. F., Grimmer, J. C., Beranoaguirre, A., Wenzel, T. & Markl, G. (2023). Two distinct age groups of melilitites, foidites and basanites from the southern Central European Volcanic Province reflect lithospheric heterogeneity. *International Journal of Earth Sciences* **112**, 881–905.

Binder, T., Marks, M. A. W., Friedrichsen, B.-E., Walter, B.F., Wentel, T., Markl, G. (2024). Bimodal volcanism in the Hegau region (SW Germany): Differentiation of primitive melilititic to nephelinitic rocks produces evolved nosean phonolites. *Lithos* **472-473**, 107565.

Blusztajn, J. & Hegner, E. (2002). Osmium isotopic systematics of melilitites from the Tertiary Central European Volcanic Province in SW Germany. *Chemical Geology* **189**, 91–103.

Bogaard, P. J., Wörner, G. & Henjes-Kunst, F. (2001). *Chemical stratigraphy and origin of volcanic rocks from the drill-core "Forschungsbohrung Vogelsberg 1996"*. In: Hoppe, A. & Schulz, R. (eds.) *Die Forschungsbohrung Vogelsberg 1996: Einblicke in einen miozänen Vulkankomplex.* Hessisches Landesamt für Umwelt und Geologie, 69–99.

Bogaard, P. J. F. & Wörner, G. (2003). Petrogenesis of Basanitic to Tholeiititic Volcanic Rocks from the Miocene Vogelsberg, Central Germany. *Journal of Petrology* **44**, 569–602.

Braun, J., Robert, X. & Simon-Labric, T. (2013). Eroding dynamic topography. *Geophysical Research Letters* **40**, 1494–1499.

Braunger, S., Marks, M. A. W., Walter, B. F., Neubauer, R., Reich, R., Wenzel, T., Parsapoor, A. & Markl, G. (2018). The Petrology of the Kaiserstuhl Volcanic Complex, SW Germany: The Importance of Metasomatized and Oxidized Lithospheric Mantle for Carbonatite Generation. *Journal of Petrology* **59**, 1731–1762.

Braunger, S., Scharrer, M., Marks, M. A., Wenzel, T. & Markl, G. (2021). Interaction between mafic dike rocks and salt deposits in the Rhine Graben, southwest Germany. *The Canadian Mineralogist* **59**, 511–531.

Bussweiler, Y., Foley, S. F., Prelević, D. & Jacob, D. E. (2015). The olivine macrocryst problem: New insights from minor and trace element compositions of olivine from Lac de Gras kimberlites, Canada. *Lithos* **220-223**, 238–252.

Butchereit, E. (1990). Mikrothermometrische Untersuchungen an Fluid- und Schmelzeinschlüssen in Olivinen der melilithführenden Olivin-Nephelinite der Schwäbischen Alb. Dissertation. Tübingen: Eberhard Karls Universität Tübingen.

Cottrell, E. & Kelley, K. A. (2011). The oxidation state of Fe in MORB glasses and the oxygen fugacity of the upper mantle. *Earth and Planetary Science Letters* **305**, 270–282.

Dautria, J.-M., Liotard, J.-M., Bosch, D. & Alard, O. (2010). 160 Ma of sporadic basaltic activity on the Languedoc volcanic line (Southern France): A peculiar case of lithosphere–asthenosphere interplay. *Lithos* **120**, 202–222.

Dèzes, P., Schmid, S. M. & Ziegler, P.A. (2004). Evolution of the European Cenozoic Rift System: interaction of the Alpine and Pyrenean orogens with their foreland lithosphere. *Tectonophysics* **389**, 1–33.

Dielforder, A., Frasca, G., Brune, S. & Ford, M. (2019). Formation of the Iberian-European Convergent Plate Boundary Fault and Its Effect on Intraplate Deformation in Central Europe. *Geochemistry, Geophysics, Geosystems* **20**, 2395–2417.

Dobosi, G. & Fodor, R. V. (1992). Magma fractionation, replenishment, and mixing as inferred from green-core clinopyroxenes in Pliocene basanite, southern Slovakia. *Lithos* **28**, 133-150.

Duda, A. & Schmincke, H.-U. (1985). Polybaric differentiation of alkali basaltic magmas: evidence from green-core clinopyroxenes (Eifel, FRG). *Contributions to Mineralogy and Petrology* **91**, 340–353.

Dunworth, E. A. & Wilson, M. (1998). Olivine Melilitites of the SW German Tertiary Volcanic Province: Mineralogy and Petrogenesis. *Journal of Petrology* **39**, 1805–1836.

Egli, D., Mosar, J., Ibele, T. & Madritsch, H. (2017). The role of precursory structures on Tertiary deformation in the Black Forest—Hegau region. *International Journal of Earth Sciences* **106**, 2297–2318.

Eynatten, H. von, Kley, J., Dunkl, I., Hoffmann, V.-E. & Simon, A. (2021). Late Cretaceous to Paleogene exhumation in Central Europe – localized inversion vs. large-scale domal uplift. *Solid Earth* **12**, 935–958.

Falloon, T. J. & Green, D. H. (1990). Solidus of carbonated fertile peridotite under fluid-saturated conditions. *Geology* **18**, 195.

Fichtner, A. & Villaseñor, A. (2015). Crust and upper mantle of the western Mediterranean – Constraints from full-waveform inversion. *Earth and Planetary Science Letters* **428**, 52–62.

Foley, S. (1991). High-pressure stability of the fluor- and hydroxy-endmembers of pargasite and K-richterite. *Geochimica et Cosmochimica Acta* **55**, 2689–2694.

Foley, S. F. (1988). The Genesis of Continental Basic Alkaline Magmas – An Interpretation in Terms of Redox Melting. *Journal of Petrology* Special Volume, 139–161.

Foley, S. F., Prelevic, D., Rehfeldt, T. & Jacob, D. E. (2013). Minor and trace elements in olivines as probes into early igneous and mantle melting processes. *Earth and Planetary Science Letters* **363**, 181–191.

Frenzel, G. (1975). Die Nephelingesteinsparagenese des Katzenbuckels im Odenwald. *Aufschluß Sonderband* **27**, 213–228.

Freudenberg, W. (1906). Geologie und Petrographie des Katzenbuckels im Odenwald. *Mitteilungen der Grossherzoglich Badischen geologischen Landesanstalt* **5**, 185–344.

Ghobadi, M., Brey, G. P., Gerdes, A., Höfer, H. E. & Keller, J. (2022). Accessories in Kaiserstuhl carbonatites and related rocks as accurate and faithful recorders of whole rock age and isotopic composition. *International Journal of Earth Sciences* **111**, 573–588.

Goes, S., Spakman, W. & Bijwaard, H. (1999). A Lower Mantle Source for Central European Volcanism. *Science* **286**, 1928–1931.

Govindaraju, K. (1994). 1994 Compilation of Working Values and Sample Description for 383 Geostandards. *Geostandards Newsletter* **18**, 1–158.

Green, D. H. & Ringwood, A. E. (1967). The stability fields of aluminous pyroxene peridotite and garnet peridotite and their relevance in upper mantle structure. *Earth and Planetary Science Letters* **3**, 151–160.

Green, D. H. (2015). Experimental petrology of peridotites, including effects of water and carbon on melting in the Earth's upper mantle. *Physics and Chemistry of Minerals* **42**, 95–122.

Grimm, K. I. (2011). *Stratigraphie von Deutschland IX. Tertiär, Teil 1: Oberrheingraben und benachbarte Tertiärgebiete.* Schweizerbart.

Grimmer, J. C., Ritter, J. R. R., Eisbacher, G. H. & Fielitz, W. (2017). The Late Variscan control on the location and asymmetry of the Upper Rhine Graben. *International Journal of Earth Sciences* **106**, 827–853.

Haase, K. M., Goldschmidt, B. & Garbe-Schönberg, C.-D. (2004). Petrogenesis of Tertiary Continental Intra-plate Lavas from the Westerwald Region, Germany. *Journal of Petrology* **45**, 883–905.

Harangi, S. (2001). Neogene to Quaternary volcanism of the Carpathian–Pannonian Region—a review. *Acta Geologica Hungarica* **44**, 223–258.

Harangi, S., Jankovics, M. É., Sági, T., Kiss, B., Lukács, R. & Soós, I. (2015). Origin and geodynamic relationships of the Late Miocene to Quaternary alkaline basalt volcanism in the Pannonian basin, eastern–central Europe. *International Journal of Earth Sciences* **104**, 2007–2032.

Harangi, S. & Lenkey, L. (2007). Genesis of the Neogene to Quaternary volcanism in the Carpathian-Pannonian region: Role of subduction, extension, and mantle plume. *Geological Society of America Special Paper* **418**, 67–92.

Harmon, R. S., Hoefs, J. & Wedepohl, K. H. (1987). Stable isotope (O, H, S) relationships in Tertiary basalts and their mantle xenoliths from the Northern Hessian Depression, W.-Germany. *Contributions to Mineralogy and Petrology* **95**, 350–369.

Hegner, E. & Vennemann, T. W. (1997). Role of fluids in the origin of Tertiary European intraplate volcanism: Evidence from O, H, and Sr isotopes in melilitites. *Geology* **25**, 1035–1038.

Hegner, E., Walter, H. J. & Satir, M. (1995). Pb-Sr-Nd isotopic compositions and trace element geochemistry of megacrysts and melilitites from the Tertiary Urach volcanic field: source composition of small volume melts under SW Germany. *Contributions to Mineralogy and Petrology* **122**, 322–335.

Hoffmann, M. (2017). Young tectonic evolution of the Northern Alpine Foreland Basin, southern Germany, based on linking geomorphology and structural geology. Dissertation. Munich: Ludwig Maximilian University of Munich.

Hofmann, A. W., Jochum, K. P., Seufert, M. & White, W. M. (1986). Nb and Pb in oceanic basalts: new constraints on mantle evolution. *Earth and Planetary Science Letters* **79**, 33–45.

Horn, P., Lippolt, H. J. & Todt, W. (1972). Kalium-Argon-Altersbestimmungen an tertiären Vulkaniten des Oberrheingrabens. I. Gesamtgesteinsalter. *Eclogae Geologicae Helvetiae* **65**, 131–156.

Hurrle, H. (1976). Ocelli- und Mandelbildung der ultrabasischen Basalte im Kalisalzlager Buggingen und im Kristallin des Schwarzwaldes. *Jahreshefte des geologischen Landesamtes Baden-Württemberg* **18**, 19–37.

Iacono-Marziano, G., Morizet, Y., Le Trong, E. & Gaillard, F. (2012). New experimental data and semi-empirical parameterization of H_2O–CO_2 solubility in mafic melts. *Geochimica et Cosmochimica Acta* **97**, 1–23.

Inoue, T., Irifune, T., Yurimoto, H. & Miyagi, I. (1998). Decomposition of K-amphibole at high pressures and implications for subduction zone volcanism. *Physics of the Earth and Planetary Interiors* **107**, 221-231.

Ionov, D. A., Hofmann, A. W. & Shimizu, N. (1994). Metasomatism-induced Melting in Mantle Xenoliths from Mongolia. *Journal of Petrology* **35**, 753–785.

Ionov, D. A., O'Reilly, S. Y., Genshaft, Y. S. & Kopylova, M. G. (1996). Carbonate-bearing mantle peridotite xenoliths from Spitsbergen: phase relationships, mineral compositions and trace-element residence. *Contributions to Mineralogy and Petrology* **125**, 375–392.

Jankovics, M. E., Taracsák, Z., Dobosi, G., Embey-Isztin, A., Batki, A., Harangi, S. & Hauzenberger, C. A. (2016). Clinopyroxene with diverse origins in alkaline basalts from the western Pannonian Basin: Implications from trace element characteristics. *Lithos* **262**, 120–134.

Jung, C., Jung, S., Hoffer, E. & Berndt, J. (2006). Petrogenesis of Tertiary Mafic Alkaline Magmas in the Hocheifel, Germany. *Journal of Petrology* **47**, 1637–1671.

Jung, S. & Hoernes, S. (2000). The major- and trace-element and isotope (Sr, Nd, O) geochemistry of Cenozoic alkaline rift-type volcanic rocks from the Rhön area (central Germany): petrology, mantle source characteristics and implications for asthenosphere–lithosphere interactions. *Journal of Volcanology and Geothermal Research* **99**, 27–53.

Jung, S. & Masberg, P. (1998). Major- and trace-element systematics and isotope geochemistry of Cenozoic mafic volcanic rocks from the Vogelsberg (central Germany) Constraints on the origin of continental alkaline and tholeiitic basalts and their mantle sources. *Journal of Volcanology and Geothermal Research* **86**, 151–177.

Jung, S., Pfänder, J. A., Brügmann, G. & Stracke, A. (2005). Sources of primitive alkaline volcanic rocks from the Central European Volcanic Province (Rhön, Germany) inferred from Hf, Os and Pb isotopes. *Contributions to Mineralogy and Petrology* **150**, 546–559.

Jung, S., Vieten, K., Romer, R. L., Mezger, K., Hoernes, S. & Satir, M. (2012). Petrogenesis of Tertiary Alkaline Magmas in the Siebengebirge, Germany. *Journal of Petrology* **53**, 2381–2409.

Keller, J., Brey, G., Lorenz, V. & Sachs, P. (1990). *Volcanism and Petrology of the Upper Rhinegraben (Urach-Hegau-Kaiserstuhl)*. In: *Urach, Hegau, Kaiserstuhl: Excursion 2A, August 27 to September 2, 1990*, 1–60.

Keller, J. & Wimmenauer, W. (2015). Rheingrabenvulkanismus: Ein Phlogopit-reiches olivinmelilithitisches Ganggestein von den Stöckenhöfen bei Freiburg (Wittnau-

Biezighofen/Schönberggebiet). *Berichte der Naturforschenden Gesellschaft zu Freiburg im Breisgau* **105**, 87–99.

Klemm, D. D. & Fazakas, H. (1975). Die Schwerspatvorkommen des Odenwaldes. *Aufschluß Sonderband* **27**, 263–266.

Klemme, S. (2004). The influence of Cr on the garnet–spinel transition in the Earth's mantle: experiments in the system $MgO–Cr_2O_3–SiO_2$ and thermodynamic modelling. *Lithos* **77**, 639–646.

Kolb, M., Paulick, H., Kirchenbaur, M. & Münker, C. (2012). Petrogenesis of Mafic to Felsic Lavas from the Oligocene Siebengebirge Volcanic Field (Germany): Implications for the Origin of Intracontinental Volcanism in Central Europe. *Journal of Petrology* **53**, 2349–2379.

Krause, O. (1969). Die Melilith-Nephelinite des Hegaus. Dissertation. Tübingen: Eberhard-Karls-Universität zu Tübingen.

Krause, O. & Weiskirchner, W. (1981). Die Olivin-Nephelinite des Hegaus. *Jahreshefte des geologischen Landesamtes Baden-Württemberg* **23**, 87–130.

Lakroud, K., Remmal, T., Makhoukhi, S. & Balcone-Boissard, H. (2020). Ba- and Ti-rich oxymica from nephelinites in the Middle Atlas Volcanic Province, northern Morocco. *Mineralogy and Petrology* **114**, 119–128.

LaTourrette, T., Hervig, R. & Holloway, J. R. (1995). Trace element partitioning between amphibole, phlogopite, and basanite melt. *Earth and Planetary Science Letters* **135**, 13–30.

Le Maitre, R. W., Streckeisen, A., Zanettin, B., Le Bas, M. J., Bonin, B., Bateman, P., Bellieni, G., Dudek, A., Efremov, S., Keller, J., Lameyre, J., Sabine, P. A., Schmid, R.,

Sørensen, H. & Woolley, A. R. (2002). *Igneous Rocks: A Classification and Glossary of Terms*. Cambridge University Press.

Li, H.-Y., Zhao, R.-P., Li, J., Tamura, Y., Spencer, C., Stern, R. J., Ryan, J. G. & Xu, Y.-G. (2021). Molybdenum isotopes unmask slab dehydration and melting beneath the Mariana arc. *Nature communications* **12**, 6015.

Loges, A., Schultze, D., Klügel, A. & Lucassen, F. (2019). Phonolitic melt production by carbonatite Mantle metasomatism: evidence from Eger Graben xenoliths. *Contributions to Mineralogy and Petrology* **174**, 93.

Lowenstern, J. B. (2001). Carbon dioxide in magmas and implications for hydrothermal systems. *Mineralium Deposita* **36**, 490–502.

Lustrino, M. & Carminati, E. (2007). Phantom plumes in Europe and the circum-Mediterranean region. *The Geological Society of America Special Paper* **430**, 723–745.

Lustrino, M. & Wilson, M. (2007). The circum-Mediterranean anorogenic Cenozoic igneous province. *Earth-Science Reviews* **81**, 1–65.

Mann, U., Marks, M. A. & Markl, G. (2006). Influence of oxygen fugacity on mineral compositions in peralkaline melts: The Katzenbuckel volcano, Southwest Germany. *Lithos* **91**, 262–285.

Mathez, E. A. (1984). Influence of degassing on oxidation states of basaltic magmas. *Nature* **310**, 371–375.

Mayer, B., Jung, S., Romer, R. L., Stracke, A., Haase, K. M. & Garbe-Schönberg, C.-D. (2013). Petrogenesis of Tertiary Hornblende-bearing Lavas in the Rhön, Germany. *Journal of Petrology* **54**, 2095–2123.

Melluso, L., Le Roex, A. P. & Morra, V. (2011). Petrogenesis and Nd-, Pb-, Sr-isotope geochemistry of the Cenozoic olivine melilitites and olivine nephelinites ("ankaratrites") in Madagascar. *Lithos* **127**, 505–521.

Mertes, H. & Schmincke, H.-U. (1985). Mafic potassic lavas of the Quaternary West Eifel volcanic field. *Contributions to Mineralogy and Petrology* **89**, 330–345.

Mertz, D. F., Löhnertz, W., Nomade, S., Pereira, A., Prelević, D. & Renne, P. R. (2015). Temporal–spatial evolution of low-SiO_2 volcanism in the Pleistocene West Eifel volcanic field (West Germany) and relationship to upwelling asthenosphere. *Journal of Geodynamics* **88**, 59–79.

Morizet, Y., Paris, M., Gaillard, F. & Scaillet B. (2010). C–O–H fluid solubility in haplobasalt under reducing conditions: An experimental study. *Chemical Geology* **279**, 1–16.

Nagayoshi, M., Kubo, T. & Kato, T. (2016). Experimental investigation of the kinetics of the spinel-to-garnet transformation in peridotite: A preliminary study. *American Mineralogist* **101**, 2020–2028.

Neave, D. A. & Putirka, K. D. (2017). A new clinopyroxene-liquid barometer, and implications for magma storage pressures under Icelandic rift zones. *American Mineralogist* **102**, 777–794.

Neumann, U., Metz, P. & Westphal, F. (1992). Vulkanismus der Schwäbischen Alb. *Beihefte zum European Journal of Mineralogy* **4**, 1–37.

Ni, H. & Keppler, H. (2013). Carbon in Silicate Melts. *Reviews in Mineralogy & Geochemistry* **75**, 251–287.

Palme, H. & O'Neill, H. (2014). *Cosmochemical Estimates of Mantle Composition*. In: Holland, H. D. & Turekian, K. K. (eds.) *The Mantle and Core*. Elsevier, 1–39.

Pfänder, J. A., Jung, S., Klügel, A., Münker, C., Romer, R. L., Sperner, B. & Rohrmüller, J. (2018). Recurrent Local Melting of Metasomatised Lithospheric Mantle in Response to Continental Rifting: Constraints from Basanites and Nephelinites/Melilitites from SE Germany. *Journal of Petrology* **59**, 667–694.

Pfänder, J. A., Jung, S., Münker, C., Stracke, A. & Mezger, K. (2012). A possible high Nb/Ta reservoir in the continental lithospheric mantle and consequences on the global Nb budget – Evidence from continental basalts from Central Germany. *Geochimica et Cosmochimica Acta* **77**, 232–251.

Pintér, Z., Foley, S. F., Yaxley, G. M., Rosenthal, A., Rapp, R. P., Lanati, A. W. & Rushmer, T. (2021). Experimental investigation of the composition of incipient melts in upper mantle peridotites in the presence of CO_2 and H_2O. *Lithos* **396–397**, 106224.

Przybyla, T., Pfänder, J. A., Münker, C., Kolb, M., Becker, M. & Hamacher, U. (2018). High-resolution $^{40}Ar/^{39}Ar$ geochronology of volcanic rocks from the Siebengebirge (Central Germany)—Implications for eruption timescales and petrogenetic evolution of intraplate volcanic fields. *International Journal of Earth Sciences* **107**, 1465–1484.

Putirka, K. D. (2008). Thermometers and Barometers for Volcanic Systems. *Reviews in Mineralogy and Geochemistry* **69**, 61–120.

Puziewicz, J., Matusiak-Małek, M., Ntaflos, T., Grégoire, M., Kaczmarek, M.-A., Aulbach, S., Ziobro, M. & Kukuła, A. (2020). Three major types of subcontinental lithospheric mantle beneath the Variscan orogen in Europe. *Lithos* **362–363**, 105467.

Ramdohr, P. (1975). Die Lagerstätten des Odenwaldes. *Aufschluß Sonderband* **27**, 235–236.

Ring, U. & Bolhar, R. (2020). Tilting, uplift, volcanism and disintegration of the South German block. *Tectonophysics* **795**, 228611.

Ring, U. & Gerdes, A. (2016). Kinematics of the Alpenrhein-Bodensee graben system in the Central Alps: Oligocene/Miocene transtension due to formation of the Western Alps arc. *Tectonics* **35**, 1367–1391.

Ritter, J. R., Jordan, M., Christensen, U. R. & Achauer, U. (2001). A mantle plume below the Eifel volcanic fields, Germany. *Earth and Planetary Science Letters* **186**, 7–14.

Rupf, I & Nitsch, E. (2008). Das Geologische Landesmodell von Baden-Württemberg: Datengrundlagen, technische Umsetzung und erste geologische Ergebnisse. *LGRB-Informationen* **21**, 1–82.

Rüpke, L. H. (2004). Effects of Plate Subduction on the Earth's Deep Water Cycles. Dissertation. Kiel: Christian-Albrechts-Universität zu Kiel.

Schubert, S., Jung, S., Pfänder, J. A., Hauff, F. & Garbe-Schönberg, D. (2015). Petrogenesis of Tertiary continental intra-plate lavas between Siebengebirge and Westerwald, Germany: Constraints from trace element systematics and Nd, Sr and Pb isotopes. *Journal of Volcanology and Geothermal Research* **305**, 84–99.

Schumacher, M. E. (2002). Upper Rhine Graben: Role of preexisting structures during rift evolution. *Tectonics* **21**, 6-1–6-17.

Seghedi, I. & Downes, H. (2011). Geochemistry and tectonic development of Cenozoic magmatism in the Carpathian–Pannonian region. *Gondwana Research* **20**, 655–672.

Seiberlich, C., Ritter, J. & Wawerzinek, B. (2013). Topography of the lithosphere–asthenosphere boundary below the Upper Rhine Graben Rift and the volcanic Eifel region, Central Europe. *Tectonophysics* **603**, 222–236.

Seifert, W. & Thomas, R. (1995). Silicate-carbonate immiscibility: a melt inclusion study of olivine melilitite and wehrlite xenoliths in tephrite from the Elbe Zone, Germany. *Chemie der Erde – Geochemistry* **55**, 263–279.

Shaw, C. S. (2004). The temporal evolution of three magmatic systems in the West Eifel volcanic field, Germany. *Journal of Volcanology and Geothermal Research* **131**, 213–240.

Staesche, A. (1995). Der genetische Zusammenhang zwischen Melilithiten und Phonolithen des Hegaus, SW-Deutschland. Diploma thesis. Tübingen: Eberhard Karls Universität Tübingen.

Stähle, V., Koch, M., McCammon, C. A., Mann, U. & Markl, G. (2002). Occurrence of low-Ti and high-Ti Freudenbergite in Alkali Syenite Dikes from the Katzenbuckel Volcano, Southwestern Germany. *The Canadian Mineralogist* **40**, 1609–1627.

Stähle, V. & Koch, M. (2003). Primary and secondary pseudobrookite minerals in volcanic rocks from the Katzenbuckel Alkaline Complex, southwestern Germany. *Swiss Bulletin of Mineralogy and Petrology* **83**, 145–158.

Stellrecht, R. & Emmermann, R. (1970). Das Olivinnephelinit-Vorkommen von Forst/Pfalz. *Oberrheinische geologische Abhandlungen* **19**, 29–41.

Stock, M. (1990). Mikrothermometrische Untersuchung der Fluid- und Schmelzeinschlüsse in Olivinen der Nephelinite vom Neuhewen und Hohenstoffeln (Hegau). Diploma thesis. Tübingen: Eberhard Karls Universität Tübingen.

Sun, C. & Dasgupta, R. (2020). Thermobarometry of CO_2-rich, silica-undersaturated melts constrains cratonic lithosphere thinning through time in areas of kimberlitic magmatism. *Earth and Planetary Science Letters* **550**, 116549.

Sundermeyer, C., Gätjen, J., Weimann, L. & Wörner, G. (2020). Timescales from magma mixing to eruption in alkaline volcanism in the Eifel volcanic fields, western Germany. *Contributions to Mineralogy and Petrology* **175**, 77.

Trønnes, R. G. (2002). Stability range and decomposition of potassic richterite and phlogopite end members at 5-15 GPa. *Mineralogy and Petrology* **74**, 129–148.

Ulianov, A., Müntener, O., Ulmer, P. & Pettke, T. (2007). Entrained Macrocryst Minerals as a Key to the Source Region of Olivine Nephelinites: Humberg, Kaiserstuhl, Germany. *Journal of Petrology* **48**, 1079–1118.

Ulrych, J., Ackerman, L., Balogh, K., Hegner, E., Jelínek, E., Pécskay, Z., Přichystal, A., Upton, B. G., Zimák, J. & Foltýnová, R. (2013). Plio-Pleistocene basanitic and melilititic series of the Bohemian Massif: K-Ar ages, major/trace element and Sr–Nd isotopic data. *Geochemistry* **73**, 429–450.

Ulrych, J., Dostal, J., Hegner, E., Balogh, K. & Ackerman, L. (2008). Late Cretaceous to Paleocene melilitic rocks of the Ohře/Eger Rift in northern Bohemia, Czech Republic: Insights into the initial stages of continental rifting. *Lithos* **101**, 141–161.

Ulrych, J., Krmíček, L., Tomek, Č., Lloyd, F. E., Ladenberger, A., Ackerman, L. & Balogh, K. (2016). Petrogenesis of Miocene alkaline volcanic suites from western Bohemia: whole rock geochemistry and Sr–Nd–Pb isotopic signatures. *Geochemistry* **76**, 77–93.

Vaněčková, M., Holub, F. V., Souček, J. & Bowes, D. R. (1993). Geochemistry and petrogenesis of the tertiary alkaline volcanic suite of the Labe tectonovolcanic zone, Czech Republic. *Mineralogy and Petrology* **48**, 17–34.

Veksler, I. V. & Lentz, D. (2006). Parental Magmas of Plutonic Carbonatites, Carbonate-Silicate Immiscibility and Decarbonation Reactions: Evidence from Melt and Fluid Inclusions. *Mineralogical Association of Canada Short Course Series* **36**, 123–150.

Velde, D. & Thiebaut, J. (1973). Quelques précisions sur la constitution minéralogique de la néphélinite à olivine et mélilite d'Essey-la-Côte (Meurthe-et-Moselle). *Bulletin de la Société française de Minéralogie et de Cristallographie* **96**, 298–302.

Velde, D. & Yoder, H. S. (1977). Melilite and melilite-bearing-bearing igneous rocks. *Carnegie Institution of Washington, Yearbook* **76**, 478–485.

Voigt, T., Kley, J. & Voigt, S. (2021). Dawn and dusk of Late Cretaceous basin inversion in central Europe. *Solid Earth* **12**, 1443–1471.

Walter, H.-J. (1994). Spurenelement- und Isotopengeochemie von Megakristallen und Melilithiten des Uracher Vulkangebietes: Signifikanz für die Genese des tertiären zentraleuropäischen Vulkanismus. Diploma thesis. Tübingen: Eberhard Karls Universität Tübingen.

Weaver, B. L. (1991). Trace element evidence for the origin of ocean-island basalts. *Geology* **19**, 123.

Wedepohl, K. H. (1985). Origin of the Tertiary basaltic volcanism in the northern Hessian Depression. *Contributions to Mineralogy and Petrology* **89**, 122–143.

Wedepohl, K. H. & Baumann, A. (1999). Central European Cenozoic plume volcanism with OIB characteristics and indications of a lower mantle source. *Contributions to Mineralogy and Petrology* **136**, 225–239.

Wiechert, U., Ionov, D. A. & Wedepohl, K. H. (1997). Spinel peridotite xenoliths from the Atsagin-Dush volcano, Dariganga lava plateau, Mongolia: a record of partial melting and cryptic metasomatism in the upper mantle. *Contributions to Mineralogy and Petrology* **126**, 345–364.

Wilson, M., Rosenbaum, J. M. & Dunworth, E. A. (1995). Melilitites: partial melts of the thermal boundary layer? *Contributions to Mineralogy and Petrology* **119**, 181–196.

Wimmenauer, W. (1952). Petrographische Untersuchungen an einigen basischen Eruptivgesteinen des Oberrheingrabens. *Neues Jahrbuch für Mineralogie - Abhandlungen (Journal of Mineralogy and Geochemistry)* **83**, 375–432.

Wimmenauer, W. (1974). *The Alkaline Province of Central Europe and France.* In: Sørensen, H. (ed.) *The Alkaline Rocks*, John Wiley, 238–271.

Witt-Eickschen, G. & O'Neill, H. S. (2005). The effect of temperature on the equilibrium distribution of trace elements between clinopyroxene, orthopyroxene, olivine and spinel in upper mantle peridotite. *Chemical Geology* **221**, 65–101.

Wörner, G., Zindler, A., Staudigel, H. & Schmincke, H.-U. (1986). Sr, Nd, and Pb isotope geochemistry of Tertiary and Quaternary alkaline volcanics from West Germany. *Earth and Planetary Science Letters* **79**, 107–119.

Yaxley, G. M., Anenburg, M., Tappe, S., Decree, S. & Guzmics, T. (2022). Carbonatites: Classification, Sources, Evolution, and Emplacement. *Annual Review of Earth and Planetary Sciences* **50**, 261–293.

Ziberna, L., Klemme, S. & Nimis, P. (2013). Garnet and spinel in fertile and depleted mantle: insights from thermodynamic modelling. *Contributions to Mineralogy and Petrology* **166**, 411–421.

Ziegler, P. A. & Dèzes, P. (2005). Evolution of the lithosphere in the area of the Rhine Rift System. *International Journal of Earth Sciences* **94**, 594–614.

Ziegler, P. A., Bertotti, G. & Cloetingh, S. (2002). Dynamic processes controlling foreland development: the role of mechanical (de)coupling of orogenic wedges and forelands. *EGU Stephan Mueller Special Publication Series* **1**, 17–56.

Ziegler, P. A., Schumacher, M. E., Dèzes, P., van Wees, J.-D. & Cloetingh, S. (2004). Post-Variscan evolution of the lithosphere in the Rhine Graben area: constraints from subsidence modelling. *Geological Society, London, Special Publications* **223**, 289–317.

TABLES

Table 1: Sample list for EPMA including locality name, coordinates, and rock type.

Sample	Locality	Latitude (°N)	Longitude (°E)	Rock type
Taunus (A)				
Ehr 42	Hörkopf	50.053756	7.945106	Fsp & Hyn b. ON
3285	Hörkopf summit	50.083742	7.940396	Mca & Fsp b. ON
75, 75-2, 75-3	Naurod (Erbsenacker)	50.124211	8.297219	ON
Ehr 27	Waldburghöhe	50.024974	7.881471	bas. Mca & Rhn b. N
Lower Main plain (B)				
RB-1, 2339, 4563, 2260	Roßdorf (quarry)	49.851361	8.770900	Sdl b. ON
Ng 6	Stetteritz	49.862740	8.798385	ON
Odenwald & Kraichgau (C)				
N 598	Geisberg (Diedesheim)	49.351084	9.115668	Mca b. NH
N 15	Neckarbischofsheim	49.296643	8.952210	ONH
N 17	Steinsberg near Weiler	49.214584	8.876936	phon. Mca b. NB
N 265	Steinsberg near Weiler	49.214584	8.876936	bas. Mca b. N
Stb Ia, Stb Ib	Steinsberg near Weiler	49.214967	8.877751	bas. Mca b. N
Stb IIa, Stb IIb	Steinsberg near Weiler	49.214543	8.877808	phon. Mca b. NB
Stb III	Steinsberg near Weiler	49.214123	8.877179	Mca b. NB
Stb IV	Steinsberg near Weiler	49.214059	8.877382	Mca b. NB
Stb Va, Stb Vb	Steinsberg near Weiler	49.213781	8.877526	phon. Mca b. NB
I 20	Waldbrunn	49.484208	9.040353	phon. Ol b. NN
Urach (D)				
U 019	Bölle	48.576610	9.442799	OM
U 018	Dietenbühl	48.453687	9.484991	Mca b. MON
M 10	Donnstetten	48.514918	9.566112	Nph b. OM
U 015	Eisenrüttel	48.434606	9.420617	Hyn b. ON
U 009	Floriansberg	48.552766	9.309166	Hyn b. OM
U 026	Floriansberg	48.552766	9.309166	Mca b. OM
U 020	Götzenbrühl	48.598122	9.460612	OM
U 021	Götzenbrühl	48.598122	9.460612	Nph b. OM
833	Hohenbol near Owen	48.593610	9.464638	Nph b. OM
U 016	Sternberg	48.394731	9.379102	OM
U 022	Sulzburg	48.561267	9.456890	OM
Lorraine (E)				
LM 455	Essey-la-Côte	48.424436	6.457035	Nph b. OM
N 164	Essey-la-Côte	48.424436	6.457035	NOM
Vosges & Pfälzerwald (F)				
FO 1, FO 2, FO 3	Forst	49.422959	8.161910	ON
LM 1434	Reichshoffen/Reichshofen	48.933541	7.667646	Nph. b. OM
CA 2584	Ribeauvillé/Rappoltsweiler – Cerisier Noir	48.240399	7.269826	ON
LM 729	Riquewihr/Reichenweiher	48.166158	7.299822	Hyn b. ON
Southern URG (G)				
8111, M 13, M 63, M 164	Buggingen potash salt deposit	47.857364	7.621192	Monchiquite
M 34, M 67, M 156	Buggingen potash salt deposit	47.857364	7.621192	OM
M 89, M 109, M 110	Buggingen potash salt deposit	47.878776	7.636801	OM
I 234	Eichwald	47.789323	7.640810	Nph b. OM
N 411	Langental	48.116561	7.933254	ON
N 476	Langental	48.115962	7.936490	ON
2018-001	Mahlberg	48.287146	7.811795	ON
2018-002	Mahlberg	48.287136	7.810812	NOM

Bonndorfer Graben & Freiburger Bucht (H)				
N 119	Berghäuser Kapelle	47.950536	7.788071	Hyn b. ON
N 168	Breitnau	47.937703	8.093403	ON
N 256	Breitnau	47.939313	8.092304	ON
N 45	Hammereisenbach	47.994605	8.309203	Mll b. ON
2018-003	Heuweiler	48.049401	7.906876	Hyn b. ON
N 55	Hirzberg	47.996718	7.871811	Hyn b. ON
N 369	Hirzberg	47.996220	7.876109	Hyn b. ON
H 161	Horben, cable car valley station	47.939616	7.863550	Mca b. ON
N 364	Jostal	47.929961	8.188687	Mca b. ON
N 46	Rautebacher Höfe	48.016845	7.879012	Hyn b. ON
N 104	Rotteckruhe	48.014930	7.912833	ON
N 94	St. Ottilien	47.996423	7.878383	Hyn b. ON
N 96	St. Ottilien	47.996423	7.878383	Hyn & Mca b. ON
N 146	St. Ottilien	48.002389	7.900098	Hyn & Mca b. ON
N 47	Uhlberg	48.017671	7.889987	Mca b. ON
N 112	Weilersbachdobel, vineyard	47.962702	7.869873	Mca b. ON
Hegau (I)				
HEG 12	Blauer Stein (Randen)	47.825537	8.597696	Mll b. ON
N 374	Blauer Stein (Randen), Steinröhren	47.826987	8.598313	Mll b. ON
HEG 17	Hohenhewen	47.835623	8.747227	Mll b. ON
HEG 04	Hohenstoffel	47.794465	8.750537	NOM
HEG 15	Neuhewen	47.879057	8.717537	Mll b. ON
HEG 20	Riedheim dyke	47.763659	8.753926	NOM
HEG 18	Sennhof	47.789871	8.755671	OM
HEG 16	Wartenberg	47.915868	8.631607	ON
I 63	Wasserburger Tal	47.900917	8.871255	ON

b. – bearing; bas. – basanitic; Fsp – feldspar; Hyn – haüyne; Mca – mica; Mll – melilite; Nph – nepheline; Rhn – rhönite; Sdl – sodalite; HM – haüyne melilitite; MON – melilite olivine nephelinite; N – noseanite; NB – nepheline basanite; NH – nepheline haüynite; NN – nepheline noseanite; NOM – nepheline olivine melilitite; OM – olivine melilitite; ON – olivine nephelinite; ONH – olivine nepheline haüynite; phon. – phonolitic.

Table 2: Modal mineralogy of studied CEVP rocks. Distinctive values are in italic, characteristic accessories in bold (modified after Binder *et al.*, 2023).

Rock series region	Ol	Cpx	Spl/ Usp	Mca	Mll	Nph +Zeo	Hyn/ Nsn/ Sdl	Pl	Afs	Acc.
Olivine nephelinites and nepheline basanites										
Vosges & Pfälzerwald	*20–30*	*40–55*	5–15	< 5	–	*5–20*	Acc.	–	–	ap
Taunus	*10–35*	*35–50*	5–15	< 10	–	*< 20*	Acc.	< 10	< 5	**ap**, ttn
Bonndorfer Graben & Freiburger Bucht	*10–40*	*20–60*	5–15	< 10	–	*< 20*	< 10	–	–	**ap**
Odenwald & Kraichgau	*15–30*	*15–35*	10–20	*< 25*	–	*5–10*	< 5	< 15	< 5	ap
Lower Main plain	*20–25*	*30–35*	10–15	< 5	–	*20–25*	< 5	–	–	ap
Southern URG & Hegau	*20–35*	*20–50*	10–15	<5	–	*10–25*	Acc.	–	–	**ap**, prv
(Phonolitic) haüynites and haüyne nephelinites										
Odenwald & Kraichgau	< 10	*10–30*	15–20	< 10	–	< 10	*10–20*	–	< 10	***ap** (< 10)*
Olivine melilitites and melilite-bearing nephelinites										
Hegau	*20–40*	10–35	10–15	< 5	*< 20*	*< 20*	< 5	–	–	**prv**, ap
Urach	*20–50*	< 30	~15	< 5	*< 40*	*< 10*	< 5	–	–	**prv**, ap
Southern URG	*20–30*	25–30	< 20	< 5	*< 20*	*10–25*	Acc.	–	–	**prv**, ap, grt
Lorraine	*25–35*	~30	10–15	Acc.	*5–10*	*< 10*	Acc.	–	–	**prv**
Vosges*	*~30*	~10	10–15	Acc.	*15–20*	*< 5*	Acc.	–	–	ap

Ol – olivine; Cpx – clinopyroxene; Spl – spinel group; Usp – ulvöspinel; Mca – mica; Mll – melilite; Nph – nepheline; Zeo – zeolites; Hyn – haüyne; Nsn – nosean; Sdl – sodalite; Pl – plagioclase; Afs – alkali feldspar; Acc. – accessory minerals; ap – apatite; prv – perovskite; grt – garnet; ttn – titanite
* The difference to 100 % results from optically not resolvable mineral phases due to alteration or microcrystalline matrix minerals.

Table 3: Petrographic, geochemical, mineral chemical, and geochronological differences between the two primitive rock groups and the evolved rock series in the southern CEVP.

Rock group	Olivine nephelinites, basanitic nephelinites & nepheline basanites	(Phonolitic) haüynites, noseanites & haüyne nephelinites	Olivine melilitites & melilite-bearing olivine nephelinites
Petrography			
Phenocrysts	clinopyroxene and olivine dominant	haüyne/nosean and clinopyroxene dominant	olivine and melilite dominant
Occurrence of feldspar	occasional	yes	no
Occurrence of perovskite	no	no	yes
Occurrence of amphibole	occasional	occasional	no
Green-core pyroxenes	frequent	no	no
Occurrence of apatite	in groundmass and as anhedral inclusions in clinopyroxene	in groundmass and as euhedral phenocrysts	only in groundmass
Whole-rock geochemistry			
MgO	medium–high (8–16 wt.%)	low (4–6 wt.%)	high–very high (10–21 wt.%)
Na_2O+K_2O	low (2.5–7.5 wt.%)	high (6.5–11.5 wt.%)	low (1.0–7.5 wt.%)
CaO	medium (11–17 wt.%)	low (5.5–10 wt.%)	high (9.5–21 wt.%)
P_2O_5	low (0.1–1.4 wt.%)	high (1.4–3.8 wt.%)	low (0.5–1.3 wt.%)
Ni	low–medium (50–500 ppm)	very low (<30 ppm)	medium–high (120–620 ppm)
Co	medium (40–65 ppm)	low (5–40 ppm)	medium–high (40–100 ppm)
Cr	low–medium (30–800 ppm)	very low (<5 ppm)	medium–high (200–1600 ppm)
Nb	low–medium (20–120 ppm)	high (130–240 ppm)	medium–high (70–160 ppm)
Zn	low–medium (60–140 ppm)	high (160–340 ppm)	low (60–120 ppm)
Y/La	high (26.7–28.4)	high (~27.5)	varying (22.4–27.8)
REE enrichment	medium	high	medium
Mineral chemistry			
Ca-Ni ratio in olivine cores	higher Ca than expected in mantle olivine	far away from mantle ratio (medium Ca, low Ni)	Ca-Ni mantle ratio abundant
Resorbed olivine cores	no	no	Fe-rich cores occur frequently
X_{Mg} in olivine rims	low–medium (0.73–0.88)	low(0.73–0.83)	medium–high (0.83–0.93)
Spinel core composition	Al-accentuated	no Mg-rich cores	Cr+Al-accentuated
Mica composition	oxy- and hydroxy-mica, K-rich, Na-accentuated	oxy- and hydroxy-mica, K-rich, Na-accentuated	F- and Ba-rich mica, Na-poor
X_{Mg} in mica	medium–high (~0.60–0.80)	medium (~0.56–0.68)	high (~0.68–0.95)
Apatite composition	incl. in cpx: hydroxyapatite; groundmass: fluorapatite	Cl-rich fluorapatite, SO_4-rich, Sr-accentuated	fluorapatite
Geochronology	73–47 Ma	68–62 Ma	27–9 Ma

FIGURES

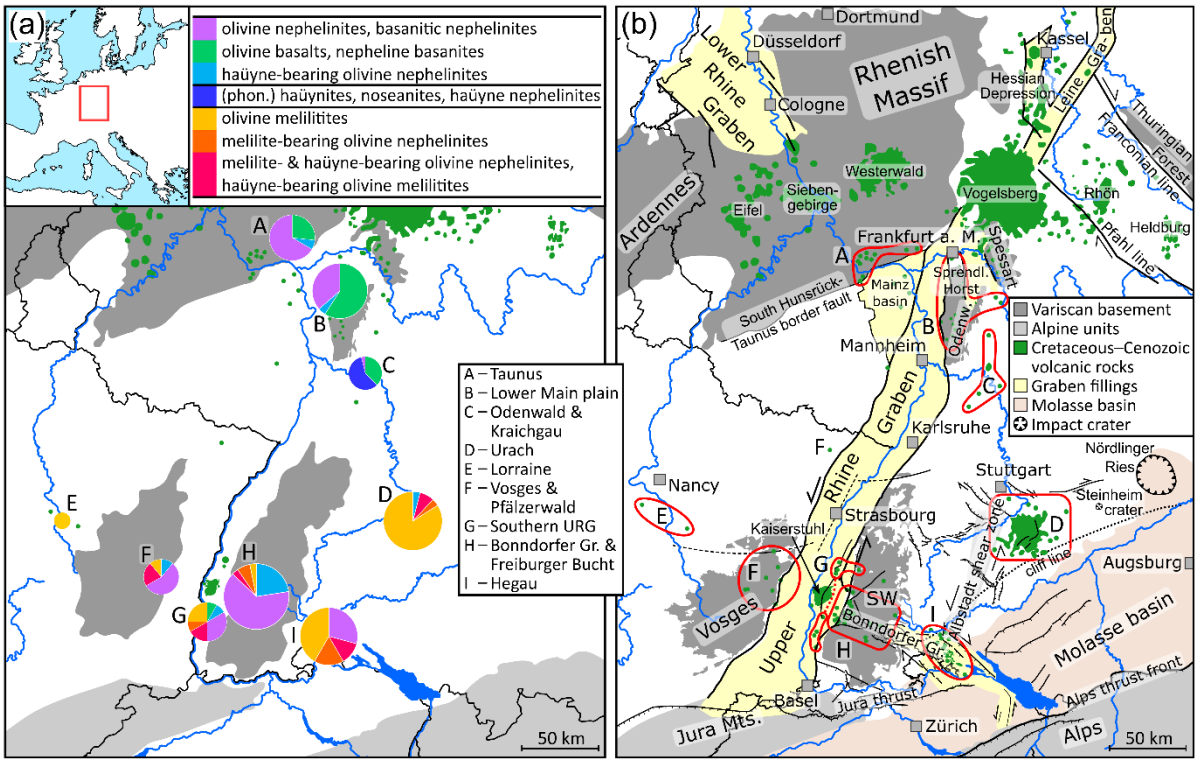

Fig. 1. Maps of the southern CEVP. **(a)** Circular diagrams show the semi-quantitative distribution of SiO_2-undersaturated rock types in each study region. Circle sizes correlate with the number of described occurrences. **(b)** Simplified geologic map showing major tectonic structures with the studied regions outlined red (modified after Egli *et al.*, 2017 and Binder *et al.*, 2023).

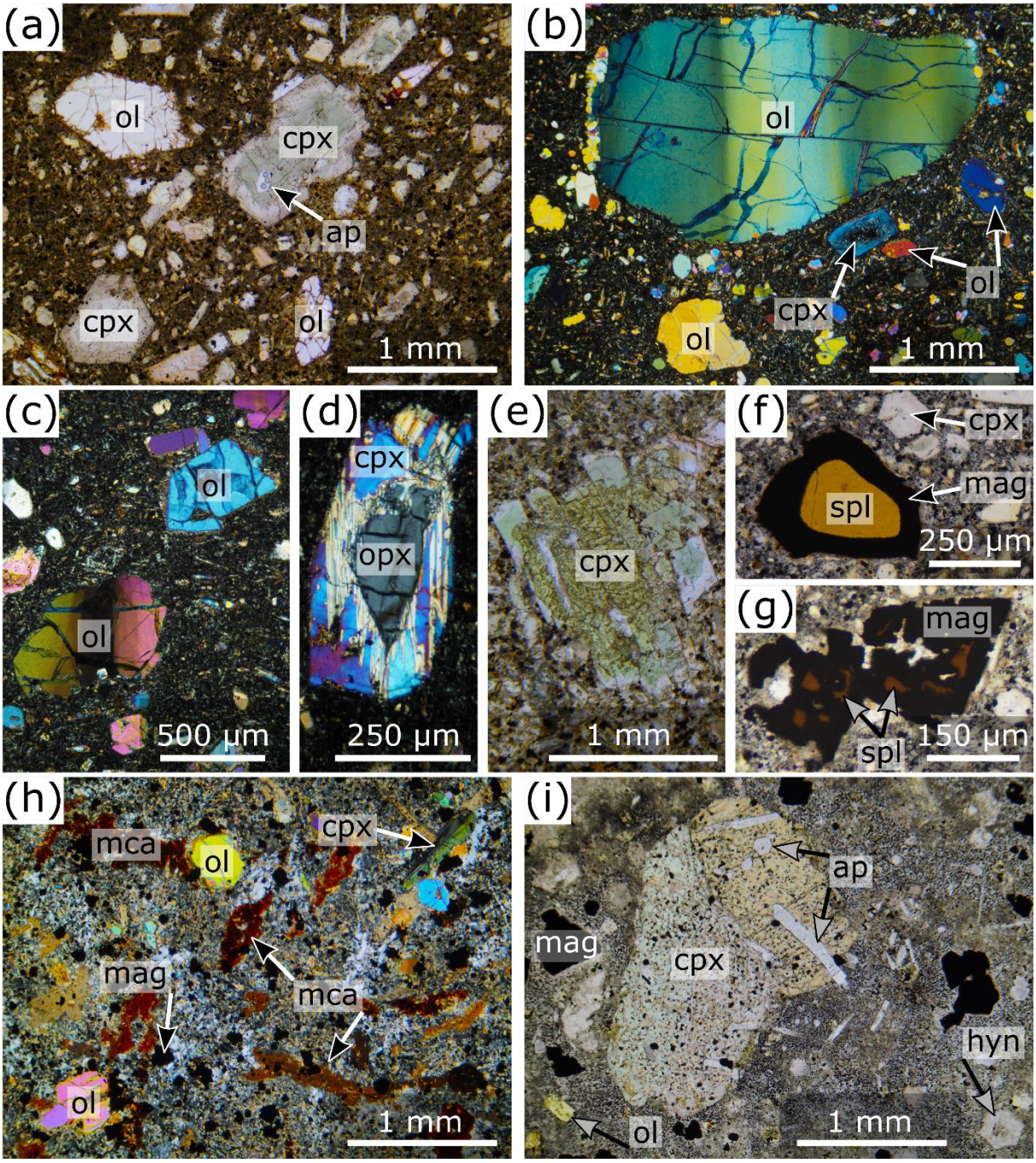

Fig. 2. Petrography of the Upper Cretaceous–Eocene CEVP rocks. **(a)** Olivine nephelinite with olivine (ol) and clinopyroxene (cpx) macrocrysts, green-core pyroxenes with apatite (ap) inclusion; microcrystalline groundmass (Rotteckruhe, Freiburger Bucht). **(b)** Olivine nephelinite with an anhedral olivine macrocryst showing wavy extinction and a euhedral clinopyroxene crystal containing an inclusion-rich core; microcrystalline groundmass (Breitnau, Bonndorfer Graben; # polarization). **(c+d)** Olivine nephelinite with anhedral olivine showing wavy extinction, euhedral olivine of similar size, partly resorbed orthopyroxene (opx) overgrown by clinopyroxene showing lamellar twinning; fine-grained groundmass (Jostal, Bonndorfer Graben; # polarization). **(e)** Olivine nephelinite with inclusion-rich resorbed green-core pyroxene showing a spongy, porous texture (Hirzberg, Freiburger Bucht). **(f+g)** Olivine nephelinite with a resorbed oxyspinel core (spl) surrounded by a magnetite-ulvöspinel$_{ss}$ (mag) fringe and oxyspinel showing porous labyrinthine to spongy dissolution structures

overgrown and partly resorbed by magnetite-ulvöspinel$_{ss}$ (Naurod/Erbsenacker, Taunus). **(h)** Mica-rich nepheline basanite with dark mica (mca), olivine, twinned sector-zoned clinopyroxene, magnetite, and fine-grained groundmass (Steinsberg, Kraichgau; # polarisation). **(i)** Olivine-bearing nepheline haüynite with poikilitic clinopyroxene, enclosing euhedral apatite, haüyne (hyn), magnetite, and olivine with fine-grained groundmass (Neckarbischofsheim, Kraichgau).

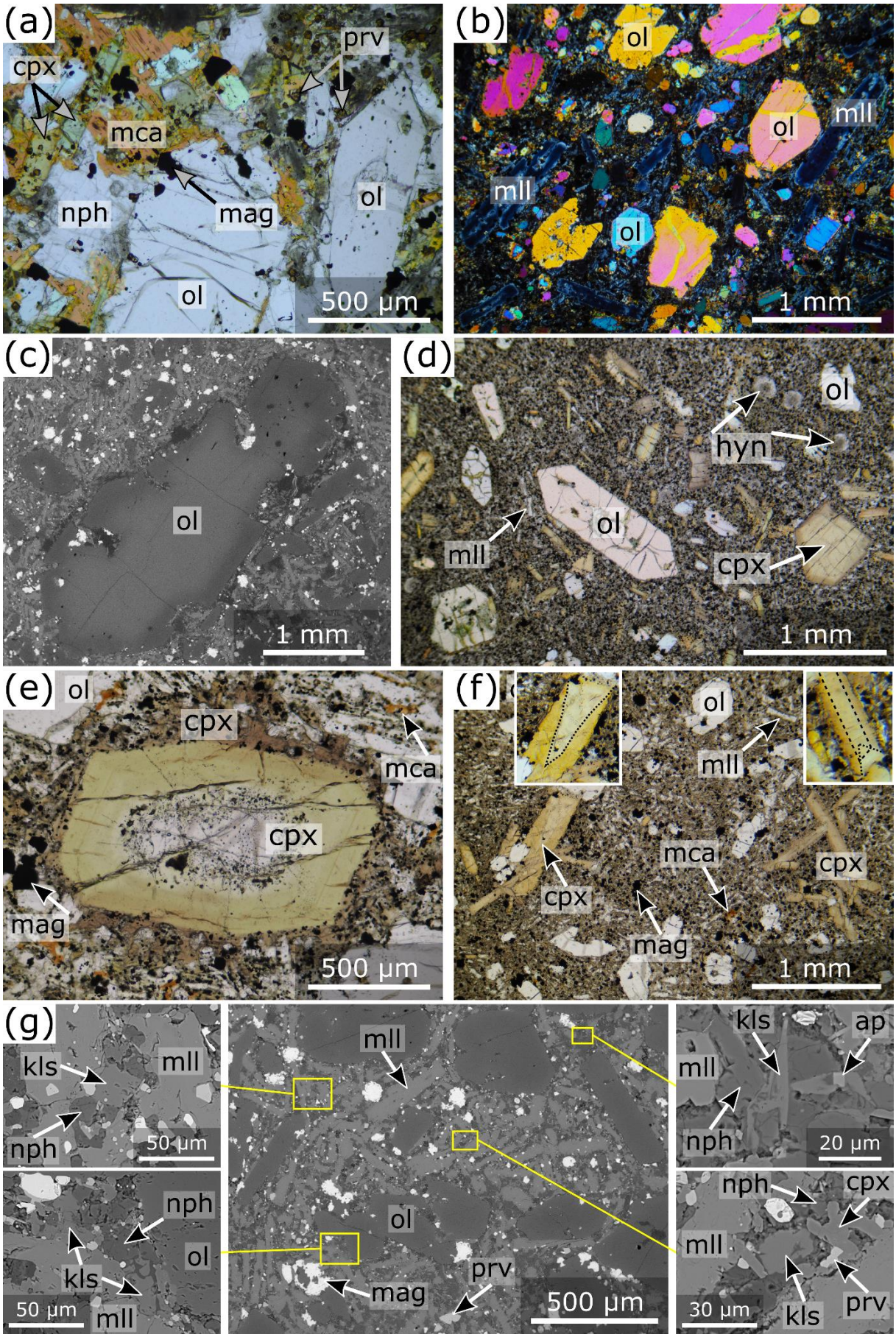
(a)
prv
cpx
mca
nph
mag
ol
ol
500 µm
(b)
ol
ol
mll
mll
ol
1 mm
(c)
ol
1 mm
(d)
ol
hyn
ol
mll
cpx
1 mm
(e)
ol
cpx
mca
cpx
mag
500 µm
(f)
ol
mll
mca
cpx
cpx
mag
1 mm
(g)
kls
mll
nph
50 µm
mll
ol
prv
mag
500 µm
kls
ap
mll
nph
20 µm
nph
ol
kls
50 µm
mll
nph
cpx
mll
kls
prv
30 µm

Fig. 3. Petrography of the Oligocene–Miocene CEVP rocks. **(a)** Mica-bearing melilite olivine nephelinite comprising euhedral to subhedral olivine; groundmass of tabular and interstitial nepheline (nph), euhedral perovskite (prv), clinopyroxene, dark mica, and magnetite-ulvöspinel$_{ss}$ (Dietenbühl, Urach). **(b)** Olivine melilitite with olivine and euhedral melilite (mll) macrocrysts (Hohenbol, Urach; # polarisation). **(c)** BSE image of an olivine melilitite showing a reversely zoned olivine macrocryst with partly resorbed Fo-depleted core surrounded by a more forsteritic rim (Sternberg, Urach). **(d)** Nepheline-bearing olivine melilitite with euhedral olivine, zoned clinopyroxene, and small haüyne crystals; fine-grained groundmass (Homboll, Hegau). **(e)** Olivine melilitite showing a euhedral clinopyroxene crystal with pale, partly resorbed and inclusion-rich core overgrown by a greenish-brownish, weakly zoned fringe, in turn surrounded by reddish-brownish late-stage clinopyroxene; groundmass of melilite, clinopyroxene, magnetite-ulvöspinel$_{ss}$, and dark mica (Wittlinger Steige, Urach). **(f)** Nepheline-bearing olivine melilitite with olivine macrocrysts and agglomerations of clinopyroxene; fine-grained groundmass (Hohenstoffeln, Hegau). **(g)** BSE image showing an olivine melilitite with rare interstitial subhedral–anhedral kalsilite, accompanied by nepheline, magnetite-ulvöspinel$_{ss}$, perovskite, and apatite (Sternberg, Urach).

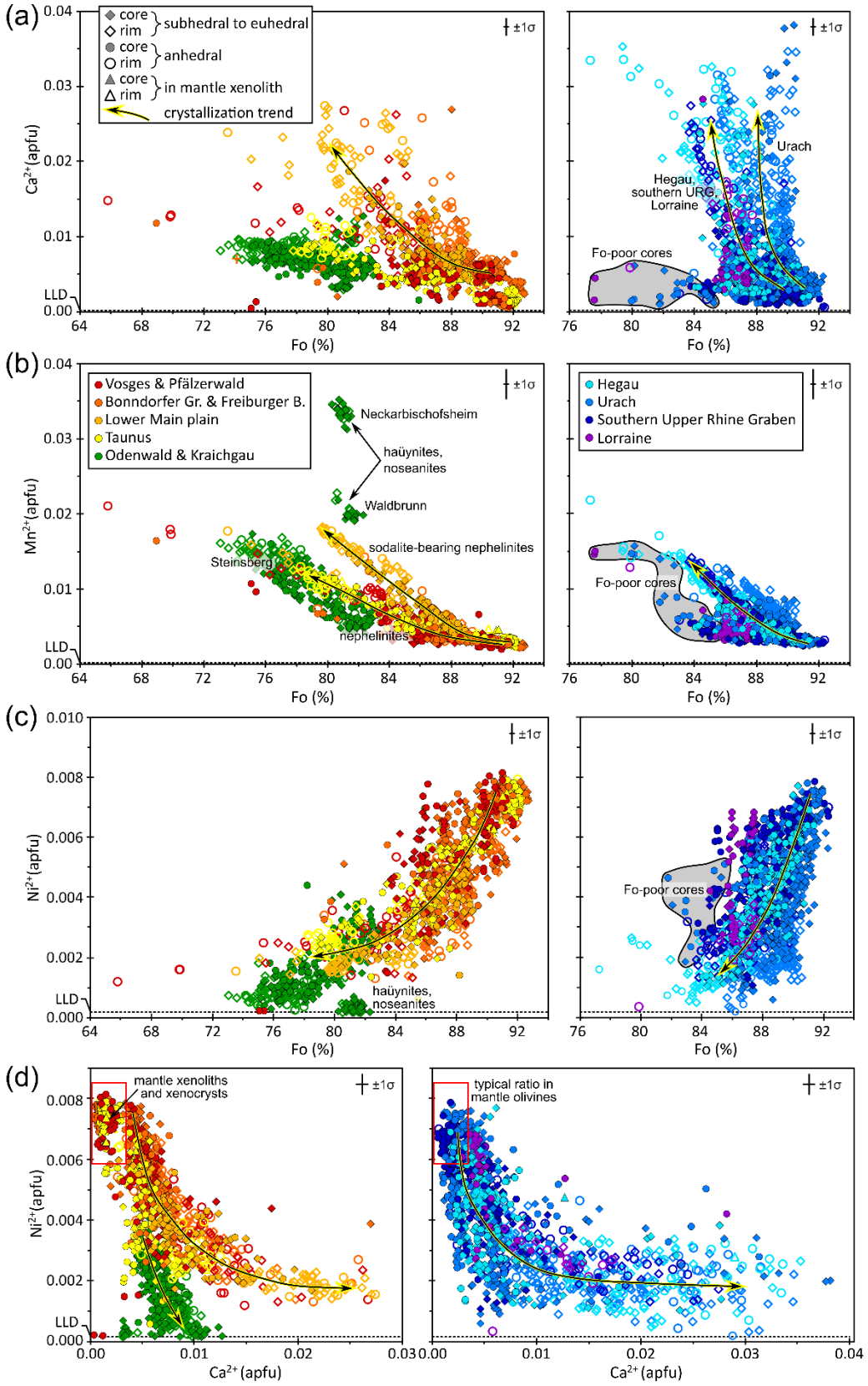

Fig. 4. Olivine composition in the CEVP rocks with data from this study supplemented by data from Braunger *et al.* (2021). LLD – lower limit of detection. Contents (in apfu) of **(a)** Ca^{2+}, **(b)** Mn^{2+}, **(c)** Ni^{2+} plotted against forsterite, and **(d)** Ca^{2+} vs. Ni^{2+}. The area outlined in red represents typical compositions of olivine in mantle peridotite (Foley *et al.*, 2013; Bussweiler *et al.*, 2015).

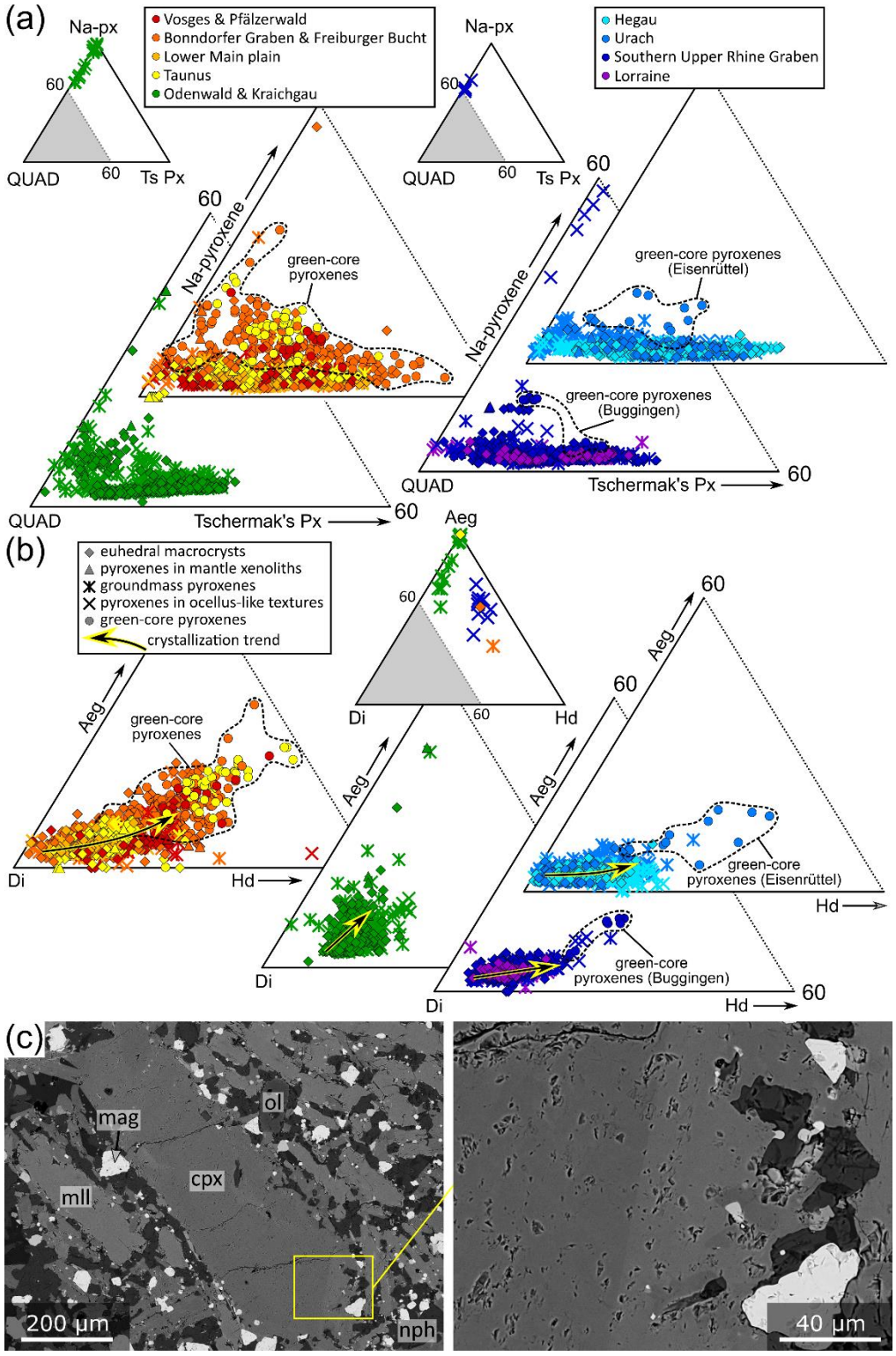

Fig. 5. Clinopyroxene composition in the CEVP rocks with data from this study supplemented by data from Braunger *et al.* (2021). **(a)** Triangular plot showing the distribution among the quadrilateral end-members (QUAD), Tschermak's clinopyroxenes ($CaXXSiO_6$ with X = Al, Fe^{3+}, Cr, Ti), and Na pyroxenes (aegirine – $NaFe^{3+}Si_2O_6$, Ti aegirine – $NaFe^{2+}_{0.5}Ti_{0.5}Si_2O_6$, jadeite – $NaAlSi_2O_6$). **(b)** Triangular plot showing the distribution among diopside (Di), aegirine (Aeg), and hedenbergite (Hd) end-members normalized to 100 %. **(c)** BSE image of a nepheline-bearing olivine melilitite (Donnstetten, Urach) showing a zoned clinopyroxene macrocryst with Al, Fe^{3+}, and Ti contents increasing towards the rim at the expense of Si and Mg.

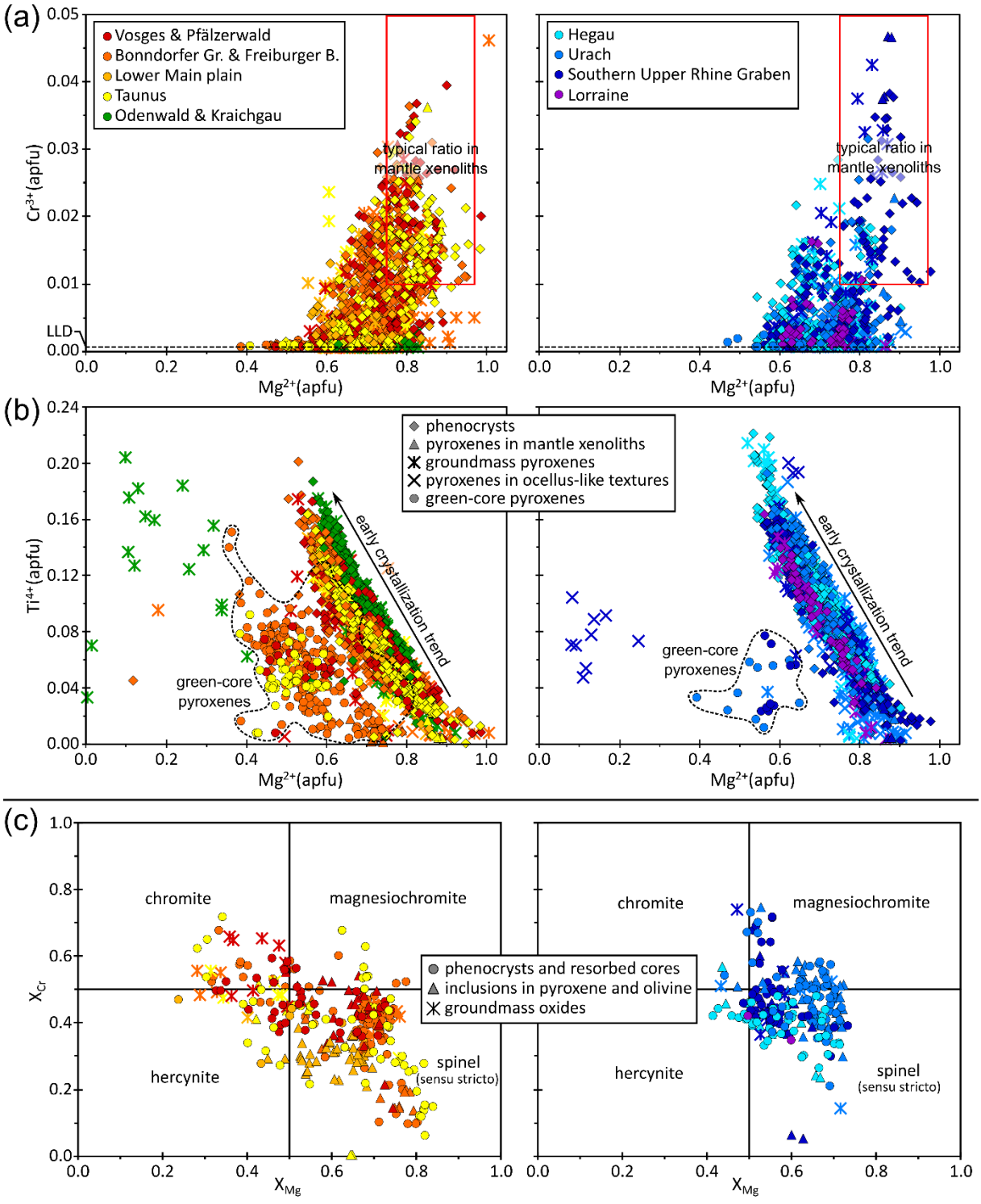

Fig. 6. **(a-b)** Clinopyroxene and **(c)** spinel composition in the CEVP rocks. Own data supplemented by Buggingen, southern URG (Braunger *et al.*, 2021). LLD – lower limit of detection; apfu – atoms per formula unit. **(a)** Mg^{2+} vs. Cr^{3+}. The area outlined in red represents the typical composition in mantle xenoliths (Witt-Eickschen & O'Neill, 2005; this study). **(b)** Mg^{2+} vs. Ti^{4+}. **(c)** Classification of Mg-Cr-Al spinels with Cr+Al (apfu) >1 using $X_{Mg} = Mg_{molar}/(Mg+Fe^{2+})_{molar}$ vs. $X_{Cr} = Cr_{molar}/(Cr+Al)_{molar}$. Thus, magnetite and ulvöspinel are not considered.

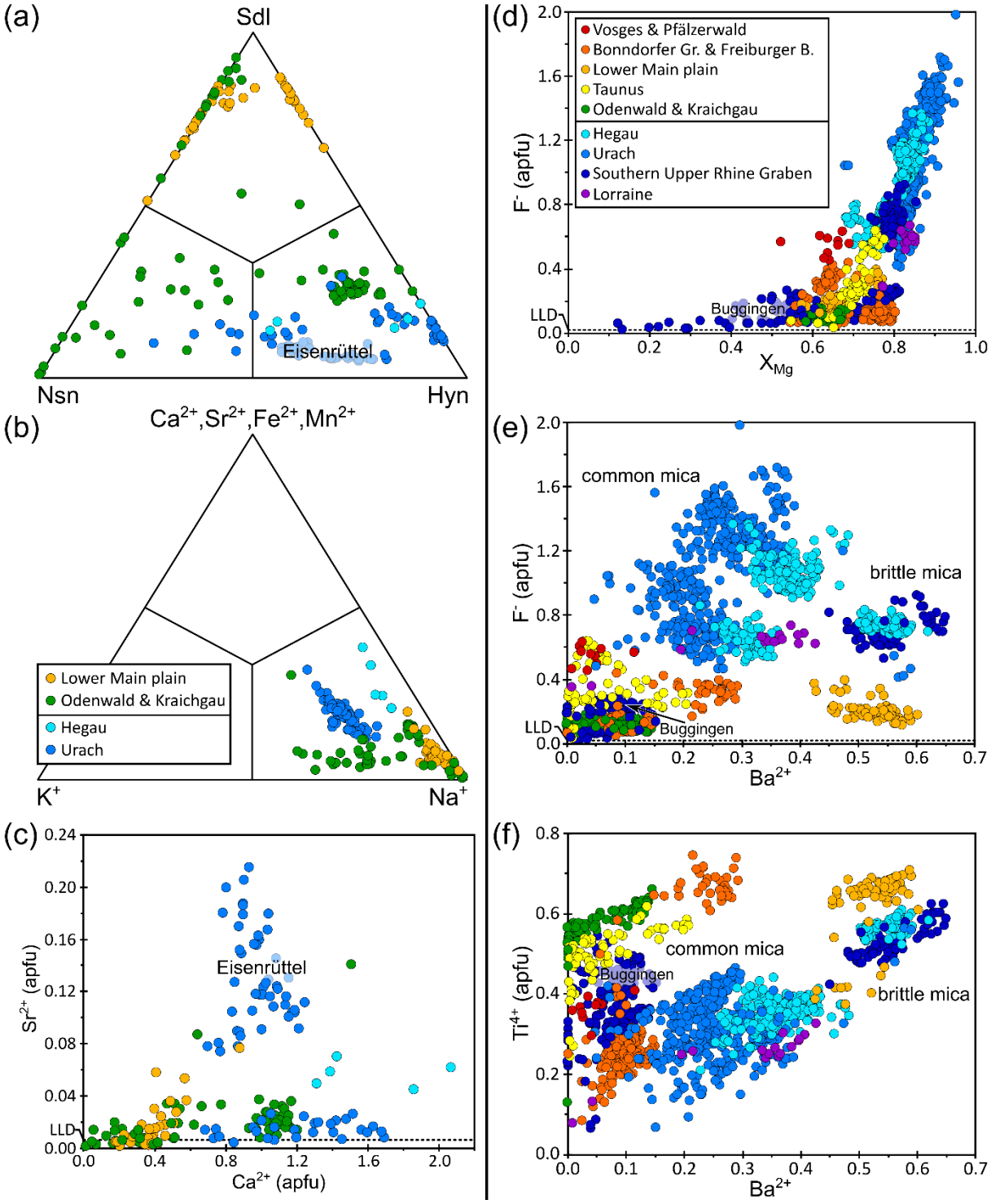

Fig. 7. (a-c) Haüyne-nosean-sodalite$_{ss}$ composition in the CEVP rocks. Triangular diagrams showing **(a)** the end-member composition of sodalite group minerals based on the ratio between 2 SO_4^{2-}, SO_4^{2-}, and 2 Cl^-, with sodalite – $Na_6[Al_6Si_6O_{24}]Cl_2$ (Sdl), haüyne – $(Na,K)_6Ca_2[Al_6Si_6O_{24}](SO_4)_2$ (Hyn), and nosean – $Na_6[Al_6Si_6O_{24}]SO_4$ (Nsn), and **(b)** the molar K-Na-Ca,Sr,Fe,Mn distribution. **(c)** Ca^{2+} (apfu) vs. Sr^{2+} (apfu). **(d-f)** Mica composition in the CEVP rocks. Own data supplemented by Buggingen, southern URG (Braunger *et al.*, 2021). **(d)** $X_{Mg} = Mg_{molar}/(Mg+Fe)_{molar}$ vs. F^-. **(e)** Ba^{2+} vs. F^-. **(f)** Ba^{2+} vs. Ti^{4+}. LLD – lower limit of detection. apfu – atoms per formula unit.

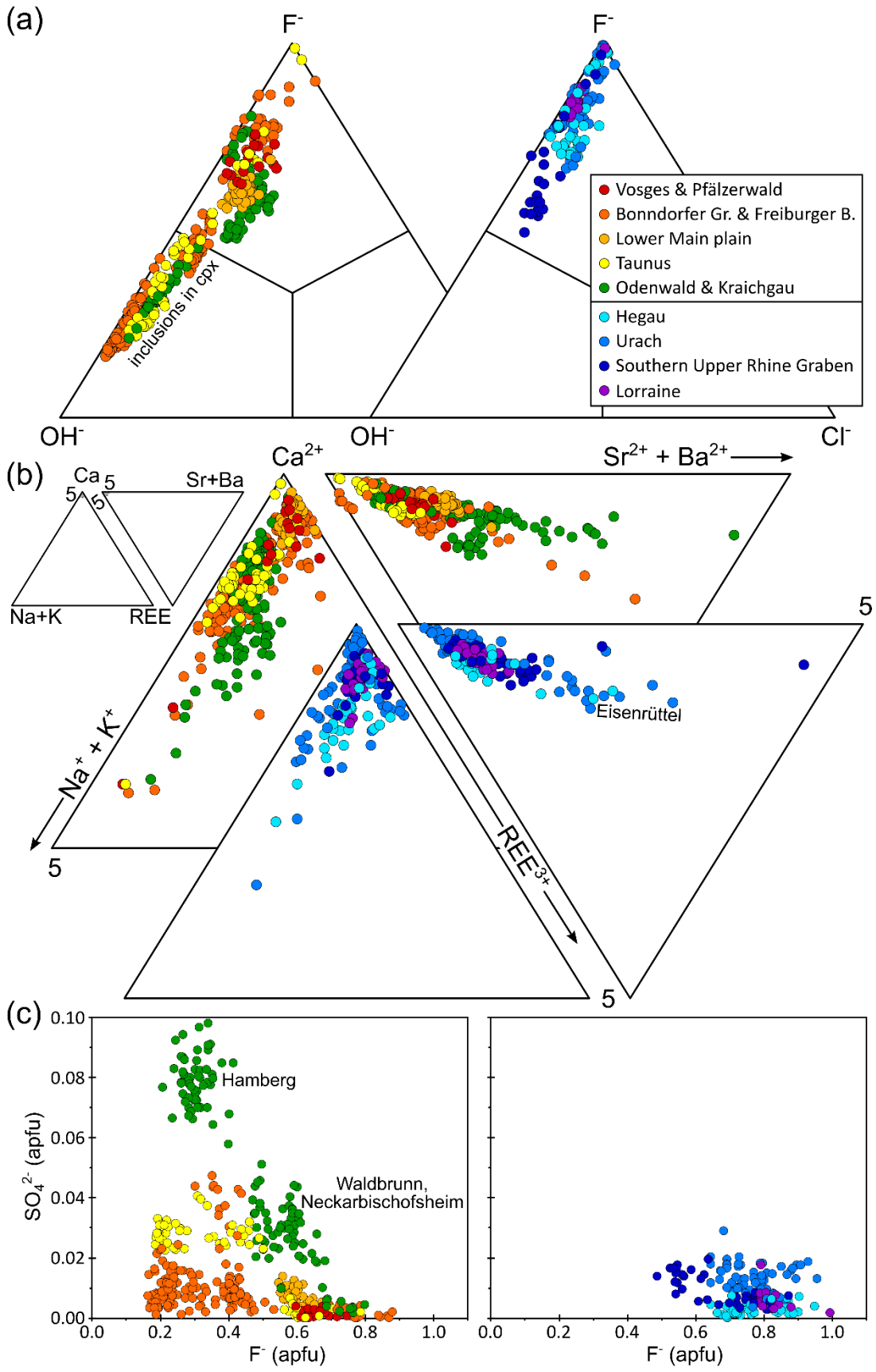

Fig. 8. Apatite composition in the CEVP rocks. **(a)** Triangular classification diagram based on the anion position (OH^-, F^-, Cl^-). **(b)** Triangular diagrams showing the molar Ca-Na+K-REE distribution and the molar Ca-Sr+Ba-REE distribution each normalized to 100 %. **(c)** F^- (apfu) vs. SO_4^{2-} (apfu).

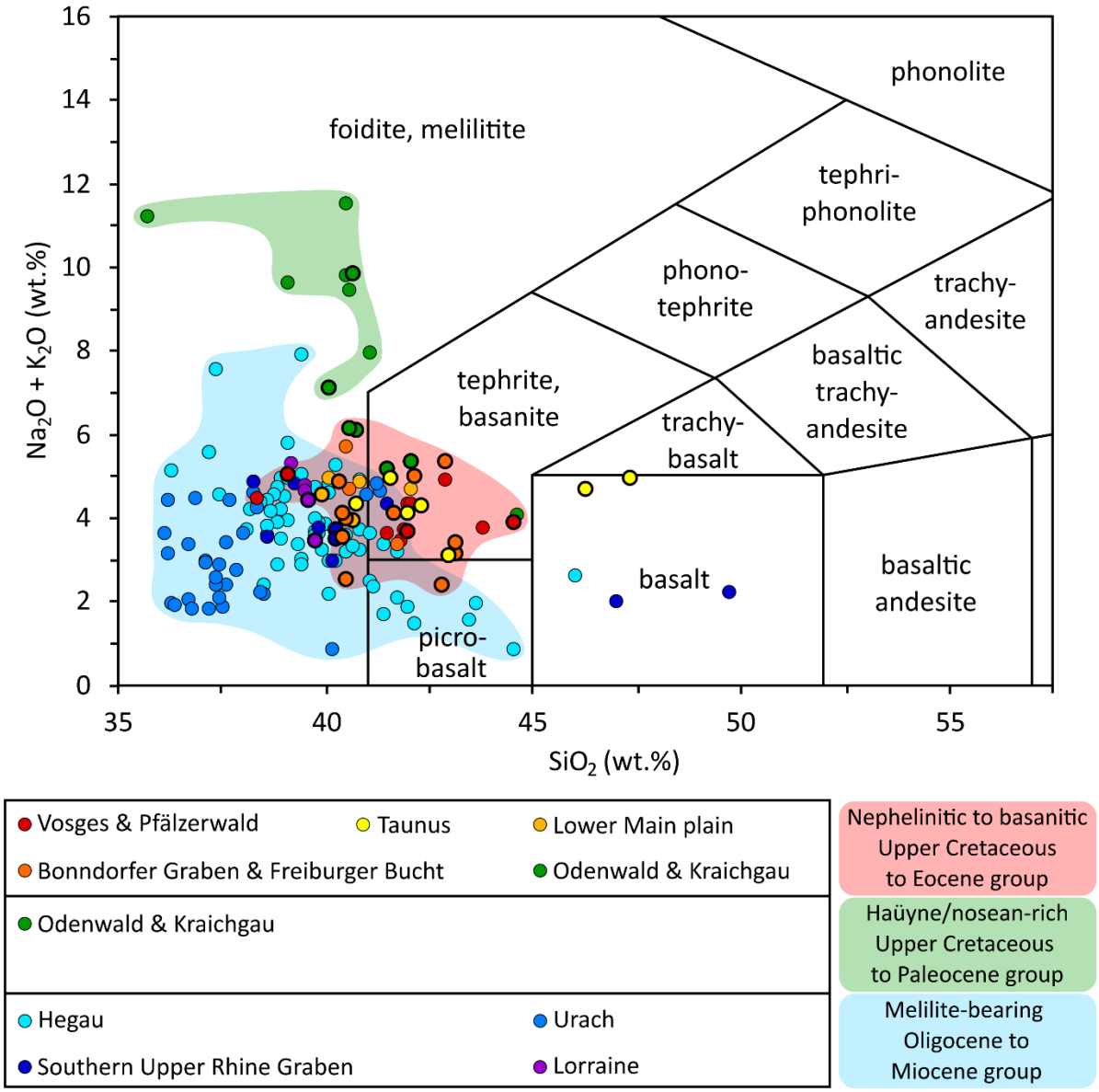

Fig. 9. TAS diagram showing compositions of the CEVP rocks with 34 new analyses (black-rimmed circles) supplemented by literature data from Becker (1904), Freudenberg (1906), Wimmenauer (1952), Krause (1969), Stellrecht & Emmermann (1970), Velde & Thibaut (1973), Wimmenauer (1974), Frenzel (1975), Hurrle (1976), Berg & Weiskirchner (1979), Krause & Weiskirchner (1981), Alibert *et al.* (1983), Butchereit (1990), Keller *et al.* (1990), Stock (1990), Neumann *et al.* (1992), Walter (1994), Hegner *et al.* (1995), Staesche (1995), Dunworth & Wilson (1998), Stähle *et al.* (2002). Data have been renormalized to a volatile-free composition. Note that the naming of the rocks was based on the mineral composition, which is why the position in the TAS diagram may differ from the assigned rock name.

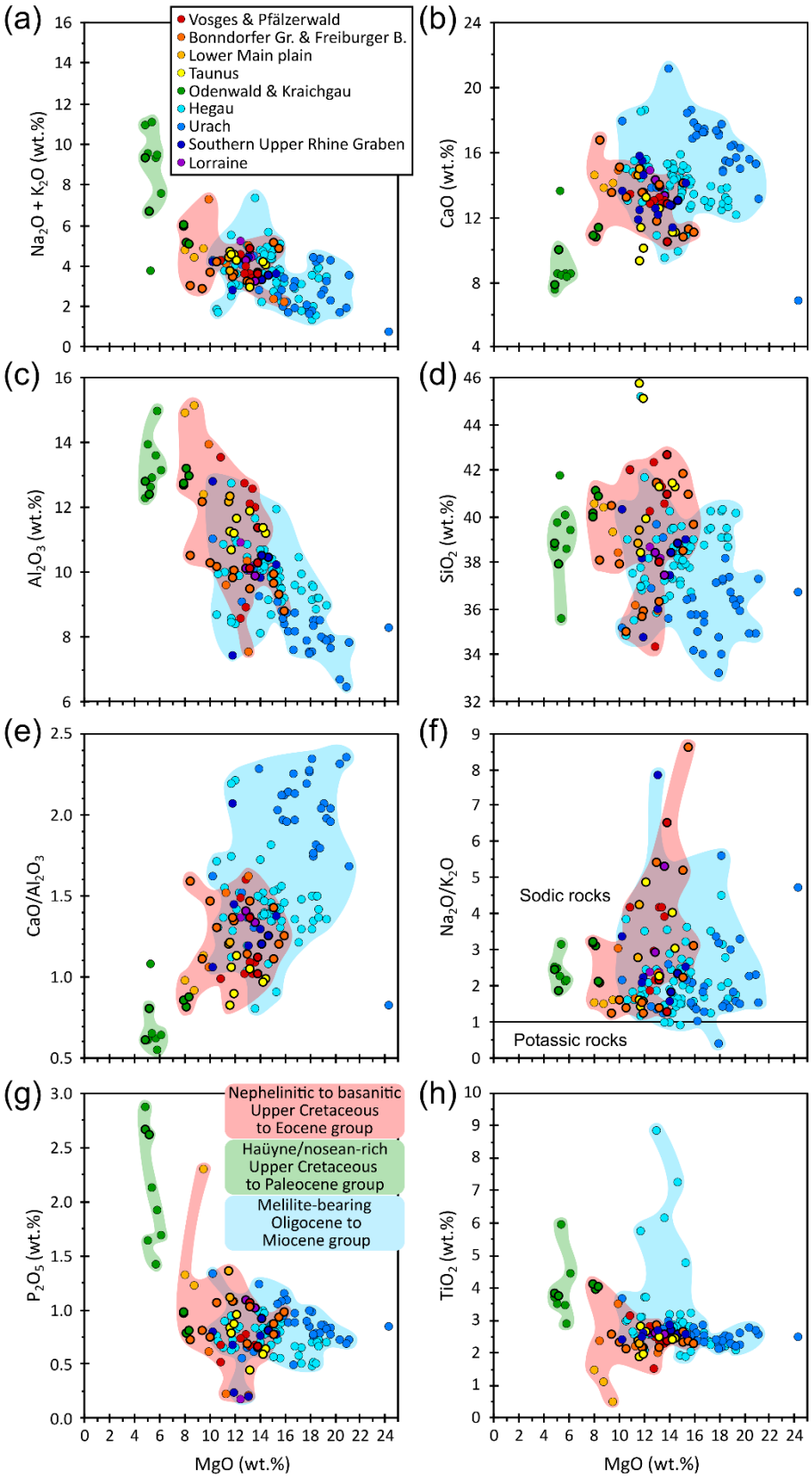

Fig. 10. Whole-rock composition of the CEVP rocks with 34 new analyses (black-rimmed circles) supplemented by literature data as cited in Fig. 9. Concentrations of **(a)** Na_2O+K_2O, **(b)** CaO, **(c)** Al_2O_3, and **(d)** SiO_2 plotted against wt.% MgO. **(e)** CaO/Al_2O_3- and **(f)** Na_2O/K_2O-ratio vs. wt.% MgO. **(g)** P_2O_5, and **(h)** TiO_2 vs. wt.% MgO. Data represent original contents not renormalized to a volatile-free composition.

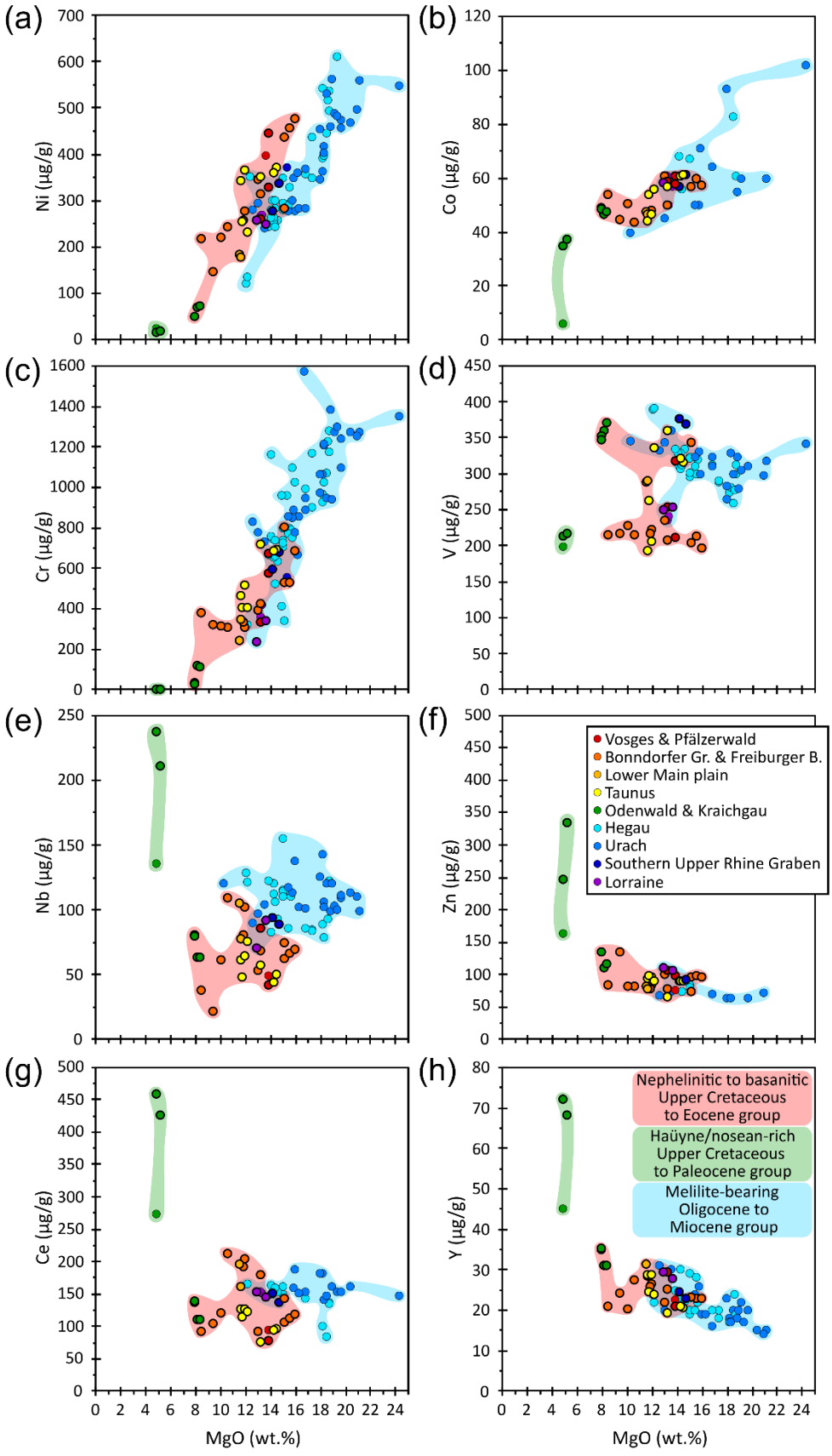

Fig. 11. Whole-rock trace element concentrations of the CEVP rocks. 34 new analyses (black-rimmed circles) supplemented by literature data as cited in Fig. 9. Concentrations (in µg/g) of **(a)** Ni, **(b)** Co, **(c)** Cr, **(d)** V, **(e)** Nb, **(f)** Zn, **(g)** Ce, and **(h)** Y plotted against wt.% MgO.

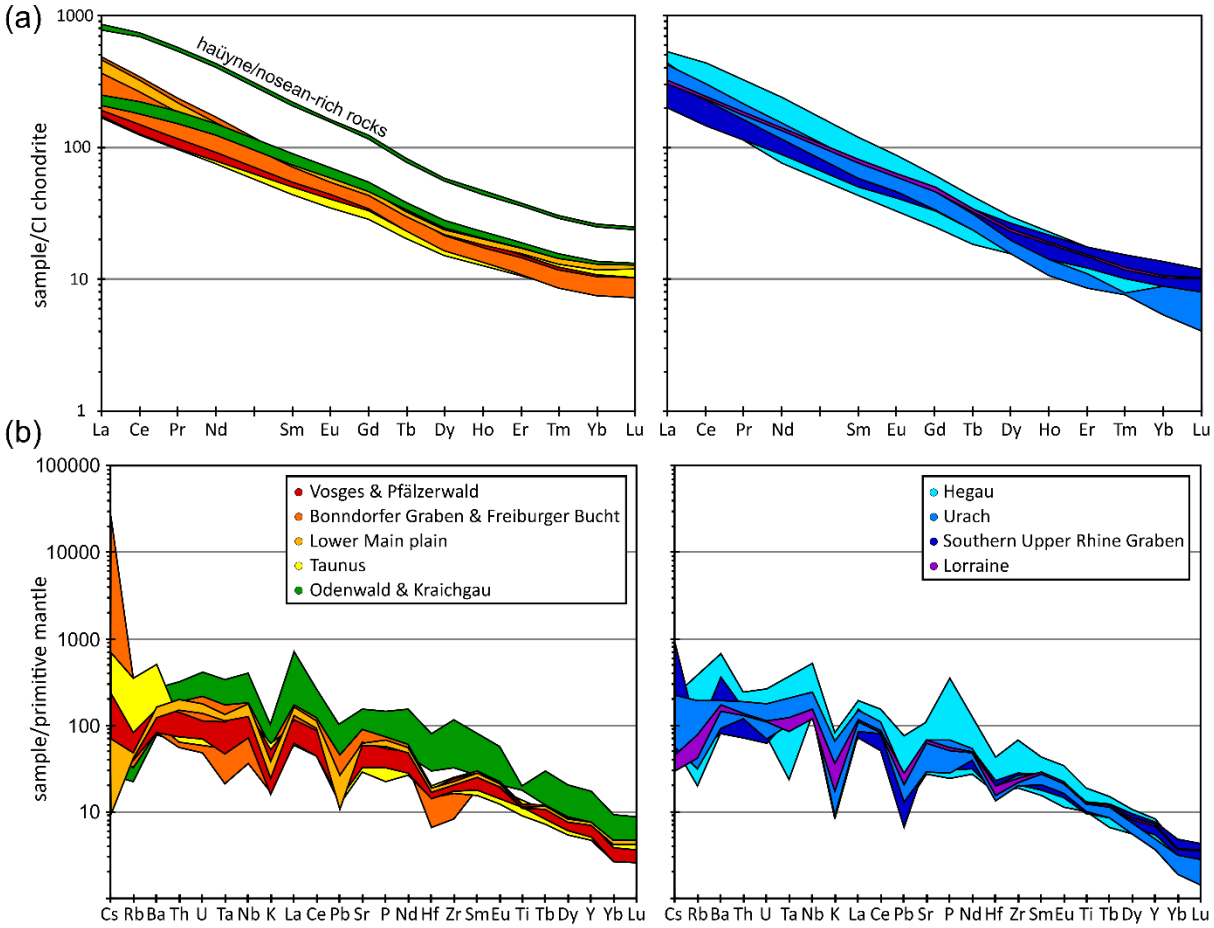

Fig. 12. (a) CI chondrite-normalized REE pattern and **(b)** primitive mantle-normalized incompatible element pattern of the CEVP rocks (normalization values from Palme & O'Neill, 2014). 34 new analyses supplemented by literature data as cited in Fig. 9; elements sorted by increasing mantle compatibility.

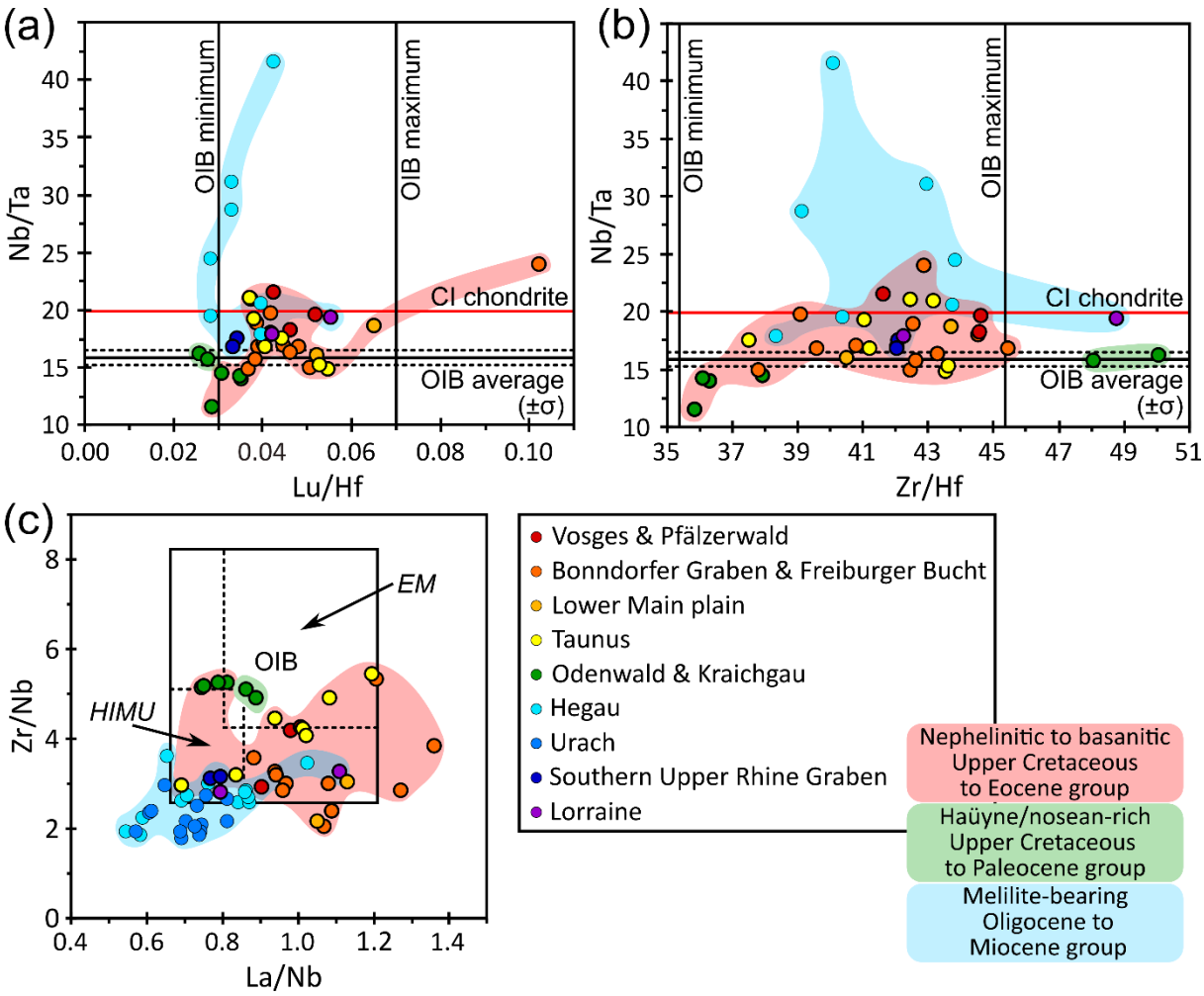

Fig. 13. Plots of different trace element ratios in the CEVP rocks. 34 new analyses supplemented by literature data as cited in Fig. 9. Values for CI chondrites and ocean island basalts (OIB) incl. enriched mantle (EM) and high-μ (HIMU) ocean island basalts from Hofmann *et al.* (1986), Weaver (1991), Pfänder *et al.* (2012), and references therein. **(a)** Lu/Hf and **(b)** Zr/Hf vs. Nb/Ta. **(c)** La/Nb vs. Zr/Nb.

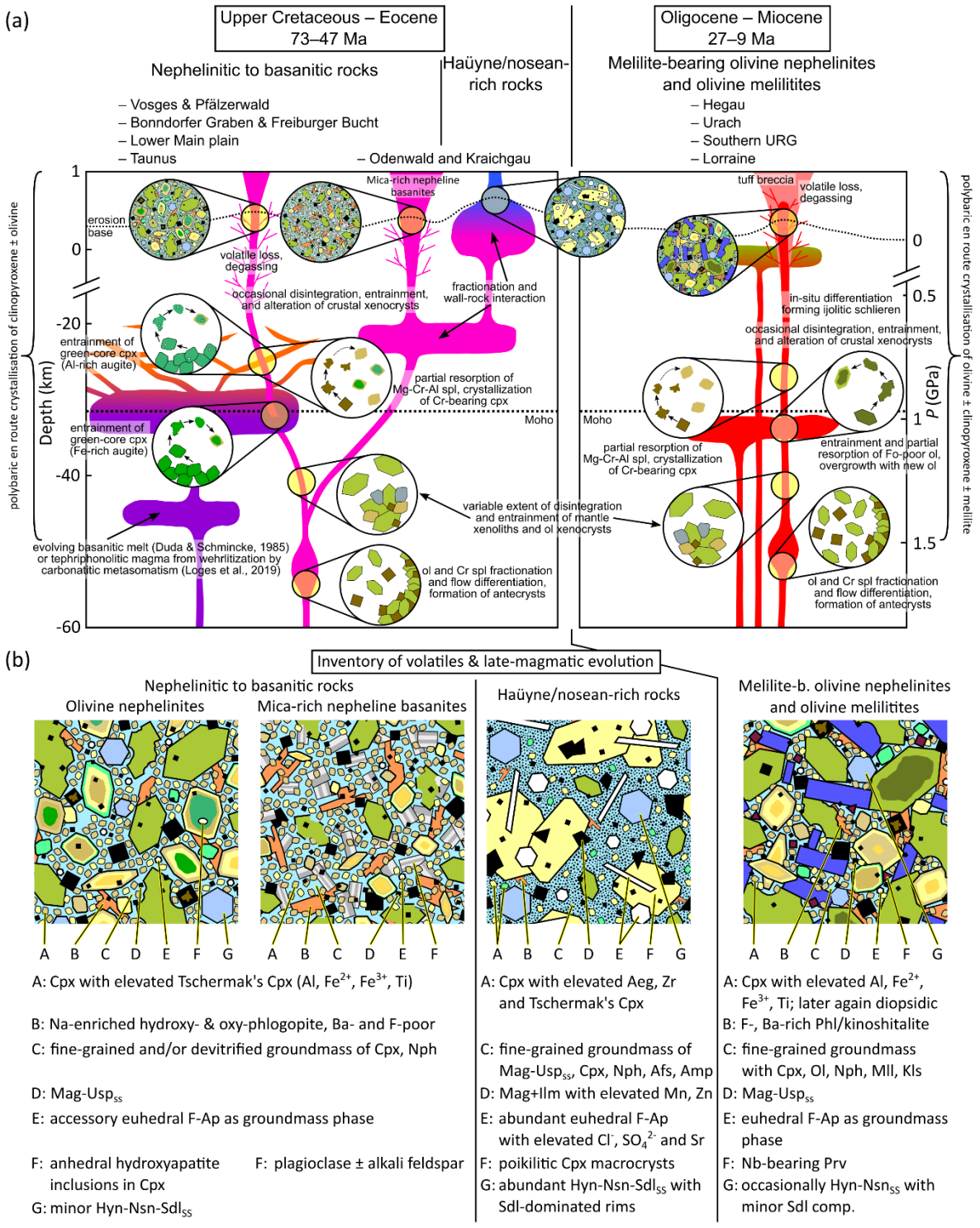

Fig. 14. (a) Schematic model for the evolution of the two groups of alkaline SiO_2-undersaturated volcanic rocks in the southern CEVP. Implied depths for incorporation of xenoliths and xenocrysts, for flow differentiation, antecryst formation, and resorption of Cr spinel and low-Fo olivine are exemplary and may also have occurred in other depth levels. Since volatile loss and degassing proceed gradually and the depths for differentiation processes in the crust can only be estimated, the pressure/depth axis is shown in a shortened form. **(b)** Microstructure, late-stage mineralogy, and mineral chemistry contribute to deciphering source characteristics, relative enrichment during magmatic evolution, and the timing of degassing. Exsolution and continuous release of CO_2 before and during crystallization of groundmass phases could explain the absence of carbonates.

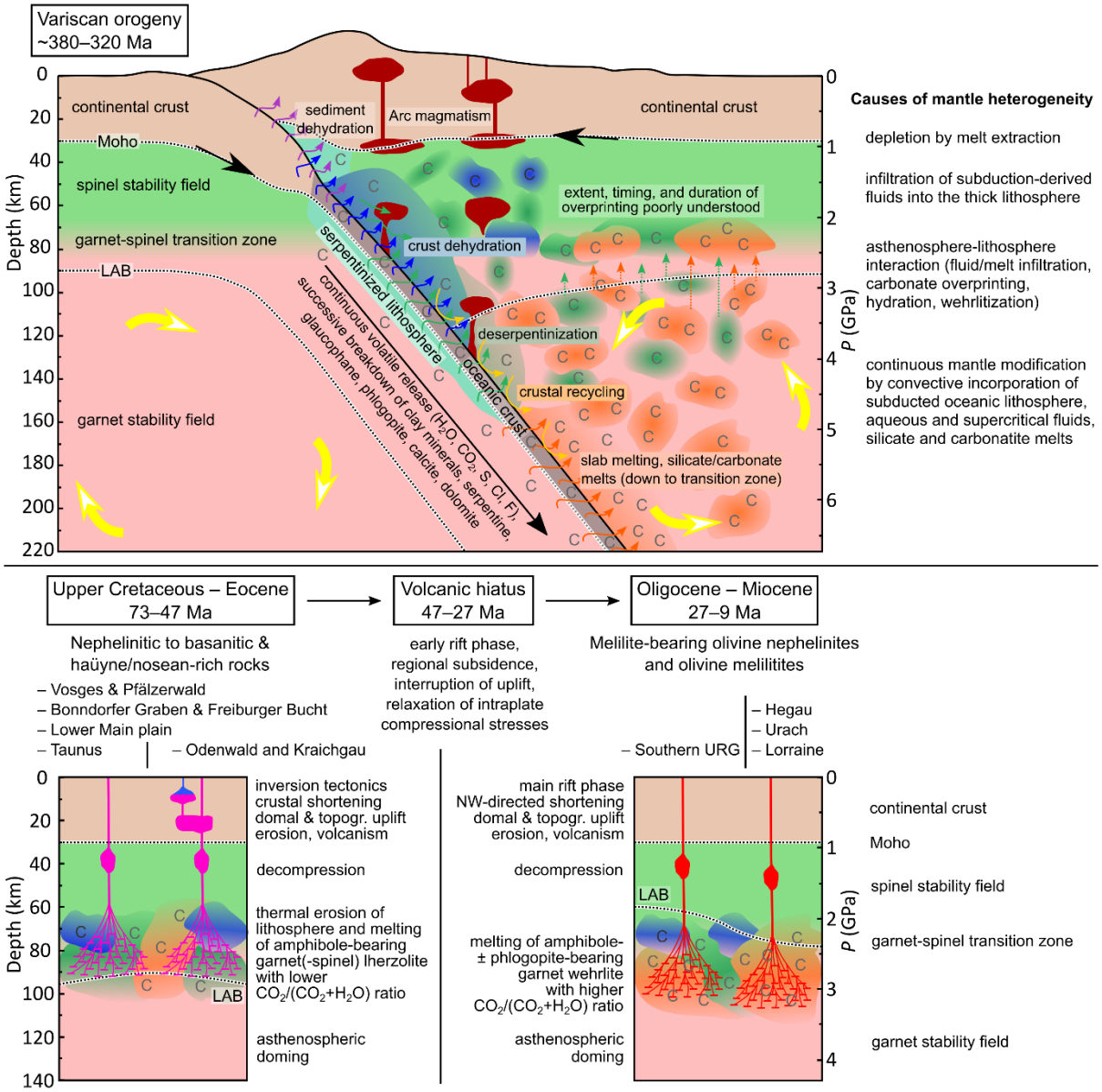

Fig. 15. Proposed petrogenetic model for the origin of metasomatism and the genesis of the southern CEVP rocks and their melt sources. Note that extent, timing, duration, and mechanisms of metasomatic processes associated with recycling of subducted crust beneath Central Europe remain poorly understood. However, the composition, age, and regional distribution of the studied magmas in the CEVP clearly indicate mantle heterogeneity and two differently metasomatized source regions for the two rock groups. Further evidence for the assumptions underlying this figure are detailed in the discussion. Assumed levels of the LAB at each stage, of the spinel and garnet stability field and garnet-spinel transition zone are from Green & Ringwood (1967), Falloon & Green (1990), Klemme (2004), Ziegler & Dézes (2005), Seiberlich *et al.* (2013), Ziberna *et al.* (2013), and Nagayoshi *et al.* (2016). Illustration of the subduction processes modified after Rüpke (2004) and Li *et al.* (2021).

SUPPLEMENTARY DATA

Supplementary data – Tables

Table A1: Complete sample list including locality name, coordinates, and rock type.

Sample	Locality	Latitude (°N)	Longitude (°E)	Rock type
Taunus (A)				
5598	Bossenhain (SW Hausen)	50.076612	8.019067	ON
2425	Eppstein (train station)	50.140889	8.384546	Mca b. ON
5781	Eppstein (tunnel)	50.141073	8.385383	Mca b. ON
Ehr 30	Guntal (W Presberg)	50.039921	7.864610	ON
Ehr 42	Hörkopf	50.053756	7.945106	Fsp & Hyn b. ON
3285	Hörkopf summit	50.083742	7.940396	Mca & Fsp b. ON
Ehr 36	Hüttental (NW Presberg)	50.062998	7.894763	ON
Ehr 29	Hüttental (S Ameisberg)	50.069490	7.877991	OB
6362, 7327, 9437, 3301	Naurod (Erbsenacker)	50.124211	8.297219	Mca b. ON
11046a, 11046b, 75, 75-2, 75-3, 4903	Naurod (Erbsenacker)	50.124211	8.297219	ON
Ehr 41	Rabenkopf	50.043358	7.989031	ON
Ehr 27	Waldburghöhe	50.024974	7.881471	bas. Mca & Rhn b. N
Ehr 28	Waldburghöhe	50.025196	7.881117	bas. Mca b. N
KU 124	Waldburghöhe	50.019664	7.876222	bas. N
Lower Main plain (B)				
279	Dietesheim (Hanau)	50.114976	8.857447	Ol b. B
8381	Klein-Steinheim (Hanau)	50.106699	8.904468	OT
2260, 2339, 4563, RB-1	Roßdorf (quarry)	49.851361	8.770900	Sdl b. ON
Ng 6	Stetteritz	49.862740	8.798385	ON
Odenwald & Kraichgau (C)				
N 595	Geisberg (Diedesheim)	49.352522	9.116222	Mca b. NH
N 598	Geisberg (Diedesheim)	49.351084	9.115668	Mca b. NH
N 11	Hamberg near Neckarelz	49.351713	9.115945	Nph b. H
N 20	Hamberg near Neckarelz	49.351713	9.115945	Mca, Ol & Nph b. H
N 14, N 16	Neckarbischofsheim	49.296643	8.952210	Hyn b. N
N 15	Neckarbischofsheim	49.296643	8.952210	ONH
N 17, N 19	Steinsberg near Weiler	49.214584	8.876936	phon. Mca b. NB
N 265	Steinsberg near Weiler	49.214584	8.876936	bas. Mca b. N
Stb Ia, Stb Ib	Steinsberg near Weiler	49.214967	8.877751	bas. Mca b. N
Stb IIa, Stb IIb	Steinsberg near Weiler	49.214543	8.877808	phon. Mca b. NB
Stb III	Steinsberg near Weiler	49.214123	8.877179	Mca b. NB
Stb IV	Steinsberg near Weiler	49.214059	8.877382	Mca b. NB
Stb Va, Stb Vb	Steinsberg near Weiler	49.213781	8.877526	phon. Mca b. NB
I 20	Waldbrunn	49.484208	9.040353	phon. Ol b. NN

Urach (D)				
U 006	Am Hofwald	48.541952	9.317226	Mca b. OM
U 012	Am Hofwald	48.541952	9.317226	Mca & Nph b. OM
U 023	Am Hofwald, N Hofbühl	48.541952	9.317226	Mca b. NOM
W 42	Autmuthbach	48.562616	9.324129	OM
U 011, U 019, U 028	Bölle	48.576610	9.442799	OM
U 002	Buckleter Kapf	48.513450	9.375249	Mca b. OM
U 003	Buckleter Kapf	48.513450	9.375249	OM
N 467, N 468	Dietenbühl	48.453687	9.484991	Nph b. OM
U 018	Dietenbühl	48.453687	9.484991	Mca b. MON
M 10	Donnstetten	48.514918	9.566112	Nph b. OM
2525, N 469, NU 1, U 008, U 015	Eisenrüttel	48.434606	9.420617	Hyn b. ON
U 009	Floriansberg	48.552766	9.309166	Hyn b. OM
U 026	Floriansberg	48.552766	9.309166	Mca b. OM
U 005	Gaisbühl	48.470729	9.196419	OM
U 020	Götzenbrühl	48.598122	9.460612	OM
U 021	Götzenbrühl	48.598122	9.460612	Nph. b. OM
L 87	Grabenstetten	48.523932	9.460616	OM
U 029	Grabenstetten	48.523932	9.460616	Hyn b. OM
833, U 030	Hohenbol near Owen	48.593610	9.464638	Nph b. OM
U 017	Hohenbol near Owen	48.593610	9.464638	Mca b. OM
U 027	Hohenbol near Owen	48.593610	9.464638	OM
U 013, U 031	Jusi	48.549984	9.338948	OM
U 004, U 007	Kälberburren	48.499375	9.415063	OM
U 024	Kraftrain	48.661386	9.493089	OM
U 014	Laichingen	48.489093	9.684878	OM
U 032	Metzingen vineyard	48.541104	9.298261	Nph b. OM
U 025	Schopfloch	48.562250	9.520106	OM
U 016	Sternberg	48.394731	9.379102	OM
1229, U 022	Sulzburg	48.561267	9.456890	OM
U 010	Wittlinger Steige	48.470536	9.431732	OM
Lorraine (E)				
LM 455, N 165	Essey-la-Côte	48.424436	6.457035	Nph b. OM
N 164	Essey-la-Côte	48.424436	6.457035	NOM
Vosges & Pfälzerwald (F)				
FO 1, FO 2, FO 3	Forst	49.422959	8.161910	ON
LM 1434	Reichshoffen/Reichshofen	48.933541	7.667646	Nph. b. OM
CA 2584	Ribeauvillé/Rappoltsweiler – Cerisier Noir	48.240399	7.269826	ON
LM 729	Riquewihr/Reichenweiher	48.166158	7.299822	Hyn b. ON
Southern URG (G)				
8111, M 13, M 63, M 164	Buggingen potash salt deposit	47.857364	7.621192	Monchiquite
M 34, M 67, M 156	Buggingen potash salt deposit	47.857364	7.621192	OM
M 89, M 109, M 110	Buggingen potash salt deposit	47.878776	7.636801	OM

I 234	Eichwald	47.789323	7.640810	Nph b. OM
N 195	Hinterhauenstein	48.192169	8.194913	Hyn b. ON
N 411	Langental	48.116561	7.933254	ON
N 476	Langental	48.115962	7.936490	ON
2018-001	Mahlberg	48.287146	7.811795	ON
2018-002	Mahlberg	48.287136	7.810812	NOM
Bonndorfer Graben & Freiburger Bucht (H)				
N 90	Attental	47.998406	7.935559	Mca b. ON
N 315	Attental	47.998063	7.937442	Mca b. ON
N 119	Berghäuser Kapelle	47.950536	7.788071	Hyn b. ON
N 113	Bohrer	47.935208	7.872614	ON
N 168	Breitnau	47.937703	8.093403	ON
N 256	Breitnau	47.939313	8.092304	ON
N 45	Hammereisenbach	47.994605	8.309203	Mll b. ON
2018-003	Heuweiler	48.049401	7.906876	Hyn b. ON
N 308	Heuweiler	48.054998	7.899648	Mca b. ON
N 55	Hirzberg	47.996718	7.871811	Hyn b. ON
N 98	Hirzberg	47.995179	7.870772	Mca HON
N 369	Hirzberg	47.996220	7.876109	Hyn b. ON
N 291	Hochkopf	47.858002	8.058043	Mll & Hyn b. ON
H 161	Horben, cable car valley station	47.939616	7.863550	Mca b. ON
N 310	Horbener Felsen	47.947960	7.881708	Mca & Ol b. N
N 364	Jostal	47.929961	8.188687	Mca b. ON
N 102	Korthaus	48.002262	7.886967	Ol & Mca b. N
N 110	Kybfelsen	47.960545	7.888399	ON
N 46	Rautebacher Höfe	48.016845	7.879012	Hyn b. ON
N 104	Rotteckruhe	48.014930	7.912833	ON
N 111	Schloßberg	47.993968	7.848422	ON
N 200	Schloßberg	47.994410	7.856720	Mca b. ON
N 350	Schloßberg	47.994590	7.856716	ON
N 545	Schwarzbergweg Menzenschwand–Hochkopf	47.840004	8.067854	Hyn b. ON
N 94	St. Ottilien	47.996423	7.878383	Hyn b. ON
N 96	St. Ottilien	47.996423	7.878383	Hyn & Mca b. ON
N 146	St. Ottilien	48.002389	7.900098	Hyn & Mca b. ON
N 311	Tannengrund	47.950377	7.878710	ON
N 47	Uhlberg	48.017671	7.889987	Mca b. ON
N 204	Uhlberg	48.017682	7.891193	Hyn b. ON
N 307	Unterglottertal	48.062408	7.912773	ON
N 112	Weilersbachdobel, vineyard	47.962702	7.869873	Mca b. ON
Hegau (I)				
HEG 10	Blauer Stein (Randen)	47.825537	8.597696	Nph & Hyn b. OM
HEG 12	Blauer Stein (Randen)	47.825537	8.597696	Mll b. ON

N 374	Blauer Stein (Randen), Steinröhren	47.826987	8.598313	Mll b. ON
HEG 01, HEG 01a	Haslen	47.814300	8.760884	OM
HEG 17	Hohenhewen	47.835623	8.747227	Mll b. ON
HEG 03a	Hohenstoffel	47.794465	8.750537	ON
HEG 04	Hohenstoffel	47.794465	8.750537	NOM
HEG 13	Homboll	47.784160	8.764518	Nph b. OM
N 333	Höwenegg	47.914362	8.738509	NOM
HEG 15	Neuhewen	47.879057	8.717537	Mll b. ON
N 323	Neuhewen	47.879056	8.717029	OM
HEG 19	Pfaffwiesen	47.776275	8.752612	Mll b. ON
N 593	Ramsen	47.817302	8.731386	ON
HEG 20	Riedheim dyke	47.763659	8.753926	NOM
HEG 14	Schachen	47.821626	8.730429	Mll & Hyn b. ON
HEG 18	Sennhof	47.789871	8.755671	OM
I 27	Tudoburg	47.879076	8.883742	ON
HEG 16, HEG 11, I 224	Wartenberg	47.915868	8.631607	ON
I 63	Wasserburger Tal	47.900917	8.871255	ON
N 290	Wasserburger Tal	47.876242	8.845515	ON

b. – bearing; bas. – basanitic; Mca – biotite; Fsp – feldspar; Hyn – haüyne; Mll – melilite; Nph – nepheline; Rhn – rhönite; Sdl – sodalite; HM – haüyne melilitite; MON – melilite olivine nephelinite; N – noseanite; NB – nepheline basanite; NH – nepheline haüynite; NN – nepheline noseanite; NOM – nepheline olivine melilitite; OM – olivine melilitite; ON – olivine nephelinite; ONH – olivine nepheline haüynite; OT – olivine tholeiite; phon. – phonolitic.

Table A2: Adjustments for the different EPMA programs.

Mineral / mineral group	**Acceleration voltage (kV)**	**Probe current (nA)**	**Probe diameter (µm)**
Olivine	20	20	0
Pyroxenes, melilite	15	20	0
Oxyspinels	20	20	0
Sodalite group	15	5	5
Mica, amphibole, alkali feldspar, rhönite	15	10	2
Perovskite	20	100	0
Titanite	20	20	0
Apatite	15	10	10

Table A3: Parameters for the EPM analyses of olivine.

Element	Line	Crystal	Spectrometer	Peak measurement time	Internal standard	Lower limit of detection		Av. standard deviation 1σ (%)
						ppm	oxide wt.%	
Mg	K_α	TAP	1	16 s	A_Diopside	80	0.013	0.5
Fe	K_α	LIF	3	16 s	A_Olivine	130	0.016	1.1
Ca	K_α	PETH	4	30 s	A_Diopside	40	0.006	2.9
Al	K_α	TAP	1	30 s	S_Al_2O_3	50	0.010	28.7
Ti	K_α	PETH	4	30 s	A_$SrTiO_3$	60	0.010	31.1
Si	K_α	TAP	1	16 s	A_Diopside	120	0.024	0.6
Mn	K_α	LIFH	4	30 s	A_Rhodonite	80	0.010	5.0
Ni	K_α	LIFH	4	30 s	M_Nickel	80	0.010	8.8

Av. – average; LIF – lithium fluoride; LIFH – lithium fluoride, high sensitivity crystal; PETH – pentaerythritol, high sensitivity crystal; TAP – thallium acid phthalate.

Table A4: Parameters for the EPM analyses of pyroxenes and melilite.

Element	Line	Crystal	Spectrometer	Peak measurement time	Internal standard	Lower limit of detection		Av. standard deviation 1σ (%)
						ppm	oxide wt.%	
Na	K_α	TAP	2	10 s	A_Albite	140	0.019	5.7
K	K_α	PETJ	3	16 s	A_Sanidine	90	0.011	45.0
Ti	K_α	PETH	4	16 s	A_$SrTiO_3$	110	0.018	3.2
Mg	K_α	TAP	2	16 s	A_Diopside	110	0.018	0.6
Ca	K_α	PETJ	3	16 s	A_Diopside	130	0.018	0.5
Zr	L_α	PETH	4	30 s	A_ZrO_2	150	0.020	39.3
Al	K_α	TAP	2	16 s	S_Al_2O_3	110	0.021	0.9
Mn	K_α	PETJ	3	16 s	A_Rhodonite	160	0.021	19.6
Sr	L_α	PETH	4	16 s	A_$SrTiO_3$	260	0.031	44.4
Si	K_α	TAP	2	16 s	A_Diopside	220	0.048	0.3
Fe	K_α	LIF	3	16 s	A_Hematite	230	0.033	1.9
Cr	K_α	LIFH	4	16 s	M_Chromium	120	0.018	32.2

Av. – average; LIF – lithium fluoride; LIFH – lithium fluoride, high sensitivity crystal; PETH – pentaerythritol, high sensitivity crystal; TAP – thallium acid phthalate.

Table A5: Parameters for the EPM analyses of the oxyspinels.

Element	Line	Crystal	Spectrometer	Peak measurement time	Internal standard	Lower limit of detection		Av. standard deviation 1σ (%)
						ppm	oxide wt.%	
Si	K_α	TAP	1	16 s	A_Diopside	90	0.020	23.9
Al	K_α	TAP	2	16 s	S_Al_2O_3	120	0.023	2.7
Cr	K_α	PETJ	3	30 s	M_Chromium	80	0.012	8.3
V	K_α	LIFH	4	30 s	M_Vanadium	80	0.011	4.5
Mg	K_α	TAP	2	16 s	A_Periclase	100	0.017	2.5
Ti	K_α	PETJ	3	16 s	A_$SrTiO_3$	120	0.020	1.9
Mn	K_α	LIFH	4	16 s	A_Bustamite	110	0.014	4.6
Fe	K_α	LIFH	4	16 s	A_Hematite	100	0.015	0.4
Ni	K_α	LIFH	4	30 s	M_Nickel	80	0.010	17.5
Zn	K_α	LIFH	4	16 s	M_Zinc	130	0.016	21.3

Av. – average; LIFH – lithium fluoride, high sensitivity crystal; PETJ – pentaerythritol, high reflectivity crystal; TAP – thallium acid phthalate.

Table A6: Parameters for the EPM analyses of the sodalite group.

Element	Line	Crystal	Spectrometer	Peak measurement time	Internal standard	Lower limit of detection		Av. standard deviation 1σ (%)
						ppm	oxide wt.%	
Si	K_α	TAP	1	16 s	A_Albite	230	0.049	0.7
Na	K_α	TAP	2	16 s	A_Albite	250	0.034	1.4
K	K_α	PETJ	3	16 s	A_Sanidine	190	0.023	3.6
Cl	K_α	PETH	4	30 s	A_Tugtupite	80	0.008	2.8
Al	K_α	TAP	1	16 s	A_Albite	190	0.036	0.7
Br	L_α	TAP	2	30 s	A_TlBrI	430	0.043	8.5
Ca	K_α	PETJ	3	16 s	A_Bustamite	200	0.028	2.7
S	K_α	PETH	4	30 s	A_Baryte	260	0.065	2.3
Mn	K_α	PETJ	3	30 s	A_Bustamite	250	0.032	58.8
Sr	L_α	PETH	4	30 s	A_$SrTiO_3$	450	0.053	15.8
Fe	K_α	LIF	3	16 s	A_Magnetite	470	0.067	10.9

Av. – average; LIF – lithium fluoride; PETH – pentaerythritol, high sensitivity crystal; PETJ – pentaerythritol, high reflectivity crystal; TAP – thallium acid phthalate.

Table A7: Parameters for the EPM analyses of mica, amphibole, alkali feldspar, and rhönite.

Element	Line	Crystal	Spectrometer	Peak measurement time	Internal standard	Lower limit of detection		Av. standard deviation 1σ (%)
						ppm	oxide wt.%	
F	K_α	LDE1	1	10 s	A_Fluorite	680	0.068	8.6
Na	K_α	TAP	2	10 s	A_Albite	210	0.028	12.2
K	K_α	PETJ	3	16 s	A_Sanidine	140	0.017	1.5
Cs	L_β	LIFH	4	16 s	A_Pollucite	840	0.089	71.3
Si	K_α	TAP	2	16 s	A_Diopside	310	0.066	0.5
Ca	K_α	PETJ	3	16 s	A_Diopside	160	0.022	20.0
Cl	K_α	PETH	4	16 s	A_Tugtupite	80	0.008	41.9
Al	K_α	TAP	2	16 s	S_Al_2O_3	160	0.030	0.8
Ti	K_α	PETJ	3	16 s	A_$SrTiO_3$	220	0.037	1.6
Ba	L_α	PETH	4	16 s	A_Baryte	310	0.035	3.3
Mg	K_α	TAP	2	16 s	A_Diopside	160	0.027	0.9
Cr	K_α	PETJ	3	16 s	M_Chromium	190	0.028	53.1
Zr	L_α	PETH	4	30 s	A_ZrO_2	270	0.036	61.2
Mn	K_α	PETJ	3	16 s	A_Rhodonite	220	0.028	24.0
V	K_α	LIFH	4	16 s	M_Vanadium	210	0.031	32.5
Fe	K_α	LIF	3	16 s	A_Magnetite	350	0.051	2.2
Zn	K_α	LIFH	4	16 s	M_Zinc	350	0.044	66.4

Av. – average; LIF – lithium fluoride; LIFH – lithium fluoride, high sensitivity crystal; PETH – pentaerythritol, high sensitivity crystal; PETJ – pentaerythritol, high reflectivity crystal; TAP – thallium acid phthalate.

Table A8: Parameters for the EPM analyses of perovskite.

Element	Line	Crystal	Spectrometer	Peak measurement time	Internal standard	Lower limit of detection		Av. standard deviation 1σ (%)
						ppm	oxide wt.%	
Si	K_α	TAP	1	16 s	A_Diopside	50	0.011	26.5
Na	K_α	TAP	2	10 s	A_Albite	80	0.011	5.0
Ca	K_α	PETJ	3	16 s	A_Diopside	40	0.006	0.1
Ta	L_α	LIFH	4	16 s	S_$Li_2Ta_2O_6$	110	0.013	24.5
Al	K_α	TAP	1	16 s	S_Al2O3	30	0.006	3.7
Mg	K_α	TAP	2	16 s	A_Periclase	40	0.007	36.7
Ti	K_α	PETJ	3	16 s	A_SrTiO3	50	0.009	0.1
Fe	K_α	LIFH	4	16 s	A_Hematite	40	0.006	3.7
K	K_α	PETJ	2	30 s	A_Sanidine	30	0.004	19.6
Nb	L_α	PETJ	3	16 s	S_$Li_2Nb_2O_6$	170	0.024	4.5
Sm	L_α	LIFH	4	30 s	REE_Sm	80	0.009	15.0
Th	M_α	PETJ	2	30 s	S_ThO_2	210	0.024	20.4
Zr	L_α	PETJ	3	30 s	A_ZrO_2	130	0.017	45.4
Pr	L_α	LIFH	4	30 s	REE_Pr	100	0.012	8.8
Y	L_α	PETJ	2	30 s	A_YAG	160	0.020	45.1
Nd	L_β	PETJ	3	30 s	REE_Nd	170	0.020	7.0
Ce	L_α	LIFH	4	30 s	REE_Ce	100	0.011	2.0
U	M_α	PETJ	2	30 s	S_UO_2	270	0.033	–
Sr	L_α	PETJ	3	30 s	A_$SrTiO_3$	180	0.021	15.5
La	L_α	LIFH	4	30 s	REE_La	170	0.020	6.2
Mn	K_α	PETJ	3	16 s	A_Bustamite	50	0.007	37.1
Ba	L_α	PETH	4	30 s	A_Baryte	60	0.006	1.3

Av. – average; LIFH – lithium fluoride, high sensitivity crystal; PETH – pentaerythritol, high sensitivity crystal; PETJ – pentaerythritol, high reflectivity crystal; TAP – thallium acid phthalate.

Table A9: Parameters for the EPM analyses of titanite.

Element	Line	Crystal	Spectrometer	Peak measurement time	Internal standard	Lower limit of detection		Av. standard deviation 1σ (%)
						ppm	oxide wt.%	
F	K_α	LDE1	1	16 s	A_Fluorite	490	0.049	78.0
Na	K_α	TAP	2	16 s	A_Albite	170	0.023	54.9
Ca	K_α	PETJ	3	16 s	A_Diopside	90	0.012	0.3
Ta	L_α	LIFH	4	30 s	S_$Li_2Ta_2O_6$	190	0.023	59.5
Si	K_α	TAP	1	16 s	A_Diopside	100	0.022	0.3
Mg	K_α	TAP	2	16 s	A_Periclase	90	0.015	53.0
Ti	K_α	PETJ	3	16 s	A_$SrTiO_3$	110	0.018	0.3
Fe	K_α	LIFH	4	16 s	A_Hematite	90	0.013	1.6
Al	K_α	TAP	1	16 s	S_Al_2O_3	70	0.013	1.6
Y	L_α	PETJ	2	30 s	A_YAG	320	0.040	56.1
Nb	L_α	PETJ	3	30 s	S_$Li_2Nb_2O_6$	270	0.038	11.0
Sm	L_α	LIFH	4	30 s	REE_Sm	160	0.019	41.6
U	M_α	PETJ	2	30 s	S_UO_2	550	0.039	–
Zr	L_α	PETJ	3	30 s	A_ZrO_2	280	0.038	18.2
Pr	L_α	LIFH	4	30 s	REE_Pr	210	0.025	45.7
Th	M_α	PETJ	2	30 s	S_ThO_2	440	0.050	53.8
Nd	L_β	PETJ	3	30 s	REE_Nd	360	0.042	22.7
Ce	L_α	LIFH	4	30 s	REE_Ce	190	0.022	7.9
Mn	K_α	PETJ	3	16 s	A_Bustamite	110	0.014	16.7
La	L_α	LIFH	4	30 s	REE_La	320	0.037	41.8

Av. – average; LDE1 – W/Si multilayer crystal; LIFH – lithium fluoride, high sensitivity crystal; PETJ – pentaerythritol, high reflectivity crystal; TAP – thallium acid phthalate.

Table A10: Parameters for the EPM analyses of apatite.

Element	Line	Crystal	Spectrometer	Peak measurement time	Internal standard	Lower limit of detection		Av. standard deviation 1σ (%)
						ppm	oxide wt.%	
F	K_α	LDE1	1	10 s	EX_Durango	530	0.053	5.1
Na	K_α	TAP	2	10 s	A_Albite	120	0.016	16.2
Mn	K_α	PETJ	3	30 s	A_Rhodonite	150	0.019	42.3
Cl	K_α	PETH	4	30 s	A_Tugtupite	60	0.006	7.2
Mg	K_α	TAP	2	30 s	A_Diopside	140	0.023	14.5
V	K_α	PETJ	3	30 s	M_Vanadium	140	0.024	38.8
S	K_α	PETH	4	30 s	A_Barite	130	0.033	16.5
As	L_α	TAP	2	30 s	A_GaAs	420	0.064	70.2
Ca	K_α	PETJ	3	16 s	EX_Durango	200	0.027	0.5
P	K_α	PETH	4	16 s	EX_Durango	180	0.041	0.5
Si	K_α	TAP	2	30 s	A_Diopside	240	0.051	9.2
K	K_α	PETJ	3	30 s	A_Sanidine	100	0.013	29.6
Sr	L_α	PETH	4	30 s	A_$SrTiO_3$	270	0.032	9.2
U	M_α	PET	3	30 s	S_UO_2	330	0.037	64.2
Ba	L_α	PETH	4	30 s	A_Barite	210	0.023	52.3
Th	M_α	PETJ	3	30 s	S_ThO_2	330	0.038	65.1
La	L_α	LIFH	4	30 s	REE_La	460	0.054	44.7
Y	L_α	PETJ	3	30 s	A_YAG	680	0.086	64.1
Ce	L_α	LIFH	4	30 s	REE_Ce	380	0.044	23.8
Fe	K_α	LIF	3	30 s	A_Hematite	250	0.032	18.4
Pr	L_α	LIFH	4	30 s	REE_Pr	440	0.051	54.9
Nd	L_α	LIFH	4	30 s	REE_Nd	370	0.043	43.1
Sm	L_α	LIFH	4	30 s	REE_Sm	360	0.042	64.8
Gd	L_α	LIFH	4	30 s	REE_Gd	400	0.046	61.2

Av. – average; LDE1 – W/Si multilayer crystal; LIF – lithium fluoride; LIFH – lithium fluoride, high sensitivity crystal; PETH – pentaerythritol, high sensitivity crystal; PETJ – pentaerythritol, high reflectivity crystal; TAP – thallium acid phthalate.

Supplementary data – Figures

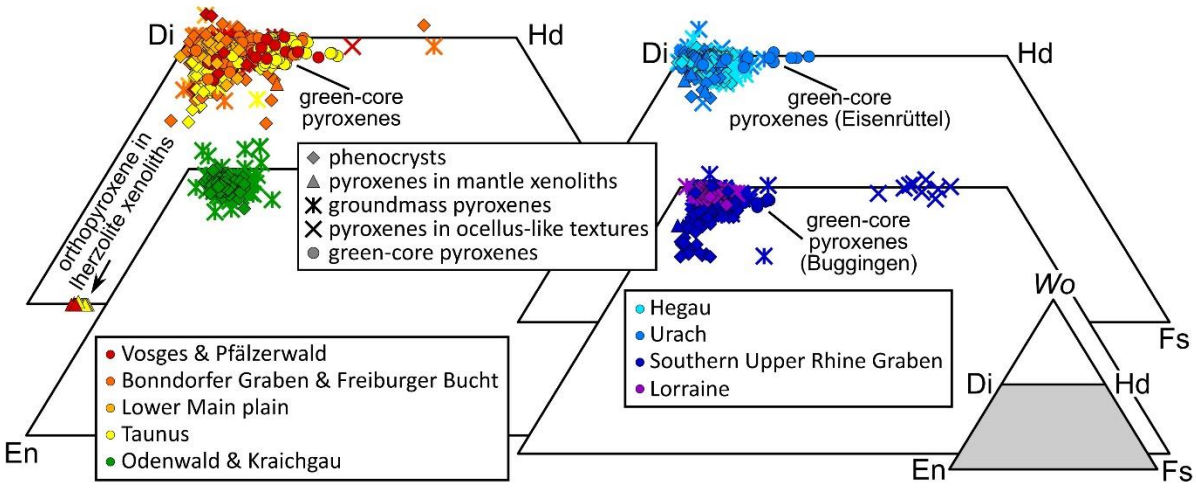

Fig. A1. Composition of the quadrilateral component of pyroxene in the studied CEVP rocks normalized to 100 %, shown in the pyroxene trapezoid. Own data supplemented by Buggingen, southern URG (Braunger et al., 2021). Diopside – $CaMgSi_2O_6$ (Di), enstatite – $Mg_2Si_2O_6$ (En), ferrosilite – $Fe_2Si_2O_6$ (Fs), hedenbergite – $CaFeSi_2O_6$ (Hd), wollastonite – $Ca_2Si_2O_6$ (Wo). Note that green-core pyroxenes exhibit an elevated hedenbergite component compared to phenocrysts. Orthopyroxene is present only in peridotite xenoliths enclosed in the Upper Cretaceous to Eocene rocks.

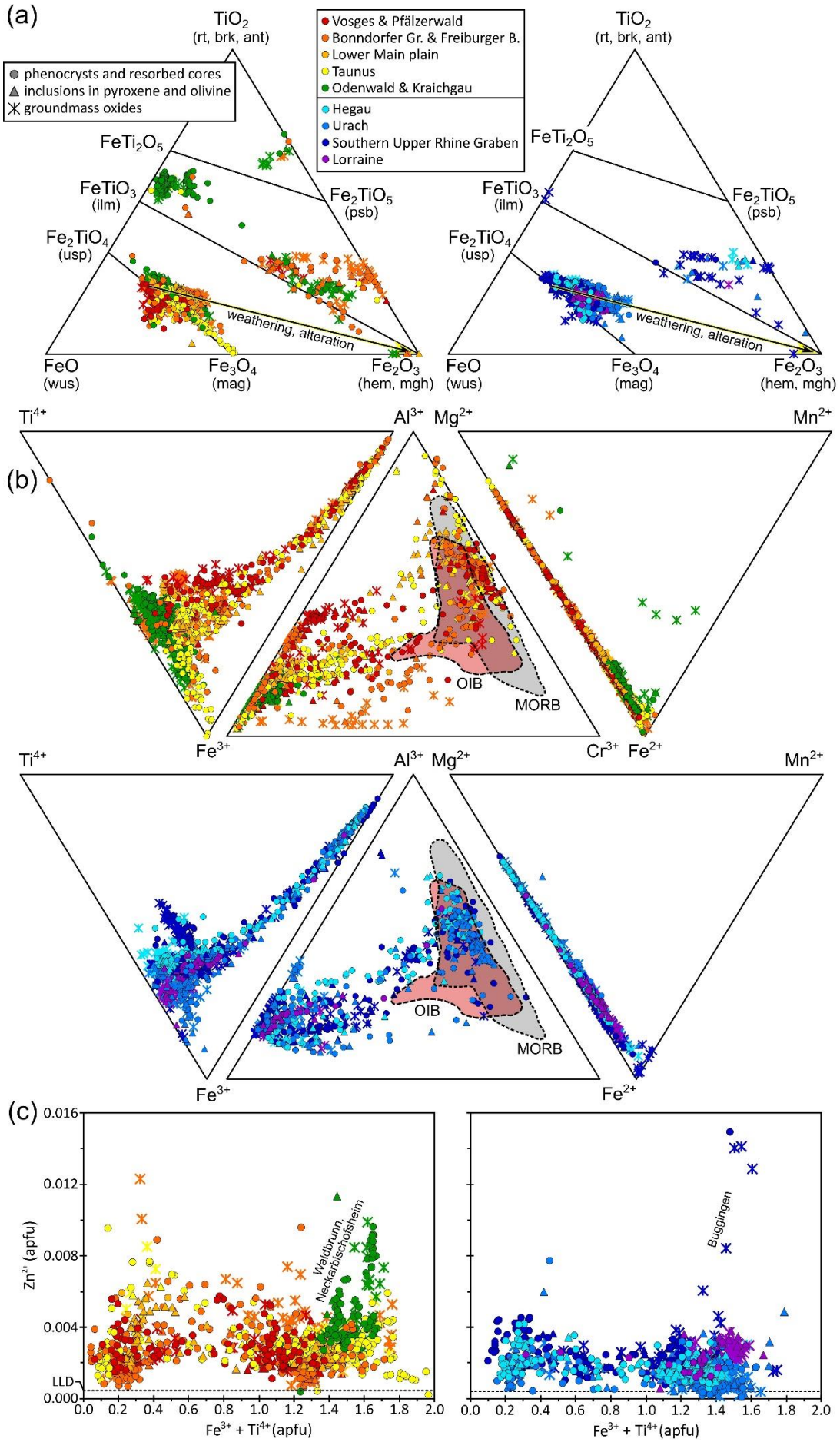
(a)
TiO2 (rt, brk, ant)
phenocrysts and resorbed cores
inclusions in pyroxene and olivine
groundmass oxides
Vosges & Pfälzerwald
Bonndorfer Gr. & Freiburger B.
Lower Main plain
Taunus
Odenwald & Kraichgau
Hegau
Urach
Southern Upper Rhine Graben
Lorraine
FeTi2O5
FeTiO3 (ilm)
Fe2TiO5 (psb)
Fe2TiO4 (usp)
weathering, alteration
FeO (wus)
Fe3O4 (mag)
Fe2O3 (hem, mgh)
(b)
Ti4+
Al3+
Mg2+
Mn2+
Fe3+
Cr3+
Fe2+
OIB
MORB
(c)
Zn2+ (apfu)
LLD
Waldorn, Neckarbischofsheim
Buggingen
Fe3+ + Ti4+ (apfu)

Fig. A2. (a) Fe-Ti oxide classification for the studied CEVP rocks based on Fe-Ti and (Fe,Ti)-O ratio. Own data supplemented by Buggingen, southern URG (Braunger *et al.*, 2021). Most data points plot along the ulvöspinel-magnetite solid solution series but may be shifted towards hematite/maghemite because of alteration and weathering. The large number of ilmenite analyses in the Odenwald and Kraichgau rocks reflects formation of exsolution lamellae in euhedral magnetite-ulvöspinel$_{ss}$ macrocrysts. The occurrence of Ti-rich hematite with uncertain stoichiometry especially in the groundmass of rocks from the Bonndorfer Graben and Freiburger Bucht region, and Buggingen is due to alteration of some samples. Small grain sizes, porous structure of the Fe oxides, presence of Fe hydroxide and of cryptocrystalline compounds may cause mixed analyses. The water content of secondary Fe-Ti oxides provokes underestimation of the analytic total (oxides wt.%) and thus an overestimation of the Fe^{3+} content, resulting in miscalculation of the Fe/O ratio. **(b-c)** Oxyspinel composition in the studied CEVP rocks. **(b)** Triangular diagrams show the molar Ti-Al-Fe^{3+}, Al-Fe^{3+}-Cr, and Mg-Mn-Fe^{2+} distribution. Typical MORB compositions are highlighted in grey and OIB compositions in red (Barnes & Roeder, 2001). Note the compositional variations between early magmatic Mg-Cr-Al oxyspinels in the melilite-bearing rocks and in the melilite-free olivine nephelinites and nepheline basanites. **(c)** Fe^{3+} + Ti^{4+} vs. Zn^{2+}. LLD – lower limit of detection. apfu – atoms per formula unit.

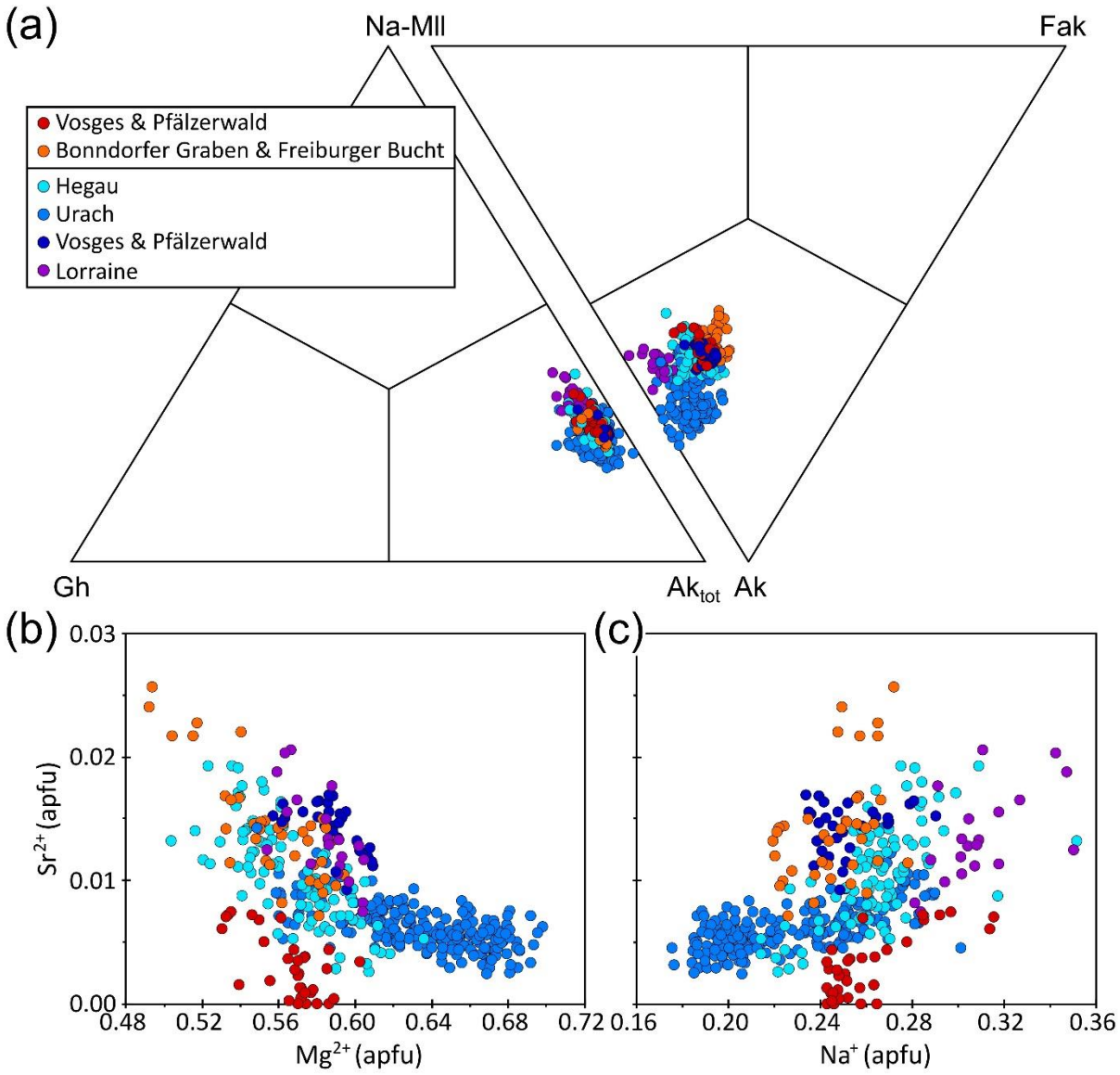

Fig. A3. Melilite composition in the studied CEVP rocks. **(a)** Triangular diagrams showing the distribution among the endmember groups (ferri)gehlenite – $Ca_2(Al,Fe^{3+})[AlSiO_7]$ (Gh), soda-melilite – $CaNa(Al,Fe^{3+})[Si_2O_7]$ (Na-Mll), and (Mg+Fe^{2+}-)åkermanite – $Ca_2(Mg,Fe)[Si_2O_7]$ (Ak_{tot}) and the distribution of the endmembers soda-melilite, ferroåkermanite – $Ca_2Fe[Si_2O_7]$ (Fak), and (magnesio)åkermanite – $Ca_2Mg[Si_2O_7]$ (Ak), normalized to 100 %. **(b)** Mg^{2+} vs. Sr^{2+}. **(c)** Na^{+} vs. Sr^{2+}. apfu – atoms per formula unit.

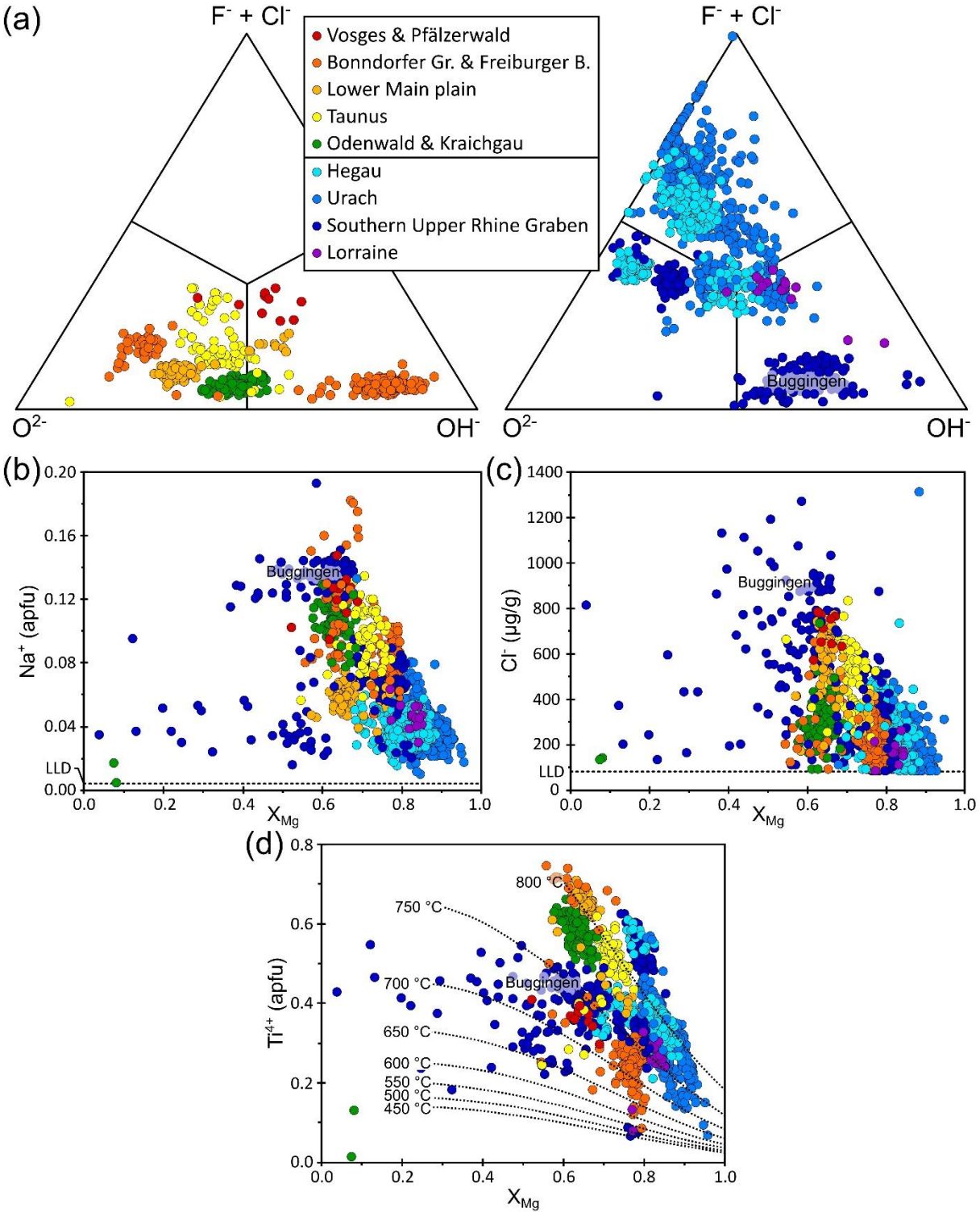

Fig. A4. Mica composition in the studied CEVP rocks. Own data supplemented by Buggingen, southern URG (Braunger *et al.*, 2021). LLD – lower limit of detection. apfu – atoms per formula unit. **(a)** Triangular diagrams showing the distribution among end-members based on the anion position (oxy-mica, fluoro- and chloro-mica, hydroxy-mica). **(b)** X_{Mg} vs. Na^{+}. **(c)** X_{Mg} vs. Cl^{-} (µg/g). **(d)** X_{Mg} vs. Ti^{4+}. *T* isotherms (°C) according to Henry *et al.* (2005) are discussed in Supplementary data, File 2.

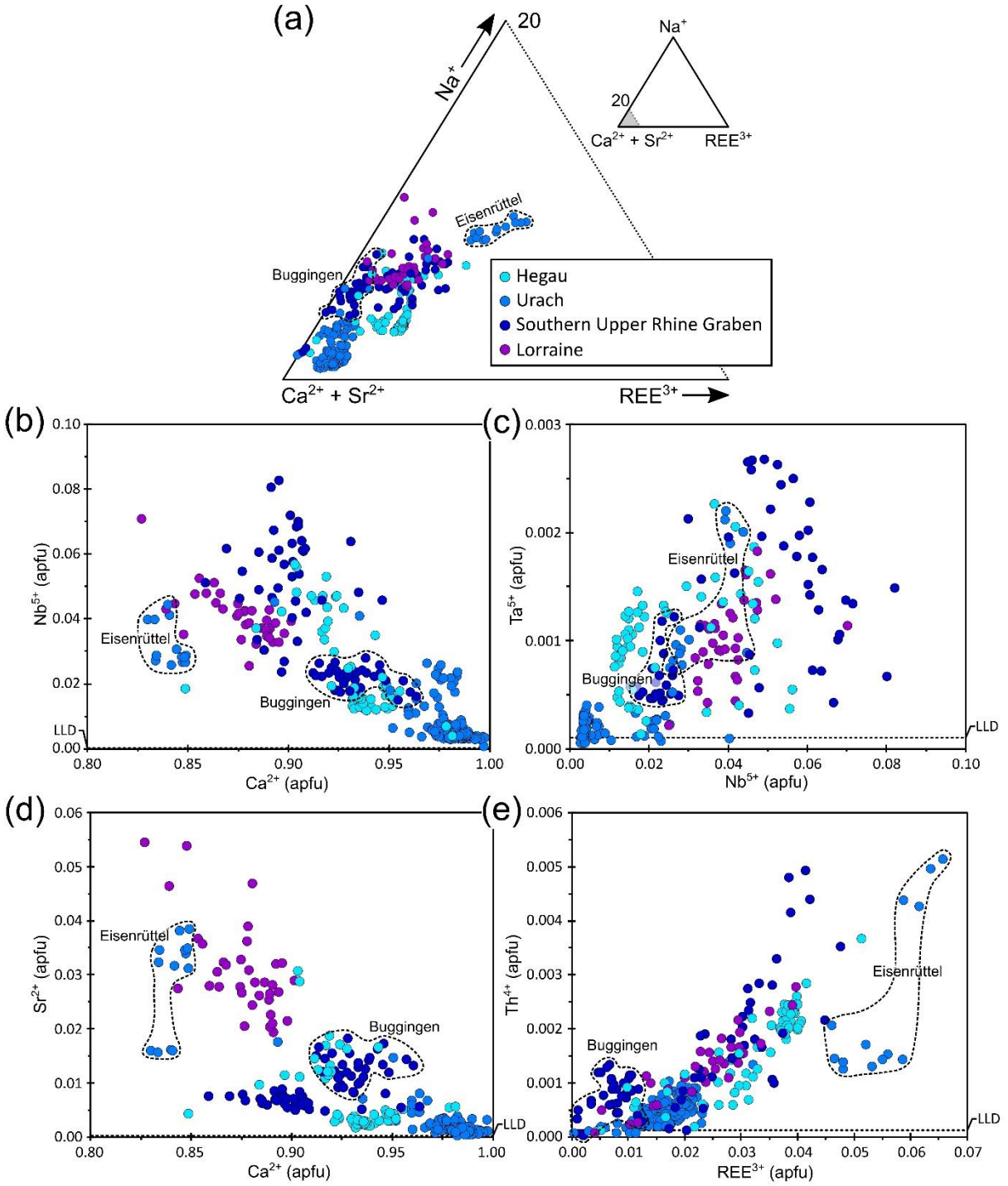

Fig. A5. Perovskite composition in the studied CEVP rocks. Own data supplemented by Buggingen, southern URG (Braunger *et al.*, 2021). Triangular diagrams showing **(a)** the molar Ca+Sr-Na-REE distribution normalized to 100 %. **(b)** Ca^{2+} vs. Nb^{5+}. **(c)** Nb^{5+} vs. Ta^{5+}. Although data points are scattered, a positive correlation between Nb and Ta is evident. **(d)** Ca^{2+} vs. Sr^{2+}. **(e)** REE^{3+} vs. Th^{4+}. LLD – lower limit of detection. apfu – atoms per formula unit.

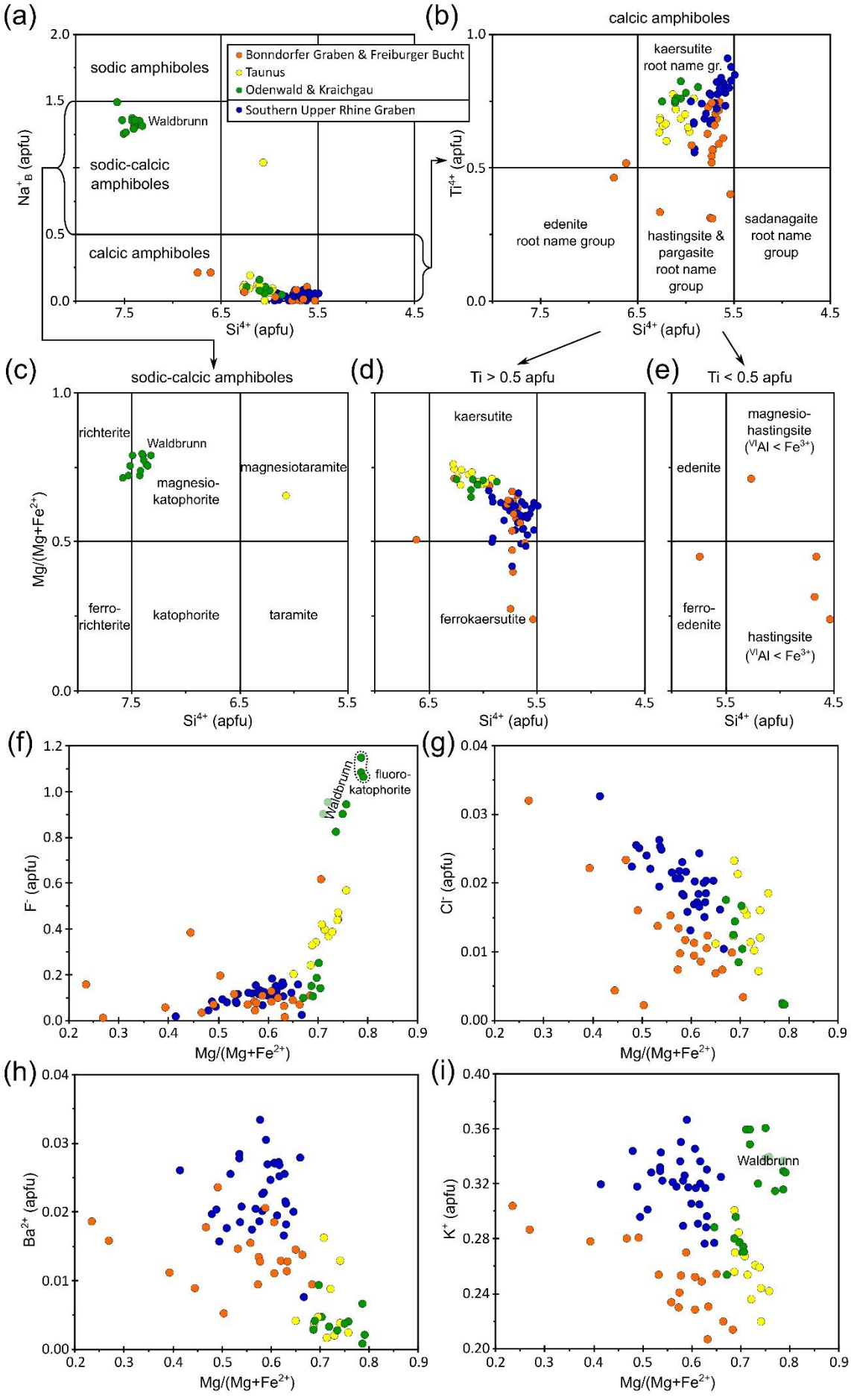
(a)
sodic amphiboles
sodic-calcic amphiboles
calcic amphiboles
Waldbrunn
Bonndorfer Graben & Freiburger Bucht
Taunus
Odenwald & Kraichgau
Southern Upper Rhine Graben
Na+B (apfu)
Si4+ (apfu)
(b)
calcic amphiboles
kaersutite root name gr.
edenite root name group
hastingsite & pargasite root name group
sadanagaite root name group
Ti4+ (apfu)
Si4+ (apfu)
(c)
sodic-calcic amphiboles
richterite
Waldbrunn
magnesio-katophorite
magnesiotaramite
ferro-richterite
katophorite
taramite
Mg/(Mg+Fe2+)
Si4+ (apfu)
(d)
Ti > 0.5 apfu
kaersutite
ferrokaersutite
Si4+ (apfu)
(e)
Ti < 0.5 apfu
magnesio-hastingsite (VIAl < Fe3+)
edenite
ferro-edenite
hastingsite (VIAl < Fe3+)
Si4+ (apfu)
(f)
Waldbrunn
fluoro-katophorite
F- (apfu)
Mg/(Mg+Fe2+)
(g)
Cl- (apfu)
Mg/(Mg+Fe2+)
(h)
Ba2+ (apfu)
Mg/(Mg+Fe2+)
(i)
Waldbrunn
K+ (apfu)
Mg/(Mg+Fe2+)

Fig. A6. (a–e) Amphibole classification scheme after Leake *et al.* (1997) for the studied CEVP rocks. Own data supplemented by Buggingen, southern URG. Si^{4+} (apfu) vs. **(a)** Na^{+}_{B} (apfu), **(b)** Ti^{4+} (apfu) for calcic amphiboles, **(c)** molar $Mg/(Mg+Fe^{2+})$ for sodic-calcic amphiboles, **(d)** for calcic amphiboles with Ti>0.5 apfu and **(e)** with Ti<0.5 apfu. **(f–i)** Amphibole composition with molar $Mg/(Mg+Fe^{2+})$ plotted against **(f)** F^{-} (apfu), **(g)** Cl^{-} (apfu), **(h)** Ba^{2+} (apfu), and **(i)** K^{+} (apfu).

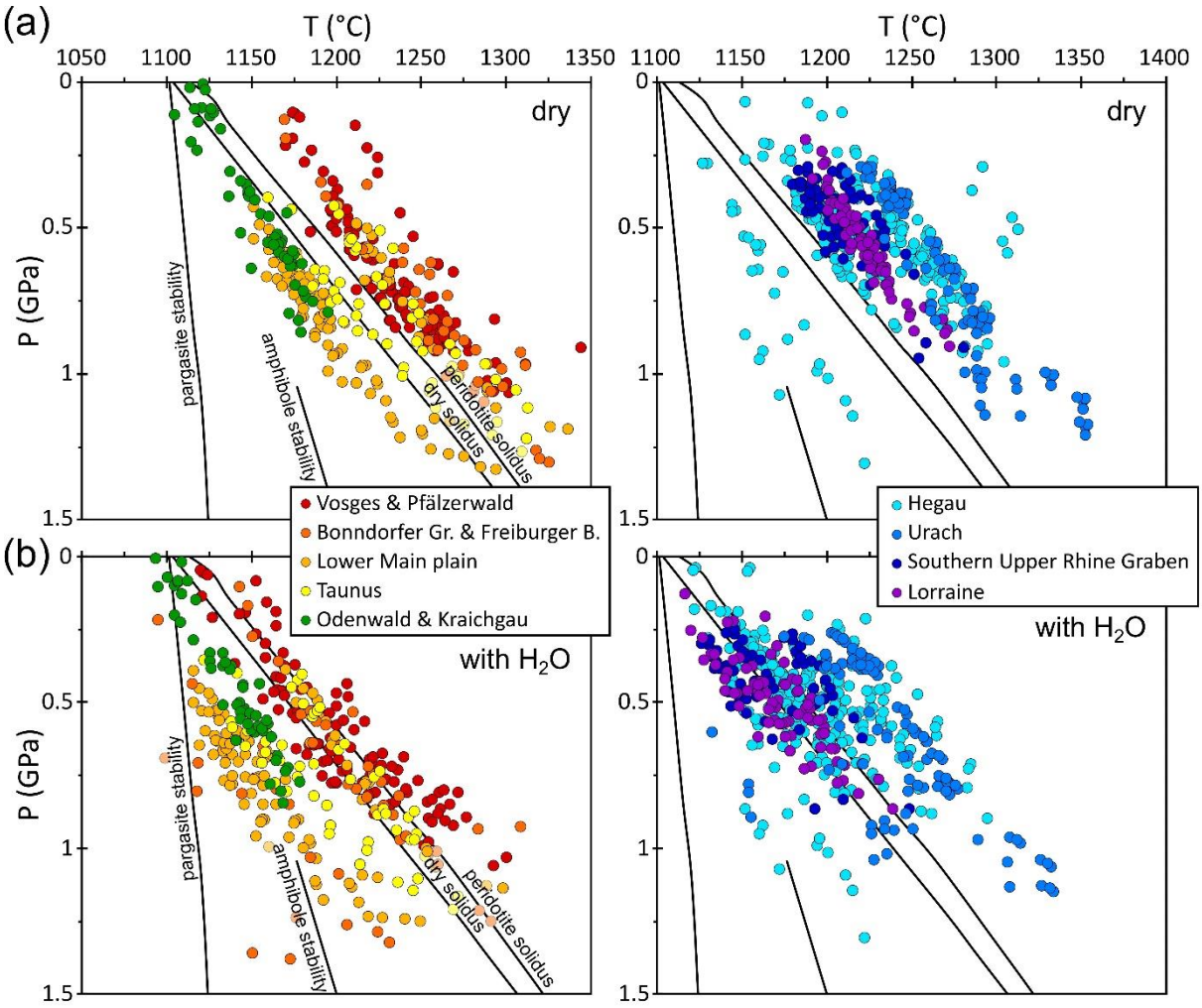

Fig. A7. Geothermobarometric results for the studied CEVP rocks. Clinopyroxene-based estimation of the *P-T* crystallization conditions based on Putirka (2008), Neave & Putirka (2017), and a whole-rock composition correction with **(a)** dry conditions and **(b)** consideration of the water content in the samples. Each data point represents a *P-T* value estimated by the model from a whole-rock analysis combined with a corresponding early-magmatic clinopyroxene core composition. Solidus conditions for different mantle lithologies and stability arrays based on McKenzie & Bickle (1988), Falloon & Green (1990), Foley (1991), Robinson & Wood (1998), Hirschmann (2000) and Kogiso *et al.* (2003).

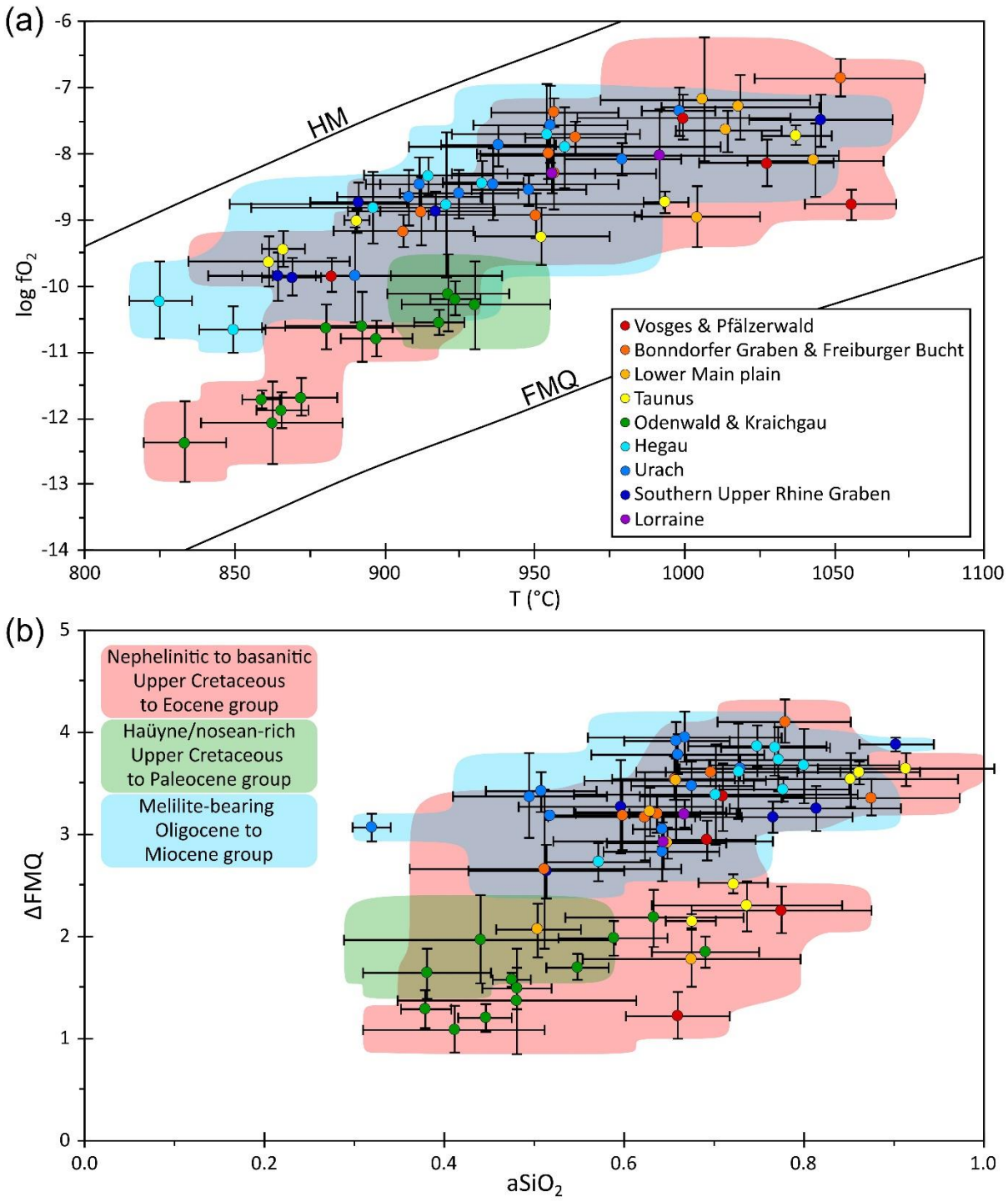

Fig. A8. QUILF-based estimation of the crystallization conditions for the studied CEVP rocks. The symbols illustrate mean values for each rock sample calculated from results of at least 30 discrete clinopyroxene-olivine-oxyspinel triplets. The error bars visualize the corresponding standard deviation (1σ) calculated from these triplets for each sample. The average uncertainty for all data points is <0.10 for $aSiO_2$ and <1.0 for fO_2 and refers to the uncertainty determined by QUILF for each triplet and is not equal the calculated standard deviation for each sample. **(a)** T (°C) vs. log fO_2 diagram with the FMQ and hematite-magnetite (HM) buffers as black lines. **(b)** $aSiO_2$ vs. ΔFMQ.

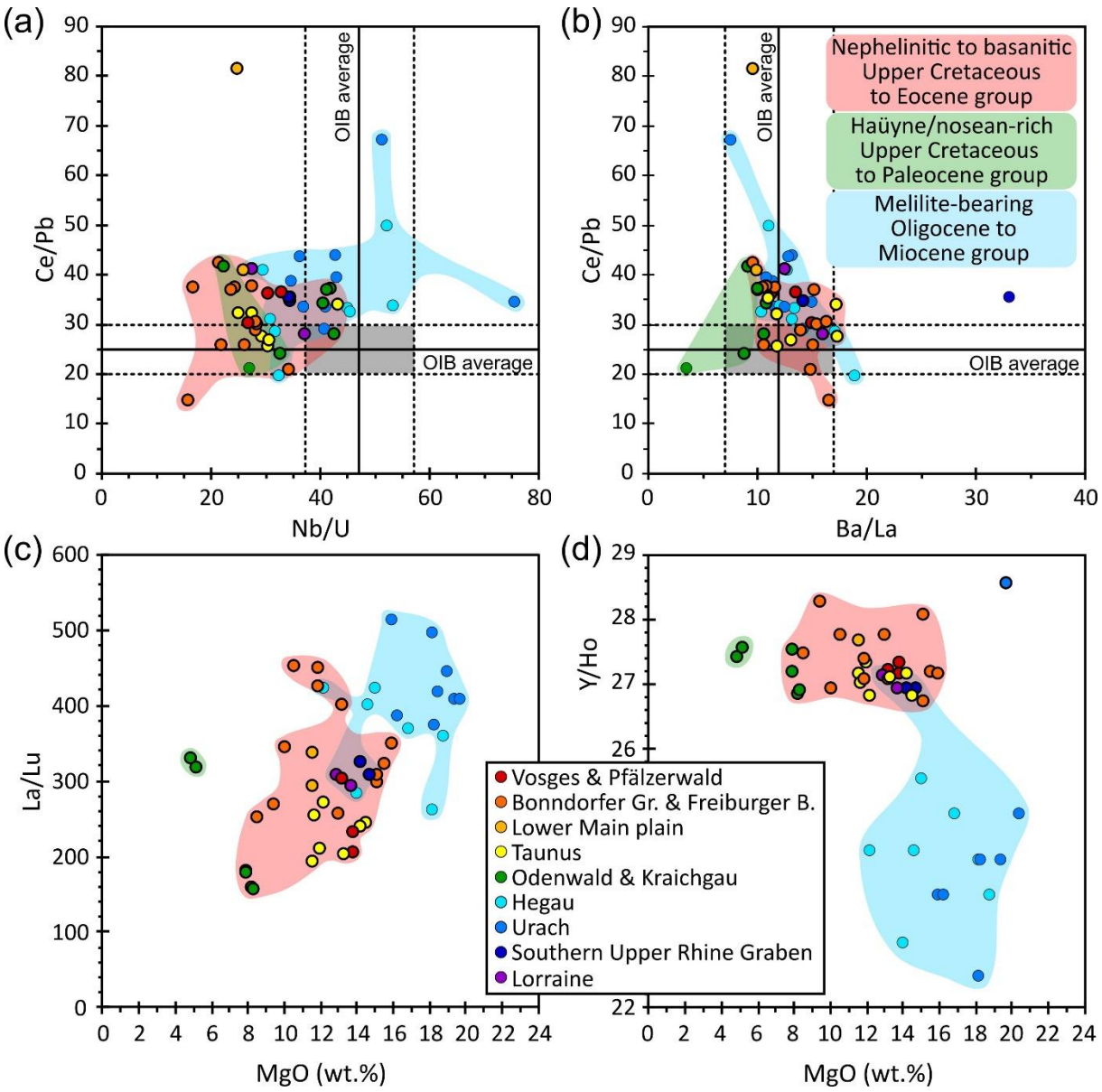

Fig. A9. Plots of different whole-rock element ratios for the studied CEVP rocks. 34 new analyses (black-rimmed circles) supplemented by literature data as stated in Fig. 9. The black lines represent the averages for OIB, the dashed lines the commonly observed ranges (Hofmann *et al.*, 1986; Weaver, 1991). **(a)** Nb/U vs. Ce/Pb. **(b)** Ba/La vs. Ce/Pb. **(c)** MgO (wt.%) vs. La/Lu. **(d)** MgO (wt.%) vs. Y/Ho.

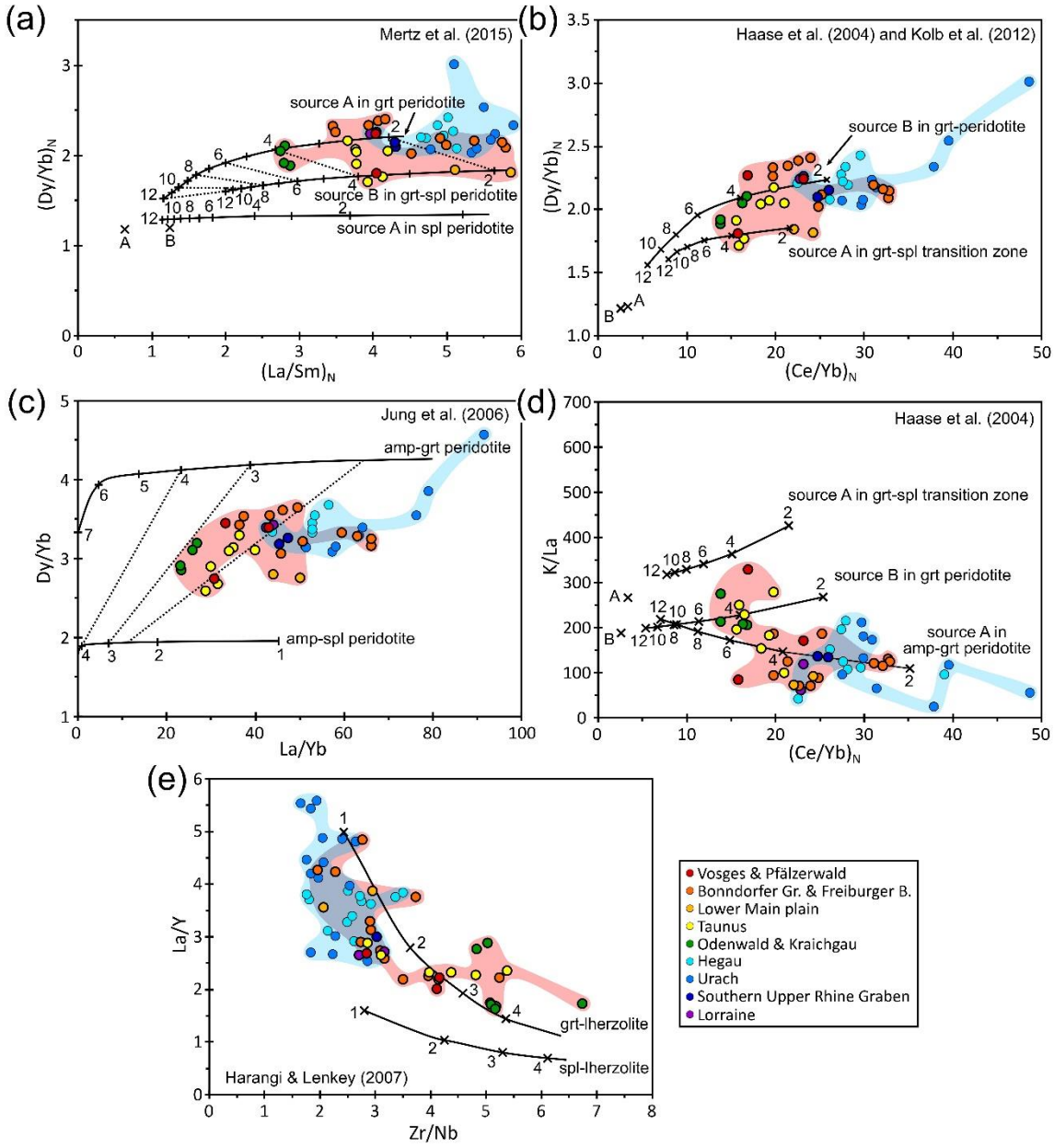

Fig. A10. Plots of various whole-rock trace element ratios for the studied CEVP rocks (new analyses plotted as black-rimmed circles), yielding indications of possible magma sources and degrees of partial melting based on models of Haase *et al.* (2004), Jung *et al.* (2006), Harangi & Lenkey (2007), Kolb *et al.* (2012), and Mertz *et al.* (2015). The numbers for each melting curve refer to the degree of partial melting (vol.%). 34 new analyses supplemented by literature data as stated in Fig. 9. **(a)** Chondrite-normalized La/Sm vs. chondrite-normalized Dy/Yb. The model curves indicate possible melting trends in the garnet peridotite stability field (source A), garnet-spinel transition zone (source B), and spinel peridotite stability field (source A). **(b)** Chondrite-normalized Ce/Yb vs. chondrite-normalized Dy/Yb. Model curves indicate possible melting trends in the garnet peridotite stability field (source B) and in the garnet-spinel transition zone (source A). **(c)** La/Yb vs. Dy/Yb. The model curves indicate possible melting trends of an amphibole-bearing garnet peridotite and an amphibole-bearing spinel peridotite. **(d)** Chondrite-normalized Ce/Yb vs. K/La. The model curves indicate possible melting trends in the garnet-spinel transition zone (source A), garnet peridotite (source B), and amphibole-garnet peridotite (source A). **(e)** Zr/Nb vs. La/Y. The model curves indicate possible melting trends of a garnet lherzolite and a spinel lherzolite.

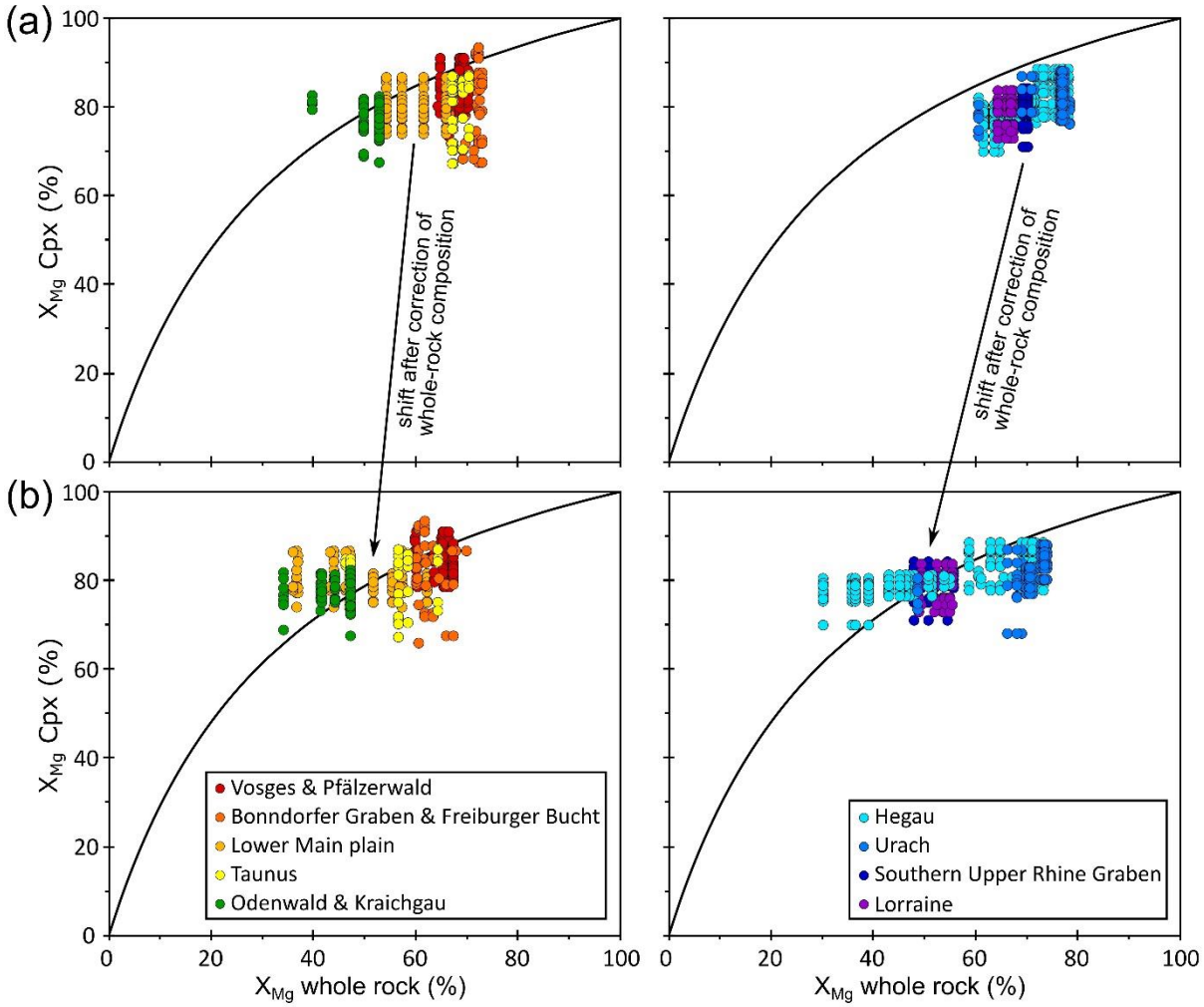

Fig. A11. The Rhodes diagram shows the expected X_{Mg} in a clinopyroxene phenocryst for a given X_{Mg} in the whole rock, assuming that the melt is in equilibrium with the clinopyroxene during crystallization ($K_D[Fe\text{-}Mg]^{Cpx\text{-}liq} = 0.27$) and that the whole-rock composition represents the melt composition. Therefore, the whole-rock composition must represent the primary melt composition and the clinopyroxene phenocrysts must be crystallized early-magmatic. **(a)** The uncorrected X_{Mg} for the whole rock plotted against X_{Mg} in centres of clinopyroxene phenocrysts implies disequilibrium conditions for all Oligocene to Miocene rocks and for numerous Upper Cretaceous to Eocene rocks. **(b)** Correcting the whole-rock composition by factoring out a volume of olivine crystals and green-core pyroxenes – each with averaged chemical compositions (using microprobe results) – that crystallized before the first clinopyroxene phenocrysts results in a shift of X_{Mg} toward lower values. This leads to a good agreement with the ratios expected at equilibrium crystallization and allows a determination of the p-T conditions according to Putirka (2008) and Neave & Putirka (2017).

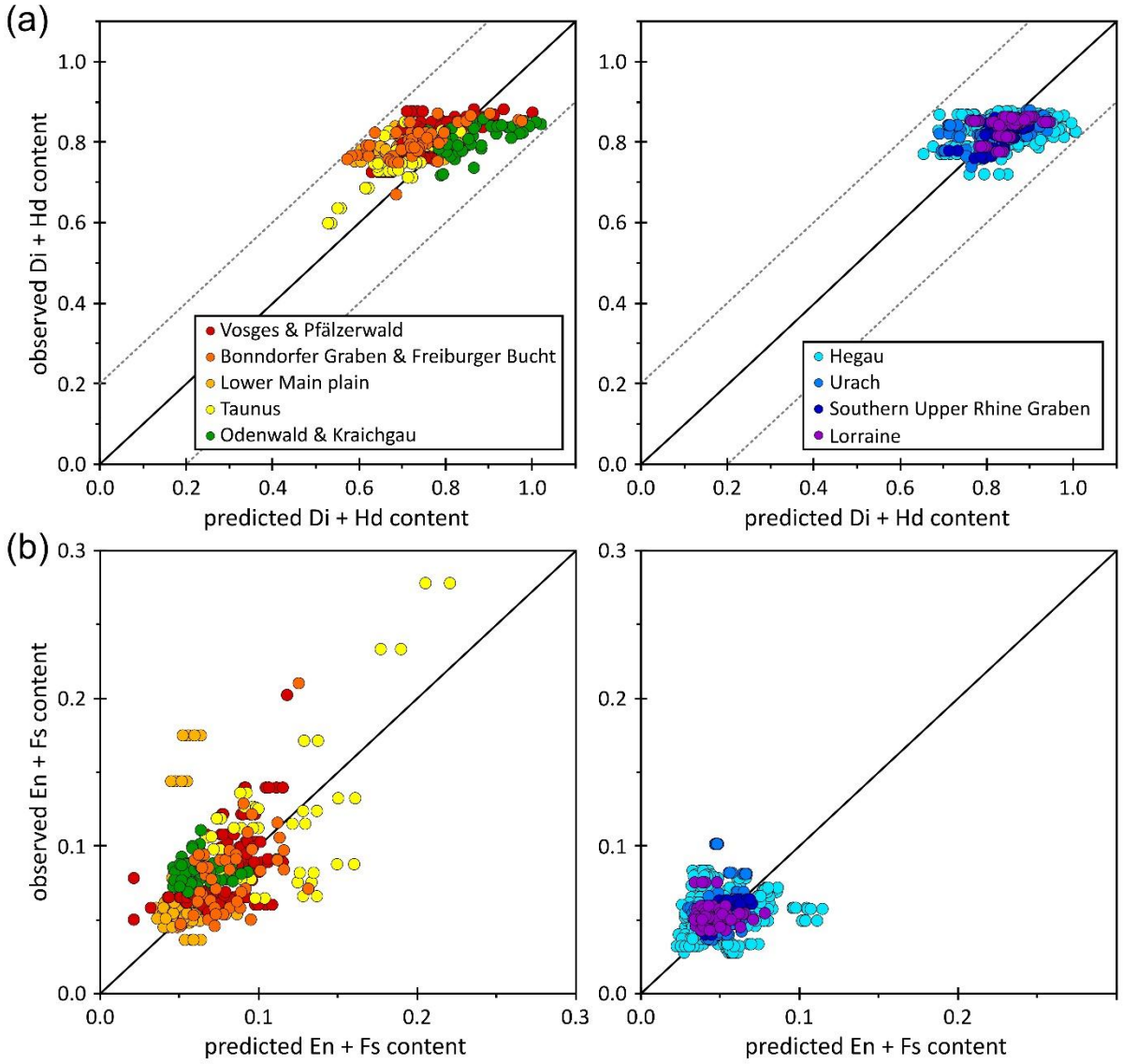

Fig. A12. Predicted equilibrium clinopyroxene endmember compositions (Putirka, 1999) vs. observed compositions for the studied CEVP rocks using the geothermobarometric model according to Putirka (2008) and Neave & Putirka (2017). **(a)** Predicted content of diopside (Di) and hedenbergite (Hd) vs. observed content. Applied threshold values for the clinopyroxene–melt pairs used are shown in grey dashed lines. **(b)** Predicted content of enstatite (En) and ferrosilite (Fs) vs. observed content.

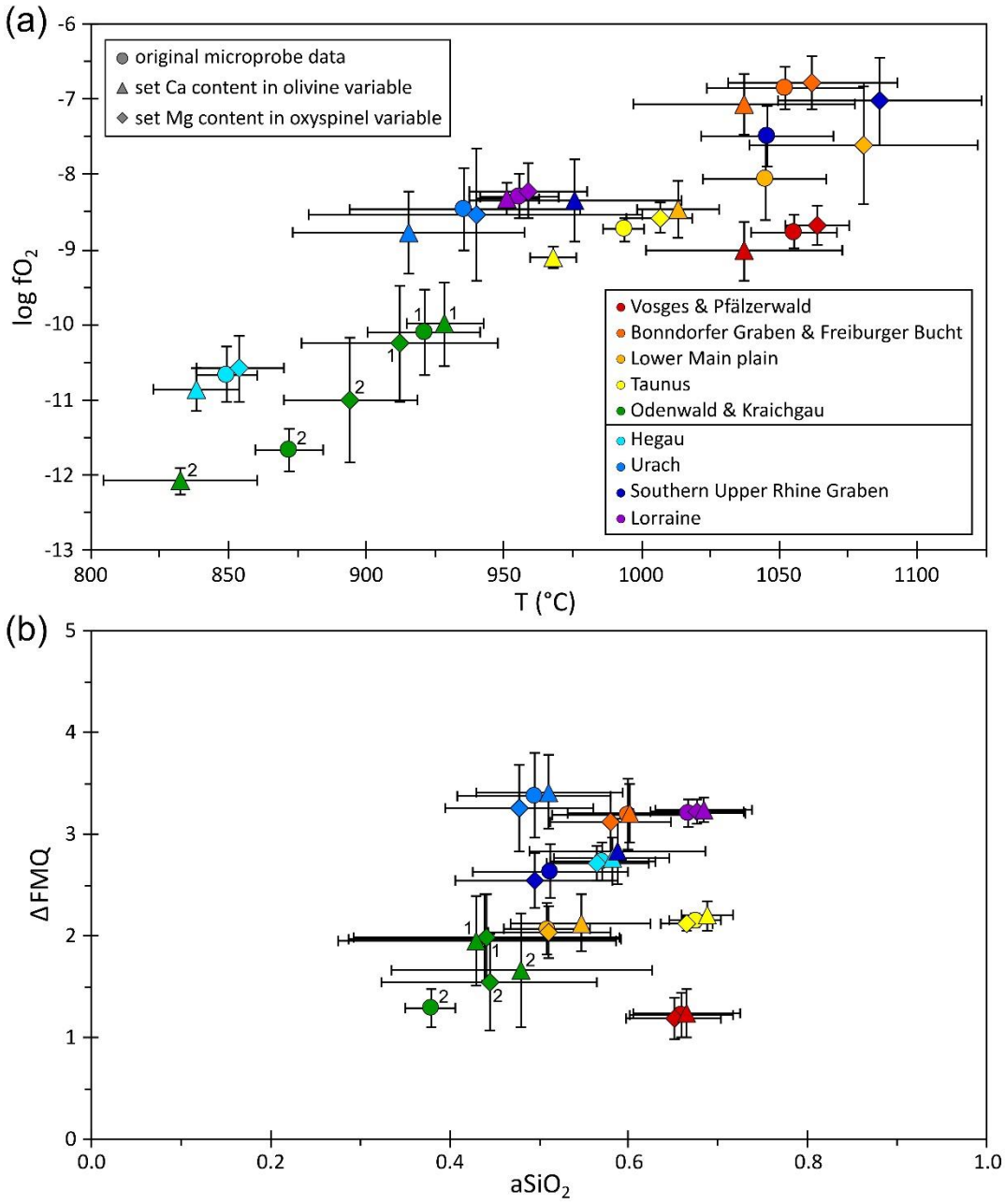

Fig. A13. Comparison of three approaches to QUILF-based estimation of the crystallization conditions for the studied CEVP rocks using ten representative samples. The potential problems of using QUILF are Mg diffusion in oxyspinel and Ca diffusion in olivine rims. The possible influence of these effects, occurring after crystallization and leading to a reduction in equilibrium temperature and a change in silica activity and oxygen fugacity, can be quantified. For this purpose, the Mg content in oxyspinel is set variable in the QUILF software in one run, and the Ca content in olivine rims in another. This iteratively calculates two new results each, which can be compared to the result using the original microprobe data for these parameters, providing an indication of the magnitude of both possible methodological errors. **(a)** T (°C) vs. log fO_2. In most cases, the magnitude of this possible methodological error is within the standard deviation of the original results and thus within the fundamental uncertainty of using QUILF. **(b)** $aSiO_2$ vs. oxygen fugacity (expressed as ΔFMQ). The possible influence of the methodological error on silica activity and on ΔFMQ is almost negligible compared to the standard deviation calculated from the original results for these two quantities.

Supplementary data – File 2

Thermodynamic calculations

A clinopyroxene-based geothermometer (Eqn. 33 in Putirka, 2008) and the geobarometer of Neave & Putirka (2017) were used for estimation of pressure (*P*) and temperature (*T*), assuming equilibrium of early-magmatic clinopyroxene cores with the parental melt. For the whole-rock composition of the samples, appropriate corrections were applied by subtracting carefully estimated fractions of average chemical compositions of xeno-/antecrystic olivine and green-core pyroxenes (Rhodes diagram with $K_D[Fe\text{-}Mg]^{Cpx\text{-}liq} = 0.27$ to test for equilibrium, given in Supplementary data, Fig. A11). The influence of H_2O was assessed by performing all calculations on both dry and H_2O-bearing basis, indicating a *T* decrease of ~17 ± 2 °C and a negligible *P* decrease of 15-30 MPa per additional 1 wt.% H_2O. Only the results where the equilibrium clinopyroxene compositions predicted by the model of Putirka (1999) approximate the observed composition (calculated after the normative scheme of Putirka *et al.*, 1996) were used for estimation of the *P*-*T* conditions (thresholds and used clinopyroxene–melt pairs depicted in Supplementary data, Fig. A12).

The QUILF software (Andersen *et al.*, 1993) was used to quantify *T*, oxygen fugacity (fO_2), and $aSiO_2$ for late-magmatic assemblages (olivine rims, Cr-poor oxyspinel, and cogenetic clinopyroxene) assuming constant *P* of 0.1 GPa. Similar calculations for early-magmatic assemblages were not possible, as no Cr-spinel is implemented in QUILF. Note that EPMA results for Mg in oxyspinel do not necessarily reflect the content at the time of crystallization because of the relatively high Mg diffusivity (e.g., Ozawa, 1984). Also, the EPMA-determined CaO content of olivine rims is generally low (<1 wt.%) and highly variable, partially due to secondary fluorescence by neighbouring Ca phases (Dalton & Lane, 1996). To account for these uncertainties, calculations were performed in three different ways and compared to each other. First, the EPMA results for Ca in olivine and Mg in oxyspinel

were used and fixed as invariable. In the subsequent two runs, the Ca content in olivine was assumed to be variable in one case, and the Mg content in oxyspinel in the other, resulting in an iteratively calculated best-fit in both cases. The deviations produced by the various calculation methods are largely limited to ± 20 K and ± 0.5 log fO_2, indicating a negligible influence on $aSiO_2$ and ΔFMQ determinations (Supplementary data, Fig. A13).

Mineral formula calculations

Mineral formula and endmember calculations were preformed according to Deer *et al.* (2009), and pyroxene endmember determination followed Mann *et al.* (2006). Additional necessary and appropriate assumptions are shown in the table below this section. Amphibole classification was conducted based on Leake *et al.* (1997). The Fe^{3+}/Fe^{2+} determination in oxyspinel, in pyroxene, and in melilite was carried out assuming an ideal lattice site occupancy of 3, 4, and 5 cations per formula unit, respectively. For the sodalite group (sodalite, nosean, haüyne), 12 cations are assumed at the tetrahedral and 1-2 anions at the sulphate/chlorine position, based on 24 O^{2-} excluding the sulphate anion. A sulphidic lazurite component must be excluded, otherwise the system is underdetermined. The formula calculation for mica is based on 8 cations per formula unit and Σ O+OH+F+Cl=12. An oxy-mica component is permitted to completely occupy the OH,F,Cl site. The H_2O content is determined by excluding H_3O^+ on the interstitial layer and allowing only Fe^{3+} on the tetrahedral position, whereas only Fe^{2+} is accepted on the octahedral position. This calculation procedure has proved successful for the present micas, since all of them have only small amounts of Fe on the octahedron anyway, with the presence of Fe^{3+} there instead of Fe^{2+} having a negligible effect on the formula determination. Additionally, K, Ba, and Na contents are usually sufficient to completely occupy the interstitial site, so H_3O^+ is not present. Apatite formulas are calculated based on 1 anion at the OH,F,Cl position and Σ PO_4^{3-}+SO_4^{2-}=3. For

the amphibole group, no vacancies are assumed at the A-position, since K+Na are >1 apfu and Ca+Na+K>2.5 apfu in all analyses. Thus, the amphibole unit cell is considered fully occupied by 16 cations. The Fe is initially assumed to be divalent and water is added until the OH,O,F,Cl position is occupied by 2 anions or the number of 16 cations per formula unit is reached. In the latter case, an oxy-amphibole component must be assumed; in the former case, the 16 cations are adjusted by adding Fe^{3+} and reducing the Fe^{2+} accordingly. Rhönite mineral formula calculation is based on 28 cations and 40 O^{2-}.

Supplementary data File 2, Table 1. Considered end members and their lattice site occupancy for the determination of pyroxene compositions. The cations were assigned according to the order shown in the table.

Name	M2	M1	T_2	O_6
Aegirine	Na^+	Fe^{3+}	Si^{4+}_2	O_6
Ca-Fe-Tschermak	Ca^{2+}	Fe^{3+}	$Fe^{3+}Si^{4+}$	O_6
Jadeite	Na^+	Al^{3+}	Si^{4+}_2	O_6
(Ti,Zr)-Aegirine	Na^+	$(Ti^{4+},Zr^{4+})_{0.5}(Mg^{2+},Fe^{2+})_{0.5}$	Si^{4+}_2	O_6
Ca-Ti-Tschermak	Ca^{2+}	$(Ti^{4+},Zr^{4+})_{0.5}(Mg^{2+},Fe^{2+})_{0.5}$	$Al^{3+}Si^{4+}$	O_6
Ca-Al-Tschermak (Kushiroite)	Ca^{2+}	Al^{3+}	$Al^{3+}Si^{4+}$	O_6
Ca-Cr-Al-Tschermak	Ca^{2+}	Cr^{3+}	$Al^{3+}Si^{4+}$	O_6
Diopside	Ca^{2+}	Mg^{2+}	Si^{4+}_2	O_6
Hedenbergite/Johannsenite	Ca^{2+}	(Fe^{2+},Mn^{2+})	Si^{4+}_2	O_6
Enstatite	Mg^{2+}	Mg^{2+}	Si^{4+}_2	O_6
Ferrosilite	Fe^{2+}	Fe^{2+}	Si^{4+}_2	O_6
Normative wollastonite	Ca^{2+}	Ca^{2+}	Si^{4+}_2	O_6

Comparison of crystallization conditions with those in other CEVP regions and application of further geothermometers

Previous *P-T* estimations based on various geothermobarometers (e.g., Lindsley, 1983; Putirka *et al.*, 1996; Soesoo, 1997; Putirka, 2008; Neave & Putirka, 2017) for related rocks in other CEVP regions (Bohemian Massif, Vogtland, Osteifel, Westeifel, KVC) resemble our temperatures for early-magmatic crystallization, ranging from 1000-1260 °C (Panina *et al.*, 2000; Abratis *et al.*, 2009; Skála *et al.*, 2015; Braunger *et al.*, 2018; Sundermeyer *et al.*, 2020), and yield pressures of 1-2 GPa (Skála *et al.*, 2015). Based on late-magmatic minerals,

further geothermometers yield similar or lower *T* compared with QUILF-derived T_{eq} (820-1060 °C; Supplementary data, Fig. A8a). Mg and Ti contents in mica indicate ~750-800 °C (Supplementary data, Fig. A4d), which must be regarded as T_{min}, as the thermometer (Henry *et al.*, 2005) is optimized for ilmenite-bearing rocks at 0.4-0.6 GPa and can cause underestimations in the order of ~60 K in magnetite-bearing lithologies. However, the composition of groundmass sanidine in a phonolitic nepheline noseanite from the Odenwald and Kraichgau region indicates even lower *T* (600-700 °C; thermometer after Fuhrman & Lindsley, 1988) and nepheline thermometry (Hamilton, 1961; Wilkinson & Hensel, 1994) on melilite-bearing rocks in the Eger Graben indicates crystallization *T* of 500-770 °C (Abratis *et al.*, 2009; Skála *et al.*, 2015). Overall, this reveals a prolonged crystallization interval over wide *T* ranges, probably due to high concentrations of volatile and incompatible elements in the parental melt and further enrichment during fractionation but does not provide reliable information on the primary melting conditions.

Redox variations during melt evolution?

The occurrence of Fe-rich, partly resorbed olivine cores exclusively in the melilite-bearing rocks (Urach, Lorraine) has been interpreted as an indication of initially low oxygen fugacity in the parental melts. Consumption of CO_2 in the early-magmatic phase by reaction with olivine and $CaCO_3$ at greater depths results in a melilite- or clinopyroxene-rich magma and exsolution of a dolomite-carbonatitic melt (see reactions 2 & 3 in the main article). This potentially affects the chemical equilibria below, involving Fe^{3+}/Fe^{2+} and CO_2/CO (e.g., Pan *et al.*, 1991; Pawley *et al.*, 1992). Accordingly, compensation of CO_2 results in CO consumption and lowers fO_2 temporarily (Seifert & Thomas, 1995).

$$CO + \frac{1}{2}O_2 \leftrightarrow CO_2 \quad \textit{and} \quad Fe_2O_3 \leftrightarrow 2\,FeO + \frac{1}{2}O_2$$

$$CO + Fe_2O_3 \leftrightarrow CO_2 + 2\,FeO$$

Consequently, the carbon oxidation reduces the Fe^{3+}/Fe^{2+} ratio in the melt, so the corresponding Mg/Fe^{2+} ratio in olivine crystallizing at this stage is comparatively low. As magmatic evolution continues and pressure decreases, CO_2 saturation in the melt causes the loss of dissolved carbonate ions and separation of a CO_2-rich vapor that may contain a non-negligible amount of CO compared to the residual melt, in which CO is practically insoluble at low pressures (Pawley *et al.*, 1992; Seifert & Thomas, 1995; Lowenstern, 2001). The continuous formation and instant release of CO into the segregating vapor phase drives the reactions to the left and induces oxidation of the remaining melt (Mathez, 1984; Brounce *et al.*, 2017), which increases its Fe^{3+}/Fe^{2+} and thus the Mg/Fe^{2+} ratio in olivine, possibly resulting in reverse zoning (Dunworth & Wilson, 1998). However, the initial fO_2 and amount of CO stored in asthenospheric–subcontinental lithospheric mantle sources, derived partial melts, and coexisting fluid/vapor phases are controversial. A significant change in the charge balance of C due to CO_2 exsolution causing oxidation of mantle-derived mafic magmas at appropriate depths is rejected by several authors, assuming an almost exclusive speciation of C as either CO_3^{2-} when dissolved in alkaline mafic melts or as CO_2 when partitioned into the vapor (e.g., Morizet *et al.*, 2010; Cottrell & Kelley, 2011; Ni & Keppler, 2013).

Contributions of the classical "mantle components/reservoirs/end-members" to melting

The La/Nb and Zr/Nb ratios might allow conclusions regarding the character of the mantle source (Fig. 13c), as these incompatible elements are not significantly affected by early fractional crystallization of olivine and/or oxyspinel. The melilite-bearing rocks have La/Nb ratios corresponding to high-μ ocean island basalts (HIMU-OIB; Weaver, 1991) and Zr/Nb ratios at the lower limit for HIMU-OIB. In contrast, the La/Nb ratios of the nephelinitic–basanitic rocks resemble enriched mantle (EM) ocean island basalts (Weaver, 1991), with the Zr/Nb ratio matching HIMU-OIB. The ambiguous source signature for the latter group may

be due to the origin of these rocks from a garnet wehrlite, previously overprinted by carbonatite metasomatism. HIMU-OIB characteristics were mostly attributed to magma sources with residual garnet and hydrous phases in the upper asthenosphere or in the lower lithospheric thermal boundary layer that point to hydrothermally altered, subducted, and recycled ancient oceanic crust (e.g., Jung & Masberg, 1998; Stracke *et al.*, 2005; Jung *et al.*, 2006; Harangi & Lenkey, 2007; Lustrino & Wilson, 2007; Kolb *et al.*, 2012). In contrast, the origin of the EM-OIB signatures remains controversial. However, all EM end-members are thought to share a common heritage of continental crust with varying proportions of lower and upper continental crust, and for some recycling of marine sediments and oceanic lithosphere from subduction zones or by crustal delamination is suspected (Willbold & Stracke, 2010).

Likewise, the composition of the early magmatic or entrained oxyspinel cores indicates different mantle reservoirs. Those cores in the melilite-free rocks are characterised by higher average Al contents at the expense of Fe^{3+} and predominantly resemble oxyspinel from mid-ocean ridge basalts (MORB), whereas those in the melilite-bearing rocks mostly have compositions in the overlapping range of oxyspinel from OIB and MORB (Supplementary data, Fig. A2a; Barnes & Roeder, 2001). Without further isotope data, an unequivocal identification of the classical mantle reservoirs/components in the melt source and a quantification of their contribution to magma formation is not meaningful.

Discussion on temperatures of melting

The estimated formation temperatures for the studied rocks are consistent with melting *T* estimates for parental magmas of other basanitic, nephelinitic, and melilititic rocks in the CEVP and elsewhere (Pannonian Basin, Madagascar), yielding 1250–1450 °C, lacking a clear distribution among distinct lithologies (Seifert & Thomas, 1995; Jung & Masberg, 1998;

Haase *et al.*, 2004; Jung *et al.*, 2006; Jung *et al.*, 2012; Kolb *et al.*, 2012; Mayer *et al.*, 2013; Harangi *et al.*, 2015; Mertz *et al.*, 2015; Mazzeo *et al.*, 2021). Since the upper stability limit for amphibole at ~3 GPa was often reported to be <1200 °C (pargasite; e.g., Wallace & Green, 1991; Green *et al.*, 2010), the need for a hot, carbonated asthenospheric initial melt, ascending into the colder lithosphere (~1100-1200 °C), partially melting it, and bequeathing the negative K anomaly along with other trace element pattern has been postulated (e.g., Wedepohl, 1985; Dunworth & Wilson, 1998; Bogaard & Wörner, 2003; Jung *et al.*, 2012; Kolb *et al.*, 2012; Mayer *et al.*, 2013; Mertz *et al.*, 2015). Pfänder *et al.* (2018) and Blusztajn & Hegner (2002) locate the entire melt formation of basanites and melilite-bearing nephelinites in the lower lithosphere in the presence of residual phlogopite at a T_{max} of 1120-1250 °C, which conflicts with the crystallization *T* and the major residual phase determined for the rocks studied in this work. However, there is much evidence from experimental results that amphibole minerals are still stable at *T* >1200 °C in mantle lithologies. Examples of this are Ca-amphibole (1230-1260 °C at ~3.0 GPa; Allen & Boettcher, 1978; Huckenholz & Gilbert, 1984; Huckenholz *et al.*, 1988; Huckenholz *et al.*, 1992), K-fluoro-richterite (1350 °C at ~3.5 GPa; Foley, 1991), or K-richterite (1330-1450 °C at 5-10 GPa; Trønnes, 2002). Likewise, OH-phlogopite is stable up to 2.5 GPa at 1280 °C and up to 5 GPa at 1350 °C in the asthenosphere (Takahashi & Kushiro, 1983; Trønnes, 2002; Harangi & Lenkey, 2007; Lustrino & Wilson, 2007), questioning the definite requirement for a second, colder lithospheric mantle source (Hegner *et al.*, 1995; Jung *et al.*, 2006).

Metasomatic enrichment prior to melting

The influence of metasomatic agents on alkaline magmatism and on upper mantle lithologies in central Europe is preserved as association of carbonatites with highly oxidized SiO_2-undersaturated alkaline rocks (e.g., Kaiserstuhl; Braunger *et al.*, 2018) and in amphibole- and

phlogopite-bearing wehrlite xenoliths and melt inclusions therein (Moreva-Perekalina, 1985; Seifert & Thomas, 1995; Witt-Eickschen, 2003; Ulrych *et al.*, 2013; Loges *et al.*, 2019). There is consensus that a subduction-related mechanism is the most likely origin for volatile-rich carbonate metasomatism (e.g., Harmon *et al.*, 1987; Hegner *et al.*, 1995; Hegner & Vennemann, 1997; Blusztajn & Hegner, 2002; Ulrych *et al.*, 2013; Ulrych *et al.*, 2016; Pfänder *et al.*, 2018). Jung & Hoernes (2000), Harangi & Lenkey (2007) and Ulrych *et al.* (2013) propose that dehydration melting of recycled oceanic lithosphere imprinted features like negative Pb anomalies (Fig. 12b), positive Nb/Ta anomalies, and low Zr/Nb ratios (Fig. 13) primarily on the source of melilititic rocks. For alkaline rocks in the Hessian Depression, Wedepohl (1985) and Kramm & Wedepohl (1990) suggested a contribution of subducted granulites and garnet amphibolites, assimilated, dehydrated, and decarbonated in the upper mantle. Hegner *et al.* (1995) ruled out direct contribution of an old crustal component to melt formation for the Urach and Hegau rocks, consistent with our results, but favoured the enrichment of partial melts derived from ancient subducted oceanic lithosphere similar to alkaline Vogelsberg rocks (Jung & Masberg, 1998). Shallow asthenospheric mantle heterogeneities may reflect subducted crustal fragments, being preserved for long times and an important host for volatiles and incompatible trace elements (Kogiso *et al.*, 2004; Meibom & Anderson, 2004). Niu & O'Hara (2003) suggested that metasomatism occurs at the interface between these portions of oceanic lithosphere and the low-velocity zone in the asthenosphere (~100-200 km), consistent with depths of >125 km (>4 GPa) assumed by Pfänder *et al.* (2018). Geochemical mantle heterogeneity on various scales and to various extent may be related to the long orogenic history in central Europe, comprising Variscan and Alpine orogeny (Harangi & Lenkey, 2007).

Embey-Isztin *et al.* (1993), Bogaard & Wörner (2003), Kolb *et al.* (2012), and Pfänder *et al.* (2018) attributed parts of the metasomatism to modification by aqueous and/or

supercritical fluids released from subducted lithologies. Jung *et al.* (2012) and Harangi *et al.* (2015) suggested that H_2O- and carbonate-bearing, eclogite-, and/or pyroxenite-derived silicate melts from greater depths infiltrated and metasomatized the subsequent melt source for the alkaline rocks in the Siebengebirge and the Pannonian Basin. The involvement of an eclogitic component, convectively incorporated into mantle peridotite, was hypothesized by Kolb *et al.* (2012) to explain a strong residual garnet signature and respective high Zr/Hf ratios in alkaline rocks from the Siebengebirge. However, a correlation between the Zr/Hf and the La/Yb ratio (for quantification of HREE depletion; not shown) is not observed in the investigated rocks of the southern CEVP and the Zr/Hf ratio is highly scattered (Fig. 13b). Consistently, Haase *et al.* (2004) excluded garnet pyroxenite and/or eclogite as dominant melt source for SiO_2-undersaturated primitive Westerwald rocks but proposed the involvement of subducted intra-plate basalts to melt formation.

Based on the composition of clinopyroxene macrocrysts and melt inclusions in an olivine nephelinite, Ulianov *et al.* (2007) proposed a mechanism for mantle metasomatism beneath the KVC by carbonatitic melts originating from the dolomite-garnet stability field (<2.2-2.4 GPa), which reacted with lherzolite at <2.0-2.2 GPa to a calciocarbonatite-wehrlite assemblage. Accordingly, subsequent non-modal melting and olivine dissolution caused formation of additional clinopyroxene and evolved carbonatitic melt, accompanied by segregation of a tephriphonolitic melt that reacted with further wehrlite, resulting in a volatile-enriched olivine nephelinitic magma, the same process with Ca-dominated and more intense carbonate metasomatism and/or lower degrees of partial melting leading instead to the formation of olivine melilitites. A positive correlation between melilite content and influence of carbonate in the respective mantle source is also indicated *within* the younger rock group: Compared to the Hegau region, where harzburgite and lherzolite xenoliths dominate, clinopyroxene-rich xenoliths such as phlogopite wehrlites prevail at Urach, suggesting

stronger carbonate metasomatism in that region, consistent with the higher melilite content in the Urach rocks (e.g., Fig. 1a; Dunworth & Wilson, 1998).

Supplementary data references

Abratis, M., Munsel, D. & Viereck-Götte, L. (2009). Melilithite und Melilith-führende Magmatite des sächsischen Vogtlands: Petrographie und Mineralchemie. *Zeitschrift für Geologische Wissenschaften* **37**, 41–79.

Alibert, C., Michard, A. & Albarède, F. (1983). The Transition from Alkali Basalts to Kimberlites: Isotope and Trace Element Evidence from Melilitites. *Contributions to Mineralogy and Petrology* **82**, 176–186.

Allen, J. C. & Boettcher, A. L. (1978). Amphiboles in andesite and basalt: II. Stability as a function of P–T–fH_2O–fO_2. *American Mineralogist* **63**, 1074–1087.

Barnes, S. J. & Roeder, P. L. (2001). The Range of Spinel Compositions in Terrestrial Mafic and Ultramafic Rocks. *Journal of Petrology* **42**, 2279–2302.

Becker, E. (1904). Der Rossbergbasalt bei Darmstadt und seine Zersetzungsprodukte. Inaugural-Dissertation. Halle (Saale): Vereinigte Friedrichs-Universität Halle-Wittenberg.

Berg, U. & Weiskirchner, W. (1979). Petrographische Untersuchungen an vulkanischen Gesteinen des Jusi (Schwäbische Alb). *Jahresberichte und Mitteilungen des Oberrheinischen Geologischen Vereins* **61**, 337–346.

Blusztajn, J. & Hegner, E. (2002). Osmium isotopic systematics of melilitites from the Tertiary Central European Volcanic Province in SW Germany. *Chemical Geology* **189**, 91–103.

Bogaard, P. J. F. & Wörner, G. (2003). Petrogenesis of Basanitic to Tholeiititic Volcanic Rocks from the Miocene Vogelsberg, Central Germany. *Journal of Petrology* **44**, 569–602.

Braunger, S., Marks, M. A. W., Walter, B. F., Neubauer, R., Reich, R., Wenzel, T., Parsapoor, A. & Markl, G. (2018). The Petrology of the Kaiserstuhl Volcanic Complex, SW Germany: The Importance of Metasomatized and Oxidized Lithospheric Mantle for Carbonatite Generation. *Journal of Petrology* **59**, 1731–1762.

Braunger, S., Scharrer, M., Marks, M. A., Wenzel, T. & Markl, G. (2021). Interaction between mafic dike rocks and salt deposits in the Rhine Graben, southwest Germany. *The Canadian Mineralogist* **59**, 511–531.

Brounce, M., Stolper, E. & Eiler, J. (2017). Redox variations in Mauna Kea lavas, the oxygen fugacity of the Hawaiian plume, and the role of volcanic gases in Earth's oxygenation. *Proceedings of the National Academy of Sciences of the United States of America* **114**, 8997–9002.

Butchereit, E. (1990). Mikrothermometrische Untersuchungen an Fluid- und Schmelzeinschlüssen in Olivinen der melilithführenden Olivin-Nephelinite der Schwäbischen Alb. Dissertation. Tübingen: Eberhard Karls Universität Tübingen.

Cottrell, E. & Kelley, K. A. (2011). The oxidation state of Fe in MORB glasses and the oxygen fugacity of the upper mantle. *Earth and Planetary Science Letters* **305**, 270–282.

Dalton, J. A. & Lane, S. J. (1996). Electron microprobe analysis of Ca in olivine close to grain boundaries; the problem of secondary X-ray fluorescence. *American Mineralogist* **81**, 194–201.

Deer, W. A., Howie, R. A. & Zussman, J. (2009). An introduction to the rock-forming minerals. Pearson/Prentice Hall.

Dunworth, E. A. & Wilson, M. (1998). Olivine Melilitites of the SW German Tertiary Volcanic Province: Mineralogy and Petrogenesis. *Journal of Petrology* **39**, 1805–1836.

Embey-Isztin, A., Downes, H., James, D. E., Upton, B. G. J., Dobosi, G., Ingram, G. A., Harmon, R. S. & Scharbert, H. G. (1993). The Petrogenesis of Pliocene Alkaline Volcanic Rocks from the Pannonian Basin, Eastern Central Europe. *Journal of Petrology* **34**, 317–343.

Falloon, T. J. & Green, D. H. (1990). Solidus of carbonated fertile peridotite under fluid-saturated conditions. *Geology* **18**, 195.

Foley, S. (1991). High-pressure stability of the fluor- and hydroxy-endmembers of pargasite and K-richterite. *Geochimica et Cosmochimica Acta* **55**, 2689–2694.

Frenzel, G. (1975). *Die Nephelingesteinsparagenese des Katzenbuckels im Odenwald*. In: Amstutz, G. C., Meisl, S. & Nickel, E. (eds.) *Mineralien und Gesteine im Odenwald: Beiträge zum heutigen Forschungsstand*, 213–228.

Freudenberg, W. (1906). Geologie und Petrographie des Katzenbuckels im Odenwald. *Mitteilungen der Grossherzoglich Badischen geologischen Landesanstalt* **5**, 185–344.

Fuhrman, M. L. & Lindsley, D. H. (1988). Ternary-feldspar modeling and thermometry. *American Mineralogist* **73**, 201–215.

Green, D. H., Hibberson, W. O., Kovács, I. & Rosenthal, A. (2010). Water and its influence on the lithosphere-asthenosphere boundary. *Nature* **467**, 448–451.

Haase, K. M., Goldschmidt, B. & Garbe-Schönberg, C.-D. (2004). Petrogenesis of Tertiary Continental Intra-plate Lavas from the Westerwald Region, Germany. *Journal of Petrology* **45**, 883–905.

Hamilton, D. L. (1961). Nephelines as Crystallization Temperature Indicators. *The Journal of Geology* **69**, 321–329.

Harangi, S. (2001). Neogene to Quaternary volcanism of the Carpathian–Pannonian Region—a review. *Acta Geologica Hungarica* **44**, 223–258.

Harangi, S., Jankovics, M. É., Sági, T., Kiss, B., Lukács, R. & Soós, I. (2015). Origin and geodynamic relationships of the Late Miocene to Quaternary alkaline basalt volcanism in the Pannonian basin, eastern–central Europe. *International Journal of Earth Sciences* **104**, 2007–2032.

Harangi, S. & Lenkey, L. (2007). *Genesis of the Neogene to Quaternary volcanism in the Carpathian-Pannonian region: Role of subduction, extension, and mantle plume*. In: Beccaluva, L., Bianchini, G. & Wilson, M. (eds.) *Cenozoic Volcanism in the Mediterranean Area*, 67–92.

Harmon, R. S., Hoefs, J. & Wedepohl, K. H. (1987). Stable isotope (O, H, S) relationships in Tertiary basalts and their mantle xenoliths from the Northern Hessian Depression, W.-Germany. *Contributions to Mineralogy and Petrology* **95**, 350–369.

Hegner, E. & Vennemann, T. W. (1997). Role of fluids in the origin of Tertiary European intraplate volcanism: Evidence from O, H, and Sr isotopes in melilitites. *Geology* **25**, 1035–1038.

Hegner, E., Walter, H. J. & Satir, M. (1995). Pb-Sr-Nd isotopic compositions and trace element geochemistry of megacrysts and melilitites from the Tertiary Urach volcanic field: source composition of small volume melts under SW Germany. *Contributions to Mineralogy and Petrology* **122**, 322–335.

Henry, D. J., Guidotti, C. V. & Thomson, J. A. (2005). The Ti-saturation surface for low-to-medium pressure metapelitic biotites: Implications for geothermometry and Ti-substitution mechanisms. *American Mineralogist* **90**, 316–328.

Hirschmann, M. M. (2000). Mantle solidus: Experimental constraints and the effects of peridotite composition. *Geochemistry, Geophysics, Geosystems* **1**, 2000GC000070.

Hofmann, A. W., Jochum, K. P., Seufert, M. & White, W. M. (1986). Nb and Pb in oceanic basalts: new constraints on mantle evolution. *Earth and Planetary Science Letters* **79**, 33–45.

Huckenholz, H. G. & Gilbert, M. C. (1984). The stability of Ca-amphibole in alkali basalts of the High Eifel region. *Fortschritte der Mineralogie* **62**, 106–107.

Huckenholz, H. G., Gilbert, M. C. & Kunzmann, T. (1992). Stability and phase relations of calcic amphiboles crystallized from magnesio-hastingsite compositions in the 1 to 45 kbar pressure range. *Neues Jahrbuch für Mineralogie - Abhandlungen (Journal of Mineralogy and Geochemistry)* **164**, 229–268.

Huckenholz, H. G., Kunzmann, T. & Spicker, C. (1988). Stability of titanian magnesio-hastingsite and its breakdown to rhönite-bearing assemblages. *Terra Cognita* **8**, 66.

Hurrle, H. (1976). Ocelli- und Mandelbildung der ultrabasischen Basalte im Kalisalzlager Buggingen und im Kristallin des Schwarzwaldes. *Jahreshefte des geologischen Landesamtes Baden-Württemberg* **18**, 19–37.

Jung, C., Jung, S., Hoffer, E. & Berndt, J. (2006). Petrogenesis of Tertiary Mafic Alkaline Magmas in the Hocheifel, Germany. *Journal of Petrology* **47**, 1637–1671.

Jung, S. & Hoernes, S. (2000). The major- and trace-element and isotope (Sr, Nd, O) geochemistry of Cenozoic alkaline rift-type volcanic rocks from the Rhön area (central Germany): petrology, mantle source characteristics and implications for asthenosphere–lithosphere interactions. *Journal of Volcanology and Geothermal Research* **99**, 27–53.

Jung, S. & Masberg, P. (1998). Major- and trace-element systematics and isotope geochemistry of Cenozoic mafic volcanic rocks from the Vogelsberg (central Germany) Constraints on the origin of continental alkaline and tholeiitic basalts and their mantle sources. *Journal of Volcanology and Geothermal Research* **86**, 151–177.

Jung, S., Vieten, K., Romer, R. L., Mezger, K., Hoernes, S. & Satir, M. (2012). Petrogenesis of Tertiary Alkaline Magmas in the Siebengebirge, Germany. *Journal of Petrology* **53**, 2381–2409.

Keller, J., Brey, G., Lorenz, V. & Sachs, P. (1990). *Volcanism and Petrology of the Upper Rhinegraben (Urach-Hegau-Kaiserstuhl)*. In: *Urach, Hegau, Kaiserstuhl: Excursion 2A, August 27 to September 2, 1990*, 1–60.

Kogiso, T., Hirschmann, M. M. & Frost, D. J. (2003). High-pressure partial melting of garnet pyroxenite: possible mafic lithologies in the source of ocean island basalts. *Earth and Planetary Science Letters* **216**, 603–617.

Kogiso, T., Hirschmann, M. M. & Reiners, P. W. (2004). Length scales of mantle heterogeneities and their relationship to ocean island basalt geochemistry. *Geochimica et Cosmochimica Acta* **68**, 345–360.

Kolb, M., Paulick, H., Kirchenbaur, M. & Münker, C. (2012). Petrogenesis of Mafic to Felsic Lavas from the Oligocene Siebengebirge Volcanic Field (Germany): Implications for the Origin of Intracontinental Volcanism in Central Europe. *Journal of Petrology* **53**, 2349–2379.

Kramm, U. & Wedepohl, K. H. (1990). Tertiary basalts and peridotite xenoliths from the Hessian Depression (NW Germany), reflecting mantle compositions low in radiogenic Nd and Sr. *Contributions to Mineralogy and Petrology* **106**, 1–8.

Krause, O. (1969). Die Melilith-Nephelinite des Hegaus. Dissertation. Tübingen: Eberhard-Karls-Universität zu Tübingen.

Krause, O. & Weiskirchner, W. (1981). Die Olivin-Nephelinite des Hegaus. *Jh. geol. Landesamt Baden-Württemberg* **23**, 87–130.

Leake, B. E., Woolley, A. R., Arps, C., Birch, W. D., Gilbert, M. C., Grice, J. D., Hawthorne, E., Kato, A., Kisch, H. J., Krivovichev, V. G., Linthout, K., Laird, J., Mandarino, J., Maresch, W. V., Nickel, E. H., Rock, N., Schumacher, J. C., Smith, D. C., Stephenson, N., Ungaretti, L., Whittaker, E. & Youzhi, G. (1997). Nomenclature of amphiboles: Report of the Subcommittee on Amphiboles of the International Mineralogical Association Commission on New Minerals and Mineral Names. *European Journal of Mineralogy* **9**, 623–651.

Lindsley, D. H. (1983). Pyroxene thermometry. *American Mineralogist* **68**, 477–493.

Loges, A., Schultze, D., Klügel, A. & Lucassen, F. (2019). Phonolitic melt production by carbonatite Mantle metasomatism: evidence from Eger Graben xenoliths. *Contributions to Mineralogy and Petrology* **174**, 93.

Lowenstern, J. B. (2001). Carbon dioxide in magmas and implications for hydrothermal systems. *Mineralium Deposita* **36**, 490–502.

Lustrino, M. & Wilson, M. (2007). The circum-Mediterranean anorogenic Cenozoic igneous province. *Earth-Science Reviews* **81**, 1–65.

Mann, U., Marks, M. A. & Markl, G. (2006). Influence of oxygen fugacity on mineral compositions in peralkaline melts: The Katzenbuckel volcano, Southwest Germany. *Lithos* **91**, 262–285.

Mathez, E. A. (1984). Influence of degassing on oxidation states of basaltic magmas. *Nature* **310**, 371–375.

Mayer, B., Jung, S., Romer, R. L., Stracke, A., Haase, K. M. & Garbe-Schönberg, C.-D. (2013). Petrogenesis of Tertiary Hornblende-bearing Lavas in the Rhön, Germany. *Journal of Petrology* **54**, 2095–2123.

Mazzeo, F. C., Rocco, I., Tucker, R. D., Morra, V., D'Antonio, M. & Melluso, L. (2021). Olivine melilitites, mantle xenoliths, and xenocrysts of the Takarindiona district: Petrogenesis, magmatic evolution, and the sub-continental lithospheric mantle of east-central Madagascar. *Journal of African Earth Sciences* **174**, 104059.

McKenzie, D. & Bickle, M. J. (1988). The Volume and Composition of Melt Generated by Extension of the Lithosphere. *Journal of Petrology* **29**, 625–679.

Meibom, A. & Anderson, D. L. (2004). The statistical upper mantle assemblage. *Earth and Planetary Science Letters* **217**, 123–139.

Mertz, D. F., Löhnertz, W., Nomade, S., Pereira, A., Prelević, D. & Renne, P. R. (2015). Temporal–spatial evolution of low-SiO2 volcanism in the Pleistocene West Eifel volcanic field (West Germany) and relationship to upwelling asthenosphere. *Journal of Geodynamics* **88**, 59–79.

Moreva-Perekalina, T. V. (1985). Ultramafic xenoliths from alkaline basalts of Finkenberg (Siebengebirge, West Germany). *Scripta Geologica* **78**, 1–65.

Morizet, Y., Paris, M., Gaillard, F. & Scaillet B. (2010). C–O–H fluid solubility in haplobasalt under reducing conditions: An experimental study. *Chemical Geology* **279**, 1–16.

Neave, D. A. & Putirka, K. D. (2017). A new clinopyroxene-liquid barometer, and implications for magma storage pressures under Icelandic rift zones. *American Mineralogist* **102**, 777–794.

Neumann, U., Metz, P. & Westphal, F. (1992). Vulkanismus der Schwäbischen Alb. *Beihefte zum European Journal of Mineralogy* **4**, 1–37.

Ni, H. & Keppler, H. (2013). Carbon in Silicate Melts. *Reviews in Mineralogy & Geochemistry* **75**, 251–287.

Niu, Y. & O'Hara, M. J. (2003). Origin of ocean island basalts: A new perspective from petrology, geochemistry, and mineral physics considerations. *Journal of Geophysical Research: Solid Earth* **108**, 5.1-5.18.

Ozawa, K. (1984). Olivine-spinel geospeedometry: Analysis of diffusion-controlled Mg-Fe^{2+} exchange. *Geochimica et Cosmochimica Acta* **48**, 2597–2611.

Pan, V., Holloway, J. R. & Hervig, R. L. (1991). The pressure and temperature dependence of carbon dioxide solubility in tholeiitic basalt melts. *Geochimica et Cosmochimica Acta* **55**, 1587–1595.

Panina, L. I., Sharygin, V. V. & Keller, J. (2000). Olivine nephelinite, tephrite, essexite, phonolite, and tinguaite from Kaiserstuhl, Germany: Evidence from melt inclusions in pyroxene. *Geochemistry International* **38**, 343–352.

Pawley, A. R., Holloway, J. R. & McMillan, P. F. (1992). The effect of oxygen fugacity on the solubility of carbon–oxygen fluids in basaltic melt. *Earth and Planetary Science Letters* **110**, 213–225.

Pfänder, J. A., Jung, S., Klügel, A., Münker, C., Romer, R. L., Sperner, B. & Rohrmüller, J. (2018). Recurrent Local Melting of Metasomatised Lithospheric Mantle in Response to Continental Rifting: Constraints from Basanites and Nephelinites/Melilitites from SE Germany. *Journal of Petrology* **59**, 667–694.

Putirka, K., Johnson, M., Kinzler, R., Longhi, J. & Walker, D. (1996). Thermobarometry of mafic igneous rocks based on clinopyroxene-liquid equilibria, 0-30 kbar. *Contributions to Mineralogy and Petrology* **123**, 92–108.

Putirka, K. D. (1999). Clinopyroxene+liquid equilibrium to 100 kbar and 2450 K. *Contributions to Mineralogy and Petrology* **135**, 151–163.

Putirka, K. D. (2008). Thermometers and Barometers for Volcanic Systems. *Reviews in Mineralogy and Geochemistry* **69**, 61–120.

Robinson, J. C. & Wood, B. J. (1998). The depth of the spinel to garnet transition at the peridotite solidus. *Earth and Planetary Science Letters* **164**, 277–284.

Seifert, W. & Thomas, R. (1995). Silicate-carbonate immiscibility: a melt inclusion study of olivine melilitite and wehrlite xenoliths in tephrite from the Elbe Zone, Germany. *Chemie der Erde – Geochemistry* **55**, 263–279.

Skála, R., Ulrych, J., Ackerman, L., Krmíček, L., Fediuk, F., Balogh, K. & Hegner, E. (2015). Upper Cretaceous to Pleistocene melilitic volcanic rocks of the Bohemian Massif: petrology and mineral chemistry. *Geologica Carpathica* **66**, 197–216.

Soesoo, A. (1997). A multivariate statistical analysis of clinopyroxene composition: Empirical coordinates for the crystallisation PT-estimations. *GFF – Geologiska Föreningens i Stockholm Förhandlingar (Journal of the Geological Society of Sweden)* **119**, 55–60.

Staesche, A. (1995). Der genetische Zusammenhang zwischen Melilithiten und Phonolithen des Hegaus, SW-Deutschland. Diploma thesis. Tübingen: Eberhard Karls Universität Tübingen.

Stähle, V., Koch, M., McCammon, C. A., Mann, U. & Markl, G. (2002). Occurrence of low-Ti and high-Ti Freudenbergite in Alkali Syenite Dikes from the Katzenbuckel Volcano, Southwestern Germany. *The Canadian Mineralogist* **40**, 1609–1627.

Stellrecht, R. & Emmermann, R. (1970). Das Olivinnephelinit-Vorkommen von Forst/Pfalz. *Oberrheinische geologische Abhandlungen* **19**, 29–41.

Stock, M. (1990). Mikrothermometrische Untersuchung der Fluid- und Schmelzeinschlüsse in Olivinen der Nephelinite vom Neuhewen und Hohenstoffeln (Hegau). Diploma thesis. Tübingen: Eberhard Karls Universität Tübingen.

Stracke, A., Hofmann, A. W. & Hart, S. R. (2005). FOZO, HIMU, and the rest of the mantle zoo. *Geochemistry, Geophysics, Geosystems* **6**, Q05007.

Sundermeyer, C., Gätjen, J., Weimann, L. & Wörner, G. (2020). Timescales from magma mixing to eruption in alkaline volcanism in the Eifel volcanic fields, western Germany. *Contributions to Mineralogy and Petrology* **175**, 77.

Takahashi, E. & Kushiro, I. (1983). Melting of a dry peridotite at high pressures and basalt magma genesis. *American Mineralogist* **68**, 859–879.

Trønnes, R. G. (2002). Stability range and decomposition of potassic richterite and phlogopite end members at 5-15 GPa. *Mineralogy and Petrology* **74**, 129–148.

Ulianov, A., Müntener, O., Ulmer, P. & Pettke, T. (2007). Entrained Macrocryst Minerals as a Key to the Source Region of Olivine Nephelinites: Humberg, Kaiserstuhl, Germany. *Journal of Petrology* **48**, 1079–1118.

Ulrych, J., Ackerman, L., Balogh, K., Hegner, E., Jelínek, E., Pécskay, Z., Přichystal, A., Upton, B. G., Zimák, J. & Foltýnová, R. (2013). Plio-Pleistocene basanitic and melilititic series of the Bohemian Massif: K-Ar ages, major/trace element and Sr–Nd isotopic data. *Geochemistry* **73**, 429–450.

Ulrych, J., Krmíček, L., Tomek, Č., Lloyd, F. E., Ladenberger, A., Ackerman, L. & Balogh, K. (2016). Petrogenesis of Miocene alkaline volcanic suites from western Bohemia: whole rock geochemistry and Sr–Nd–Pb isotopic signatures. *Geochemistry* **76**, 77–93.

Velde, D. & Thiebaut, J. (1973). Quelques précisions sur la constitution minéralogique de la néphélinite à olivine et mélilite d'Essey-la-Côte (Meurthe-et-Moselle). *Bulletin de la Société française de Minéralogie et de Cristallographie* **96**, 298–302.

Wallace, M. & Green, D. H. (1991). The effect of bulk rock composition on the stability of amphibole in the upper mantle: Implications for solidus positions and mantle metasomatism. *Mineralogy and Petrology* **44**, 1–19.

Walter, H.-J. (1994). Spurenelement- und Isotopengeochemie von Megakristallen und Melilithiten des Uracher Vulkangebietes: Signifikanz für die Genese des tertiären zentraleuropäischen Vulkanismus. Diploma thesis. Tübingen: Eberhard Karls Universität Tübingen.

Weaver, B. L. (1991). Trace element evidence for the origin of ocean-island basalts. *Geology* **19**, 123.

Wedepohl, K. H. (1985). Origin of the Tertiary basaltic volcanism in the northern Hessian Depression. *Contributions to Mineralogy and Petrology* **89**, 122–143.

Wilkinson, J. F. G. & Hensel, H. D. (1994). Nephelines and analcimes in some alkaline igneous rocks. *Contributions to Mineralogy and Petrology* **118**, 79–91.

Willbold, M. & Stracke, A. (2010). Formation of enriched mantle components by recycling of upper and lower continental crust. *Chemical Geology* **276**, 188–197.

Wimmenauer, W. (1952). Petrographische Untersuchungen an einigen basischen Eruptivgesteinen des Oberrheingrabens. *Neues Jahrbuch für Mineralogie - Abhandlungen (Journal of Mineralogy and Geochemistry)* **83**, 375–432.

Wimmenauer, W. (1974). *The Alkaline province of Central Europe and France.* In: Sørensen, H. (ed.) *The Alkaline Rocks*, 238–271.

Witt-Eickschen, G. (2003). Lithospheric Mantle Evolution beneath the Eifel (Germany): Constraints from Sr-Nd-Pb Isotopes and Trace Element Abundances in Spinel Peridotite and Pyroxenite Xenoliths. *Journal of Petrology* **44**, 1077–1095.

Anlage III

Akzeptierte Publikation

Arbeit 3

Binder T, Marks MAW, Friedrichsen B-E, Walter BF, Wenzel T, Markl G (2024a) Bimodal volcanism in the Hegau region (SW Germany): Differentiation of primitive melilititic to nephelinitic rocks produces evolved nosean phonolites. Lithos 472–473:107565. https://doi.org/10.1016/j.lithos.2024.107565.

LITHOS 472-473 (2024) 107565

Contents lists available at ScienceDirect

LITHOS

journal homepage: www.elsevier.com/locate/lithos

Bimodal volcanism in the Hegau region (SW Germany): Differentiation of primitive melilititic to nephelinitic rocks produces evolved nosean phonolites

Thomas Binder [a,*], Michael A.W. Marks [a], Brian-Eric Friedrichsen [a], Benjamin F. Walter [b], Thomas Wenzel [a], Gregor Markl [a]

[a] Department of Geosciences, Eberhard Karls Universität Tübingen, Schnarrenbergstraße 94–96, 72076 Tübingen, Germany
[b] Chair of Geochemistry & Economic Geology and Laboratory of Environmental and Raw Materials Analyses (LERA), Karlsruhe Institute of Technology, Adenauerring 20b, 76131 Karlsruhe, Germany

ARTICLE INFO

Keywords:
Bimodal volcanism
Central European Volcanic Province
Magmatic differentiation
Melilite-bearing olivine nephelinite
Mineral chemistry
Nosean phonolite

ABSTRACT

Peculiar bimodal volcanism in the Hegau region (SW Germany) comprises two contrasting SiO_2-undersaturated rock suites.

(I) Primitive olivine melilitites and melilite-bearing olivine nephelinites (12–9 Ma) are characterized by high MgO, CaO, Fe_2O_3, TiO_2, Ni, V, F, moderate alkalis, Al_2O_3, P_2O_5, Ba, Nb, Zr, and low SiO_2, Rb, Pb, and U concentrations. The rocks are composed of forsteritic olivine, diopsidic clinopyroxene, melilite, perovskite, Cr-bearing oxyspinel, F- and Ba-rich mica, and fluorapatite. In rare cases, they contain coeval coarse-grained ijolite patches generated by rapid in-situ fractionation in small melt pockets.

(II) Evolved nosean phonolites (14–11 Ma) comprise high alkalis, Al_2O_3, SiO_2, Rb, Nb, Zr, U, Pb, S, and low MgO, CaO, Fe_2O_3, TiO_2, P_2O_5, Ba, Ni, and V concentrations, and contain abundant Ba-bearing alkali feldspar and nosean-haüyne-sodalite$_{ss}$ macrocrysts, aegirine-augitic clinopyroxene, as well as accessory apatite, titanite, zircon, and pyrochlore.

The melilititic–nephelinitic rocks formed by low degrees of partial melting of a carbonated amphibole ± phlogopite-bearing garnet wehrlite in the uppermost asthenosphere or in the thermal boundary layer and occur also in neighbouring regions. However, their coexistence with evolved nosean phonolites is a unique and so far, unexplained feature in the southern Central European Volcanic Province.

Thermodynamic modelling implies that removal of 11–19% oxyspinel, 4–10% olivine, 42–57% clinopyroxene, <3% mica, <9% feldspathoids, <8% feldspar from melilititic–nephelinitic parental melts at upper crustal conditions (~200 MPa) results in significant amounts of phonolitic residues that are compositionally similar to the exposed nosean phonolites. Strongly negative P and Ti anomalies and a trough of MREE in primitive mantle-normalized trace element patterns of phonolites indicate additional fractionation of titanite and apatite, consistent with the mineralogy of coarse-grained (nepheline) syenitic cumulates, which are present as enclaves in both rock suites. The modelling results suggest crystallization of the (nepheline) syenite cumulates between 1050 and 800 °C and ascent and eruption of the phonolite residues at no less than ~900 °C with complete solidification of the observed assemblage at >750 °C. Significant crustal assimilation during fractionation appears unnecessary to explain the mineralogical, mineral chemical, and geochemical characteristics of the phonolites. Prolonged upper crustal differentiation of the magmas in one case (nosean phonolites) and fast ascent of primitive melts in the other (olivine melilitites and melilite-bearing olivine nephelinites) can be explained by stress field changes from an extensional to a more compressive regime, the magma ascent becoming thereby increasingly structurally controlled and supported by brittle deformation.

* Corresponding author.
E-mail addresses: thomas.binder@uni-tuebingen.de (T. Binder), michael.marks@uni-tuebingen.de (M.A.W. Marks), brian-eric.friedrichsen@student.uni-tuebingen.de (B.-E. Friedrichsen), b.walter@kit.edu (B.F. Walter), gregor.markl@uni-tuebingen.de (G. Markl).

https://doi.org/10.1016/j.lithos.2024.107565
Received 10 November 2023; Received in revised form 28 February 2024; Accepted 1 March 2024
Available online 7 March 2024

1. Introduction

Bimodal volcanism is characterized by the eruption of mafic and felsic lavas in the same volcanic region, and usually shows a lack of intermediately composed rocks (*Daly gap*; e.g., Berger et al., 2009; Freundt-Malecha, 2001; Zhao et al., 2023). Such districts are commonly associated with extensional regimes, especially continental but also oceanic rifts (e.g., Corti, 2009; Deering et al., 2011; Lacasse et al., 2007; Rooney, 2020; Trua et al., 1999) as well as arc and back-arc magmatism (e.g., Chen et al., 2018; Lexa et al., 2010; Tamura and Tatsumi, 2002).

Many concepts explaining bimodal rock suites involve different initial magma sources that occur either coincidentally or causally related in the same region, for example if the same geodynamic process causes partial melting of different lithologies and/or if the melting degree strongly varied in time, both of which produce different parental melts (e.g., Chen et al., 2018; Hoernle and Schmincke, 1993; Rooney et al., 2007; Zou and Zindler, 1996). Other models involve the well-known scenario of magmatic underplating, where ascending mafic magmas (mostly basalts or andesites) pond at the Moho or in the lower crust and provide heat and fluids that are transferred upward and facilitate partial melting of overlying felsic lithologies (producing mostly granites/rhyolites; e.g., Peccerillo et al., 2007; Tamura and Tatsumi, 2002; Trua et al., 1999).

In other cases, the felsic compositions are last products of a differentiation path (via fractional crystallization) of the primitive magma compositions of the same volcanic region (e.g., Berger et al., 2009; Kong et al., 2023; Peccerillo et al., 2007; Ulrych et al., 2003; Vaněčková et al., 1993; Wörner and Schmincke, 1984). Elsewhere, significant crustal assimilation is additionally required to derive evolved assemblages from primitive ones (Corti, 2009; Peccerillo et al., 2003; Rooney, 2020; Schmitt et al., 2017; Trua et al., 1999). The absence of exposed intermediate rocks in bimodal volcanic regions has been explained by high viscosity and/or density of intermediate magmas, preventing ascent and emplacement at or near the surface (Freundt-Malecha, 2001 and references therein). Other concepts assume a general suppression of formation of intermediate rocks, i.e., fractionation of predominantly mafic minerals first and mostly felsic minerals thereafter with only little overlap (Peccerillo et al., 2003 and references therein). Accordingly, the intermediate differentiation stage was exceeded within a narrow temperature interval and with a low crystallization rate for thermodynamic and geochemical reasons. However, plutonic enclaves in volcanic rocks support the existence of cumulates of intermediate composition in crustal magma chambers and sometimes minor volumes of intermediate rocks like trachyandesites, trachybasalts, phonotephrites, or tephriphonolites do occur (e.g., Anti-Atlas, East African Rift, Eger Graben, Canary Islands, Rhön, Siebengebirge; Berger et al., 2009; Corti, 2009; Freundt-Malecha, 2001; Jung et al., 2012; Jung et al., 2013; Sliwinski et al., 2015; Ulrych et al., 2005; Ulrych et al., 2011; Vaněčková et al., 1993; Zaitsev et al., 2012). Peccerillo et al. (2003) suggest that small quantities of intermediate, crystal-rich melts form a thin mushy interlayer between the mafic and felsic lithologies of a fractionating, continuously fed magma chamber and can be easily entrained, constituting plutonic enclaves in the melts while rarely erupting themselves.

The association of primitive mafic melilitites, foidites, or basanites with evolved felsic phonolites is particularly known from several regions in the Central European Volcanic Province (CEVP) and was explained by fractionation of olivine, oxyspinel, and clinopyroxene followed by plagioclase, sanidine, and sometimes amphibole, phlogopite, apatite, sodalite-haüyne-nosean$_{ss}$, titanite, and/or garnet in upper crustal magma reservoirs (e.g., Braunger et al., 2018; Büchner et al., 2015; Jung et al., 2013; Schleicher et al., 1990; Vaněčková et al., 1993; Wilson et al., 1995b; Wörner and Schmincke, 1984). In the Hegau region, the southernmost district of the CEVP (study area), however, cross-cutting relationships between primitive olivine melilitites to melilite-bearing olivine nephelinites and evolved nosean phonolites are missing. Furthermore, direct evidence for magma mixing or continuous fractionation trends that would manifest themselves in intermediate rocks are absent, as both rock suites occur in separate volcanic centres (cf. Fig. 1).

Except for scarce whole-rock analyses (von Engelhardt and Weiskirchner, 1961; Keller et al., 1990; Mahfoud and Beck, 1989), comprehensive mineral chemical and whole-rock geochemical analyses for the phonolites are still lacking. In the present study, extensive petrographic and mineral chemical data for the volcanic to subvolcanic rocks of the Hegau region (except for the tuffs) and their coarse-grained enclaves are presented and combined with fractional crystallization modelling using MELTS to shed light on the genetic relationship between primitive and evolved rocks and on the volcanic evolution in this area as a textbook example of Central European bimodal rock suites.

2. Geological setting

The Hegau volcanic region lies in SW Germany directly north of the High Rhine and northwest of Lake Constance with the NW-SE-trending, parallel Hegau and Überlinger See graben systems (Theilen-Willige, 2011). It is situated at the southeastern end of the Bonndorf Graben (Fig. 1a), which crosses the Schwarzwald and hits the Upper Rhine Graben (URG) in the west near Freiburg. The former three grabens are collectively known as Freiburg-Bonndorf-Bodensee Fault zone (FBBFZ; Egli et al., 2017). Additionally, the seismically active Albstadt shear zone (e.g., Ring and Bolhar, 2020) commences in the Hegau region and trends parallel to the URG, terminating immediately west of the Urach volcanic field, whose activity lasted from 19 to 12 Ma (Binder et al., 2023). Although major rifting processes occurred in the Miocene, post-Variscan, Paleozoic–Mesozoic precursor structures probably had a large impact on the recent fault systems in the ~15–25 km wide graben complex, possibly tapping the upper mantle by reactivation of deep-seated faults (Egli et al., 2017; Ring and Bolhar, 2020). This is supported by the length of the FBBFZ (~100 km), indicating a major crustal-scale deformation zone (Egli et al., 2017). Since the Early Miocene, graben formation has been intensified by NE-oriented extension and mainly NW-directed subvertical shortening (Ring and Bolhar, 2020).

The Hegau region is characterized by bimodal volcanism (Fig. 1a; Mahfoud and Beck, 1989; Mäussnest and Schreiner, 1982): In the north and west, ~25 isolated vents/necks and, more rarely, dykes of primitive olivine melilitites and melilite-bearing olivine-nephelinites (continuous transition, in the following referred to as melilitites–nephelinites) and tuffs of the same composition occur. In contrast, in the eastern central Hegau region, six prominent domes of evolved nosean phonolite dominate the landscape (Fig. 1b). Especially between these two volcanic fields and in the southeast, there are numerous mafic tuff vents and extensive tuff blankets, whose crystal load comprises mainly augite, hornblende, and phlogopite, and which are mostly lapilli tuffs.

As the southern CEVP predominantly comprises melilititic, foiditic, and basanitic rocks (Binder et al., 2023), the phonolites of the Hegau together with those from Katzenbuckel (Mann et al., 2006) and the Kaiserstuhl volcanic complex (KVC; e.g., Braunger et al., 2018) represent a peculiarity but are comparable to volcanic rocks from the French Massif Central (Wilson et al., 1995a and references therein). Based on geochronology (Binder et al., 2023), the olivine melilitites and melilite-bearing olivine nephelinites, and ijolitic patches therein (12–9 Ma) are the youngest rocks (of the entire southern CEVP), whereas the nosean phonolites are slightly older (14–11 Ma). Syenite and nepheline syenite enclaves in the phonolites, in the melilititic–nephelinitic rocks, and in the mafic tuffs show the same age range (15–11 Ma). The primitive melilitites–nephelinites of the Hegau region were produced by low-degree partial melting of an amphibole ±phlogopite-bearing garnet peridotite in the uppermost asthenosphere or the lower lithospheric thermal boundary layer, which underwent CO_2- and Ca-rich subduction-related metasomatism (Alibert et al., 1983; Binder et al., 2024; Blusztajn and Hegner, 2002; Dunworth and Wilson, 1998; Hegner and Vennemann, 1997). Mobilization, infiltration, and emplacement of

metasomatic agents probably occurred in consequence of continuous dehydration and recycling of Variscan oceanic lithosphere, comprising the release of Ca-rich carbonates, further volatiles, and incompatible elements into the mantle (Binder et al., in press).

Graben and basin fillings of the Hegau region consist of Oligocene–Miocene Alpine molasse sediments, and are underlain by Upper Jurassic limestones (Schreiner, 2008). The deposition of conglomerates (17–15 Ma) and particularly the *Juranagelfluh* sediments (<15 Ma) reflect an important stage of erosion and unroofing in the Alpine foreland as a result of pronounced uplift of the Vosges-Swabian arc (Ring and Bolhar, 2020). Bedding inclines to the southeast at up to 5° due to gradually increasing subsidence caused by the loading of the Alpine orogen (Egli et al., 2017). Distinct step faults on the southwestern flanks of the Hegau Graben system reach into the basement and dip subvertically to subhorizontally to the NE (e.g., Randen, Schienerberg faults; Fig. 1a), adding up to an offset of ~300 m, while northeastern graben faults are less well defined and dip SW, displaying a maximum offset of ~120 m (Mindelsee fault; Fig. 1a; Egli et al., 2017; Schreiner, 2008). The wedge-like sedimentary sequence thickens from the NW basin edge to 1600 m at the western end of Lake Constance (Schreiner, 2008).

3. Material and methods

For petrographic examination, 44 thin sections from 23 localities of the Hegau region were available (Table 1). The samples originate from collections of the University of Tübingen and the LGRB Freiburg (Germany); in addition, several localities were resampled to augment the inventory. All thin sections were studied by light microscopy and scanning electron microscopy (*Phenom XL, Thermo Fisher Scientific*) at the Department of Geosciences, University of Tübingen. A subset of the samples was used in the geochronological and petrological studies of Binder et al. (2023) and Binder et al. (in press). For the present study, 15 samples (ijolite, nosean phonolite, nepheline syenite, syenite) from seven localities (Table 1) were selected for electron probe microanalysis (EPMA).

3.1. Whole-rock geochemistry

Whole-rock analyses (major, minor, and trace elements) of twelve fresh to weakly altered samples from all six nosean phonolite domes of the Hegau region (Table 1) were performed at the Laboratory of Environmental and Raw Materials Analysis (LERA, Institute for Applied Geosciences), Karlsruhe Institute of Technology (Germany), using wavelength dispersive XRF (*S4 Explorer, Bruker AXS*) and ICP-MS (*iCap RQ, Thermo Fisher Scientific*). The data protocol given in the Supplementary data, File 1 comprises the analyses of the reference material, reference values for the standards, deviations from the reference values, acid blind analyses and their 1σ. To determine the mass loss on ignition, one gram of the powdered sample was heated to 950 °C for 3 h. For XRF, fused beads were prepared with a Li tetraborate/metaborate mixture (*Spectroflux 110, Alfa Aesar*) as flux. The certified standards AGV-1 (andesite), GS-N (granite), SY-2 and SY-3 (syenites) were measured intermittently as secondary reference materials during the same session as our samples (Govindaraju, 1994; CRM-TMDW-A, *High-Purity standards, Inc.*), yielding an accuracy in the range of 2.5% for most elements and 8% for Ti and Mn relative to sample composition.

For ICP-MS, 100 mg of powdered rock was treated by HNO_3-HF-$HClO_4$ acid digestion. A sample was heated together with 65% HNO_3 (subboiled), 40% HF (Suprapur®), and 65% $HClO_4$ (Normatom®) in a closed Teflon vessel for 16 h at 120 °C, assuring a total silicate decomposition. After evaporating the acids to incipient dryness, the residue was redissolved in 65% HNO_3 (subboiled) and evaporated again (three times) for purification purposes. The final residue was dissolved in 50 mL of ultrapure H_2O. The quality of the ICP-MS trace element analyses was ensured by including the two certified reference materials SY-2 and SY-3 (Govindaraju, 1994), an in-house phonolite standard, and two

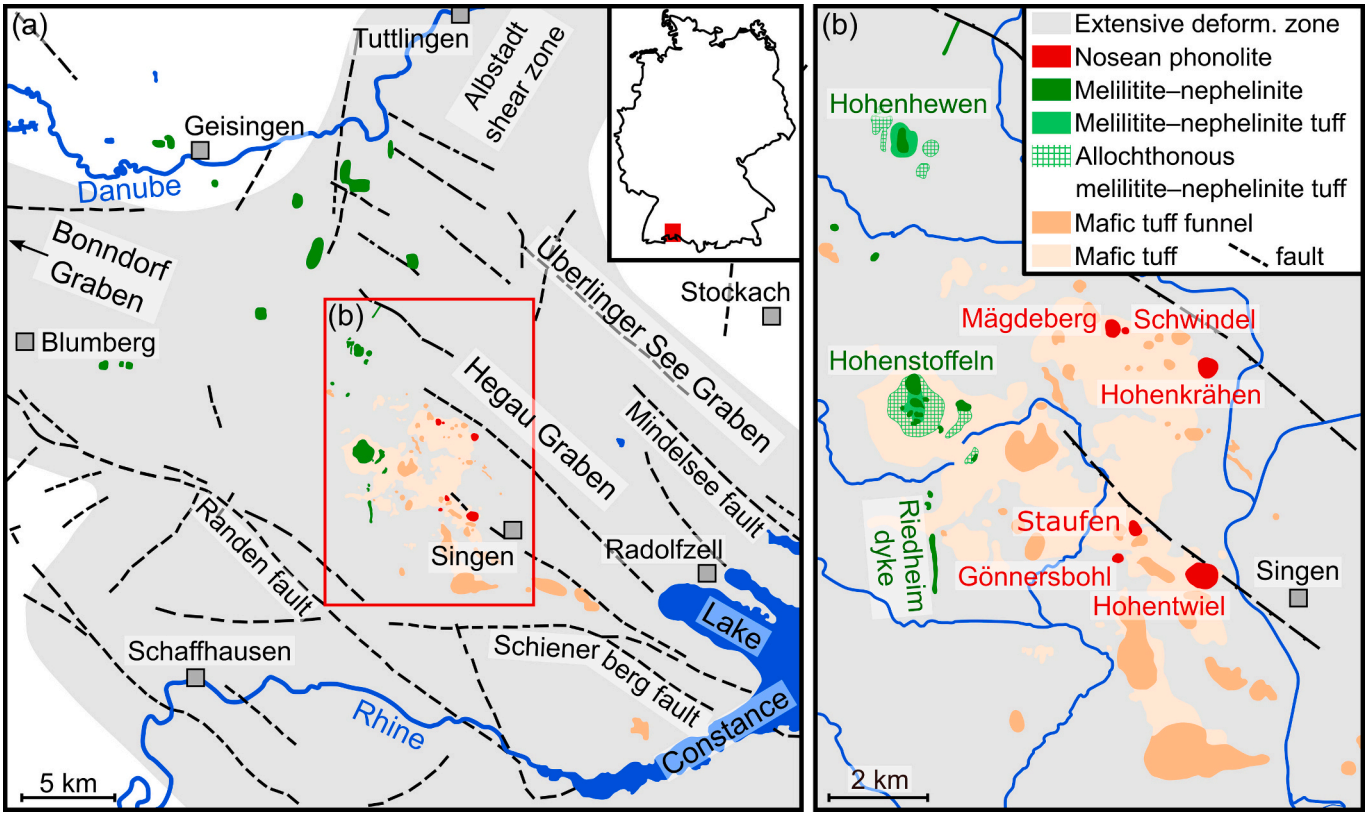

Fig. 1. (a) Simplified map of the Hegau region showing the different volcanic rock units and major fault structures (after Egli et al., 2017). (b) Enlarged section of the central Hegau region with its melilititic–nephelinitic vents in the west and phonolite domes in the east. Large areas in between are covered by mafic tuffs.

Table 1
Sample list including locality name, coordinates, and rock type.

Sample	Locality	Latitude (°N)	Longitude (°E)	Rock type
HEG 10	Blauer Stein (Randen)	47.825537	8.597696	Nph & Hyn b. ol melilitite
HEG 12	Blauer Stein (Randen)	47.825537	8.597696	Mll-b. olivine nephelinite
N 374	Blauer Stein (Randen), Steinröhren	47.826987	8.598313	Mll-b. olivine nephelinite
HEG 01, HEG 01a	Haslen	47.814300	8.760884	Olivine melilitite
HEG 03a	Hohenstoffeln	47.794465	8.750537	Mll-b. olivine nephelinite
HEG 04	Hohenstoffeln	47.794465	8.750537	Nepheline olivine melilitite
HEG 13	Homboll	47.784160	8.764518	Nph-b. olivine melilitite
N 333	Höwenegg	47.914362	8.738509	Nepheline olivine melilitite
HEG 15	Neuhewen	47.879057	8.717537	Mll-b. olivine nephelinite
N 323	Neuhewen	47.879056	8.717029	Olivine melilitite
HEG 19	Pfaffwiesen	47.776275	8.752612	Mll-b. olivine nephelinite
N 593	Ramsen	47.817302	8.731386	Mll-b. olivine nephelinite
HEG 20	Riedheim dyke	47.763659	8.753926	Nepheline olivine melilitite
HEG 14	Schachen	47.821626	8.730429	Mll & Hyn b. ol nephelinite
HEG 18	Sennhof	47.789871	8.755671	Olivine melilitite
I 27	Tudoburg	47.879076	8.883742	Mll-b. olivine nephelinite
HEG 16, HEG 11, I 224	Wartenberg	47.915868	8.631607	Mll-b. olivine nephelinite
I 63	Wasserburger Tal	47.900917	8.871255	Mll-b. olivine nephelinite
N 290	Wasserburger Tal	47.876242	8.845515	Mll-b. olivine nephelinite
HEG 02	Hohenstoffeln	47.794465	8.750537	Ijolite
HEG 03	Hohenstoffeln	47.794465	8.750537	Mll-b. ol nephelinite, ijolite
HEG 05	Hohenstoffeln (EPMA)	47.794465	8.750537	Ijolite
HEG 17	Hohenhewen	47.835623	8.747227	Mll-b. ol nephelinite, ijolite
GB-1	Gönnersbohl (EPMA, WR)	47.767451	8.798665	Nosean phonolite, syenite
GB-2	Gönnersbohl (EPMA)	47.767451	8.798665	Nosean phonolite, syenite
GB-3	Gönnersbohl	47.767451	8.798665	Nosean phonolite, syenite
HG-1	Hohentwiel (EPMA)	47.764720	8.818884	Nosean phonolite
HK-1	Hohenkrähen (EPMA, WR)	47.798777	8.820079	Nosean phonolite
HK-2	Hohenkrähen (EPMA, WR)	47.798777	8.820079	Nosean phonolite
HW-1	Hohentwiel (WR)	47.764720	8.818884	Nosean phonolite, syenite
HW-2	Hohentwiel (EPMA, WR)	47.764720	8.818884	Nosean phonolite, syenite
HW-2a	Hohentwiel (EPMA)	47.764720	8.818884	Nosean phonolite, syenite
HW-3	Hohentwiel (EPMA, WR)	47.764720	8.818884	Nosean phonolite
MB-1	Mägdeberg (EPMA)	47.805260	8.797495	Nosean phonolite
MB-2	Mägdeberg (WR)	47.805260	8.797495	Nosean phonolite
MB-3	Mägdeberg (WR)	47.805260	8.797495	Nosean phonolite
MB-4	Mägdeberg (EPMA, WR)	47.805260	8.797495	Nosean phonolite
SCH-1	Schwindel (EPMA, WR)	47.805017	8.800298	Nosean phonolite
ST-1	Staufen (EPMA, WR)	47.771704	8.806615	Nosean phonolite
ST-2	Staufen (EPMA, WR)	47.771704	8.806615	Nosean phonolite
HEG 06	Hohenstoffeln (EPMA)	47.794465	8.750537	Nepheline syenite
HEG 08	Hohenstoffeln	47.794465	8.750537	Syenite
E 403	2 km E Weil	47.817306	8.731385	Nepheline syenite
N 248	2 km E Weil	47.817306	8.731385	Nepheline syenite

b. – bearing; EPMA – electron probe microanalyses performed on the sample for this study; Hyn – haüyne; Mll – melilite; Nph – nepheline; Ol – olivine; WR – whole-rock analysis performed on the sample.

blank samples into the protocol. The accuracy relative to sample composition was 10% for most trace elements, except for Sc, Cr, Ni, Cs, Hf, Ta, W, and some HREEs (25%).

The contents of total C and S were determined by combusting powdered material in an O_2 flow with an induction furnace at 2000 °C (*CS 2000, Eltra*). The reference materials steel ($n = 7$) and cast iron ($n = 2$) were used for calibration and quality control. Accuracy relative to sample composition was in the range 1%; the 1σ was 0.7% for steel, 2.5% for cast iron.

3.2. EPMA

The mineral chemistry was determined using a *JEOL JXA 8230* electron probe microanalyzer in wave-length dispersive mode at the Department of Geosciences, University of Tübingen. Depending on the composition of the minerals, different configurations (acceleration voltage, probe current, probe diameter) were applied (Supplementary data, Table A1). The specific sensitivities of the mineral surface to the probe current were a critical factor when performing the adjustments. Peak count times were fixed at 10 s for light and volatile elements in clinopyroxene, perovskite, apatite, and amphibole (Na, F), 16 s for the other major elements, and 30 s for minor elements, with background count time being each half of peak count time. The calibration was carried out by using synthetic and natural reference materials, and by application of several peak overlap corrections (Cr—V, V—Ti, F—Fe, F—Ce, Ce—Ba, Pr—La, Ba—Ti). An internal φ(ρz) raw data correction was performed for all analyses except oxyspinel and ilmenite analyses, for which ZAF correction was applied. Specific parameters for the analytical protocols are given in Supplementary data, Tables A2–8, details of mineral formula and endmember calculations in Supplementary data, File 2, and all analytical results in File 3. The results of the mineral chemical analyses performed in this study are supplemented by data from nine localities of melilitites–nephelinites from the Hegau region (Binder et al., in press).

3.3. Fractionation modelling using MELTS

Using the easyMELTS graphical user interface (version 0.2.4) of the MELTS software platform (Ghiorso and Sack, 1995), fractional crystallization of the primitive melilititic–nephelinitic Hegau magmas was modelled based on the thermodynamic database and algorithms provided in the rhyolite-MELTS 1.2.0 version (Ghiorso and Gualda, 2015; Gualda et al., 2012). This version is optimised for crystallization in bulk compositions at 0–3 GPa that are not saturated with quartz, considering

also the H_2O-CO_2 fluid saturation model of Ghiorso and Gualda (2015). It represents the best approximation of the MELTS software package for fractional crystallization of mafic alkaline SiO_2-undersaturated magmas at crustal depths and was successfully tested for very similar rock types (Kong et al., 2023; Mourey et al., 2023; Sliwinski et al., 2015 and references therein). The isothermal computation mode for each individual step and a temperature increment of −10 K were used for the modelling, while the pressure was set constant (cf. Supplementary data, File 4). Only solids were considered as fractionating phases and the fO_2 buffer was set to ΔFMQ +3, based on thermodynamic modelling for these rocks (Binder et al., in press) and because Braunger et al. (2018) determined a similarly high ΔFMQ of +2 to +3 for the KVC olivine nephelinites. All available whole-rock analyses of melilititic–nephelinitic rocks of the Hegau region (Supplementary data, File 1) were used as input data to largely cover the entire geochemical range of conceivable parental magma compositions. These span H_2O contents from 0.0 to 3.9 wt% (Supplementary data, Fig. A1) and CO_2 contents from 0.0 to 0.2 wt%, extending beyond the ranges of other work dealing with MELTS modelling of alkaline rocks (Mourey et al., 2023; Sliwinski et al., 2015). Note, however, that modelling was not applicable to some whole-rock compositions and resulted in a software error (see Discussion for details). The calculations were performed assuming crustal pressures of 200, 500, and 1000 MPa during fractional crystallization (cf. Kong et al., 2023; Mourey et al., 2023). The modelled evolution of the residual melt composition was compared with whole-rock data for the Hegau phonolites (this study; Alibert et al., 1983; Dunworth and Wilson, 1998; von Engelhardt and Weiskirchner, 1961; Keller et al., 1990; Krause, 1969; Krause and Weiskirchner, 1981; Staesche, 1995; Stock, 1990; Wimmenauer, 1974).

4. Results

4.1. Petrography

Based on mineral assemblages (Table 2) and (micro)textures, primitive melilititic–nephelinitic, evolved phonolitic rocks, and coarse-grained ijolitic patches and (nepheline) syenite enclaves were distinguished.

4.1.1. Olivine melilitites and melilite-bearing olivine nephelinites

These porphyritic rocks contain high amounts of olivine macrocrysts (20–40 vol%), comprising variable proportions of euhedral to subhedral crystals and subhedral to anhedral, rounded, partly sheared, ruptured crystals, which occasionally exhibit wavy extinction. A separation of the different types is not always univocal, as transitions in habitus and crystal size may be blurred (Figs. 2a & b). Further, the rocks show tabular to lath-shaped, yellowish–reddish brown euhedral clinopyroxene macrocrysts (5–20 vol%), and small melilite crystals (<10 vol%; Figs. 2a & b) embedded in a groundmass of euhedral clinopyroxene (10–35 vol%), titanomagnetite (10–15 vol%), melilite (<20 vol%), olivine (<10 vol%), interstitial nepheline (<20 vol%), and accessory euhedral perovskite and apatite. Clinopyroxene often shows concentric and/or hourglass sector zoning and rarely, pale, partly resorbed and inclusion-rich cores are present. Some samples contain anhedral dark mica (<5 vol%; Fig. 2a), euhedral medium-grained haüyne macrocrysts (<5 vol%; Fig. 2a & b), and/or clinopyroxene glomerocryts (Fig. 2a).

4.1.2. Ijolites

Coarse-grained and irregularly shaped ijolitic patches within the melilites–nephelinites are delimited by a few millimetres wide transition zone that bridges the difference between the two rock types regarding composition and texture (Fig. 2c). The ijolite is characterized by a parquet texture of tabular euhedral to subhedral nepheline and its alteration products (50–60 vol%; Figs. 2d-f) and euhedral reddish or greenish brown clinopyroxene (~30 vol%) that is mostly concentrically (Fig. 2e) and/or hourglass sector zoned (Fig. 2f). These minerals are accompanied by medium-grained, squat or skeletal titanomagnetite (~10 vol%; Figs. 2d, e & g), euhedral apatite (Fig. 2f & g), interstitial carbonate (Fig. 2d), purple skeletal crystals and crystal groups of perovskite (Figs. 2g & h), and subordinate subhedral to anhedral dark mica (Fig. 2e).

4.1.3. Nosean phonolites

The phonolites are characterized by large macrocrysts of euhedral nosean-haüyne-sodalite$_{ss}$ (10–25 vol%), with deep blue irregular shaped domains representing the S-rich primary composition of this sodalite-group mineral (see below) and light glaucous nosean-rich areas (Figs. 3a & b). A second population of medium-sized crystals exhibits only these paler colours (Figs. 3a & b) and many crystals of nosean-haüyne-sodalite$_{ss}$ are completely altered (Fig. 3c). Other macrocrysts are euhedral medium-grained yellow or yellowish green to bottle-green clinopyroxene (<10 vol%; Figs. 3c & d; mostly aegirine-augite), alkali feldspar of variable size (<25 vol%; Fig. 3c & e), and occasional rhombical titanite (Fig. 3c) that rarely shows twinning (Fig. 3e). Common accessories are euhedral to subhedral apatite (Fig. 3e; occurring also in crystal groups, Fig. 3f), zircon, and pyrochlore. All these minerals are embedded in a groundmass (50–80 vol%) of alkali feldspar, nosean, nepheline, and aegirine-augite (Figs. 3a-e).

4.1.4. Syenites and nepheline syenites

Coarse-grained syenite and nepheline syenite enclaves occur in the phonolites (Fig. 4a) and in the melilititic–nephelinitic rocks. They are mineralogically similar but vary in terms of the mineral proportions, sometimes within the same enclave (Fig. 4b). The rocks consist of tabular euhedral to subhedral alkali feldspar (50–65 vol%; Figs. 4b-g), nepheline (<35 vol%; Figs. 4d & e), euhedral to subhedral clinopyroxene (<30 vol%; aegirine-augite; Figs. 4a-c, f & g), subhedral to anhedral dark mica (<5 vol%; Figs. 4b-g), interstitial carbonate (Figs. 4e-g), and

Table 2
Sample list including locality name, coordinates, and rock type. Modal mineralogy of investigated volcanic rocks in the Hegau region. Distinctive values are in grey, characteristic accessories are in bold.

Rock series	Ol	Cpx	Spl/ Usp	Bt/ Phl	Mll	Nph +Zeo	Hyn/ Nsn/Sdl	Afs	Acc.
Olivine melilitites and melilite-bearing nephelinites	20–40	10–35	10–15	<5	<20	<20	< 5	–	**Prv,** Ap
Ijolites	–	~30	~10	Acc.	–	50–60	–	–	**Prv, Ap**
Nosean phonolites	–	10–20	Acc.	Acc.	–	15–30	15–25	40–50	**Ttn, Ap,** Zrn, Pcl
Syenites and nepheline syenites	–	<30	Acc.	< 5	–	<35	–	50–65	**Ttn, Ap** (<30 vol.%!), **Zrn, Pcl,** Tho, Thr

Ol – olivine; Cpx – clinopyroxene; Spl – spinel group (including magnetite); Usp – ulvöspinel; Bt – biotite; Phl – phlogopite; Mll – melilite; Nph – nepheline; Zeo – zeolites; Hyn – haüyne; Nsn – nosean; Sdl – sodalite; Afs – alkali feldspar; Acc. – accessory minerals; ap – apatite; prv – perovskite; ttn – titanite; zrn – zircon; pcl – pyrochlore; tho – thorianite; thr – thorite.

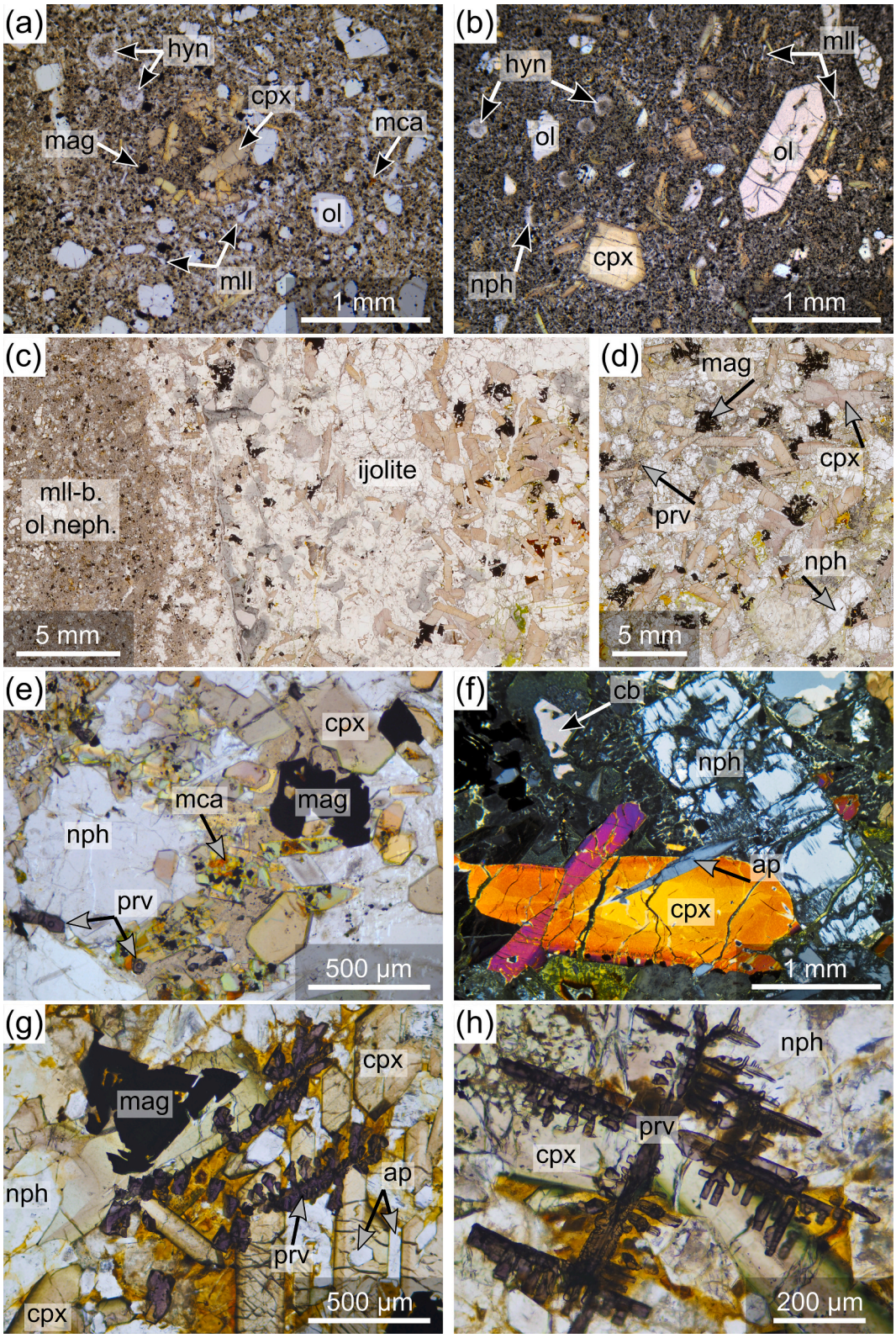

Fig. 2. Petrographic features of the Hegau melilitites–nephelinites and ijolitic patches therein. (a) Nepheline- and haüyne-bearing olivine melilitite with olivine and haüyne macrocrysts and clinopyroxene glomerocryts in fine-grained groundmass with accessory dark mica (Blauer Stein). (b) Nepheline-bearing olivine melilitite with olivine and zoned clinopyroxene macrocrysts, euhedral haüyne, and subhedral nepheline in fine-grained groundmass (Homboll). (c) Border zone between melilite-bearing olivine nephelinite and irregularly shaped ijolite patch (Hohenstoffeln). (d) Ijolite with tabular nepheline, euhedral reddish-brownish and greenish-brownish clinopyroxene, skeletal magnetite, and skeletal perovskite (Hohenstoffeln). (e) Ijolite-like textures with tabular nepheline, euhedral reddish-brownish and greenish-brownish clinopyroxene, skeletal magnetite, little perovskite, and dark mica within a melilite-bearing olivine nephelinite (Hohenhewen). (f-h) Ijolite (Hohenstoffeln) with (f) euhedral tabular nepheline, sector- and concentrically zoned subhedral clinopyroxene, needles and hexagonal cross-sections of apatite, and interstitial carbonate (crossed polarization), (g) euhedral–subhedral skeletal perovskite and magnetite crystals accompanied by tabular nepheline and euhedral clinopyroxene and apatite crystals, and (h) euhedral skeletal perovskite surrounded by clinopyroxene and nepheline.

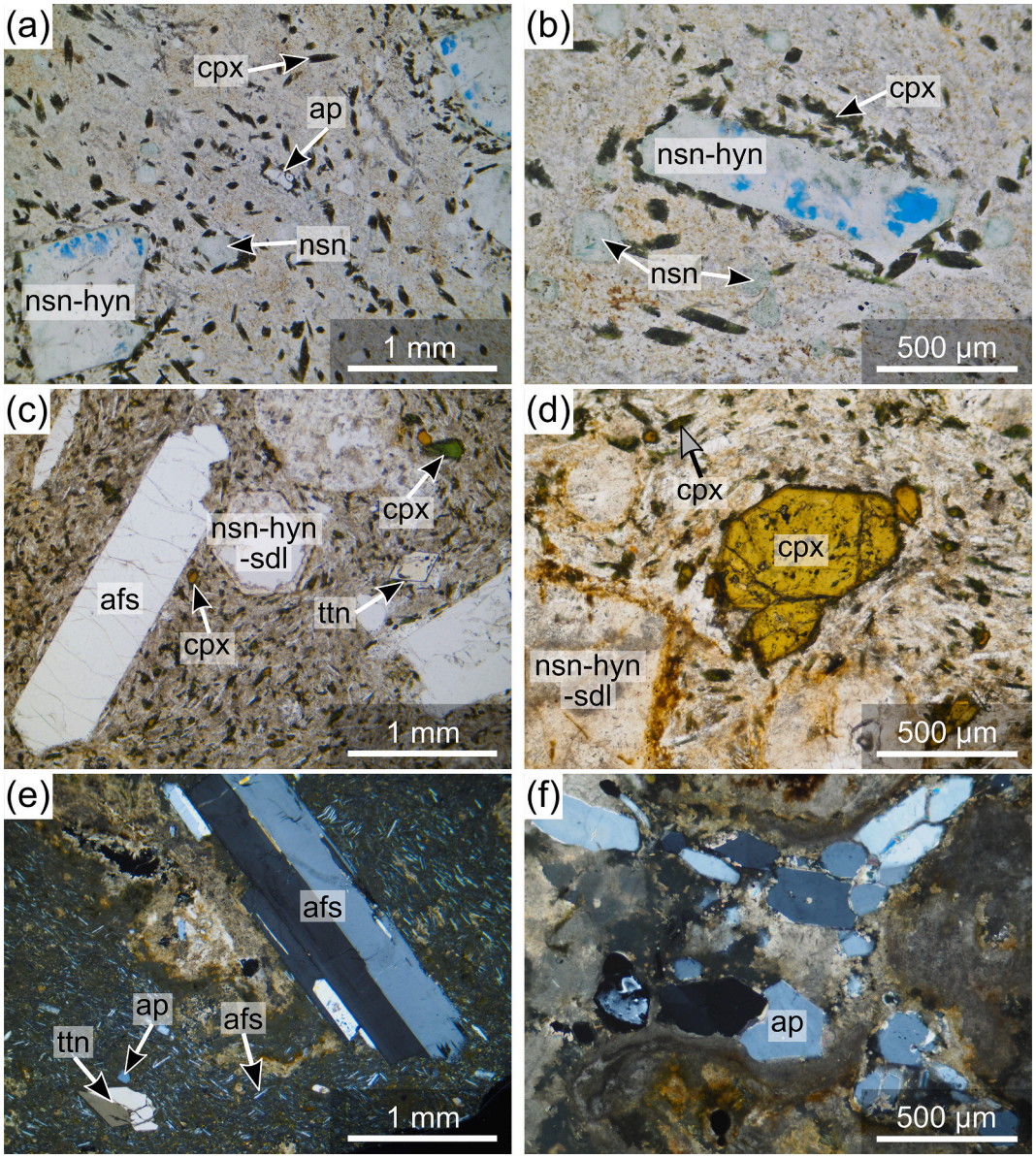

Fig. 3. Petrographic features of the Hegau nosean phonolites with (a) altered euhedral sodalite-group macrocrysts showing exsolution textures (of mainly haüyne-nosean$_{ss}$) in a groundmass of clinopyroxene (aegirine-augite), alkali feldspar, nepheline, sodalite-group minerals, and apatite (Hohenkrähen), (b) altered nosean crystals and a tabular euhedral macrocryst of exsolving haüyne-nosean$_{ss}$ fringed by small euhedral–subhedral clinopyroxene (aegirine-augite) microcrysts within a fine-grained grundmass of alkali feldspar, nepheline, and aegirine-augite (Hohenkrähen), (c) macrocrysts of alkali feldspar, a strongly altered sodalite-group mineral, titanite, and clinopyroxene in a groundmass of alkali feldspar, aegirine-augite, and nepheline (Hohentwiel), (d) macrocrysts of clinopyroxene and strongly altered haüyne-nosean-sodalite$_{ss}$ in a groundmass of euhedral–subhedral alkali feldspar, clinopyroxene, and nepheline (Hohenkrähen), (e) a twinned alkali feldspar macrocryst, a euhedral titanite crystal and microcrysts of apatite and alkali feldspar in a cryptocrystalline groundmass of clinopyroxene, alkali feldspar, and nepheline (crossed polarization; Hohentwiel), and (f) an agglomeration of euhedral–subhedral apatite crystals within a strongly altered groundmass (crossed polarization; Hohentwiel).

minor opaque phases. Few samples contain up to 30 vol% apatite, others only accessory amounts. Further accessories are euhedral titanite (Figs. 4f & g), irregularly or concentrically zoned pyrochlore (Figs. 4h-j), and zircon (Figs. 4e-g & k). Rarely, thorite and thorianite occur, sometimes as small inclusions in zircon (Fig. 4k).

4.2. *Whole-rock geochemistry*

Consistent with mineralogy, most melilitites–nephelinites plot in the lower part of the foidite/melilitite field in the TAS diagram (Fig. 5). However, some occurrences have slightly elevated SiO_2 contents classifying them as picrobasalts, rarely as tephrites or basanites. Nosean phonolites fall within the range of phonolites in the TAS diagram, except for four analyses with slightly lower $Na_2O + K_2O$ contents defining them as tephriphonolite, trachyandesite, or trachyte.

Major and trace element compositions (Figs. 6–7; Supplementary data, File 1) show clear differences between the various rock types in the Hegau region. The melilitites–nephelinites show high MgO contents (10–20 wt%), while the ijolitic patches therein have a content of only 7 wt% and the phonolites below 1.1 wt% MgO. $Na_2O + K_2O$ contents are low in the melilititic–nephelinitic rocks, slightly elevated in the ijolite, and high in the phonolites (Fig. 6a), whereas the opposite is observed for CaO, with the ijolite having the same contents as the primitive rocks (Fig. 6b). Al_2O_3 contents are moderate in the melilititic–nephelinitic rocks, mildly increased in the ijolite, and high in the phonolites (Fig. 6c). Likewise, the SiO_2 content is lowest in the ijolite and in the primitive

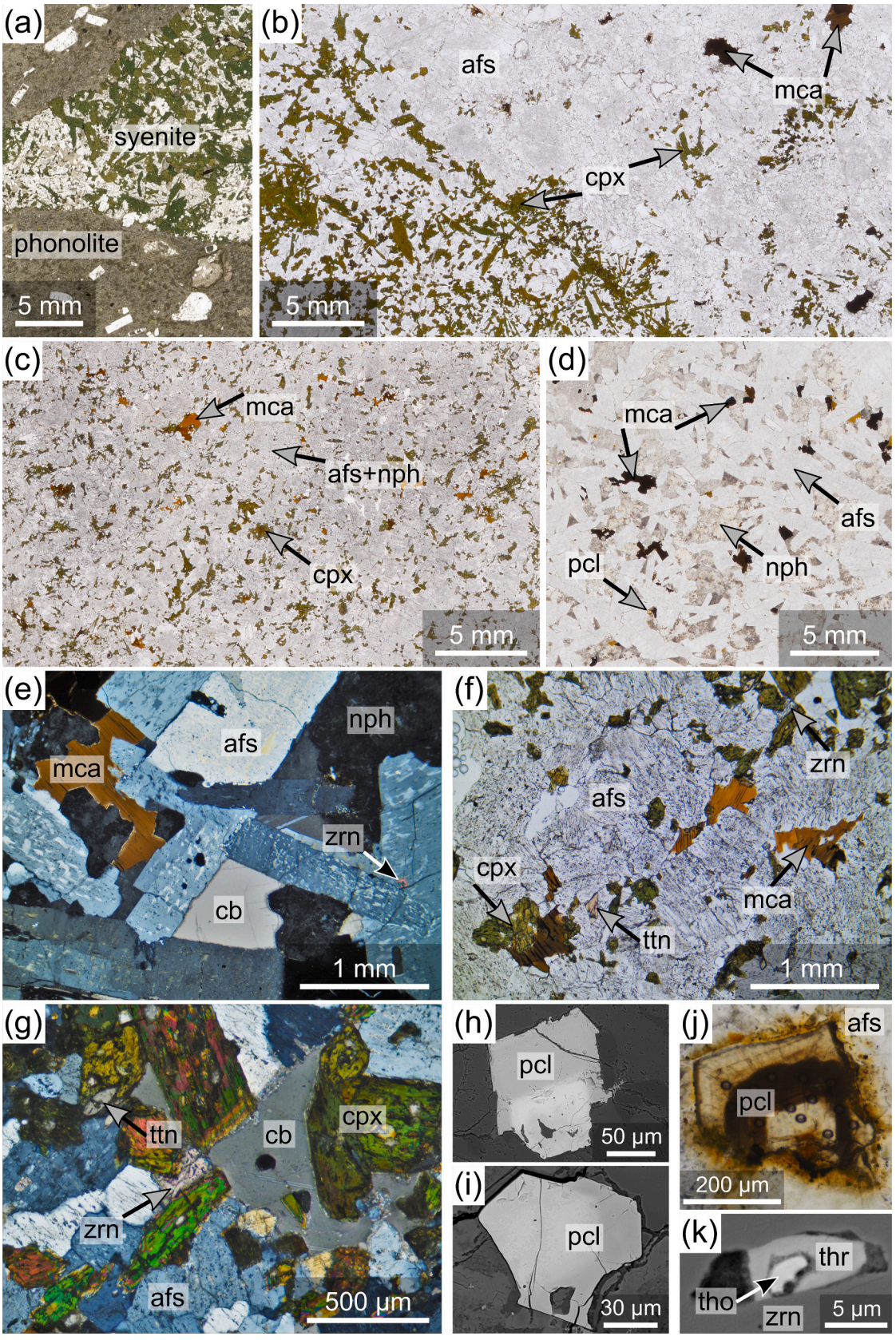

(caption on next page)

Fig. 4. Petrographic features of the Hegau (nepheline) syenites. (a) Syenite enclave within a nosean phonolite (Gönnersbohl). (b) Syenite with a mesocratic domain of clinopyroxene (aegirine-augite), alkali feldspar, and subordinate dark mica and a leucocratic domain of alkali feldspar, dark mica, and subordinate clinopyroxene (Hohenstoffeln). (c) Mesocratic nepheline syenite with alkali feldspar, nepheline, clinopyroxene (aegirine-augite), and dark mica (Hohenstoffeln). (d + e) Leucocratic nepheline syenite from a mafic tuff (2 km E Weil) with (d) alkali feldspar, nepheline, dark mica, and accessory pyrochlore and (e) tabular euhedral–subhedral alkali feldspar – exhibiting exsolved irregular perthite intergrowth –, anhedral tabular dark mica, altered nepheline, interstitial carbonate, and accessory zircon; crossed polarization. (f + g) Mesocratic nepheline syenite enclave from a nepheline-bearing olivine melilitite (Hohenstoffeln) with (f) subhedral–anhedral tabular alkali feldspar, clinopyroxene, dark mica, and accessory euhedral titanite and anhedral zircon and (g) tabular euhedral–subhedral clinopyroxene, subhedral alkali feldspar, interstitial carbonate, and accessory euhedral titanite and anhedral zircon; crossed polarization. (h + i) BSE images show chemically zoned pyrochlore microcrysts with (h) concentric zoning and (i) irregular–diffuse zoning, each due to differences in the U-Th-REE concentrations (nepheline syenite enclave from mafic tuff 2 km E Weil). (j) Concentrically chemically zoned pyrochlore microcryst with U-Th-rich metamict domains and transparent Nb-dominated zones embedded in alkali feldspar (2 km E Weil). (k) BSE image shows an inclusion of thorianite within an inclusion of thorite within a zircon crystal (nepheline syenite enclave from a nepheline-bearing olivine melilitite, Hohenstoffeln).

rocks and highest in the phonolites (Fig. 6d). Fe_2O_3, TiO_2, and P_2O_5 contents strongly decrease from the primitive rocks towards the evolved ones (Figs. 6e-g). The ijolite, however, exhibits the highest P_2O_5 concentrations (Fig. 6g). The Na/K ratio varies considerably in the melilitites–nephelinites and in the phonolites but decreases on average as the rocks evolve (Fig. 6h).

The Cr and Ni concentrations are high in the primitive rocks and decrease with decreasing MgO contents, whereas they are very low in the phonolites (Fig. 7a-b). Moderate Nb and Zr and high V concentrations in the melilititic–nephelinitic rocks contrast high Nb and Zr and moderate V contents in the evolved rocks (Fig. 7b-d). Rb, Pb, and U concentrations are significantly higher in the phonolites than in the primitive rocks (Fig. 7f-h).

Compared to the primitive mantle (Fig. 8a; Palme and O'Neill, 2014), the melilititic–nephelinitic rocks are strongly enriched in LREE (~80–130 times) but only slightly enriched in HREE (~2.5–5 times). The phonolites also show high enrichment for LREE (~45–150 times) and only moderate enrichment for HREE (~3–7 times), but additionally exhibit a trough for MREE (~2.5–13 times), whereas the primitive volcanic rocks are more enriched in these elements (~7–20 times). The primitive mantle-normalized trace element patterns show decreasing enrichment with increasing mantle compatibility in all volcanic Hegau rocks, albeit there are prominent exceptions (Fig. 8b). The melilititic–nephelinitic rocks have negative Rb, K, Pb, and positive Nb and P anomalies. In contrast, the phonolites reveal prominent positive U, Nb, and Zr anomalies and negative Ta, P, and Ti anomalies, while the K anomaly is absent and a slight positive Pb anomaly present.

4.3. Mineral chemistry

4.3.1. Clinopyroxene

Clinopyroxene in the melilitites–nephelinites is generally unzoned and dominated by quadrilateral end-members (>60%; mostly Di + Hd; Fig. 9a), with varying tschermakitic components (<40%; FeTs, CaTiTs, CaAlTs, CrAlTs) and only ~5% Na pyroxene (Aeg, Ti-Aeg, Jd). In the ijolitic patches, clinopyroxene is similar in composition, with crystal rims, however, exhibiting higher proportions of Na pyroxene (up to 21%) at low Tschermak's substitution (<8%). In contrast, clinopyroxene

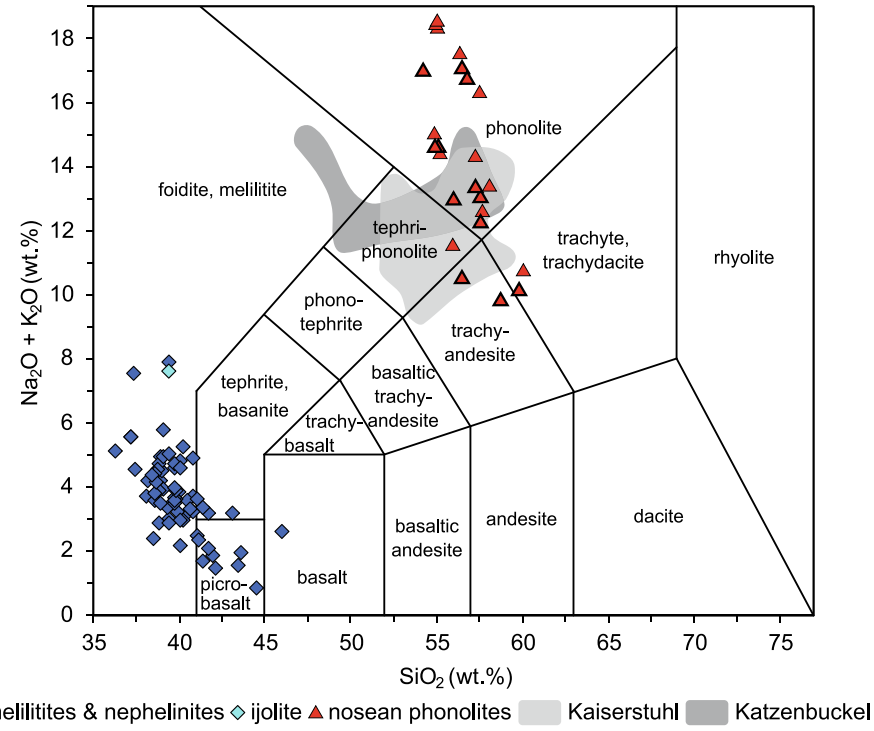

Fig. 5. TAS diagram showing compositions of the volcanic Hegau rocks. 12 new analyses (black-rimmed triangles) were supplemented by literature data from Alibert et al. (1983), Dunworth and Wilson (1998), von Engelhardt and Weiskirchner (1961), Keller et al. (1990), Krause (1969), Krause and Weiskirchner (1981), Staesche (1995), Stock (1990), and Wimmenauer (1974). All data have been renormalized to a volatile-free composition. For comparison, the compositions of the other phonolites of the southern CEVP are shown, namely those of the Kaiserstuhl (Braunger et al., 2018 and references therein) and Katzenbuckel (Frenzel, 1975; Freudenberg, 1906; Stähle and Koch, 2003). The naming of the rocks in the Petrography chapter is based on mineral compositions, so the position in the TAS diagram may differ from the assigned rock name.

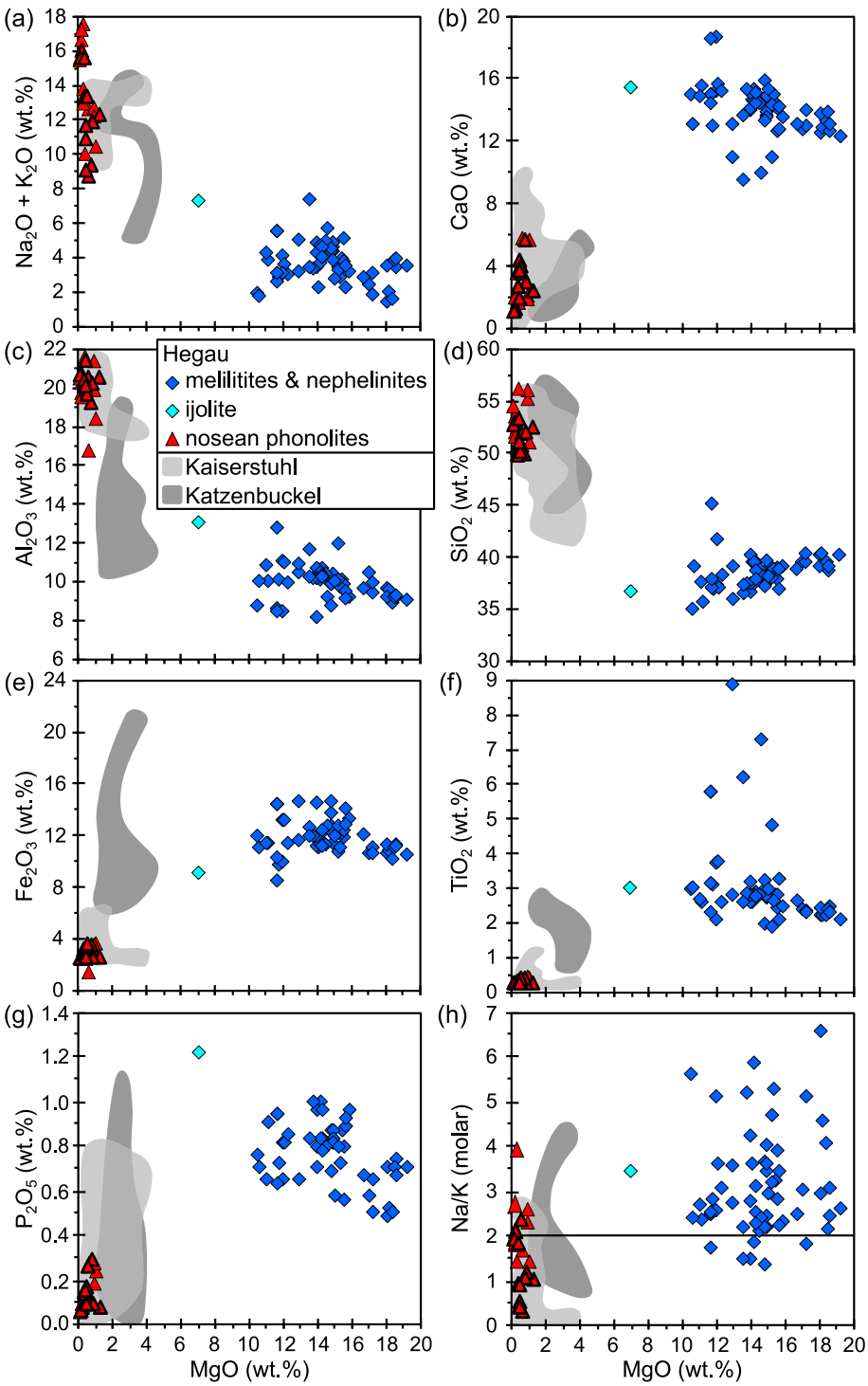

Fig. 6. Whole-rock major element composition of the igneous Hegau rocks. 12 new analyses (black-rimmed triangles) were supplemented by literature data stated in Fig. 5. Concentrations of (a) $Na_2O + K_2O$, (b) CaO, (c) Al_2O_3, (d) SiO_2, (e) Fe_2O_3, (f) TiO_2, and (g) P_2O_5 plotted against wt% MgO. (h) Molar Na/K-ratio vs. wt% MgO. All data represent original contents not renormalized to a volatile-free composition. For comparison, the compositions of the Kaiserstuhl and Katzenbuckel phonolites are also shown.

in phonolites exhibits variable and increased proportions of Na pyroxenes (7–70%) and up to 27% Tschermak's pyroxene at the expense of the quadrilateral components. Clinopyroxene in the groundmass of phonolites resembles clinopyroxene in (nepheline) syenites and is on average even more dominated by Na end-members (up to 80%) at lower tschermakitic components.

While diopsidic clinopyroxene in the melilitites–nephelinites contains a maximum of 25% hedenbergite component, the proportion in the crystal rims of the ijolite can increase up to 51%, with the aegirine component reaching up to 21% (Fig. 9b). The trend for clinopyroxene in the phonolites and (nepheline) syenites is evolving more strongly towards aegirine (8–81%) at hedenbergite components of 20–45%, although some pyroxene crystals show a lower hedenbergite content (5–20%) deviating from the general trend.

In the primitive rocks and the ijolitic patches, the Al content reaches up to 0.6 apfu and increases with decreasing Mg contents that range

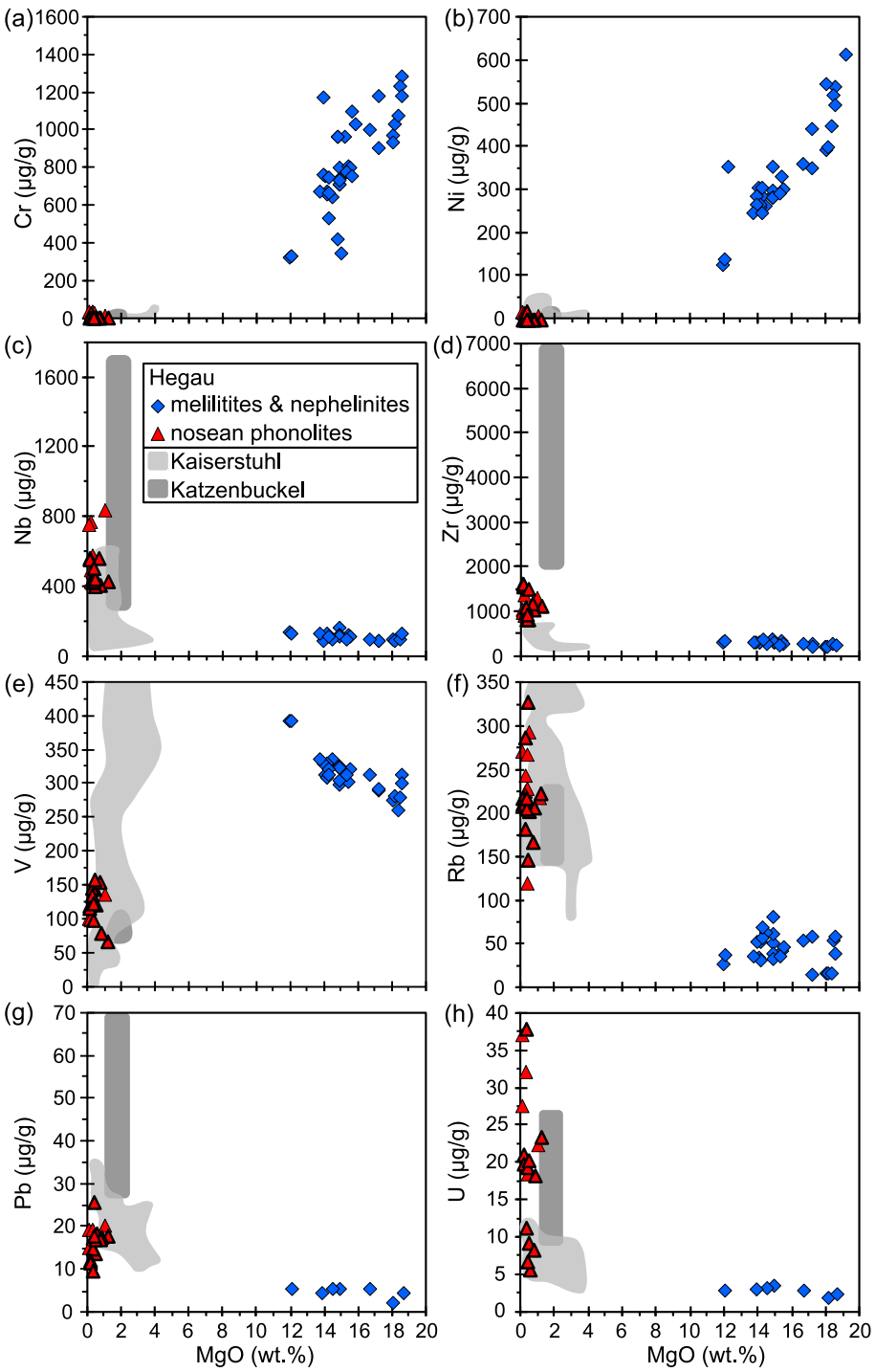

Fig. 7. Whole-rock trace element composition of the igneous Hegau rocks. 12 new analyses (black-rimmed triangles) were supplemented by literature data stated in Fig. 5. Concentrations (in µg/g) of (a) Cr, (b) Ni, (c) Nb, (d) Zr, (e) V, (f) Rb, (g) Pb, and (h) U plotted against wt% MgO. For comparison, the compositions of the Kaiserstuhl and Katzenbuckel phonolites are also shown.

from 0.52 to 0.88 apfu (Fig. 9c). Clinopyroxene rims in ijolite deviate from this trend and exhibit remarkably low Al (<0.05 apfu) and Mg concentrations (0.28–0.58 apfu). Clinopyroxene in the phonolites and (nepheline) syenites has even lower Mg contents (0.03–0.58 apfu), with the Al content (0.02–0.39 apfu) varying at Mg concentrations above 0.45 apfu but decreasing continuously at lower Mg contents. The same is observed for the Ti content (Fig. 9d), which is generally lower in the clinopyroxene rims of ijolite (0.04–0.08 apfu) and in the clinopyroxene of phonolites and (nepheline) syenites (<0.08 apfu) compared to that in the melilitites–nephelinites and to the macrocryst cores in the ijolite (<0.22 apfu). Usually, Zr does not exceed 1500 ppm; only in groundmass pyroxenes in phonolites, and in (nepheline) syenites Zr reach up to 6000 ppm (Fig. 9e).

4.3.2. *Alkali feldspar*

Alkali feldspar macrocrysts and microcrysts in the phonolites show no compositional differences and are $Or_{60-85}Ab_{15-40}$ with up to 8% celsian (Ba component) and variations within macrocrysts expressed in concentric zoning (Fig. 10a). The anorthite component (<0.4%; Fig. 10a) and Sr contents (2300 ppm) are very low. Alkali feldspar in the

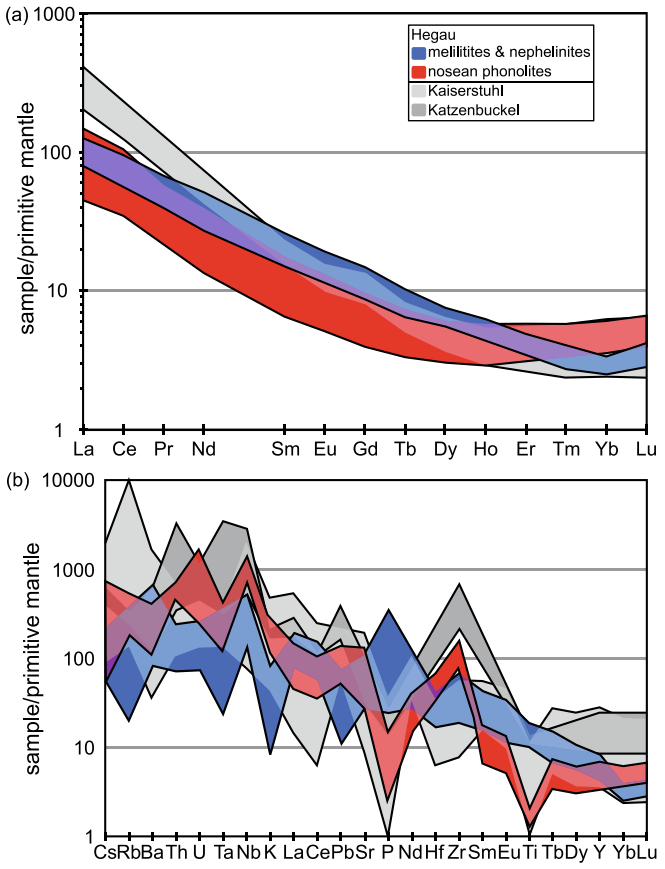

Fig. 8. Primitive mantle-normalized (a) REE pattern and (b) incompatible element pattern of the igneous Hegau rocks (normalization values from Palme and O'Neill, 2014); elements sorted by increasing mantle compatibility. Analyses are from the literature stated in Fig. 5. For comparison, the compositions of the Kaiserstuhl and Katzenbuckel phonolites are also shown.

(nepheline) syenites largely resembles this composition with few crystals reaching Or_{93}.

4.3.3. Sodalite-group minerals

Haüyne-nosean-sodalite$_{ss}$ in melilitites–nephelinites is dominated by haüyne with a sodalite content of 15–20%, while those in the phonolites comprise two populations: (1) large macrocrysts with irregularly shaped deep blue S-rich, Cl-bearing unaltered domains ($Nsn_{48-65}Hyn_{28-45}Sdl_{6-10}$) and altered colourless to light glaucous domains ($Nsn_{89-100}Hyn_{0-11}Sdl_{0-1}$) and (2) smaller relatively homogeneous crystals exclusively having the latter composition (Figs. 3a, b & 10b). Further, haüyne-nosean-sodalite$_{ss}$ in the primitive rocks contains significant amounts of Ca and minor K, substituting 20–35% and ~ 10% of the Na, respectively. In contrast, a maximum of 4% of the Na in the S-rich, Cl-bearing domains and 21–37% in the altered domains in the macrocrysts of the phonolites are replaced by K, while Ca is almost completely absent (Fig. 10c).

4.3.4. Oxyspinel

Skeletal oxyspinel crystals in the ijolitic patches are magnetite-ulvöspinel$_{ss}$ covering the same compositional range as in the melilititic–nephelinitic host rocks; exsolution lamellae in the skeletal crystals are Fe-rich ilmenite (Supplementary data, Fig. A2a). Mn (0.03–0.06 apfu), Zn (300–800 ppm), and V contents (2300–6000 ppm) largely correspond to the contents in most evolved oxyspinel of the primitive rocks and are comparatively high (Supplementary data, Fig. A2b-d). Oxyspinel is almost absent in the nosean phonolites.

4.3.5. Perovskite

Skeletal perovskite in the ijolitic patches is generally more enriched in various trace elements than accessory perovskite in the melilititic–nephelinitic host rocks. However, the initial point of the mineral chemical evolution of the skeletal perovskite is always in the compositional range of the perovskite in the host rocks (Figs. 11a & b). Nb reaches up to 0.10 apfu and correlates positively with Ta (<3000 ppm; Fig. 11c) and Sr increases up to 0.05 apfu, correlating negatively with Ti (Fig. 11d). In perovskite in the ijolite, Fe (~0.01–0.03 apfu) decreases with advancing crystallization (Fig. 11e). Th (<6000 ppm) correlates positively with the REEs (<0.05 apfu), with the accessory perovskite in the melilitites–nephelinites sharing the same compositional range as the skeletal perovskite in the ijolite (Fig. 11f).

4.3.6. Titanite

Titanite in the phonolites contains up to 0.04 apfu Zr, 9300 ppm LREE+Y, 0.06 apfu Nb, and 0.08–0.12 apfu Al + Fe (Supplementary Data, Fig. A3). Differences in the contents of these elements cause irregular to concentric zoning in the crystals, but without a distinct core-rim trend (Supplementary Data, Fig. A3c).

4.3.7. Apatite

Apatite in melilitites–nephelinites and ijolite is fluorapatite, with a subordinate hydroxyapatite component and the chlorapatite component reaching 1–13%. Apatite in the phonolites varies between fluorapatite (24–89%) and hydroxyapatite (11–74%), the chlorapatite component being <2% (Fig. 12a). Apatite in the (nepheline) syenites is fluorapatite-hydroxyapatite$_{ss}$ lacking any detectable Cl. There are no significant differences between apatite in the different rocks regarding Na, Sr, Ba, and REEs (Fig. 12b).

5. Discussion

In the following, the genetic relationships between primitive olivine melilitites and melilite-bearing olivine nephelinites, rare ijolitic patches therein, (nepheline) syenite enclaves, and evolved nosean phonolites will be discussed and a comprehensive model for the magmatic evolution of the Hegau region will be presented.

5.1. Rare ijolite patches in melilititic–nephelinitic rocks: Evidence for rapid in-situ differentiation

In-situ differentiation in primitive olivine melilitites and melilite-bearing olivine nephelinites from Hohenstoffeln and Hohenhewen (Fig. 1b) is implied by rare coarse-grained and irregularly shaped ijolitic patches (Figs. 2c-g). Their geochemical composition is more evolved than that of the volcanic host as the contents of MgO, alkalis, Al_2O_3, and Fe_2O_3 fall between those of the melilitites–nephelinites and the nosean phonolites. Other compounds are slightly lower (e.g., SiO_2) or slightly higher (e.g., CaO, TiO_2, P_2O_5) than in the primitive rocks and do not fall on a linear trajectory between primitive and evolved rock suite (Fig. 6). This is reflected by the lack of olivine in the ijolitic patches, while clinopyroxene, nepheline, titanomagnetite, perovskite, and apatite are abundant (Figs. 2e-h). The crystallization trend of clinopyroxene evolves from diopsidic cores, which resemble the composition in the host rock, to aegirine- and hedenbergite-rich rims with similar Al and Ti contents as observed in phonolites and nepheline syenites (Fig. 9). Abundant skeletal perovskite and magnetite indicate rapid growth and a high degree of supersaturation of corresponding elements in the trapped residues due to fast undercooling (Figs. 2d, g & h; Gornitz, 1981). Compared to the composition in the host rock, perovskite shows continuous enrichment of Nb, Ta, Na, Sr, Th, and REE (Fig. 11), apatite is Cl- and H_2O-rich (Fig. 12), and magnetite is Mn- and V-rich (Supplementary data, Fig. A2), which indicates relative enrichment of these elements in the residual melt pockets (Fig. 2c). An interpretation of such in-situ fractionation as missing link between melilitites–nephelinites

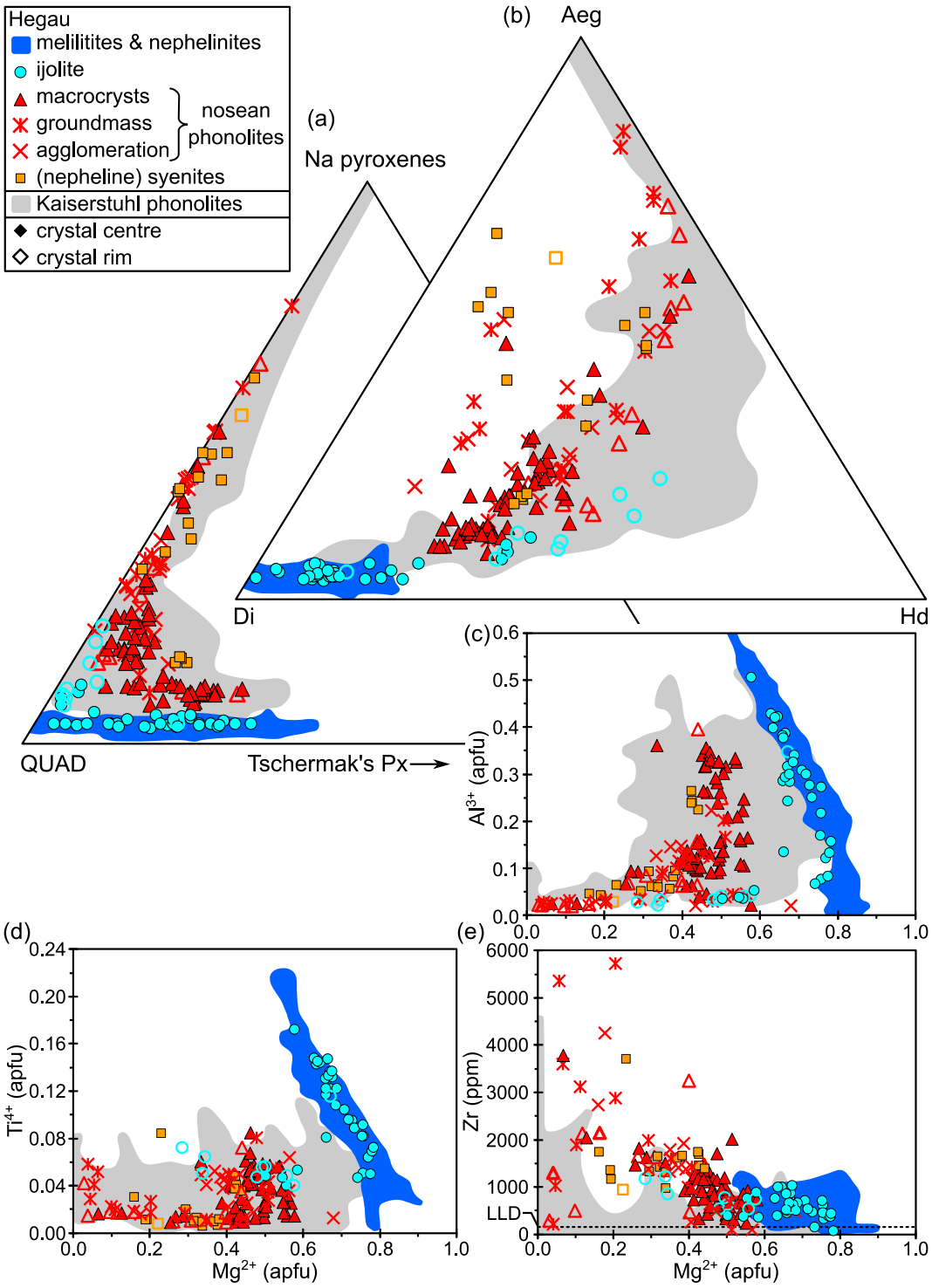

Fig. 9. Clinopyroxene composition in the igneous Hegau rocks. Data of this work supplemented by Binder et al. (in press). For comparison, the composition of clinopyroxene in the Kaiserstuhl phonolites is also shown (Braunger et al., 2018). (a) Triangular plot showing the distribution among the quadrilateral end-members (QUAD), Tschermak's clinopyroxenes ($CaXXSiO_6$ with X = Al, Fe^{3+}, Cr, Ti), and Na pyroxenes (aegirine – $NaFe^{3+}Si_2O_6$, Ti aegirine – $NaFe^{2+}_{0.5}Ti_{0.5}Si_2O_6$, jadeite – $NaAlSi_2O_6$). (b) Triangular plot showing the distribution among the end-members diopside (Di), aegirine (Aeg), and hedenbergite (Hd) normalized to 100%. Mg^{2+} vs. (c) Al^{3+}, (d) Ti^{4+}, and (e) Zr. apfu – atoms per formula unit; LLD – lower limit of detection; ppm – parts per million.

and nosean phonolites is possible, although an expected increase in SiO_2 content and alkali feldspar saturation required for the evolution towards phonolites or nepheline syenites is not observed. It is suggested that in-situ crystallization under close-to-equilibrium conditions without sufficient removal of solids (i.e., lack of fractionation) and rapid cooling of the rocks prevented more extensive differentiation towards SiO_2-rich and CaO-, TiO_2-, P_2O_5-poor phonolitic compositions, a shallow fractionation trend which is often observed in plutonic rocks (e.g., in the Fen complex, Norway; Andersen, 1988).

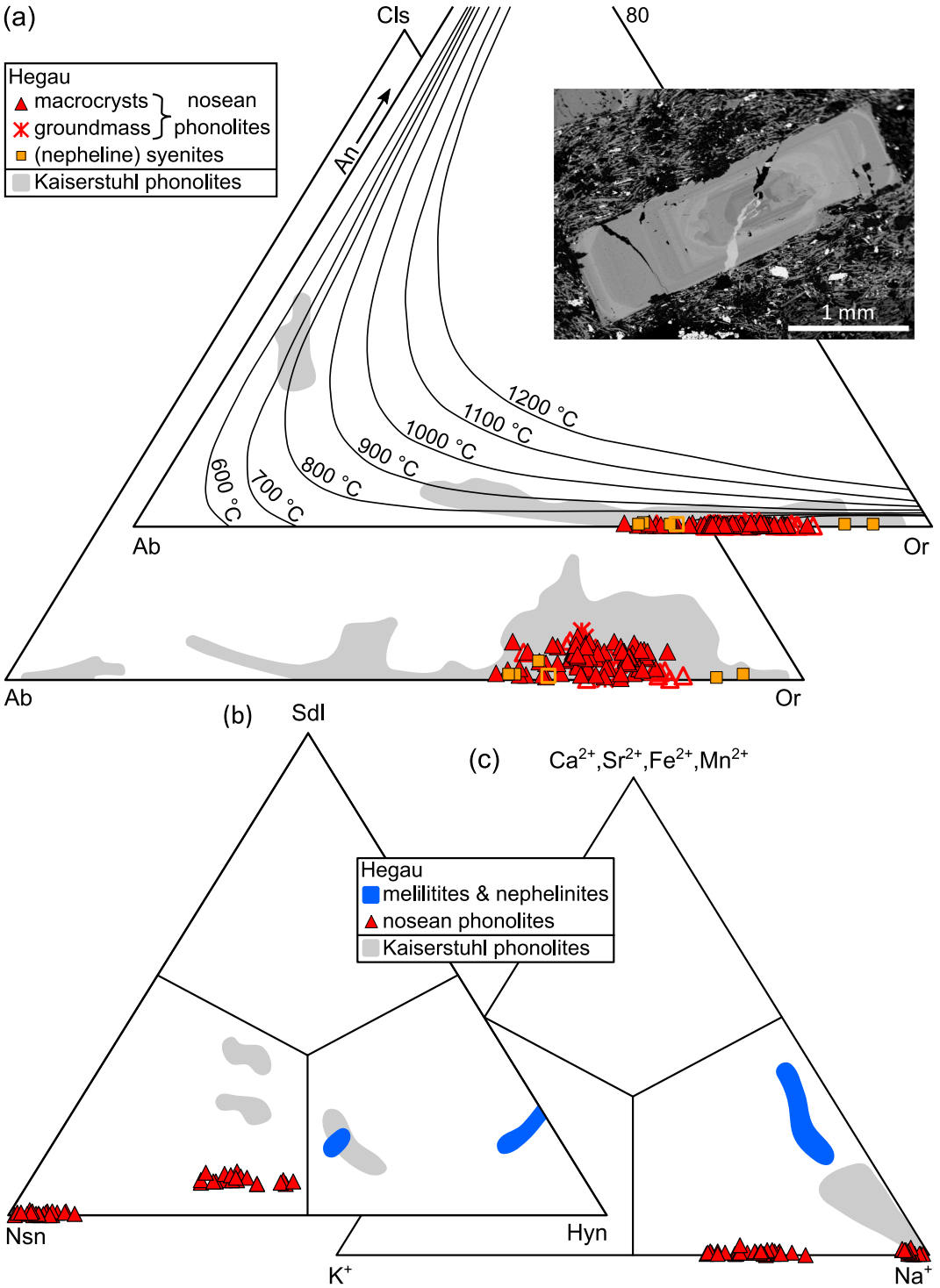

Fig. 10. Composition of feldspar and sodalite-group minerals in the igneous Hegau rocks. Data of this work supplemented by Binder et al. (in press). For comparison, the composition of feldspar and haüyne-nosean-sodalite$_{ss}$ in the Kaiserstuhl phonolites is also shown (Braunger et al., 2018). (a) Concentric compositional zoning of an alkali feldspar macrocryst in a nosean phonolite (Gönnersbohl) and triangular diagrams showing the distribution among the feldspar end-members celsian (Cls; Ba[$Al_2Si_2O_8$]), albite (Ab; Na[$AlSi_3O_8$]), and orthoclase (Or; K[$AlSi_3O_8$]) normalized to 100% and anorthite (An; Ca[$Al_2Si_2O_8$]), albite, and orthoclase normalized to 100%. Isotherms according to Fuhrman and Lindsley (1988). Triangular diagrams showing (b) the end-member composition of sodalite-group minerals based on the ratio between 2 SO_4^{2-}, SO_4^{2-}, and 2 Cl^-, with sodalite – $Na_6[Al_6Si_6O_{24}]Cl_2$ (Sdl), haüyne – $(Na,K)_6Ca_2[Al_6Si_6O_{24}](SO_4)_2$ (Hyn), and nosean – $Na_6[Al_6Si_6O_{24}]SO_4$ (Nsn), and (c) the molar K-Na-Ca,Sr,Fe,Mn distribution.

5.2. Nosean phonolites: products of fractional crystallization of melilititic–nephelinitic melts

Primitive melilitites–nephelinites and evolved phonolites show overlapping age ranges (12–9 Ma and 14–11 Ma, respectively), but phonolitic volcanism started earlier and the existence of evolved rocks in the crust at the time of eruption of the primitive magmas is indicated by the entrained coarse-grained (nepheline) syenitic enclaves (Fig. 4a). These can be interpreted as cumulate rocks with alkali feldspar ± aegirine-augite as dominant cumulus crystals and variable amounts of

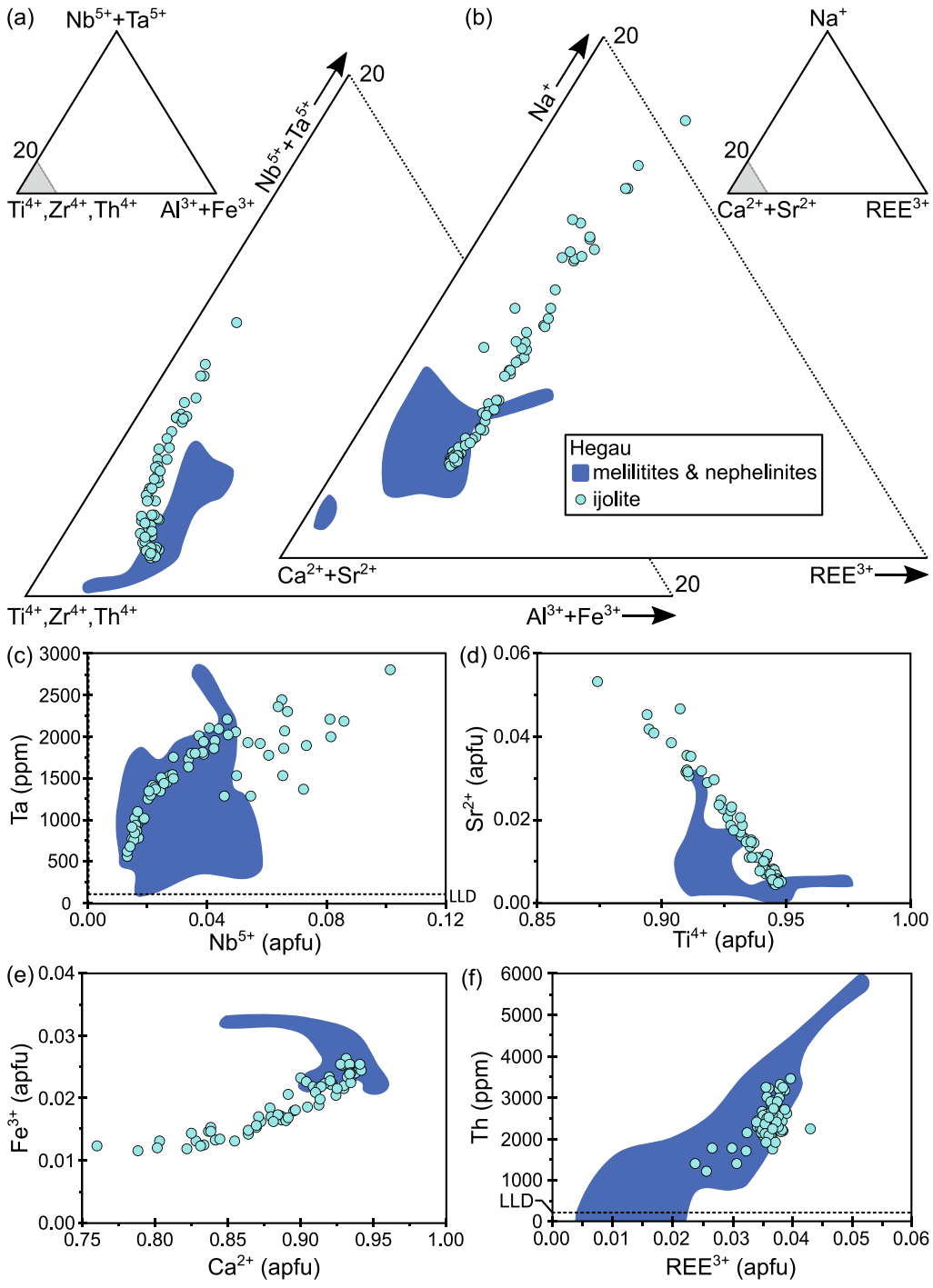

Fig. 11. Perovskite composition in the igneous Hegau rocks. Data of this work supplemented by Binder et al. (in press). Triangular diagrams showing (a) the molar Nb + Ta-Ti + Zr + Th-Al + Fe^{3+} and (b) the Na-REE-Ca + Sr distribution normalized to 100%. (c) Nb^{5+} vs. Ta, (d) Ti^{4+} vs. Sr^{2+}, (e) Ca^{2+} vs. Fe^{3+}, and (f) REE^{3+} vs. Th. apfu – atoms per formula unit; LLD – lower limit of detection; ppm – parts per million.

nepheline, aegirine-augite, alkali feldspar, dark mica, and little carbonate representing the intercumulus melt (Figs. 4b-g). The variable proportions of nepheline and clinopyroxene, partly within the same enclave (Fig. 4b), indicate a layered arrangement of mesocratic and leucocratic lithologies and point to an evolving and convecting magma chamber that may have experienced repeated magma replenishment.

Since all recorded enclaves mirror an already highly fractionated and thus SiO_2- and alkali-enriched magma composition, the question remains as to the primary magma composition from which the nosean phonolites evolved by differentiation, and whether this could be the same magma composition represented by the primitive melilitites–nephelinites. In this case, the older phonolitic volcanoes would have erupted only after significant magmatic differentiation in the crust, while the mostly younger melilititic–nephelinitic magmas would have been transported "directly" from mantle to surface. The evolution of clinopyroxene composition (Fig. 9) and the presence of sodalite group minerals (Fig. 10) in both the melilitites–nephelinites and phonolites support this assumption. The differences between primitive and evolved rocks in terms of clinopyroxene composition are consistent with the evolution of the whole-rock composition towards very low MgO and

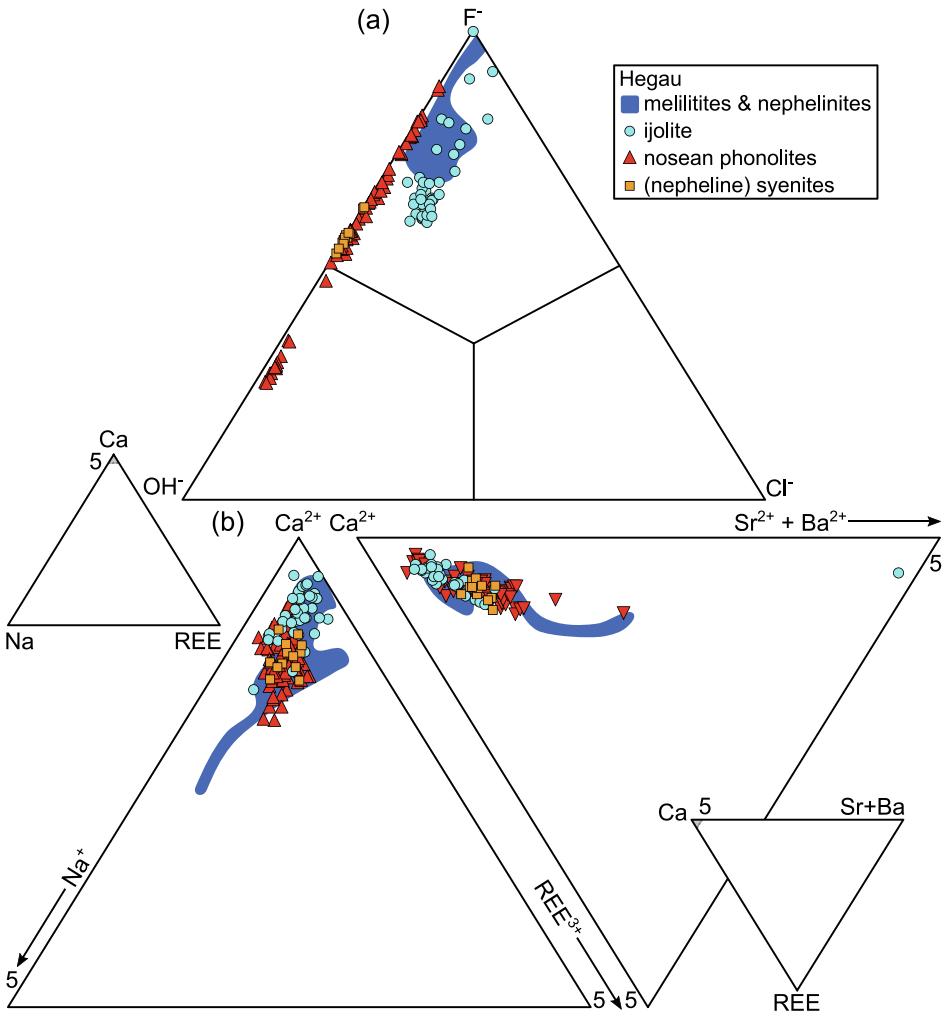

Fig. 12. Apatite composition in the igneous Hegau rocks. Data of this work supplemented by Binder et al. (in press). (a) Triangular classification diagram based on the anion position (OH^-, F^-, Cl^-). (b) Triangular diagrams showing the molar Ca-Na-REE and Ca-Sr + Ba-REE distribution each normalized to 100%.

CaO, and low $Fe_2O_3^{tot}$ contents (Figs. 6b & e). The marked decrease in CaO content and increase in K_2O content relative to the primitive rocks is also evident in the composition of the sodalite-group minerals: in the phonolites, these minerals lack Ca, but partially contain K, whereas for those in the melilitites–nephelinites, a high Ca content and hardly any K is observed (Fig. 10c). Higher Na_2O, Al_2O_3, and SiO_2 contents in phonolites (Figs. 5 & 6c) are reflected by abundant nepheline and alkali feldspar and the presence of titanite instead of perovskite, as it was observed in the primitive rocks including their ijolitic patches.

The primitive mantle-normalized REE patterns show a continuous decrease in enrichment towards the HREE, which for the primitive rocks can be explained by residual garnet in the mantle source that fractionates LREE from HREE (e.g., Kolb et al., 2012; Ulrych et al., 2011). The phonolites show a comparable enrichment factor for the REE, but with a marked trough of the MREE and higher contents of HREE relative to the primitive rocks (Fig. 8a). This can be explained by titanite fractionation, a mineral that enriches MREE over LREE and HREE (Prowatke and Klemme, 2005), and is supported by a remarkable negative Ti anomaly in the primitive mantle-normalized trace element pattern for phonolites (Fig. 8b), and by low Ca and Ti contents in the whole rock (Figs. 6b & f). Likewise, the fractionation of Zr from Hf (Zr/Hf = 78–103) and Nb from Ta (Nb/Ta = 38–82) in the phonolites (Fig. 8b; Supplementary data, File 1) can be attributed to titanite fractionation, as this mineral is more compatible for the heavy than the lighter geochemical twins (e.g., Berger et al., 2014). In contrast, the Zr/Hf ratios in the primitive melilitites–nephelinites are lower and relatively constant (38–44; cf. primitive mantle: ~34), whereas the Nb/Ta ratios vary already considerably (18–42; cf. primitive mantle: ~14), which may be attributed to different amounts of residual phlogopite (Green et al., 2000) or prior carbonate metasomatism in their mantle source (e.g., Pfänder et al., 2012).

The general lack of strong REE enrichment in the phonolites relative to the melilitites–nephelinites (Fig. 8a) is caused by apatite and possibly pyrochlore fractionation, in accordance with a striking P trough in the trace element pattern of the phonolites (Fig. 8b), and with low Ca contents in the whole rock. Abundant apatite, titanite, and accessory pyrochlore (Figs. 4h-k) in the entrained (nepheline) syenites corroborates fractionation of these minerals to generate the residual phonolitic melt. The remaining trace element patterns reflect relative enrichment of certain incompatible elements (e.g., Cs, Th, U, Ta, K, Nb, Hf, and Zr) in the evolved melt manifested by the accessories zircon, titanite, and pyrochlore, and elevated contents of Zr in clinopyroxene (Fig. 9e) as well as orthoclase-rich feldspar in the phonolites (Fig. 10a). The partly high Ba concentrations in alkali feldspar of the groundmass and in zoned phenocrysts (Fig. 10a) can be explained by high Ba contents in the parental melt (Fig. 8b) and further enrichment during fractionation, as is typical of nephelinite-derived phonolites (Le Bas, 1987). The lack of Cl in apatite in the nosean phonolites compared to ijolite and the primitive rocks (Fig. 12) may be due to the presence of abundant haüyne-nosean-sodalite$_{ss}$ in the evolved rocks incorporating all the Cl.

The slightly positive Pb anomaly compared to the strongly negative one in the primitive rocks (Fig. 8b), low Ce/Pb and strongly varying Nb/U ratios (Supplementary data, Fig. A4) could indicate assimilation of continental crust, as this would lower these ratios in mantle-derived magmas (e.g., Jung et al., 2012). In the CEVP and elsewhere, the formation of phonolites has been attributed mainly to fractional crystallization with subordinate to negligible crustal assimilation (Berger et al., 2009; Bourdon et al., 1994; Ulrych et al., 2003; Vaněčková et al., 1993; Wörner and Schmincke, 1984) or to significant and various amounts of crustal assimilation of e.g., mica schists, granites, paragneisses, metapelites, and mafic granulites (Jung et al., 2013; Kolb et al., 2012; Panina et al., 2000; Schleicher et al., 1990; Schmitt et al., 2017). However, verification and quantification of assimilation in the case of the Hegau phonolites would require isotopic data.

5.3. A thermodynamic modelling approach

To test the hypothesis that phonolites originate from fractional crystallization of olivine melilitites and melilite-bearing olivine nephelinites, the MELTS software package was used. Temperatures of up to 1350 °C for partial melting of the source lithology of the primitive melilitites–nephelinites of the Hegau region have been inferred by Binder et al. (in press) and are consistent with those for similar rocks from the CEVP (e.g., Jung et al., 2012; Mayer et al., 2013). However,

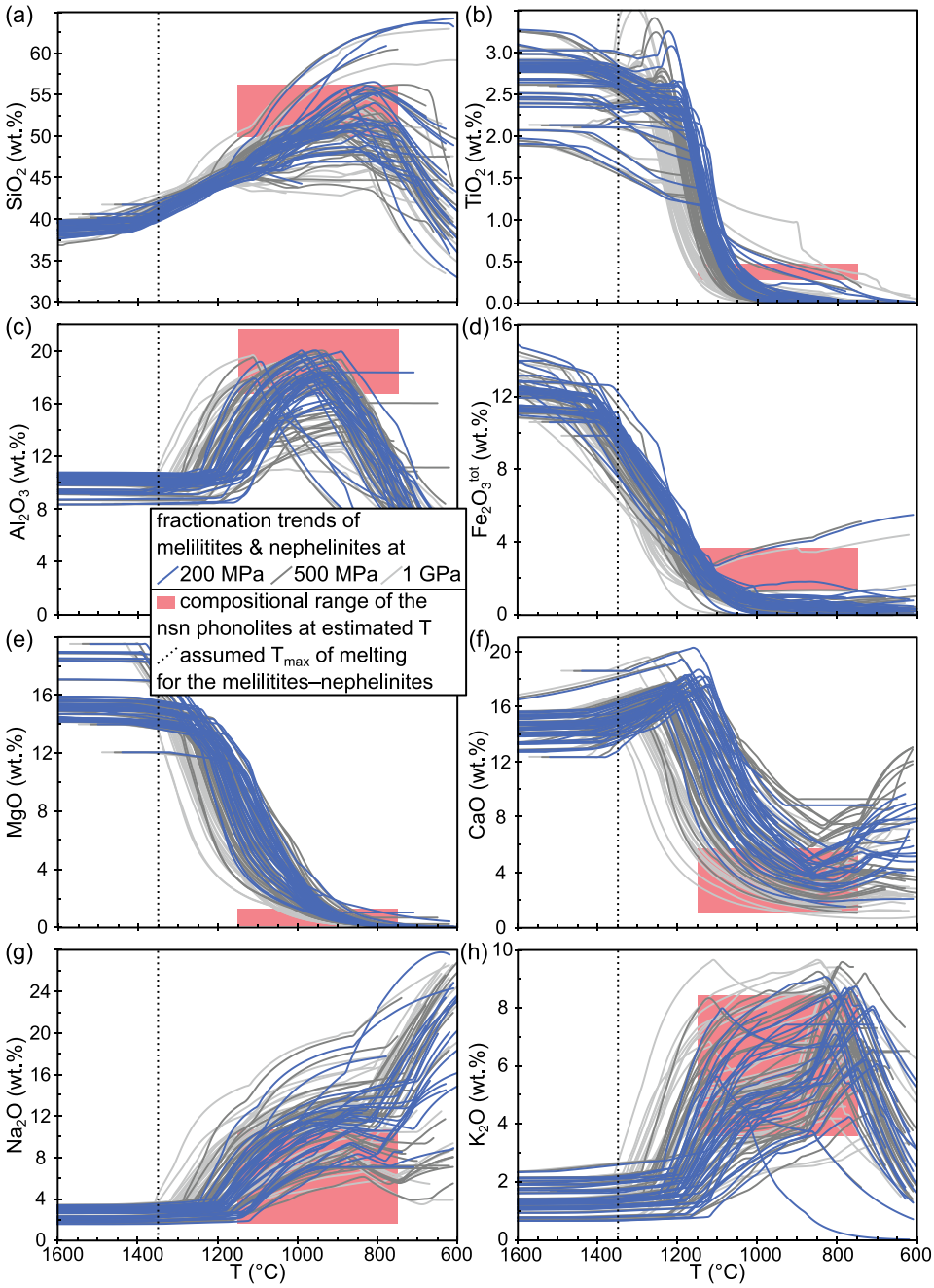

Fig. 13. Results of fractional crystallization modelling of melilititic–nephelinitic Hegau magmas at 200, 500 and 1000 MPa using MELTS (Ghiorso and Sack, 1995). The whole-rock compositions of the primitive rocks served as input data. For all major oxides, including (a) SiO_2, (b) TiO_2, (c) Al_2O_3, (d) $Fe_2O_3^{tot}$, (e) MgO, (f) CaO, (g) Na_2O, and (h) K_2O (each in wt%), phonolitic compositions can be realized by magmatic differentiation without significant crustal assimilation at temperatures of 750–1150 °C. The light red rectangles show the range of the whole-rock composition of the Hegau phonolites. (For interpretation of the references to colour in this figure legend, the reader is referred to the web version of this article.)

actual modelling was performed and depicted with higher starting temperatures to identify and avoid potential artifacts (discussed below). Residual melt fractions of >95 mass% and thus no significant changes in melt composition are predicted for most model curves until plausible liquidus temperatures for melilitites–nephelinites are reached (Figs. 13 & 14). Therefore, the used model parameters and most whole-rock analyses of the melilitites–nephelinites are considered suitable for testing fractional crystallization towards phonolites. A corresponding composition should be achieved at realistic temperatures and with a quantifiable residual melt fraction to propose fractional crystallization of melilititic–nephelinitic magmas in a closed system without requiring significant assimilation. All the phonolites have porphyritic textures, which indicates continuous crystallization during cooling. Additionally, magma convection and replenishment events can result in cumulate remobilization and remelting and/or entrainment of cumulate crystals, resetting the melt towards less evolved compositions and rendering a wide temperature interval conceivable (e.g., Sliwinski et al., 2015; Wörner and Wright, 1984). Thus, different element contents would not necessarily reach the concentrations observed in the nosean phonolites at the same temperature.

For crustal pressures between 200 and 1000 MPa, the range of whole-rock compositions of the phonolites can be reproduced (except for Mn and P) at temperatures of 750–1150 °C (Figs. 13 & 14; Supplementary data, Fig. A1), with upper crustal pressures (i.e., 200 MPa)

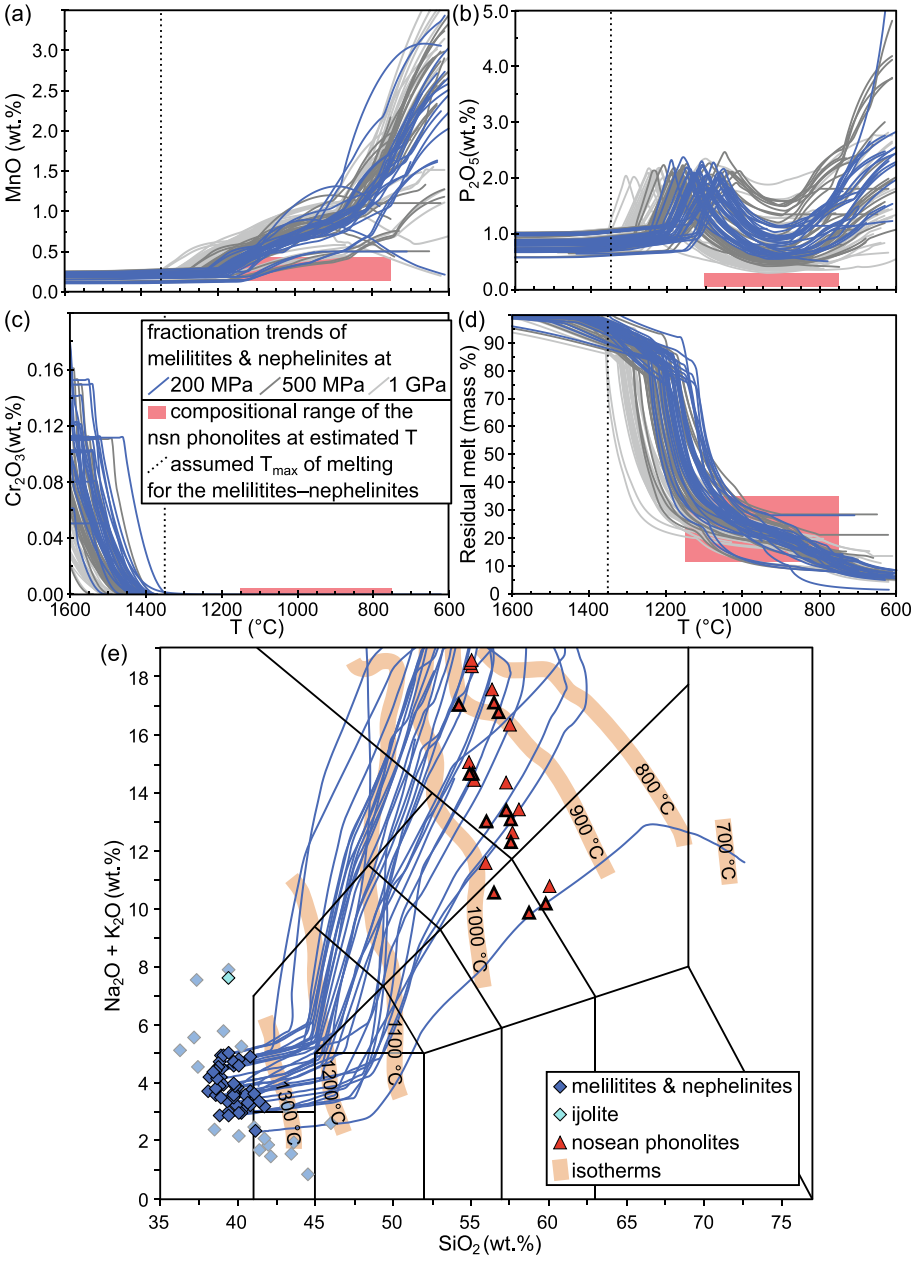

Fig. 14. Results of fractional crystallization modelling of melilititic–nephelinitic Hegau magmas at 200, 500 and 1000 MPa using MELTS (Ghiorso and Sack, 1995). The whole-rock compositions of the primitive rocks served as input data. (a) MnO, (b) P_2O_5, and (c) Cr_2O_3 (each in wt%). (d) Melt residues of ~12–35 mass% of the initial magma are responsible for most calculated phonolite compositions, regardless of formation pressure. (e) TAS diagram showing compositions of the volcanic Hegau rocks. 12 new analyses (black-rimmed triangles) were supplemented by literature data stated in Fig. 5. The trajectories show the melt evolution of melilititic–nephelinitic magmas predicted by MELTS modelling with whole-rock compositions of the primitive rocks as input data. For compositions from which no graphs emanate (pale blue squares), fractionation modelling was not successful. (For interpretation of the references to colour in this figure legend, the reader is referred to the web version of this article.)

tending to achieve the best-fit compositions. Geothermometric results for fractional crystallization towards phonolitic composition elsewhere reveal a similarly wide temperature range. Monchiquite- and tephrite-derived KVC phonolites started crystallizing at ~880–960 °C (Braunger et al., 2018) or at ~1040–1060 °C (Panina et al., 2000), while for the nephelinite-derived Katzenbuckel phonolite ~780–880 °C were estimated (Mann et al., 2006). The basanite-derived Laacher See mafic phonolite (East Eifel) reveals melt temperatures of ~860–1060 °C and the more evolved felsic one 720–860 °C (Berndt et al., 2001; Bourdon et al., 1994; Ginibre et al., 2004; Schmitt et al., 2010; Wörner and Wright, 1984). However, for sanidine and plagioclase (~950–1125 °C) and haüyne and apatite phenocrysts (1120–1180 °C) in the Upper Laacher See Tephra even higher crystallization temperatures were postulated (Sharygin et al., 2005). Alkaline rocks from Tenerife underwent a two-stage evolution from basanites via phonotephrites to phonolites with main crystallization intervals at ~1150–1110 °C and ~925–875 °C (Sliwinski et al., 2015).

No thermodynamic data for the Mn clinopyroxene end-member johannsenite and for fluorapatite are implemented in the MELTS database, which explains observed misfits concerning MnO and P_2O_5 (Figs. 14a & b). Further, the modelled Cr content drops by fractionation of oxyspinel well before the assumed melting temperatures for the primitive rocks are reached (Fig. 14c). This may be due to the lack of a Cr-bearing pyroxene in the MELTS database and/or excessively high Cr contents in the rocks because of Cr-rich oxyspinel and Cr-diopside xenocrysts (see Binder et al., in press). For a few whole-rock compositions of the primitive rocks with particularly low or high alkali contents, the modelling attempt resulted in an abortion of the computation, so that no differentiation path could be determined (pale blue squares in Fig. 14e). This may indicate that those whole-rock compositions do not represent primary melt compositions due to high xenocryst and antecryst loads, hydrothermal alteration, or low-temperature weathering.

Overall, modelling implies that, depending on the assumed initial composition and depth of the magma chamber, ~12–35 mass% of the initial melilititic–nephelinitic melt remains as residue when phonolitic compositions are reached (Fig. 14d). This agrees with estimates for phonolite evolution from Laacher See, for which 30 mass% derivative melt of a basanitic magma were calculated (Wörner and Schmincke, 1984). During melt evolution, SiO_2 and $Na_2O + K_2O$ enrichment is predicted, resulting in differentiation trajectories via basanites/tephrites ±(trachy)basalts, phonotephrites and tephriphonolites ±alkali-rich foidites to phonolites (blue curves in Fig. 14e). In particular, the lower alkali melilititic–nephelinitic magmas undergo a melt evolution resulting in the observed SiO_2 and alkali contents of the nosean phonolites at ~850–1000 °C (Fig. 14e).

Early fractionation of olivine (4–10%) and oxyspinel (11–19%) is predicted for most initial compositions (Figs. 15a & b). However, up to 3 mass% oxyspinel crystallization postulated at >1350 °C is likely caused by entrainment of mantle xenocrysts, leading to such modelling artifacts. These are only small quantities, so the effect should be negligible for the overall modelling, especially since this very early alleged fractionation partially corrects excessive Cr and Mg contents in whole-rock compositions towards actual melt compositions. Subsequently, extensive clinopyroxene fractionation (42–57%) is predicted (Fig. 15c), consistent with clinopyroxene in the mesocratic (nepheline) syenite enclaves (Table 2; Figs. 4f & g). Considering variable amounts of macrocrysts, but also microcrysts of clinopyroxene in the phonolites (<10% in total; Table 2; Figs. 3a-d), it can be assumed that its crystallization occurred over a long time and temperature interval and that fractionation and separation was not yet completed at the time of ascent of the phonolitic melt. This suggests temperatures of >900 °C at the time of melt extraction as clinopyroxene formation stops at lower temperatures (Fig. 15c).

Mica fractionation (<3%) is forecast from 1050 to 800 °C (Fig. 15d), supported by the mineralogy of (nepheline) syenites and phonolites (Table 2; Figs. 4e & f). The onset of feldspathoid crystallization (~3–9%), with two exceptions, occurs below 1000 °C, that of feldspar (mostly ~2–8%) below ~950 °C, continuing in each case until complete solidification of the proposed melts (Figs. 15e & f). Since the (nepheline) syenites also contain both phases as major minerals, formation of these rocks must have continued until cooling to at least 900 °C, more likely 800 °C. This correlates well with the crystallization of the phonolites as volcanic counterparts, and feldspar geothermometry, yielding temperatures below 800 °C (Fig. 10a).

It must be considered that the thermodynamic database of MELTS does not contain sodalite-group minerals, so nepheline is possibly overestimated and depending on the Na/K ratio and $aSiO_2$, additional feldspathoids (leucite, kalsilite) are erroneously predicted. However, the total amount of feldspathoids formed is plausible, since their average stoichiometry is similar with respect to the Al-Si-alkali ratio, and they form under comparable physicochemical conditions. The onset of garnet crystallization, which occurs in neither the nosean phonolites nor the (nepheline) syenites, is predicted at 750–700 °C (Fig. 15g), most likely representing sub-solidus temperatures for the rocks (e.g., Braunger et al., 2018; Mann et al., 2006). However, MELTS only includes the pyralspite solid solution series and the grossular end-member, but not andradite, so interpretations regarding garnet formation must be questioned. Further, 1–2% apatite fractionation may have been slightly underestimated (Fig. 15h) as the software considers only hydroxyapatite, yet F-dominated apatite prevails in the primitive and evolved rocks (Fig. 12a).

In summary, we propose crystallization of the phonolites between 1050 and 750 °C from an evolved magma of initially melilititic–nephelinitic composition, resembling the geochemical characteristics of the primitive Hegau rocks. Fractional crystallization occurred mainly in the upper crust (~200 MPa) and formed (nepheline) syenitic cumulates at 1050–800 °C, fragments of which were entrained into the ascending phonolitic, melilititic–nephelinitic magmas, and into melts forming the mafic augite-hornblende-phlogopite tuffs, causing the contemporaneous and subsequent eruptions in the Hegau region. Fractionation of 11–19% oxyspinel, 4–10% olivine, 42–57% clinopyroxene, <3% mica, <9% feldspathoids, <8% feldspar in the order mentioned, and minor amounts of titanite and apatite (~2%) result in a phonolitic melt residue representing ~12–35 mass% of the initial melt. Given the lack of isotope data, crustal contamination (assimilation) during fractional crystallization cannot be ruled out, although the modelling results imply that it is not required to explain the observed phonolite compositions.

5.4. The Daly gap and implications for magma ascent and emplacement

Why did pronounced upper crustal differentiation processes in the central eastern Hegau region at ~15–11 Ma (ages of nepheline syenites and syenites) culminated in the emplacement of phonolite domes 14–11 Myr ago, whereas largely undifferentiated primitive melilititic–nephelinitic lavas were emplaced in the northern and western Hegau region during and after phonolitic activity from 12 to 9 Ma? We suggest that the compositional gap between primitive and evolved magmas is due to the largely separated crystallization and segregation of specific mineral phases and the thermodynamically and rheologically favoured timing of melt extraction. MELTS modelling shows that down to a temperature of ~1100–1050 °C, predominantly the mafic minerals oxyspinel, olivine, and clinopyroxene as well as small amounts of apatite crystallize from a fractionating primitive, initially melilitite- and nepheline-normative magma and consequently reduce the melt to ~30–50% of the bulk (Figs. 14d & 15a-c). The lack of entrained enclaves or individual crystals of such wehrlitic to olivine-pyroxenitic cumulates in the phonolites is probably the result of effective gravitational separation of these dense mafic cumulus minerals from the light intermediate to felsic residual melt or complete dissolution because of strong disequilibrium with the continuously evolving residual melt.

Clinopyroxene and apatite formation continued down to ~900 °C,

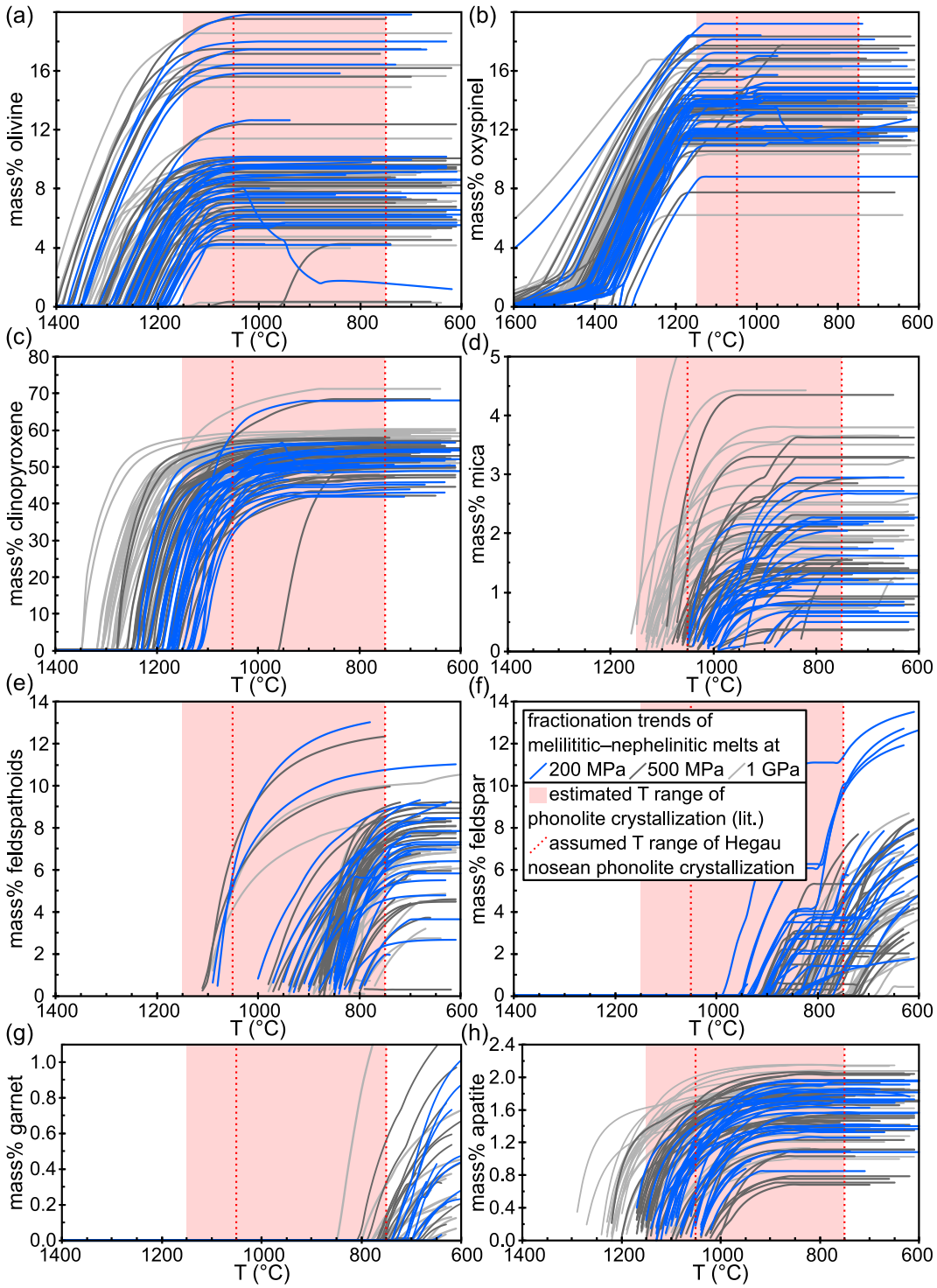

Fig. 15. Results of fractional crystallization modelling of melilititic–nephelinitic Hegau magmas at 200, 500 and 1000 MPa using MELTS (Ghiorso and Sack, 1995). The whole-rock compositions of the primitive rocks served as input data. Estimated fractionation of phases depending on temperature; (a) olivine, (b) oxyspinel, (c) clinopyroxene, (d) mica, (e) feldspathoids, (f) feldspar, (g) garnet, and (h) apatite (each in mass%).

while mica, feldspar, and feldspathoids started crystallizing between 1050 and 950 °C, proceeding until the phonolites solidified. This period of fractional crystallization is well recorded by the macrocryst load of the nosean phonolites and by the differently composed (nepheline) syenite cumulate enclaves (Table 2). They are characterized by a continuous evolution of mesocratic (nepheline) syenites with up to 30 vol% clinopyroxene and 5 vol% dark mica ± apatite, titanite, and zircon to leucocratic (nepheline) syenites with alkali feldspar and dark mica ± nepheline, carbonate, titanite, pyrochlore, zircon, thorite, and thorianite (Fig. 4). Possibly, magma replenishment of intermediate composition triggered the eruption of the phonolites with entrainment of cumulate fragments and crystals at a temperature > 900 °C when clinopyroxene and apatite still crystallized. Related models to explain compositional gaps in bimodal alkaline volcanism (Canary Islands, Ethiopian Rift) likewise include substantial temporal separation between the crystallization of mafic and felsic minerals and preferential magma mobilization

at specific times. This is explained by exceeding the intermediate differentiation stage within a narrow temperature interval with a respectively low crystallization rate (Peccerillo et al., 2003) or by optimal melt extraction from a crystal mush at intermediate crystallinity (i.e., 30–60% fractionation; Sliwinski et al., 2015). Accordingly, the latter is associated with favourable rheological conditions and released heat of crystallization, which lowers the crystallization rate, providing time for crystal-magma separation.

Moreover, variations of density and plasticity of different basement lithologies and deflection along the interface of low-angle thrust faults may have affected the buoyancy of mafic melts, protracting ascent and allowing differentiation of the magmas in some cases (e.g., Lusatian Volcanic field; Büchner et al., 2015). In the Eger Graben, primitive olivine melilitites and olivine nephelinites are associated with phases of compressional stress and occur mainly in the pre-rift and subordinately in the late-rift period, while more evolved rocks dominate in the *syn*-rift phase under extensional stresses (Ulrych et al., 2011). Accordingly, volcanic rocks coeval with compressive stresses are associated with major faults, whereas volcanism coinciding with extensional stress shows a much weaker structural control, which may hinder rapid ascent and protract differentiation. Similarly, Przybyla et al. (2018) suggest a phase of intense rifting, i.e., a discrete event of lithosphere stretching and/or disruption to have caused a short phase of felsic volcanism in the Siebengebirge near Bonn, whereas undifferentiated mafic lavas erupted over a longer period before and after (>8 Myr). They propose a magmatic plumbing system, which emptied from the top down over more evolved to more primitive lavas within <1 Myr.

Analogously, we propose a structurally controlled mechanism for differentiation, ascent, eruption, and emplacement of the Hegau magmas governed by the regional geodynamic evolution. The latest possible onset of upper crustal differentiation processes is documented by the oldest (nepheline) syenite ages (~15 Ma, Hohenstoffeln; Fig. 1; Binder et al., 2023) and extends over wide areas of the Hegau basement. This is evidenced by corresponding enclaves in numerous occurrences of volcanic rocks scattered throughout the region and consistent with remote sensing and GIS studies, indicating an extensive sub-surface, ring-shaped magmatic structure (Theilen-Willige, 2011). Pronounced uplift in the Vosges-Swabian arc, i.e., at the southern end of the South German Block including the Hegau region, reflected by a phase of intensified erosion in the Swabian Alb (Ring and Bolhar, 2020), may have triggered this magmatic activity. Uplift and erosion proceeded during late Miocene to early Pliocene shortening and provoked thin-skinned thrusting and folding in the Jura Mountains and Molasse basin (<12–10 Ma; Becker, 2000; von Hagke et al., 2012), overlapping with the age of the younger primitive volcanic rocks in the study area. Thus, intensified uplift and rifting may have firstly led to the development of larger upper crustal magma chambers and associated differentiation processes producing (nepheline) syenite cumulates and phonolitic melts. Subsequently, ongoing, progressive graben formation and disruption of the upper crust by emergence of local and/or (re) activation of deep-seated fault systems may have facilitated rapid magma ascent such that eruptions of melilititic–nephelinitic melts and mafic tuffs occurred without extensive fractionation. Obviously, this does not exclude a temporal overlap of the different manifestations of volcanism in the Hegau region, which can be explained by the spatial heterogeneity of the faulted crust.

6. Conclusions

Based on petrography, mineral chemistry, fractionation modelling, and previous U—Pb geochronology, the following model for the magmatic evolution in the Hegau region is proposed.

(1) The composition of evolved nosean phonolites (14–11 Ma) can be modelled by fractional crystallization of a melilititic–nephelinitic magma, whose composition resembles that of regional primitive olivine melilitites and melilite-bearing olivine nephelinites (12–9 Ma). Fractionation of 11–19% oxyspinel, 4–10% olivine, 42–57% clinopyroxene, <3% mica, <9% feldspathoids, <8% feldspar, and minor amounts of titanite and apatite results in phonolitic residues that represent ~12–35 mass% of the initial melt. The large compositional range of the nosean phonolites is explained by relatively small differences in potential parental melt compositions and variable degrees of fractionation. Crustal assimilation is not excluded but not essential to explain the mineralogical, mineral chemical, and geochemical features.

(2) The modelled compositions representing the observed phonolite compositions best were achieved for a pressure of 200 MPa, consistent with upper crustal formation conditions for phonolites in the CEVP and elsewhere. The predicted mineral assemblages agree largely with the petrography of the nosean phonolites and (nepheline) syenite cumulates, suggesting that the latter crystallized at temperatures of 1050–800 °C and that the phonolite melt was extracted at >900 °C.

(3) A temporal progression from evolved rocks that experienced prolonged differentiation in upper crustal magma chambers (nosean phonolites) towards near-primary, fast ascending primitive melts (melilititic–nephelinitic rocks) could explain the sequence of eruptions in the Hegau region. The onset of magmatism corresponds temporally with a regional phase of intensified erosion in response to pronounced uplift in the Vosges-Swabian arc. This may have firstly led to the development of larger upper crustal magma chambers and associated differentiation processes that produced (nepheline) syenite cumulates and phonolitic melts. Increased uplift and erosion during late Miocene to early Pliocene crustal shortening coincide with the age of the younger, but more primitive volcanic rocks. Thus, ongoing, progressive graben formation may have facilitated magma ascent such that eruptions of melilititic–nephelinitic melts and mafic tuffs occurred without extensive prior fractionation.

Funding

This work was supported by the Deutsche Forschungsgemeinschaft (DFG) [grant MA 2563/19 & WA 3116/6]. The funding source was not involved in the study design, in the collection, analysis and interpretation of data, in the writing of the manuscript, and in the decision to submit the article for publication.

Declaration of competing interest

Thomas Binder reports financial support was provided by Deutsche Forschungsgemeinschaft. If there are other authors, they declare that they have no known competing financial interests or personal relationships that could have appeared to influence the work reported in this paper.

Data availability

The data underlying this article are available in the article and in its online supplementary data. Whole-rock geochemistry was supplemented by literature data from Alibert et al. (1983), Dunworth and Wilson (1998), Engelhardt and von Engelhardt and Weiskirchner (1961), Keller et al. (1990), Krause (1969), Krause and Weiskirchner (1981), Staesche (1995), Stock (1990), and Wimmenauer (1974).

Acknowledgements

We are grateful to the Deutsche Forschungsgemeinschaft (DFG) for financial support for the acquisition of the electron probe microanalyzer [grant: INST 37/1026-1 FUGG]. We thank the Landesamt für Geologie,

Rohstoffe und Bergbau (LGRB, Freiburg im Breisgau) and Udo Neumann (University of Tübingen) for providing samples used in this study. Thanks also to Simone Schafflick and Philip Werner (University of Tübingen) for sample preparation. Moreover, we thank Elisabeth Eiche, Claudia Mößner, and Janine Wagner (LERA, KIT) for their support in the whole-rock analyses. We gratefully acknowledge the constructive reviews by Juliana Troch and an anonymous reviewer, as well as the handling by the co-editor-in-chief Greg Shellnutt.

Appendix A. Supplementary data

Supplementary data to this article can be found online at https://doi.org/10.1016/j.lithos.2024.107565.

References

Alibert, C., Michard, A., Albarède, F., 1983. The transition from alkali basalts to kimberlites: Isotope and trace element evidence from melilitites. Contrib. Mineral. Petrol. 82, 176–186.
Andersen, T., 1988. Evolution of peralkaline calcite carbonatite magma in the Fen complex, Southeast Norway. Lithos 22, 99–112.
Becker, A., 2000. The Jura Mountains — an active foreland fold-and-thrust belt? Tectonophysics 321, 381–406.
Berger, J., Ennih, N., Mercier, J.-C.C., Liégeois, J.-P., Demaiffe, D., 2009. The role of fractional crystallization and late-stage peralkaline melt segregation in the mineralogical evolution of Cenozoic nephelinites/phonolites from Saghro (SE Morocco). Mineral. Mag. 73, 59–82.
Berger, J., Ennih, N., Liégeois, J.-P., 2014. Extreme trace elements fractionation in Cenozoic nephelinites and phonolites from the Moroccan Anti-Atlas (Eastern Saghro). Lithos 210-211, 69–88.
Berndt, J., Holtz, F., Koepke, J., 2001. Experimental constraints on storage conditions in the chemically zoned phonolitic magma chamber of the Laacher See volcano. Contrib. Mineral. Petrol. 140, 469–486.
Binder, T., Marks, M., Walter, B.F., Wenzel, T., Markl, G., 2024. Two Distinct Metasomatized Mantle Sources Produced Two Groups of Alkaline SiO_2-undersaturated Rocks in the Southern Central European Volcanic Province. J. Petrol. in press.
Binder, T., Marks, M.A.W., Walter, B.F., Wenzel, T., Markl, G., Gerdes, A., Grimmer, J., Beranoaguirre, A., 2023. Two distinct age groups of melilitites, foidites, and basanites from the southern central European Volcanic Province reflect lithospheric heterogeneity. Int. J. Earth Sci. 112, 881–905.
Blusztajn, J., Hegner, E., 2002. Osmium isotopic systematics of melilitites from the Tertiary central European Volcanic Province in SW Germany. Chem. Geol. 189, 91–103.
Bourdon, B., Zindler, A., Wörner, G., 1994. Evolution of the Laacher See magma chamber: evidence from SIMS and TIMS measurements of U-Th disequilibria in minerals and glasses. Earth Planet. Sci. Lett. 126, 75–90.
Braunger, S., Marks, M.A.W., Walter, B.F., Neubauer, R., Reich, R., Wenzel, T., Parsapoor, A., Markl, G., 2018. The Petrology of the Kaiserstuhl Volcanic complex, SW Germany: the Importance of Metasomatized and Oxidized Lithospheric Mantle for Carbonatite Generation. J. Petrol. 59, 1731–1762.
Büchner, J., Tietz, O., Viereck, L., Suhr, P., Abratis, M., 2015. Volcanology, geochemistry and age of the Lausitz Volcanic Field. Int. J. Earth Sci. 104, 2057–2083.
Chen, L., Zheng, Y.-F., Zhao, Z.-F., 2018. A common crustal component in the sources of bimodal magmatism: Geochemical evidence from Mesozoic volcanics in the Middle-lower Yangtze Valley, South China. GSA Bull. 130, 1959–1980.
Corti, G., 2009. Continental rift evolution: from rift initiation to incipient break-up in the Main Ethiopian Rift, East Africa. Earth Sci. Rev. 96, 1–53.
Deering, C.D., Bachmann, O., Dufek, J., Gravley, D.M., 2011. Rift-Related transition from Andesite to Rhyolite Volcanism in the Taupo Volcanic Zone (New Zealand) Controlled by Crystal–melt Dynamics in Mush zones with Variable Mineral Assemblages. J. Petrol. 52, 2243–2263.
Dunworth, E.A., Wilson, M., 1998. Olivine Melilitites of the SW German Tertiary Volcanic Province: Mineralogy and Petrogenesis. J. Petrol. 39, 1805–1836.
Egli, D., Mosar, J., Ibele, T., Madritsch, H., 2017. The role of precursory structures on Tertiary deformation in the Black Forest—Hegau region. Int. J. Earth Sci. 106, 2297–2318.
von Engelhardt, W., Weiskirchner, W., 1961. Einführung zu den Exkursionen der Deutschen Mineralogischen Gesellschaft: zu den Vulkanschloten der Schwäbischen Alb und in den Hegau während der 39. Jahrestagung in Tübingen vom 11. bis 17. September 1961. Jahrestag. Deuts. Mineral. Gesellsch. 39, 1–24.
Frenzel, G., 1975. Die Nephelingesteinsparagenese des Katzenbuckels im Odenwald. In: Amstutz, G.C., Meisl, S., Nickel, E. (Eds.), Mineralien und Gesteine im Odenwald: Beiträge zum heutigen Forschungsstand. Heidelberg, pp. 213–228.
Freudenberg, W., 1906. Geologie und Petrographie des Katzenbuckels im Odenwald. Mitteilung. Grossherzogl. Badisch. Geol. Landesanst. 5, 185–344.
Freundt-Malecha, B., 2001. Plutonic rocks of intermediate composition on Gran Canaria: the missing link of the bimodal volcanic rock suite. Contrib. Mineral. Petrol. 141, 430–445.
Fuhrman, M.L., Lindsley, D.H., 1988. Ternary-feldspar modeling and thermometry. Am. Mineral. 73, 201–215.
Ghiorso, M.S., Gualda, G.A.R., 2015. An H_2O–CO_2 mixed fluid saturation model compatible with rhyolite-MELTS. Contrib. Mineral. Petrol. 169.
Ghiorso, M.S., Sack, R.O., 1995. Chemical mass transfer in magmatic processes IV. A revised and internally consistent thermodynamic model for the interpolation and extrapolation of liquid-solid equilibria in magmatic systems at elevated temperatures and pressures. Contrib. Mineral. Petrol. 119, 197–212.
Ginibre, C., Wörner, G., Kronz, A., 2004. Structure and Dynamics of the Laacher See Magma Chamber (Eifel, Germany) from Major and Trace Element Zoning in Sanidine: a Cathodoluminescence and Electron Microprobe Study. J. Petrol. 45, 2197–2223.
Gornitz, V., 1981. Skeletal crystals. In: Frye, K. (Ed.), The Encyclopedia of Mineralogy. Hutchinson Ross Publishing Company, Boston, MA, pp. 469–473.
Govindaraju, K., 1994. 1994 Compilation of Working Values and Sample Description for 383 Geostandards. Geostand. Newslett. 18, 1–158.
Green, T.H., Blundy, J.D., Adam, J., Yaxley, G.M., 2000. SIMS determination of trace element partition coefficients between garnet, clinopyroxene and hydrous basaltic liquids at 2–7.5 GPa and 1080–1200°C. Lithos 53, 165–187.
Gualda, G.A.R., Ghiorso, M.S., Lemons, R.V., Carley, T.L., 2012. Rhyolite-MELTS: a Modified Calibration of MELTS Optimized for Silica-rich, Fluid-bearing Magmatic Systems. J. Petrol. 53, 875–890.
von Hagke, C., Cederbom, C.E., Oncken, O., Stöckli, D.F., Rahn, M.K., Schlunegger, F., 2012. Linking the northern Alps with their foreland: the latest exhumation history resolved by low-temperature thermochronology. Tectonics 31, 1–25.
Hegner, E., Vennemann, T.W., 1997. Role of fluids in the origin of Tertiary European intraplate volcanism: evidence from O, H, and Sr isotopes in melilitites. Geology 25, 1035–1038.
Hoernle, K., Schmincke, H.-U., 1993. The Role of Partial Melting in the 15-Ma Geochemical Evolution of Gran Canaria: a Blob Model for the Canary Hotspot. J. Petrol. 34, 599–626.
Jung, S., Vieten, K., Romer, R.L., Mezger, K., Hoernes, S., Satir, M., 2012. Petrogenesis of Tertiary Alkaline Magmas in the Siebengebirge, Germany. J. Petrol. 53, 2381–2409.
Jung, S., Mezger, K., Hauff, F., Pack, A., Hoernes, S., 2013. Petrogenesis of rift-related tephrites, phonolites and trachytes (central European Volcanic Province, Rhön, FRG): Constraints from Sr, Nd, Pb and O isotopes. Chem. Geol. 354, 203–215.
Keller, J., Brey, G., Lorenz, V., Sachs, P., 1990. Volcanism and Petrology of the Upper Rhinegraben (Urach-Hegau-Kaiserstuhl). In: Urach, Hegau, Kaiserstuhl: Excursion 2A, August 27 to September 2, 1990. Mainz, pp. 1–60.
Kolb, M., Paulick, H., Kirchenbaur, M., Münker, C., 2012. Petrogenesis of Mafic to Felsic Lavas from the Oligocene Siebengebirge Volcanic Field (Germany): Implications for the Origin of Intracontinental Volcanism in Central Europe. J. Petrol. 53, 2349–2379.
Kong, W., Zhang, Z., Zhang, D., Wang, C., Santosh, M., Liu, B., Wei, B., 2023. New insights into deep carbon recycling and formation of nepheline-bearing alkaline rocks from Sr-Nd-Mg isotope compositions. GSA Bull. 135, 1530–1546.
Krause, O., 1969. Die Melilith-Nephelinite des Hegaus. Dissertation. Tübingen, p. 103.
Krause, O., Weiskirchner, W., 1981. Die Olivin-Nephelinite des Hegaus. Jahresh. Geol. Landes. Baden-Württemb. 23, 87–130.
Lacasse, C., Sigurdsson, H., Carey, S.N., Jóhannesson, H., Thomas, L.E., Rogers, N.W., 2007. Bimodal volcanism at the Katla subglacial caldera, Iceland: insight into the geochemistry and petrogenesis of rhyolitic magmas. Bull. Volcanol. 69, 373–399.
Le Bas, M.J., 1987. Nephelinites and carbonatites. Geol. Soc. Lond. Spec. Publ. 30, 53–83.
Lexa, J., Seghedi, I., Németh, K., Szakács, A., Konečny, V., Pécskay, Z., Fülöp, A., Kovacs, M., 2010. Neogene-Quaternary Volcanic forms in the Carpathian-Pannonian Region: a review. Cent. Eur. J. Geosci. 2, 207–270.
Mahfoud, R.F., Beck, J.N., 1989. Alkaline basalt-phonolite rocks from the Singen area, Hegau, southern F.R.G. Chem. Geol. 74, 217–227.
Mann, U., Marks, M.A., Markl, G., 2006. Influence of oxygen fugacity on mineral compositions in peralkaline melts: the Katzenbuckel volcano, Southwest Germany. Lithos 91, 262–285.
Mäussnest, O., Schreiner, A., 1982. Karte der Vorkommen von Vulkangesteinen im Hegau. Abhandl. Geol. Landes. Baden-Württemb. 10, 1–48.
Mayer, B., Jung, S., Romer, R.L., Stracke, A., Haase, K.M., Garbe-Schönberg, C.D., 2013. Petrogenesis of Tertiary Hornblende-bearing Lavas in the Rhön, Germany. J. Petrol. 54, 2095–2123.
Mourey, A.J., France, L., Ildefonse, B., Gurenko, A., Laporte, D., 2023. Genesis of Carbonatite at Oldoinyo Lengai (Tanzania) from Olivine Nephelinite: Protracted Melt Evolution and Reactive Porous Flow in Deep Crustal Mushes. J. Petrol. 64, egad084.
Palme, H., O'Neill, H., 2014. Cosmochemical estimates of Mantle Composition. In: Holland, H.D., Turekian, K.K. (Eds.), The Mantle and Core, 2nd ed. Elsevier, Amsterdam, Heidelberg, pp. 1–39.
Panina, L.I., Sharygin, V.V., Keller, J., 2000. Olivine nephelinite, tephrite, essexite, phonolite, and tinguaite from Kaiserstuhl, Germany: evidence from melt inclusions in pyroxene. Geochem. Int. 38, 343–352.
Peccerillo, A., Barberio, M.R., Yirgu, G., Ayalew, D., Barbieri, M., Wu, T.W., 2003. Relationships between Mafic and Peralkaline Silicic Magmatism in Continental Rift Settings: a Petrological, Geochemical and Isotopic Study of the Gedemsa Volcano, Central Ethiopian Rift. J. Petrol. 44, 2003–2032.
Peccerillo, A., Donati, C., Santo, A.P., Orlando, A., Yirgu, G., Ayalew, D., 2007. Petrogenesis of silicic peralkaline rocks in the Ethiopian rift: Geochemical evidence and volcanological implications. J. Afr. Earth Sci. 48, 161–173.
Pfänder, J.A., Jung, S., Münker, C., Stracke, A., Mezger, K., 2012. A possible high Nb/Ta reservoir in the continental lithospheric mantle and consequences on the global Nb budget – evidence from continental basalts from Central Germany. Geochim. Cosmochim. Acta 77, 232–251.

Prowatke, S., Klemme, S., 2005. Effect of melt composition on the partitioning of trace elements between titanite and silicate melt. Geochim. Cosmochim. Acta 69, 695–709.
Przybyla, T., Pfänder, J.A., Münker, C., Kolb, M., Becker, M., Hamacher, U., 2018. High-resolution $^{40}Ar/^{39}Ar$ geochronology of volcanic rocks from the Siebengebirge (Central Germany)—Implications for eruption timescales and petrogenetic evolution of intraplate volcanic fields. Int. J. Earth Sci. 107, 1465–1484.
Ring, U., Bolhar, R., 2020. Tilting, uplift, volcanism and disintegration of the south German block. Tectonophysics 795, 228611.
Rooney, T., Furman, T., Bastow, I., Ayalew, D., Yirgu, G., 2007. Lithospheric modification during crustal extension in the Main Ethiopian Rift. J. Geophys. Res. Solid Earth 112. B10201.
Rooney, T.O., 2020. The Cenozoic magmatism of East Africa: Part II – Rifting of the mobile belt. Lithos 360-361, 105291.
Schleicher, H., Keller, J., Kramm, U., 1990. Isotope studies on alkaline volcanics and carbonatites from the Kaiserstuhl, Federal Republic of Germany. Lithos 26, 21–35.
Schmitt, A.K., Wetzel, F., Cooper, K.M., Zou, H., Wörner, G., 2010. Magmatic Longevity of Laacher See Volcano (Eifel, Germany) Indicated by U–Th Dating of Intrusive Carbonatites. J. Petrol. 51, 1053–1085.
Schmitt, A.K., Klitzke, M., Gerdes, A., Schäfer, C., 2017. Zircon Hafnium–Oxygen Isotope and Trace Element Petrochronology of Intraplate Volcanic Rocks from the Eifel (Germany) and Implications for Mantle versus Crustal Origins of Zircon Megacrysts. J. Petrol. 58, 1841–1870.
Schreiner, A., 2008. Hegau und westlicher Bodensee, 3rd ed. Borntraeger, Berlin, Stuttgart, p. 90.
Sharygin, V.V., Di Muro, A., Madyukov, I.A., 2005. Crystallization Temperature of Haüyne from Phonolite (ULST, E.Eifel, Germany) and Haüynophyre (Vulture volcano, Italy): Evidence from Silicate Melt Inclusions. Abstract E-book of ECROFI 18.
Sliwinski, J.T., Bachmann, O., Ellis, B.S., Dávila-Harris, P., Nelson, B.K., Dufek, J., 2015. Eruption of shallow crystal cumulates during explosive phonolitic eruptions on Tenerife, Canary Islands. J. Petrol. 56, 2173–2194.
Staesche, A., 1995. Der genetische Zusammenhang zwischen Melilithiten und Phonolithen des Hegaus, SW-Deutschland (Diploma thesis). Tübingen, p. 66.
Stähle, V., Koch, M., 2003. Primary and secondary pseudobrookite minerals in volcanic rocks from the Katzenbuckel Alkaline complex, southwestern Germany. Swiss Bull. Mineral. Petrol. 83, 145–158.
Stock, M., 1990. Mikrothermometrische Untersuchung der Fluid- und Schmelzeinschlüsse in Olivinen der Nephelinite vom Neuhewen und Hohenstoffeln (Hegau). Diploma thesis. Tübingen, p. 86.
Tamura, Y., Tatsumi, Y., 2002. Remelting of an Andesitic Crust as a possible Origin for Rhyolitic Magma in Oceanic Arcs: an example from the Izu-Bonin Arc. J. Petrol. 43, 1029–1047.
Theilen-Willige, B., 2011. Remote sensing and GIS studies of the Hegau Volcanic Area in SW Germany. Photogram. – Fernerkund. – Geoinform. 2011, 361–372.
Trua, T., Deniel, C., Mazzuoli, R., 1999. Crustal control in the genesis of Plio-Quaternary bimodal magmatism of the Main Ethiopian Rift (MER): geochemical and isotopic (Sr, Nd, Pb) evidence. Chem. Geol. 155, 201–231.
Ulrych, J., Lloyd, F.E., Balogh, K., 2003. Age Relations and Geochemical Constraints of Cenozoic Alkaline Volcanic Series in W Bohemia: a Review. GeoLines 15, 168–180.
Ulrych, J., Lloyd, F.E., Balogh, K., Hegner, E., Langrová, A., Lang, M., Novák, J.K., Řanda, Z., 2005. Petrogenesis of alkali pyroxenite and ijolite xenoliths from the Tertiary Loucna–Oberwiesenthal Volcanic Centre, Bohemian Massif in the light of new mineralogical, geochemical, and isotopic data. Neues Jahrb. Mineral. - Abhandlung. (J. Mineral. Geochem.) 182, 57–79.
Ulrych, J., Dostal, J., Adamovič, J., Jelínek, E., Špaček, P., Hegner, E., Balogh, K., 2011. Recurrent Cenozoic volcanic activity in the Bohemian Massif (Czech Republic). Lithos 123, 133–144.
Vaněčková, M., Holub, F.V., Souček, J., Bowes, D.R., 1993. Geochemistry and petrogenesis of the tertiary alkaline volcanic suite of the Labe tectonovolcanic zone, Czech Republic. Mineral. Petrol. 48, 17–34.
Wilson, M., Downes, H., Cebriá, J.-M., 1995a. Contrasting fractionation trends in coexisting Continental Alkaline Magma Series; Cantal, Massif Central, France. J. Petrol. 36, 1729–1753.
Wilson, M., Rosenbaum, J.M., Dunworth, E.A., 1995b. Melilitites: partial melts of the thermal boundary layer? Contrib. Mineral. Petrol. 119, 181–196.
Wimmenauer, W., 1974. The Alkaline Province of Central Europe and France. In: Sørensen, H. (Ed.), The Alkaline Rocks, pp. 238–271.
Wörner, G., Schmincke, H.-U., 1984. Petrogenesis of the Zoned Laacher See Tephra. J. Petrol. 25, 836–851.
Wörner, G., Wright, T.L., 1984. Evidence for Magma mixing within the Laacher See Magma Chamber (East Eifel, Germany). J. Volcanol. Geotherm. Res. 22, 301–327.
Zaitsev, A.N., Marks, M., Wenzel, T., Spratt, J., Sharygin, V.V., Strekopytov, S., Markl, G., 2012. Mineralogy, geochemistry and petrology of the phonolitic to nephelinitic Sadiman volcano, Crater Highlands, Tanzania. Lithos 152, 66–83.
Zhao, K., Xu, X., Bachmann, O., Nan, T., Xia, Y., 2023. H_2O-controlled eruptive filtering on the bimodality of Continental Volcanism across tectonic settings. J. Petrol. 64, egad006.
Zou, H., Zindler, A., 1996. Constraints on the degree of dynamic partial melting and source composition using concentration ratios in magmas. Geochim. Cosmochim. Acta 60, 711–717.